

# **Glacial response to global climate changes: cosmogenic nuclide chronologies from high and low latitudes**



**Stefan Strasky**

Diss. ETH No. 17569  
2008



DISS. ETH NO. 17569

**GLACIAL RESPONSE TO GLOBAL CLIMATE CHANGES:  
COSMOGENIC NUCLIDE CHRONOLOGIES  
FROM HIGH AND LOW LATITUDES**

A dissertation submitted to

ETH ZURICH

for the degree of

Doctor of Sciences

presented by

STEFAN STRASKY

dipl. Erdw. BENEFRI, University of Bern

born 10.02.1976

citizen of

Schwändi GL

accepted on the recommendation of

Prof. Dr. Rainer Wieler, ETH Zurich, examiner

Prof. Dr. Christian Schlüchter, University of Bern, co-examiner

Prof. Dr. Carlo Baroni, University of Pisa, co-examiner

Dr. Samuel Niedermann, GFZ-Potsdam, co-examiner

Prof. Dr. Sean Willett, ETH Zurich, co-examiner

2008

**Front cover**

Campbell glacier tongue flowing into the Ross Sea, Terra Nova Bay, Antarctica. Horizontal width of the picture is ~5 km.

**Back cover**

Impressions from fieldwork in Tibet, Antarctica and Europe. From top to down: (1) Landscape in the Shaluli Mountains (view north from Chuanxi Plateau), Tibet. (2) Terminal moraine and tongue basin of the Cuo Ji Gang Wa palaeoglacier, Chuanxi Plateau, Tibet. (3) Large erratic boulder (sample BROW3; ~250 m<sup>3</sup>). In the background are Boomerang glacier and Mt. Keinath (on the right-hand side of the picture), Deep Freeze Range, Antarctica. (4) Sampling for surface exposure dating. Beacon sandstone sample rhs1, Ricker Hills, Antarctica. (5) Aletsch glacier (Switzerland), the largest and longest glacier in the European Alps. During glacial periods, the Aletsch glacier region was a large ice field that fed into the Rhône valley glacier. (6) Alpine erratic boulder (sample MO-04-01) found on top of the Montoz anticline, Jura Mountains, Switzerland.

# CONTENTS

<b>Abstract</b>	<b>1</b>
<b>Zusammenfassung</b>	<b>3</b>
<b>1 Introduction</b>	<b>5</b>
1.1 Glacial response to climate change	5
1.2 Cosmogenic nuclides: principles and application to glacial systems	5
1.3 Multiple cosmogenic nuclide analyses	6
1.4 Outline of the thesis	7
<b>2 Cosmogenic nuclide production on earth</b>	<b>9</b>
2.1 Introduction	9
2.2 Artificial targets to refine production rate scaling factors for surface exposure dating	11
2.2.1 Introduction	11
2.2.2 Experimental procedures	13
2.2.3 Exposure sites	19
2.2.4 Results	21
2.2.5 Discussion and Conclusions	24
<b>3 Antarctica</b>	<b>29</b>
3.1 Introduction	29
3.2 Surface exposure ages imply multiple low-amplitude Pleistocene variations in East Antarctic Ice Sheet, Ricker Hills, Victoria Land	31
3.2.1 Introduction	32
3.2.2 Study site	33
3.2.3 Sampling	37
3.2.4 Surface exposure dating	38
3.2.5 Results	41
3.2.6 Discussion	43
3.2.7 Conclusions	48

3.3	Multiple cosmogenic nuclides document complex Pleistocene exposure history of glacial drifts in Terra Nova Bay (northern Victoria Land, Antarctica)	53
3.3.1	Introduction	54
3.3.2	Study area	55
3.3.3	Cosmogenic surface exposure dating (SED)	59
3.3.4	Results	64
3.3.5	Discussion	66
3.3.6	Conclusions	69
<b>4</b>	<b>Tibet</b>	<b>75</b>
4.1	Introduction	75
4.2	Glacier extension on the eastern Tibetan Plateau in response to MIS 2 cooling, with a contribution to $^{10}\text{Be}$ and $^{21}\text{Ne}$ methodology	77
4.2.1	Introduction	78
4.2.2	Geology and climate	79
4.2.3	Fieldwork and methods	84
4.2.4	Results	89
4.2.5	Discussion	93
4.2.6	Conclusions	103
4.3	Late Glacial ice advances in southeast Tibet	111
4.3.1	Introduction	111
4.3.2	Study area	114
4.3.3	Cosmogenic nuclide exposure ages	116
4.3.4	Discussion	121
4.3.5	Conclusions	123
<b>5</b>	<b>Europe</b>	<b>129</b>
5.1	Introduction	129
5.2	Oberflächenalter zweier Findlinge aus Niedersachsen – Zeugen einer alten fennoskandischen Vergletscherung in Norddeutschland [Surface exposure dating of two erratic boulders from Niedersachsen – evidence of an old Fennoscandian Ice Sheet advance in Northern Germany]	131
5.2.1	Einführung	132
5.2.2	Probenlokalitäten und Probennahme	134

5.2.3	Die Methode der Oberflächenaltersbestimmung mit kosmogenen Nukliden	135
5.2.4	Resultate	137
5.2.5	Schlussfolgerungen	139
5.3	First results of cosmogenic dated pre-last glaciation erratics from the Montoz area, Jura Mountains, Switzerland	143
5.3.1	Introduction	143
5.3.2	Evidence for glaciation of the Jura Mountains	144
5.3.3	Distribution of the erratic boulders	147
5.3.4	Cosmogenic dating	148
5.3.5	Discussion	154
5.3.6	Conclusions	155
<b>6</b>	<b>Conclusions and outlook</b>	<b>161</b>
<b>I</b>	<b>References</b>	<b>163</b>
<b>II</b>	<b>Appendix</b>	<b>169</b>
<b>III</b>	<b>Dank</b>	<b>181</b>
<b>IV</b>	<b>Curriculum Vitae</b>	<b>185</b>





## ABSTRACT

A direct and visible effect of climate change on the continents is the variable size of ice sheets and glaciers. Considerable ice fluctuations happened in the past, but when and to what extent they occurred is not well known. The main goal of this work was to establish local glacial chronologies in key areas for the global climate system (Antarctica, Tibet, northern Europe) and thus to add information needed to further complete the picture of how glaciers responded to climate change. Therefore, moraines and erratic boulders, the direct proof of ice advance or ice sheet expansion, were mapped and dated with in situ produced cosmogenic  $^{21}\text{Ne}$ ,  $^{10}\text{Be}$  and  $^{26}\text{Al}$ . S. Strasky measured all neon data presented in this work while A.A. Graf and L. Di Nicola investigated the radionuclides on aliquots of the same samples more or less contemporaneously within the framework of two related PhD projects at the University of Bern.

In **Antarctica** the main emphasis was put on East Antarctic Ice Sheet (EAIS) variations that predate the last glacial maximum (LGM). Past ice volume fluctuations were studied in two presently ice-free areas of Victoria Land, the Ricker Hills, a nunatak at the boundary of the EAIS, and the Northern Foothills, a coastal piedmont in the Terra Nova Bay area. Results from surface exposure ages of erratic boulders from the Ricker Hills suggest that several EAIS variations occurred during the Pleistocene with a major ice advance between 1.13 and 1.38 Ma. However, all recorded ice fluctuations were of limited extent of less than ~500 m above present ice levels. Restricted ice volume changes are also indicated from the Northern Foothills throughout the Pleistocene. Cosmogenic nuclide analyses of a glacially scoured bedrock surface revealed that coastal summits were sculpted about 4–6 Ma ago and have remained ice-free ever since. Below the rounded summits, surfaces were repeatedly exposed and buried by low-erosive ice, as indicated by complex exposure histories of all studied erratic boulders. This finding clearly demonstrates that pre-exposure is much more important than previously assumed and multiple nuclide analyses are a prerequisite for any meaningful surface exposure dating in polar areas.

In **Tibet** the time structure of glacier variations within the last glacial cycle was investigated in two monsoon-influenced sites on the southeastern margin of the Tibetan Plateau. In the surrounding area of Garzê, northern Shaluli Mountains,  $^{10}\text{Be}$  exposure ages of a well-defined terminal moraine succession cluster around 20 ka, suggesting a major ice advance during

marine isotope stage (MIS) 2, thus being synchronous to the global LGM. However, a significant difference between  $^{21}\text{Ne}$  and  $^{10}\text{Be}$  exposure ages was observed for these samples and was attributed to a nucleogenic neon component. Evidence for a Late Glacial signal was found in both study sites, more prominent in the Kangding area, and points to the possibility of a link between North Atlantic and east Asian glacial climate.

In **Europe** the focus of interest was the timing of the most extensive Quaternary glaciation of the Alps and the largest extent of the Fennoscandian Ice Sheet in Northern Germany. Two large erratic boulders on a Saalian surface in Niedersachsen, far beyond the LGM ice sheet margin, were analysed for cosmogenic nuclides. The data hint at a major ice sheet expansion during MIS 6. A similar result was found for erratic boulders of Alpine origin, deposited on top of the Swiss Jura Mountains. Surface exposure ages between 126 and 184 ka point most likely to the penultimate glaciation in MIS 6.

As **cosmogenic nuclide production on earth** is crucial for surface exposure dating and currently no consensus on using a common set of production rate scaling factors has yet been reached, a long-term experiment was continued to measure cosmogenic noble gases ( $^3\text{He}$  and  $^{21}\text{Ne}$ ) as a function of the geographical position in artificial quartz targets. Tests with newly designed targets have shown the suitability of the set-up for this purpose and first measurements of two targets exposed at different altitudes in Antarctica for a period of one year revealed promising results.

## ZUSAMMENFASSUNG

Die variable Grösse von Gletschern und Eisschildern ist ein direkter und unübersehbarer Effekt der Klimaveränderungen auf den Kontinenten. In vergangenen Zeiten resultierten beträchtliche Eisschwankungen; wann genau sie stattfanden und von welchem Ausmass sie waren, ist für viele Gebiete noch nicht ausreichend geklärt. Das Hauptziel dieser Arbeit war es, lokale Gletschergeschichten zu rekonstruieren – dies in Regionen von globaler Klimabedeutung (Antarktis, Tibet, Nordeuropa), weil damit ein Beitrag für ein besseres Verständnis der klimabedingten Gletscherschwankungen geleistet werden soll. Zu diesem Zweck wurden Moränen und Findlinge – Zeugen früherer Eisvorstösse – kartiert und deren Oberflächenalter mittels in situ produzierten kosmogenen Nukliden ( $^{21}\text{Ne}$ ,  $^{10}\text{Be}$ ,  $^{26}\text{Al}$ ) bestimmt. Alle Neon-Daten wurden von S. Strasky ermittelt; zusätzliche Analysen von Radionukliden an Aliquots derselben Proben erfolgten im Rahmen zweier zeitgleich durchgeführter Dissertationen an der Universität Bern von A.A. Graf und L. Di Nicola.

In der **Antarktis** galt das Hauptaugenmerk den Variationen des ostantarktischen Eisschildes (EAIS), die vor dem letzteiszeitlichen glazialen Maximalstand (LGM) entstanden waren. Dazu wurden in zwei gegenwärtig eisfreien Gebieten von Victoria Land, den Ricker Hills, einem Nunatak am Rande des EAIS, und den Northern Foothills, einem Piedmont im Küstengebiet der Terra Nova Bay, vergangene Eisvolumen-Veränderungen untersucht. Resultate von Oberflächenaltersbestimmungen an Findlingen aus den Ricker Hills weisen auf mehrere pleistozäne EAIS-Schwankungen und einen wesentlichen Eisvorstoss in der Zeit zwischen 1.38 und 1.13 Ma vor heute hin. Alle beobachteten Eisfluktuationen waren jedoch von reduziertem Ausmass und reichten weniger als rund 500 m über das heutige Eisniveau. Für beschränkte Eisausdehnungen während des ganzen Pleistozäns sprechen auch Resultate aus den Northern Foothills. Gemäss Analysen von kosmogenen Nukliden in Gletscher-überschliffenen Felsoberflächen wurden die Gipfel in der Küstenregion vor zirka 4–6 Ma glazial überprägt und sind seither eisfrei geblieben. Unterhalb der überschliffenen Gipfel wurde die Landschaft mehrfach von schwach erodierendem Eis bedeckt und nachträglich wieder exponiert, was sich in den komplexen Expositions-Geschichten aller untersuchten Findlinge zeigt. Dieses Ergebnis verdeutlicht, dass Vorbestrahlung weitaus bedeutender ist als bisher angenommen und Analysen mehrerer kosmogener Nuklide eine Voraussetzung für jegliche aussagekräftigen Oberflächenaltersbestimmungen in polaren Gebieten sind.

In **Tibet** wurde die zeitliche Abfolge von Gletscherschwankungen innerhalb der letzten Eiszeit in zwei Monsun-beeinflussten Gebieten am Südostrand des tibetischen Plateaus untersucht. In der weiteren Umgebung von Garzê (nördliche Shaluli-Berge) häufen sich  $^{10}\text{Be}$ -Oberflächenalter einer gut definierten Endmoränenabfolge um die 20 ka und weisen somit auf einen bedeutenden Eisvorstoss während des marinen Isotopen-Stadiums 2 hin; dieser Vorstoss fand somit zeitgleich mit dem globalen LGM statt. Die  $^{21}\text{Ne}$ -Oberflächenalter dieser Proben unterscheiden sich jedoch beträchtlich von den  $^{10}\text{Be}$ -Altern; diese Abweichung kann mit einer nukleogenen Neon-Komponente erklärt werden. Hinweise auf eine Gletscheraktivität im Spätglazial stammen aus beiden Untersuchungsgebieten (etwas ausgeprägter aus der Region Kangding) und sind Indiz für eine mögliche Verbindung zwischen nordatlantischem und ostasiatischem Gletscherklima.

In **Europa** lag der Schwerpunkt des Interesses in der zeitlichen Erfassung der grössten quartären Vergletscherung der Alpen und der maximalen Ausdehnung des fennoskandischen Eisschildes in Norddeutschland. Zwei grosse Findlinge der Saale-zeitlichen Ablagerungen in Niedersachsen, weit ausserhalb des LGM-Eisschildrandes, wurden auf kosmogene Nuklide untersucht. Die Daten weisen auf eine bedeutende Ausdehnung des fennoskandischen Eisschildes im marinen Isotopen-Stadium 6 hin. Ein ähnliches Ergebnis lieferten Findlinge alpiner Herkunft, die auf den südlichsten Antiklinalen im Schweizer Jura abgelagert worden waren. Oberflächenalter zwischen 184 und 126 ka deuten auf die vorletzte Eiszeit im marinen Isotopen-Stadium 6 hin.

Die **Produktion kosmogener Nuklide auf der Erde** ist ein entscheidender Parameter für Oberflächenaltersbestimmungen. Bisher konnte aber noch keine Übereinstimmung für den einheitlichen Gebrauch von Skalierfaktoren zur Ermittlung lokaler Produktionsraten gefunden werden. Als Beitrag zur Lösung dieser Problematik wird ein Langzeit-Experiment zur Messung kosmogener Edelgase ( $^3\text{He}$  und  $^{21}\text{Ne}$ ) in Abhängigkeit der geografischen Position in künstlichen Quarz-Targets fortgesetzt. Tests mit neu entwickelten Targets haben gezeigt, dass die Experiment-Anordnung für besagten Zweck geeignet ist, und erste Messungen an zwei während eines Jahres in der Antarktis in unterschiedlichen Höhen exponierten Targets ergaben viel versprechende Resultate.

# 1 INTRODUCTION

## 1.1 Glacial response to climate change

---

Glaciers and ice sheets are among the clearest signals of climate change, because they respond directly to trends in temperature and precipitation. Moreover, their sensitivity to changing surrounding conditions (Oerlemans, 2001) and the resulting meltwater is of prime concern to society, as even a modest change in ice balance could strongly affect future sea level (Lemke et al., 2007). The year-to-year climate variability influences the mass balance at the glacier surface (net balance between accumulation and ablation), which is subsequently transmitted down-glacier to produce a delayed reaction of an integrated climatic change over time at the glacier front. Response times vary from 10–50 years for most valley glaciers (Oerlemans, 1994), up to several centuries for the largest glaciers and ice caps with small slopes and cold-based ice (Paterson, 1994).

As a consequence of the close relationship between climate change and glacial response, the extent of former glaciers can be used to reconstruct palaeoclimatic information. By combining detailed geological mapping and dating of palaeoglacial features, such as moraines and glacial drifts, fundamental evidence about both timing and amplitude of palaeoglaciation can be obtained. A powerful tool for absolute dating the palaeoglacial record is surface exposure dating using in situ produced cosmogenic nuclides in rock surfaces (Fabel and Harbor, 1999). Applying this method to key areas of global palaeoclimate significance, in order to precisely date terrestrial geological signatures of ice volume variations, provides additional support to the palaeoclimate archives of deep-sea sediments and ice cores, and all serve as input parameters when modelling the future climate.

## 1.2 Cosmogenic nuclides: principles and application to glacial systems

---

Cosmogenic nuclides are produced at the earth's surface by the interaction of secondary cosmic ray particles (mainly neutrons) with target nuclei in minerals. The cosmogenic nuclide inventory of minerals from surface or near surface rocks is, therefore, indicative of the duration of exposure to cosmic radiation. However, measuring cosmogenic nuclides in terrestrial

samples is a challenging issue as concentrations are generally very low. Owing to developments in accelerator and noble gas mass spectrometry during the last quarter of the twentieth century, measurements of the low cosmogenic nuclide concentrations in terrestrial samples and, consequently, exposure age determinations, became possible. The ability to measure surface exposure ages, i.e. to be able to put landscape evolution into a real time frame, has had a broad impact on quantitative geomorphology. Numerous applications have since used cosmogenic nuclides to solve various questions in surficial geology over a wide range of time-scales and a number of publications have reviewed the fundamental principles and applications of the method (Lal, 1988; 1991; Cerling and Craig, 1994; Kurz and Brook, 1994; Gosse and Phillips, 2001; Bierman et al., 2002; Niedermann, 2002).

In glacial geology the main goal of cosmogenic nuclide dating is to shed light on the time structure of former glacier variations and to establish absolutely dated glacial chronologies. Dating erratic boulders from distinct moraines or surfaces is the most widely used approach for this purpose and has been successfully applied all over the world (e.g. Kaplan et al., 2005; Owen et al., 2005; Fink et al., 2006; Ivy-Ochs et al., 2006a; Rinterknecht et al., 2006; Schaefer et al., 2006; Staiger et al., 2006). However, more data is needed from high and low latitudes and from both hemispheres to unravel the secrets of (palaeo)glacier–climate interactions and to answer the question whether glacial response is syn- (e.g. Ivy-Ochs et al., 1999; Schaefer et al., 2006) or asynchronous (e.g. Gillespie and Molnar, 1995) to climate change on a global scale.

### **1.3 Multiple cosmogenic nuclide analyses**

---

Studies on erratic boulders are generally based on the assumption that no cosmogenic nuclides are initially present prior to deposition and accumulation of cosmogenic nuclides starts with the melt-out (~deposition) of the boulder from the ice. This implies that the original surfaces of the erratic boulders were either shielded from incoming cosmic rays or glacial erosion exceeded ~2 m (penetration depth of most relevant secondary cosmic ray particles in rocks) and removed all inherited nuclides from prior exposure times (Fabel and Harbor, 1999). Davis et al. (1999) and Abbühl et al. (2008) showed with multiple cosmogenic nuclide analyses that inheritance in erratic boulders is, in fact, within the framework of their studies of

minor importance for wet-based glacial systems. This was also found by Putkonen and Swanson (2003), who attributed exposure age variability of erratic boulders from a single moraine to erosion and exhumation processes (leading to younger exposure ages) rather than to nuclide inheritance and, as a consequence, suggested that the oldest boulder age best represents the age of a moraine. However, this approach is only valid for glacial landscapes outside the polar areas, which evolved below strongly erosive ice bodies. Conversely, in polar regions where the ice is frozen to the ground, glacial erosion is less effective. After retreat of a cold-based ice body, the overridden rock surfaces or erratic boulders may still contain some cosmogenic nuclides from an exposure period prior to the last ice advance (Fabel et al., 2002; Sugden et al., 2005), and thus the cosmogenic “clock” is not completely reset and the “clock” starts at an inherited time. A single nuclide measurement does not allow the identification of such a complex exposure history and would lead to an erroneous exposure age. This can be overcome by the analyses of multiple cosmogenic nuclides (Lal, 1991), although a quantitative separation of different exposure periods is not (yet) possible. Nevertheless, in addition to the ability of detecting potential nuclide inheritance, multiple cosmogenic nuclide analyses may yield valuable information about sample-specific erosion rates (Lal, 1991) and enhance the reliability of surface exposure ages. It is in this respect that this thesis assesses local glacial chronologies from high and low latitudes by combined analyses of in situ produced cosmogenic  $^{10}\text{Be}$  and  $^{21}\text{Ne}$  in quartz-bearing erratic boulders.

## 1.4 Outline of the thesis

---

As a matter of fact surface exposure dating with in situ produced cosmogenic nuclides is an approved method in geology. As stated above a number of publications discussed applications and analytical techniques of  $^{10}\text{Be}$  (e.g. Bierman et al., 2002) and  $^{21}\text{Ne}$  (e.g. Niedermann, 2002), the two nuclides mainly used in this work to determine exposure ages. Additionally, previous work within the same consortium (Institute of Isotope Geochemistry and Mineral Resources, ETH Zurich; Institute for Particle Physics PSI/ETH Zurich; Institute of Geological Sciences, University of Bern) has successfully used internal laboratory facilities to determine cosmogenic nuclide ages (Bruno, 1995; Ivy-Ochs, 1996; Schäfer, 2000; Tschudi, 2000; Kelly, 2003; Kober, 2004; Oberholzer, 2004; Akçar, 2006). Therefore, I omit a methodological chapter with basic principles of surface exposure dating and refer the reader to the mentioned

literature. I discuss a more specific methodological aspect related to cosmogenic nuclide production on earth in chapter 2 and present first results of an experiment, set up to refine production rate scaling factors for surface exposure dating.

However, the main goal of this thesis is to supply cosmogenic nuclide chronologies from glacial systems in key areas for the global climate. Six individual field sites were selected, two each in Antarctica, Tibet and Europe (chapters 3, 4 & 5). S. Strasky is responsible for all noble gas data from these sites. Additional radionuclide data were obtained in collaboration with the Institute of Geological Sciences of the University of Bern, by A.A. Graf (Europe and Tibet) and L. Di Nicola (Antarctica).

Work carried out in Antarctica focuses on former East Antarctic Ice Sheet variations and is based on samples mainly collected during the XX and XXI Italian Antarctic Expeditions (2004–2006) to Terra Nova Bay. Results are presented in sections 3.2 and 3.3 from a nunatak at the margin of the East Antarctic Ice Sheet and from a coastal piedmont, respectively. Due to the combined analyses of cosmogenic  $^{21}\text{Ne}$ ,  $^{10}\text{Be}$  and  $^{26}\text{Al}$  on the same samples it was found that nuclide inheritance is much more important than previously assumed and has to be considered when working in Antarctica (section 3.3). Especially the combination of the stable  $^{21}\text{Ne}$  and the radionuclide  $^{10}\text{Be}$  was useful in this respect.

Chapter 4 includes two studies from eastern Tibet. The first is presented in section 4.2 and shows clear evidence of a local ice advance in the investigated area during marine isotope stage 2, conflicting with findings from other surface exposure dating studies in Tibet. Additionally, section 4.2 contains a methodological discussion about a potential nucleogenic neon component, which might have to be considered in future research. In the following section 4.3 it is shown that glacial response to climate change can be abrupt – also in Tibet, far away from the North Atlantic key region – as indicated from cosmogenic nuclide measurements of erratic boulders from a valley glacier system.

After the high latitude and high altitude sites chapter 5 describes two studies from Europe focussing on the timing of the maximum Pleistocene ice extent, and thus contributes to the historical discussion of classical Quaternary stratigraphy. When the Fennoscandian Ice Sheet reached its maximum position in Northern Germany and Alpine glaciation was most extensive was tried to answer in sections 5.2 and 5.3, respectively.



## 2 COSMOGENIC NUCLIDE PRODUCTION ON EARTH

### 2.1 Introduction

---

Production of cosmogenic nuclides in terrestrial rocks is a function of the cosmic ray flux that reaches the earth's surface. In space, the flux of cosmic radiation is almost isotropic and consists dominantly of protons (~90 %), with lesser amounts of alpha particles (~8 %) and minor contributions from heavier nuclei (Gaisser, 1990). Upon entry into the earth's atmosphere these high energetic particles interact with other nuclei in the air, mainly in spallation reactions, where additional particles with sufficient energy to induce further nuclear reactions are ejected. These nucleon interactions attenuate the cosmic ray flux approximately exponentially with atmospheric depth and produce a cascade of secondary particles (Fig. 2.1). Lal and Peters (1967) give a detailed description on the propagation of fluxes and energy spectra of nuclear interacting particles in the atmosphere. On the way through the atmosphere, the composition of the cosmic ray flux changes and neutrons become dominant over protons. Particles of this neutron-dominated secondary cosmic ray flux are ultimately responsible for cosmogenic nuclide production on earth.

Besides the strong altitude-dependence of the cosmic ray flux, also a latitudinal variation is observed. This is due to the influence of the earth's geomagnetic field on trajectories of the primary cosmic ray particles. Because the primary particles are charged, the magnetic field deflects them and acts as a filter, keeping out particles with energies lower than that necessary to overcome the magnetic field force vector (cutoff rigidity). Only particles with rigidities (energy to charge ratios) above the cutoff rigidity can penetrate the earth's magnetic field. Cutoff rigidities are highest at the equator, where the earth's magnetic field lines are approximately parallel to the surface and lowest at the poles, where magnetic field lines are perpendicular to the surface (Shea et al., 1987). At latitudes higher than about 55°, the cutoff rigidity drops below the minimum rigidity of cosmic ray particles existing within the solar system, and all primary particles are admitted. Therefore, the cosmic ray flux does not increase further above ~55°.

As cosmogenic nuclide production in rocks is directly proportional to the cosmic ray flux at the specific site, accurate knowledge of the latitude and altitude variability of the secondary

particle flux is required for surface exposure dating. Lal (1991) presented the first method to scale cosmogenic nuclide production rates from one site (e.g. a calibration site) to another with different geomagnetic latitude and different altitude. During the last years a lot of work has been done to better understand the spatial variability of cosmogenic nuclide production systematics on earth and to estimate also the influences of temporal parameter changes. Since the pioneering work of Lal (1991) a number of other production rate scaling routines have been published (Dunai, 2000; Stone, 2000; Dunai, 2001; Masarik et al., 2001; Desilets and Zreda, 2003; Pigati and Lifton, 2004; Lifton et al., 2005; Desilets et al., 2006; Staiger et al., 2007). However, they still differ considerably from each other and it is up to the user to assess the different scaling procedures and decide which are the most appropriate for a given study site. Currently, the Cosmic Ray prOduced NUclide Systematics (CRONUS) project is addressing the problem of cosmogenic nuclide production rate scaling with the goal to improve present accuracy of production rates anywhere on earth from perhaps some 20 % today to about 5 %. Within the CRONUS project an experiment was launched to empirically determine the variability of production rates of cosmogenic noble gases ( $^3\text{He}$  and  $^{21}\text{Ne}$ ) as a function of the geographical position in artificial targets. The experiment set-up and the first results of two test targets, exposed at different altitudes in Antarctica for one year, are presented in section 2.2.

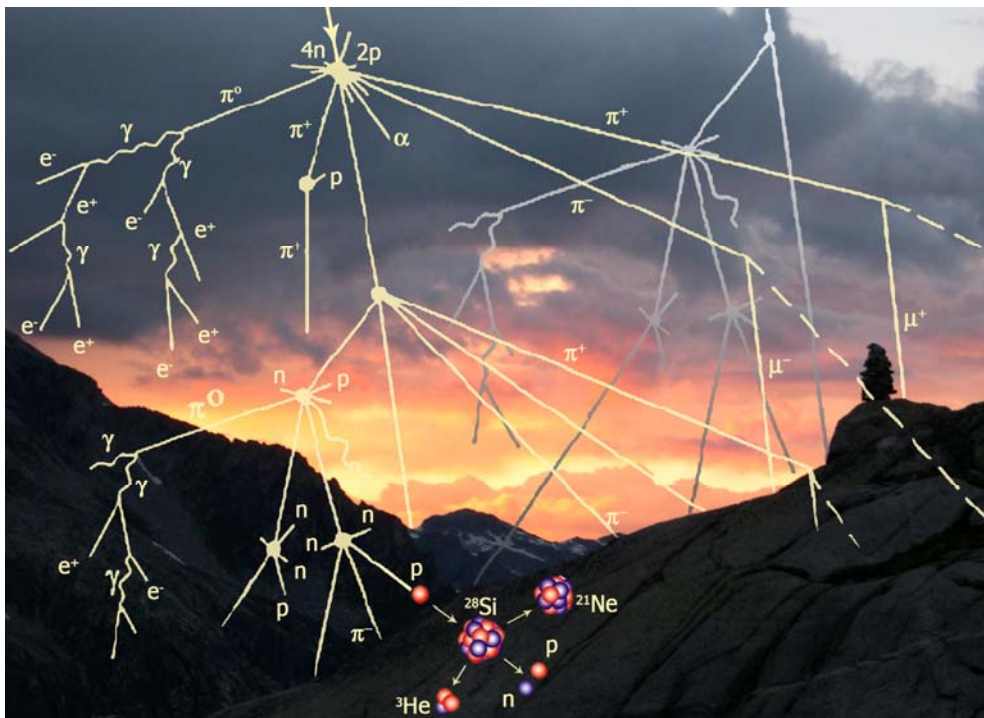


**Fig. 2.1.** Schematic illustration of a cosmic ray air shower (cascade) and a spallation reaction (after Gosse and Phillips, 2001).

## 2.2 Artificial targets to refine production rate scaling factors for surface exposure dating

---

*In collaboration with:* Rainer Wieler <sup>1</sup>, Heinrich Baur <sup>1</sup> and Christian Schlüchter <sup>2</sup>

<sup>1</sup> *Institute of Isotope Geochemistry and Mineral Resources, ETH Zurich, 8092 Zurich, Switzerland*

<sup>2</sup> *Institute of Geological Sciences, University of Bern, 3012 Bern, Switzerland*

---

**Abstract:** A fundamental problem in surface exposure dating with in situ produced cosmogenic nuclides is the scaling of production rates from one site to another with different altitude and latitude. Although considerable effort has been made regarding this problem, no consensus on using a common set of scaling factors has yet been reached. In this study, we present artificial quartz targets for measuring the variability of production rates of cosmogenic noble gases (<sup>3</sup>He and <sup>21</sup>Ne) as a function of the geographical position. The artificial targets, each filled with 1 kg of synthetic quartz sand, have shown to be suitable for this purpose. From two targets exposed at different altitudes in Antarctica we were able to measure cosmic ray produced <sup>21</sup>Ne and <sup>3</sup>He after one year of exposure and to calculate site-specific scaling factors.

### 2.2.1 Introduction

Surface exposure dating with in situ produced terrestrial cosmogenic nuclides is a powerful tool for dating rock surfaces absolutely and estimating erosion rates (Cerling and Craig, 1994; Gosse and Phillips, 2001; Niedermann, 2002). A crucial parameter, however, is the production rate of a nuclide of interest at the sampling site. As the cosmic ray intensity depends on the exact location within the troposphere, also the cosmogenic nuclide production rates vary with the geographical position. Accurate scaling of production rates from a calibration site to another with different geomagnetic latitude and altitude is therefore required. Hence, considerable effort has been made over the last decade to improve the knowledge of production systematics of cosmogenic nuclides on earth. Lal (1991) proposed the first scaling formalism, based on stars produced in photographic emulsions by cosmic ray spallation events and neutron monitor data from the 1950s. His assumptions that a homogeneous atmosphere (standard atmosphere with constant sea level pressure, temperature and adiabatic lapse rate) surrounds the globe and the earth's magnetic field consists of a pure dipole component have

been criticized and encouraged several authors to a more complex approach of the scaling problem. Dunai (2000) incorporated the effect of the non-dipole field components on the original neutron monitor data used by Lal (1991) while Stone (2000) considered deviations of the standard atmosphere and a more precise estimate of the muonic contribution to cosmogenic nuclide production and thus significantly improved the production rate scaling method of Lal (1991). Subsequent studies used more neutron data with wider geographic and temporal coverage to further refine production rate scaling procedures mainly for non-dipole components and temporal variations in strength and geometry of the geomagnetic field (Dunai, 2001; Masarik et al., 2001; Desilets and Zreda, 2003; Pigati and Lifton, 2004; Lifton et al., 2005; Desilets et al., 2006). Apart from that, Staiger et al. (2007) showed that temporal changes in production rates due to climate-controlled atmospheric variations may also influence cosmogenic nuclide production rates and should be incorporated in the scaling formalisms.

However, no consensus on using a common set of scaling factors for surface exposure dating has yet been reached. This lack of consensus motivated the international community to initiate the CRONUS (Cosmic Ray prOduced NUclide Systematics on earth) project, which aims to improve the current accuracy of production rates anywhere on earth. In collaboration with the EU-supported CRONUS-EU project, we approach the scaling problem by measuring the variability of production rates of cosmogenic noble gases ( $^3\text{He}$  and  $^{21}\text{Ne}$ ) as a function of the geographical position in artificial targets. So far, only limited work to constrain scaling factors by analyses of artificial targets has been published. Most of the experiments were carried out on water targets using  $^3\text{H}$ ,  $^3\text{He}$ ,  $^7\text{Be}$  and  $^{10}\text{Be}$  to determine the altitude dependence of cosmogenic nuclide production rates (Nishiizumi et al., 1996; Brown et al., 2000). In addition, Graf et al. (1996) investigated the  $^{21}\text{Ne}$  production rate in a silicon target at mountain altitudes. Furthermore, altitude and latitude scaling experiments using  $^7\text{Be}$  in water (Graham et al., 2000) and  $^3\text{He}$  and  $^{21}\text{Ne}$  in quartz targets (Schäfer, 2000; Kober, 2004) were presented, but the results are not yet sufficient to verify the scaling methods. As quartz is the most commonly used mineral in surface exposure dating, we further optimized the quartz targets of Schäfer (2000) and Kober (2004). The aim of our study is to show the applicability of newly designed artificial quartz targets to refine production rate scaling factors for surface exposure dating.

### 2.2.2 Experimental procedures

In order to improve production rate scaling factors for surface exposure dating we are exposing artificial quartz targets along altitude and latitude transects during one to two years and subsequently measure the cosmic ray produced  $^3\text{He}$  and  $^{21}\text{Ne}$  concentrations. So far, six test targets have been exposed for this study and two of them were recovered and analysed. Another twelve targets were exposed in a follow-up study and will be investigated in the near future. All noble gas analyses have been – and will be – carried out by a unique mass spectrometer, yielding a sensitivity for helium and neon which is about two orders of magnitude higher than typical values for conventional instruments (Baur, 1999). The spectrometer is equipped with an inverse turbo molecular-drag pump integrated into the ion source, which concentrates the gas into a small ionization volume. The compression of the gas into a small ionization chamber causes the number of ionized atoms per unit volume to grow, hence increases the sensitivity. This makes it a unique and perfectly suited mass spectrometer for precise analyses of the relatively low noble gas amounts expected in the artificially exposed targets.

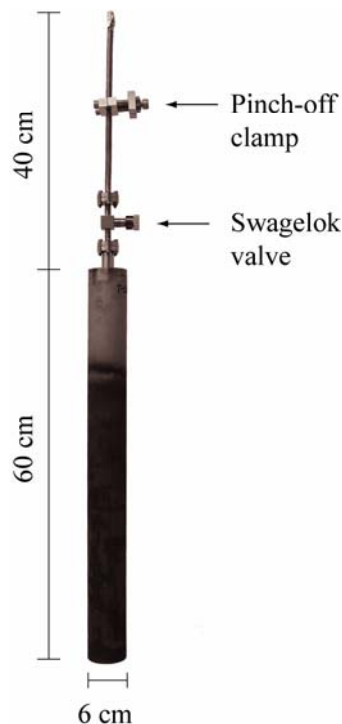


**Fig. 2.2.** Target container used in this study. Wall thickness tube: 2.6 mm; bottom thickness: 3.0 mm.

#### *Target container*

The target containers built for this experiment are an enhanced version of the containers used by Schäfer (2000) and Kober (2004). The vacuum containers are designed to contain 1 kg quartz sand and to allow a good degassing prior to exposure. Seamless stainless steel (material no. 1.4301) as container material allows degassing up to almost 1000 °C.

To maintain a vacuum in the container and prevent any air contamination during exposure times the containers are equipped with two valves. A “Swagelok Bellows-Sealed” valve, tested for leakage before mounting, is fixed at the top end of the container. On the other side of this valve, in the elongation of the container there is a copper tube with a stainless steel pinch-off clamp. Fig. 2.2 shows an example of a target container with the double seal arrangement and gives information about the target dimensions.

### *Target material*

The target material selected for the experiment is quartz, for several reasons. Quartz is the most commonly used mineral for exposure dating. It has a relatively simple chemical composition, and both, cosmogenic helium and neon are produced (sea level high latitude production rates in quartz are 124 at/g/yr for  $^3\text{He}$  (Masarik and Reedy, 1995) and 20.3 at/g/yr for  $^{21}\text{Ne}$  (Niedermann, 2000)) and can be extracted from the mineral following approved techniques (e.g. Brook and Kurz, 1993; Niedermann et al., 1993). Although a fraction of the cosmic ray produced  $^3\text{He}$  is often lost from quartz by diffusion (e.g. Brook and Kurz, 1993; Bruno et al., 1997), the retention of  $^3\text{He}$  in quartz does not influence our experiment, as the targets are under vacuum and thus represent a closed system.

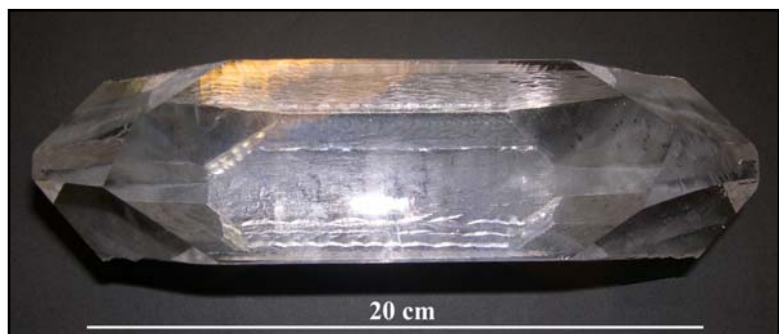


**Fig. 2.3.** Target material: artificially grown single quartz crystal before crushing.

To fill each target container with 1 kg quartz, several kilograms of high-purity quartz sand are required. Kober (2004) showed that the industrial quartz sand (Fluka, no. 83340) used in the artificial targets by Schäfer (2000) is not appropriate for the experiment, because of non-cosmogenic/non-atmospheric  $^3\text{He}$  and  $^{21}\text{Ne}$  components. Therefore we tested two other high-purity quartz sands (SIPUR A3 from the Bremthaler Quarzitwerk GmbH (Germany) and a synthetic quartz from Morion Company (USA)) for their applicability in artificial targets. Gamma ray spectrometry measurements for both quartz sands revealed U and Th concentrations <16 and <49 ppb, respectively, which is below the detection limit of the method and

also below the 120 ppb U and 172 ppb Th measured in the Fluka quartz sand. Furthermore, blank measurements yield promising results and clearly favour the synthetic quartz over the natural SIPUR A3 (see next section). We therefore selected the synthetic quartz as target material. Several kilograms of artificially grown single quartz crystals (Fig. 2.3) were crushed to grain sizes between 0.315 and 1 mm, washed with water to remove the finest fraction and subsequently filled into the target containers.



**Fig. 2.4.** Gas extraction configuration: the artificial target is put into the furnace. Note that the pinch-off clamp (missing in the picture) is mounted and closed before decoupling the target from the system.

#### *Degassing prior to exposure and blank measurements*

A prerequisite for a successful artificial target experiment is the complete degassing of the quartz prior to exposure. During degassing any previously accumulated cosmogenic  $^3\text{He}$  and  $^{21}\text{Ne}$  and, more importantly, trapped (atmospheric) helium and neon are released from quartz and can be pumped away. An effective degassing ensures that the targets are free of cosmogenic  $^3\text{He}$  and  $^{21}\text{Ne}$  before they are exposed at specific sites and that reduced trapped noble gas amounts allow a better identification of cosmogenic excesses over trapped components.  $^3\text{He}$  degasses at relatively low temperatures of a few 10s °C. Cosmogenic  $^{21}\text{Ne}$  on the other hand is released from quartz at higher temperatures, mostly between 100 and 600 °C, depending on extraction times and effective grain sizes (Niedermann, 2002). After heating quartz (grain size  $\sim 100\ \mu\text{m}$  or less) to 600 °C only about 2.5 % of cosmogenic  $^{21}\text{Ne}$  remains

in the mineral (Niedermann et al., 1993). Heating quartz to higher temperatures further reduces this fraction; after 800 °C almost no cosmogenic  $^{21}\text{Ne}$  is left in quartz (Niedermann et al., 1993). The goal for the artificial targets was therefore to degas the synthetic quartz sand used in the targets at temperatures of at least 800 °C. A particular furnace was built for this purpose and installed next to the mass spectrometer, allowing in-vacuo heating of the target and in a later phase gas extraction and analyses through stepwise heating, an approved method for discriminating between cosmogenic and non-cosmogenic components (Niedermann, 2002). Fig. 2.4 illustrates the degassing configuration.

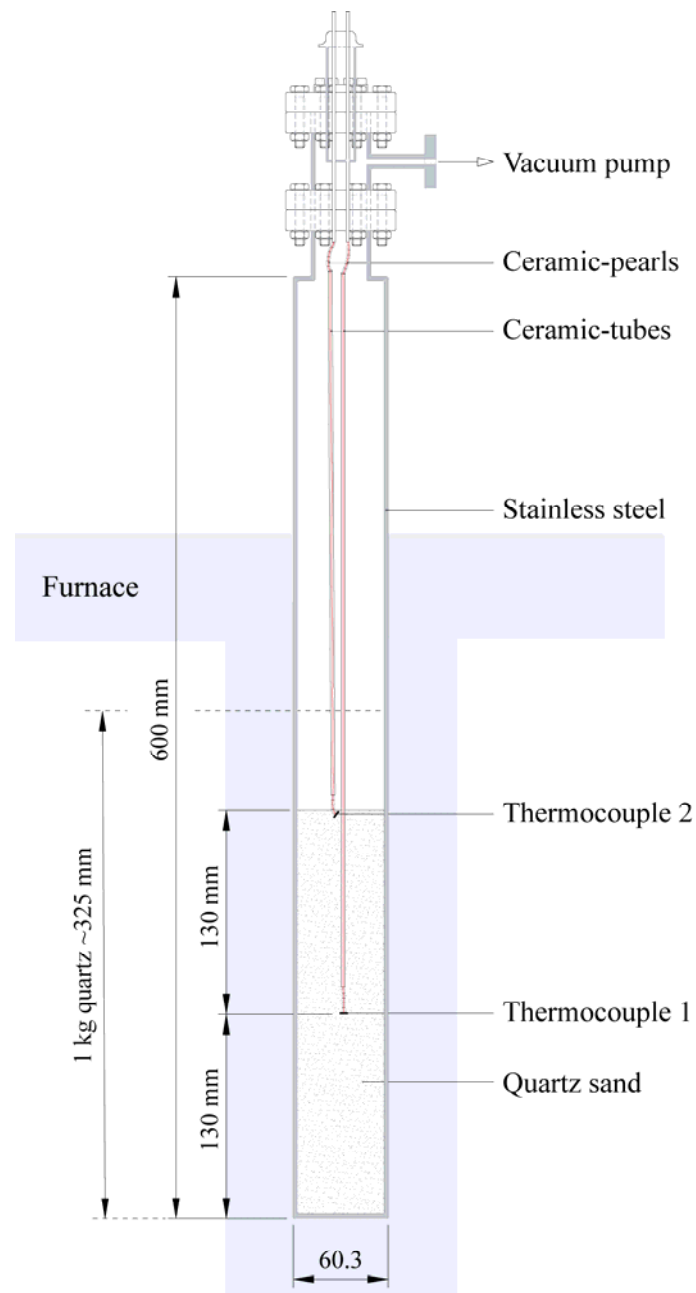


**Fig. 2.5.** Prototype container filled with 800 g quartz sand and equipped with thermocouples for inside-target temperature measurements.



Due to the low thermal conductivity of quartz sand in vacuum and the less effective degassing than anticipated in the pilot study (Kober, 2004) we draw special attention to the inside-target temperature of the quartz sand upon heating. We installed two thermocouples in a prototype container filled with 800 g quartz sand (Fig. 2.5) in order to control the effective temperature reached by the quartz in the innermost part of the container during degassing. Despite the poor thermal conductivity of quartz in vacuum, after a heating period of ~2.5 hours and an external temperature of 900 °C, the temperature reached by the quartz in the innermost part of the container is at least 800 °C, assuring complete degassing of helium and neon (Fig. 2.6). To reinforce total degassing, we heated each target for 2–4 days at the external temperature of 900 °C.

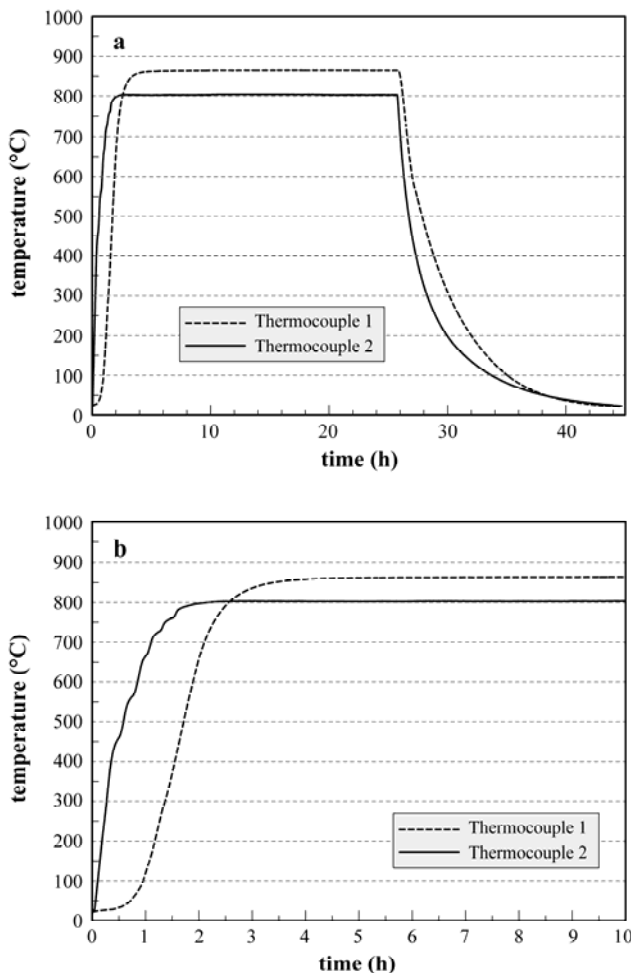


**Fig. 2.6.** Inside-target quartz temperature pattern. **a.** After 26 hours heating the furnace was switched off. **b.** Enlargement of the first 10 hours heating at external 900 °C. See thermocouple positions in Fig. 2.5.

After degassing, the targets were checked for their helium and neon blanks. Typical blank values for synthetic and SIPUR A3 quartz sands are reported in Table 2.1. The overall isotopic neon and helium blank compositions for all temperature steps are close to atmospheric values. Comparing blank values of the two different quartz types clearly shows that synthetic quartz yields lower blanks than SIPUR A3. Although the higher blanks of

SIPUR A3 may be explained partly by longer gas accumulation times, the drastic blank increase with higher temperatures is not observed in the synthetic quartz and supports its suitability for the artificial targets.

**Table 2.1.** Neon and helium isotope data for typical blanks.

Quartz	Heating Temp. (°C); Time (min)	$^{20}\text{Ne}$ ( $10^4$ at $\text{g}^{-1}$ )	$^{21}\text{Ne}/^{20}\text{Ne}$ ( $10^{-3}$ )	$^{22}\text{Ne}/^{20}\text{Ne}$	$^4\text{He}$ ( $10^6$ at $\text{g}^{-1}$ )	$^3\text{He}$ (at $\text{g}^{-1}$ )	$^3\text{He}/^4\text{He}$ ( $10^{-6}$ )	$R/R_a$
Syn- thetic	20; 180	$3.55 \pm 0.07$	$3.04 \pm 0.12$	$0.0963 \pm 0.0019$	$5.30 \pm 0.09$	$11 \pm 4$	$2.15 \pm 0.77$	1.56
	400; 240	$4.24 \pm 0.12$	$2.90 \pm 0.17$	$0.0995 \pm 0.0026$	$5.20 \pm 0.10$	$13 \pm 4$	$2.56 \pm 0.74$	1.85
	600; 300	$3.43 \pm 0.10$	$3.13 \pm 0.13$	$0.0961 \pm 0.0025$	$5.25 \pm 0.16$	$10 \pm 4$	$1.91 \pm 0.80$	1.38
	800; 180	$8.21 \pm 0.10$	$3.18 \pm 0.21$	$0.1010 \pm 0.0012$	$5.26 \pm 0.09$	$13 \pm 5$	$2.45 \pm 0.97$	1.77
SIPUR A3	20; 240	$5.66 \pm 0.05$	$3.24 \pm 0.17$	$0.0977 \pm 0.0028$	$7.31 \pm 0.05$	$21 \pm 6$	$2.81 \pm 0.81$	2.03
	400; 1770	$76.0 \pm 0.4$	$3.29 \pm 0.06$	$0.1036 \pm 0.0021$	$13.3 \pm 0.2$	$36 \pm 6$	$2.72 \pm 0.44$	1.96
	600; 1260	$839 \pm 4$	$3.73 \pm 0.06$	$0.1026 \pm 0.0003$	$25.3 \pm 0.1$	$51 \pm 7$	$2.00 \pm 0.29$	1.45
	800; 1050	$1923 \pm 8$	$3.78 \pm 0.04$	$0.1027 \pm 0.0006$	$67.0 \pm 0.1$	$94 \pm 8$	$1.40 \pm 0.12$	1.01

Uncertainties are  $1\sigma$  and include statistical, sensitivity and mass discrimination errors. Absolute errors of neon and helium abundances are not included in the noble gas data, but are about 2 % as determined with two independent air-calibrations.  $R_a$  is the atmospheric  $^3\text{He}/^4\text{He}$  ratio.

To further test the use of synthetic quartz for our experiment we measured the neon concentrations in a procedure generally applied to surface exposure dating. A non-degassed synthetic quartz aliquot of 32 mg was analysed in three temperature steps at 600, 800 and 1750 °C. The results of these test measurements are given in Table 2.2 and are visualized in a neon three-isotope plot (Fig. 2.7). The data of all temperature steps cluster around the atmospheric neon composition and further proof the suitability of the synthetic quartz as target material.

**Table 2.2.** Neon data of synthetic quartz analysed according to standard cosmogenic neon extraction techniques for surface exposure dating.

Sample	Heating Temperature (°C); Time (min)	$^{20}\text{Ne}$ ( $10^9$ atoms $\text{g}^{-1}$ )	$^{21}\text{Ne}/^{20}\text{Ne}$ ( $10^{-3}$ )	$^{22}\text{Ne}/^{20}\text{Ne}$
Synthetic quartz	600; 45	$2.65 \pm 0.03$	$2.99 \pm 0.09$	$0.1023 \pm 0.0013$
	800; 20	$1.67 \pm 0.01$	$2.98 \pm 0.15$	$0.1025 \pm 0.0012$
	1750; 20	$3.26 \pm 0.02$	$2.84 \pm 0.07$	$0.1020 \pm 0.0016$

Uncertainties are  $1\sigma$  and include statistical, sensitivity and mass discrimination errors. Absolute errors of neon abundances are not included in the noble gas data, but are about 2 % as determined with two independent air-calibrations.

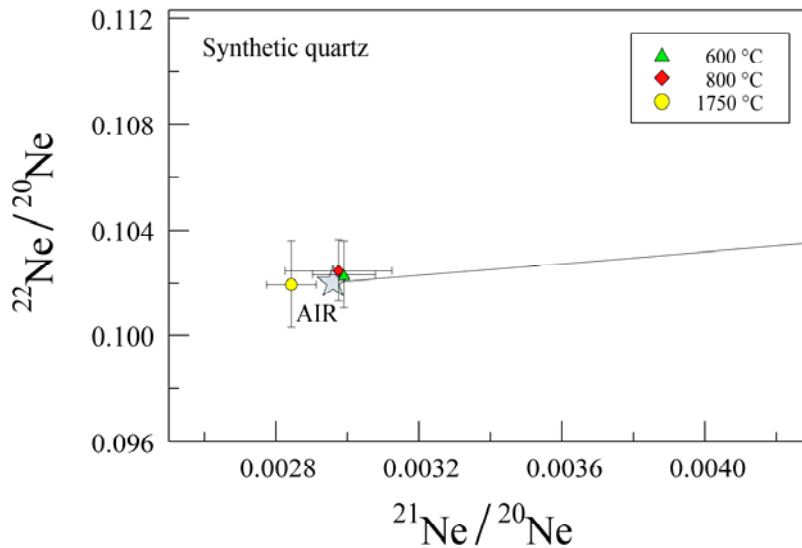


**Fig. 2.7.** Neon three-isotope diagram showing atmospheric neon concentrations of the synthetic quartz. The line is the atmospheric-cosmogenic mixing line for quartz (Niedermann et al., 1993).

### 2.2.3 Exposure sites

In the context of our first test experiments we exposed six artificial targets in Antarctica and Tibet. For the follow-up study, twelve quartz targets were exposed along an altitude transect between 400 and 4554 m a.s.l. in Switzerland and Italy, but these targets do not belong to the test set and are not subject of this work. Details of the six test exposure sites and dates are listed in Table 2.3. The high latitude position of Antarctica and the high-elevated Tibetan Plateau are perfectly suited for the experiment, because cosmogenic nuclide production rates increase with latitudes and altitudes and thus the expected amounts of cosmic ray produced nuclides in the quartz targets should allow verification of the applicability of newly designed targets to refine cosmogenic nuclide production rate scaling factors.

**Table 2.3.** Exposure details.

Target	Location	Latitude	Longitude	Altitude (m a.s.l.)	Exposure date	Recovery date	Exposure time (days)
T-01	Tourmaline Pl., Antarctica	S 74°09'03"	E 163°38'55"	1885	30.12.2004	25.12.2005	360
T-02	Mt. Frustum, Antarctica	S 73°22'51"	E 162°55'37"	3102	15.12.2004	14.12.2005	364
T-03	Garzê, Tibet	N 31°37'45"	E 099°59'18"	3383	12.08.2005	n	
T-04*	Garzê, Tibet	N 31°37'45"	E 099°59'18"	3383	12.08.2005	n	
T-05	Mt. Frustum, Antarctica	S 73°22'51"	E 162°55'37"	3102	14.12.2005	n	
T-06	Tourmaline Pl., Antarctica	S 74°09'03"	E 163°38'55"	1885	25.12.2005	n	

n = not yet recovered

\* = empty target

The first two targets were exposed in Antarctica at altitudes of 1885 and 3102 m above sea level (a.s.l.), respectively. After ~1 year of exposure they were recovered and replaced with new targets in order to reproduce the outcome of the first two targets in a later stage. Another two targets were exposed in Tibet at an elevation of 3383 m a.s.l.



**Fig. 2.8.** Exposure sites. **a.** Mount Frustum, Antarctica; **b.** Tourmaline Plateau, Antarctica; **c.** Garzê, Tibet.

Both Tibetan targets were deposited at the same site, separated by 50 cm from each other. In contrast to all other targets, one of these two targets is empty. This empty target will help to quantify the background and estimate the nuclide production from the target container. This is important as any production of  $^{21}\text{Ne}$  or  $^3\text{He}$  other than from cosmic ray induced spallation reactions in the quartz may influence the experiment. At the same time, intermittent or permanent shielding of the target may also affect the study. Each sampling site was therefore carefully evaluated for the likelihood of intermittent shielding (snow cover) and was selected where shielding from the surrounding topography was at a minimum. Antarctic targets were exposed at windy mountain peaks with open sky conditions (Figs. 2.8a and b). Unfortunately, this was not possible for the Tibetan targets. Those targets were exposed on top of an archway in a small town (Fig. 2.8c) and shielding from surrounding buildings and mountains had to be performed with an inclinometer (Fig. 2.9).

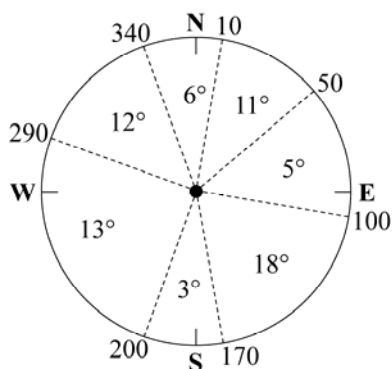


**Fig. 2.9.** Scheme for the shielding of the Tibetan targets by surrounding buildings and mountains. The numbers in the circle are the shielding values for the particular azimuth segments. As the intensity of the cosmic radiation in any particular direction  $F(\varphi)$  is given approximately by  $F_0 \sin^{2.3} \varphi$ , where  $F_0$  is the maximum intensity and  $\varphi$  the inclination angle, shielding values up to 20 degrees have small effects on cosmogenic nuclide production, hence the specific shielding configuration of the Tibetan targets is negligible. Targets are oriented E-W.

To protect the artificial targets from weather and other influences during exposure and transport we put each target in a glass fibre reinforced polyester box (Fig. 2.8). The effect of self-shielding from the target container and the box will be estimated by model calculations at the University of Bratislava, under the guidance of Jozef Masarik, another member of the CRONUS-EU team. However, as long as self-shielding is not too high, it does not significantly influence our experiment, as it is the same for all targets and our main interest is in the scaling of cosmogenic nuclide production rates from one site to another and not in the determination of absolute production rates.

## 2.2.4 Results

Helium and neon data of the first two exposed Antarctic targets are presented in Tables 2.4 and 2.5.

**Table 2.4.** Neon data for the two Antarctic targets.

Sample	Heating Temp. (°C); Time (min)	$^{20}\text{Ne}$ ( $10^5$ atoms $\text{g}^{-1}$ )	$^{21}\text{Ne}/^{20}\text{Ne}$ ( $10^{-3}$ )	$^{22}\text{Ne}/^{20}\text{Ne}$	$^{21}\text{Ne}_{\text{cos}}$ (atoms $\text{g}^{-1}$ )	$^{21}\text{Ne}_{\text{cos}}$ released (%)
T-01 (split)	20; -	$11.84 \pm 0.04$	$2.97 \pm 0.05$	$0.1015 \pm 0.0006$	$18 \pm 73$	9
	400; 360	$4.37 \pm 0.03$	$3.07 \pm 0.05$	$0.1030 \pm 0.0008$	$49 \pm 33$	24
	600; 240	$4.13 \pm 0.03$	$3.16 \pm 0.08$	$0.1098 \pm 0.0011$	$83 \pm 41$	41
	800; 480	$4.20 \pm 0.04$	$3.08 \pm 0.06$	$0.1046 \pm 0.0007$	$51 \pm 43$	25
T-02 (split)	20; -	$4.22 \pm 0.02$	$3.07 \pm 0.08$	$0.1018 \pm 0.0009$	$47 \pm 43$	15
	400; 360	$1.88 \pm 0.02$	$3.73 \pm 0.12$	$0.1020 \pm 0.0015$	$146 \pm 29$	48
	600; 360	$0.97 \pm 0.02$	$4.07 \pm 0.09$	$0.1016 \pm 0.0011$	$107 \pm 15$	35
	800; 450	$2.39 \pm 0.02$	$2.98 \pm 0.07$	$0.1020 \pm 0.0011$	$6 \pm 22$	2
T-02 (rest)	20; -	$1.99 \pm 0.02$	$2.99 \pm 0.11$	$0.1009 \pm 0.0007$	$6 \pm 29$	6
	400; 540	$0.91 \pm 0.01$	$3.59 \pm 0.13$	$0.1012 \pm 0.0005$	$58 \pm 16$	55
	600; 540	$0.69 \pm 0.02$	$3.56 \pm 0.07$	$0.1019 \pm 0.0017$	$42 \pm 12$	40
	800; 630	$1.63 \pm 0.01$	$2.96 \pm 0.06$	$0.1016 \pm 0.0005$	$0 \pm 11$	0

Uncertainties are  $1\sigma$  and include statistical, sensitivity and mass discrimination errors. Absolute errors of neon abundances are not included in the data, but are about 2 % as determined with two independent air-calibrations.

$^{21}\text{Ne}_{\text{cos}}$  is the excess of  $^{21}\text{Ne}$  over air.

The results are quite promising as we were able to detect cosmic ray produced  $^3\text{He}$  and  $^{21}\text{Ne}$  in both artificial targets, even though analytical procedures were not optimal. Because we had to expect large gas amounts (e.g. due to leakage of valves or significant blank increase) we didn't expand the total gas of the first target (T-01) into the mass spectrometer. Therefore, the

valve at the target was closed before event inlet and only a split of the gas was measured. The remaining gas in the target was subsequently pumped away. This procedure turned out to be inadequate as noble gas concentrations were very low and a significant fraction of the gas (~28 %) was lost. Nevertheless, we decided to repeat this measure protocol also for the second target (T-02) in order to be able to compare the results from the two targets. However, instead of pumping the remaining gas away, we analysed it in a second stage and referred to it as “rest”.

**Table 2.5.** Helium data for the two Antarctic targets.

Sample	Heating Temp. (°C); Time (min)	<sup>4</sup> He (10 <sup>6</sup> atoms g <sup>-1</sup> )	<sup>3</sup> He (atoms g <sup>-1</sup> )	<sup>3</sup> He <sub>cos</sub> (atoms g <sup>-1</sup> )	<sup>3</sup> He/ <sup>4</sup> He (10 <sup>-6</sup> )	R/R <sub>a</sub>
T-01 (split)	20; -	12.29 ± 0.18	170 ± 17	153 ± 17	13.8 ± 1.4	10.0
	400; 360	79.78 ± 0.20	425 ± 30	315 ± 30	5.33 ± 0.38	3.9
	600; 240	78.37 ± 0.16	15 ± 16	0 ± 0	0.19 ± 0.20	0.1
	800; 480	12.95 ± 0.22	55 ± 12	37 ± 12	4.25 ± 0.89	3.1
T-02 (split)	20; -	9.92 ± 0.22	207 ± 23	193 ± 23	20.8 ± 2.3	15.1
	400; 360	13.05 ± 0.15	949 ± 40	931 ± 40	72.7 ± 3.2	52.6
	600; 360	11.13 ± 0.19	29 ± 12	14 ± 12	2.6 ± 1.1	1.9
	800; 450	9.02 ± 0.14	38 ± 10	26 ± 10	4.3 ± 1.1	3.1
T-02 (rest)	20; -	8.26 ± 0.12	120 ± 13	109 ± 13	14.6 ± 1.5	10.5
	400; 540	9.97 ± 0.10	319 ± 24	305 ± 24	32.0 ± 2.4	23.1
	600; 540	9.19 ± 0.11	22 ± 7	9 ± 7	2.39 ± 0.71	1.7
	800; 630	8.60 ± 0.12	8 ± 8	0 ± 0	0.98 ± 0.96	0.7

Uncertainties are 1 $\sigma$  and include statistical, sensitivity and mass discrimination errors. Absolute errors of helium abundances are not included in the noble gas data, but are about 2 % as determined with two independent air-calibrations. <sup>3</sup>He<sub>cos</sub> is the <sup>3</sup>He excess over air, assuming all <sup>4</sup>He is atmospheric. R<sub>a</sub> is the atmospheric <sup>3</sup>He/<sup>4</sup>He ratio.

Owing to dilution difficulties of the calibration gas used to determine helium and neon concentrations in this study, absolute values presented in the Tables have to be handled very carefully and only relative values are used for the discussion and conclusions. But this is not a problem, because absolute mean production rates can, in any case, not reliably be determined after an exposure period of one year as instantaneous production rates also depend on solar activity. A coordinated simultaneous exposure of targets helps to minimize the effect of solar activity variations on our experiment.

Apart from measuring procedures, which have to be optimized for the follow-up targets, stepwise heating of the Antarctic test targets from room temperature to 400, 600 and 800 °C revealed successful extraction of cosmogenic noble gases from the target material (Tables 2.4 & 2.5 and Figs. 2.10 & 2.11). As expected, most of the  $^3\text{He}$  was released from quartz in the 400 °C temperature steps and heating to higher temperatures did not further increase the  $^3\text{He}$  inventories. However, a remarkable amount of  $^3\text{He}$  was observed in the room temperature steps (Fig. 2.10a). This indicates that  $^3\text{He}$  is lost from synthetic quartz by diffusion even at low temperatures and already after one year.

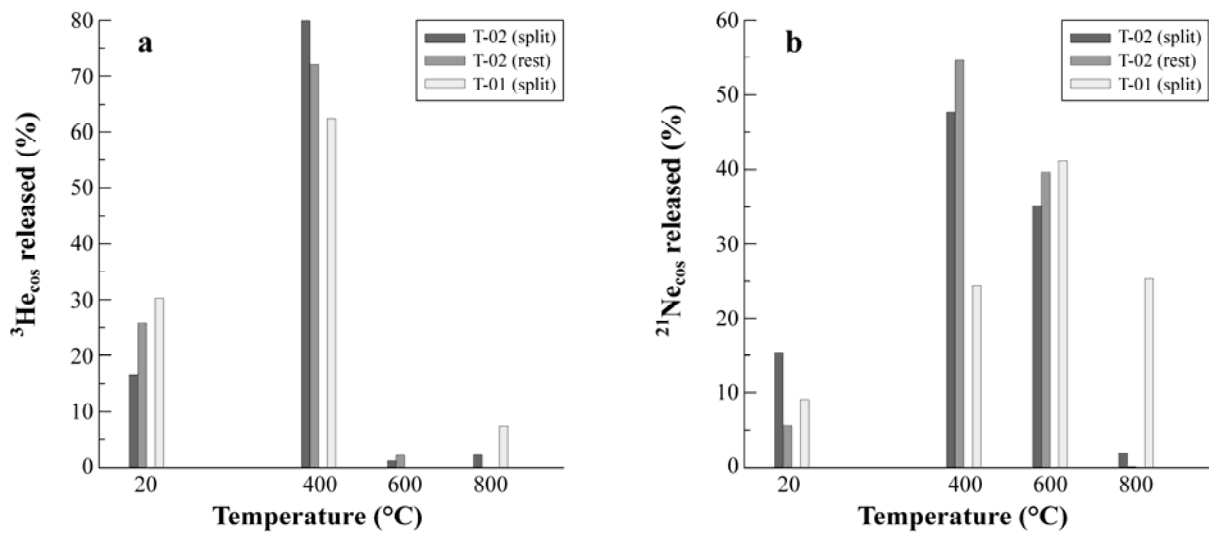


**Fig. 2.10.** Release patterns for cosmic ray produced  $^3\text{He}$  (a.) and  $^{21}\text{Ne}$  (b.) from synthetic quartz targets after ~1 year of exposure in Antarctica.  $^3\text{He}_{\text{cos}}$  and  $^{21}\text{Ne}_{\text{cos}}$  are calculated as excesses over air.

On the other hand, the release pattern for cosmic ray produced  $^{21}\text{Ne}$  revealed that the major fraction of cosmogenic  $^{21}\text{Ne}$  degasses at 400 and 600 °C (Fig. 2.10b) as described by Niedermann et al. (1993). The  $^{21}\text{Ne}$  signal in the 800 °C temperature step of T-01 (split) is due to an insufficient heating time at 600 °C or a non-cosmogenic neon component. As the neon three-isotope diagram of T-01 (split) shows considerable  $^{22}\text{Ne}$  excesses we cannot rule out any non-cosmogenic neon in this target (Fig. 2.11a). By contrast, no  $^{22}\text{Ne}$  excesses are observed in T-02 and the 400 and 600 °C temperature steps indicate clear cosmogenic signals (Fig. 2.11b).

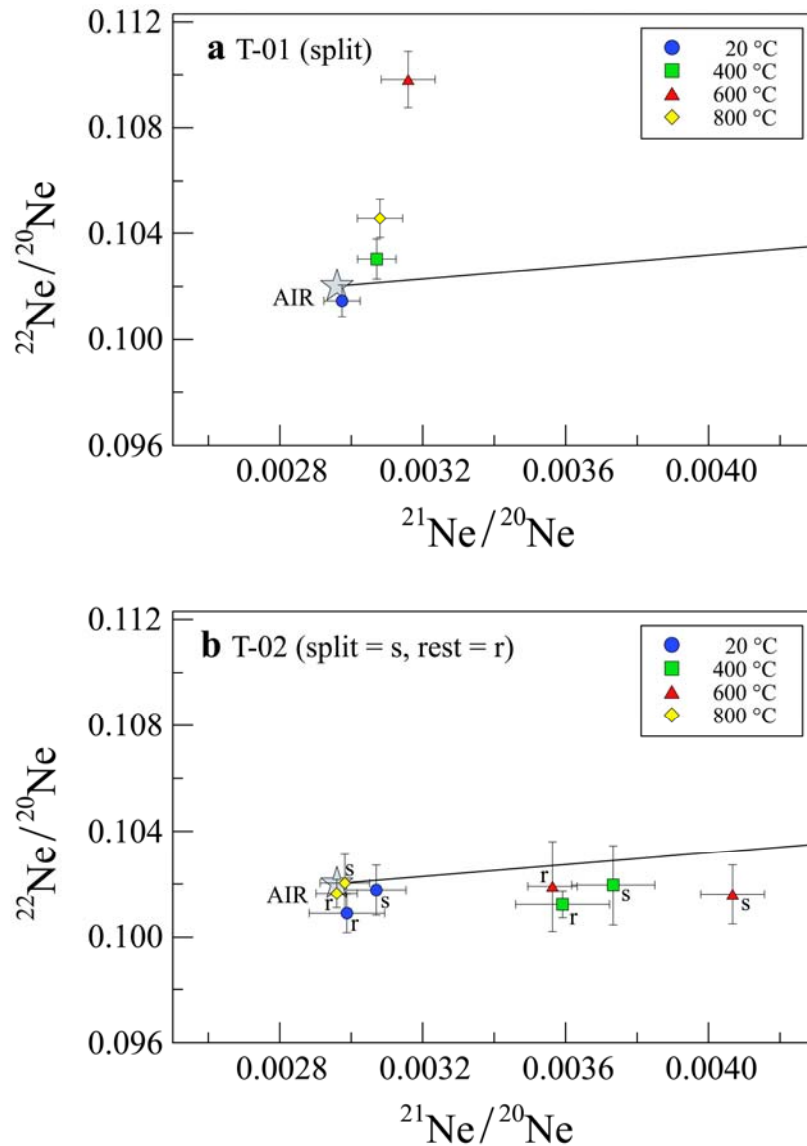


**Fig. 2.11.** Neon three-isotope plots for T-01 (a.) and T-02 (b.). The line in the graphs is the atmospheric-cosmogenic mixing line, described by Niedermann et al. (1993).

### 2.2.5 Discussion and Conclusions

Cosmogenic nuclide production rates vary significantly with altitude and latitude. Can we measure this spatial variation in artificial targets and if so, do the target measurements allow improving production rate scaling factors for cosmogenic nuclides? As analyses of the first two Antarctic targets revealed, the higher elevated target contained, in fact, significantly more cosmogenic nuclides than the lower elevated target. However, applied experimental procedures lack the precision to meet the requirements to refine cosmogenic nuclide production rate scaling factors but with a few analytical improvements and the same targets the challenging goal should become feasible.



**Table 2.6.** Calculated and predicted scaling factors for the two Antarctic targets.

Target	Altitude (m a.s.l.)	Exposure time (days)	$^{21}\text{Ne}_{\text{cos}}$ <sup>a</sup> (atoms g <sup>-1</sup> )	$^3\text{He}_{\text{cos}}$ <sup>b</sup> (atoms g <sup>-1</sup> )	$^{21}\text{Ne}$ scaling factor <sup>c</sup> (T-02/T-01)	$^3\text{He}$ scaling factor <sup>c</sup> (T-02/T-01)	Scaling factor (Stone, 2000)
T-01 (split)	1885	360	(132 ± 53)	468 ± 34	(1.90 ± 0.80)	2.38 ± 0.20	2.23
T-02 (split)	3102	364	253 ± 33	1124 ± 46			

The  $^{21}\text{Ne}$  concentration of T-01 (number in brackets) should be interpreted carefully, as the 600 °C step shows an extremely high  $^{22}\text{Ne}/^{20}\text{Ne}$  ratio (Fig. 2.11a), implying a considerable non-cosmogenic neon component.

<sup>a</sup> = sum of 400 and 600 °C steps

<sup>b</sup> = sum of 20 and 400 °C steps

<sup>c</sup> = calculated for equal exposure times of 365 days

Helium and neon data from the relevant temperature steps (20 & 400 °C for  $^3\text{He}$ ; 400 & 600 °C for  $^{21}\text{Ne}$ ) of the first two Antarctic test targets allow calculating preliminary scaling factors from one target site to the other. For the given exposure configuration and an extrapolated exposure time of 365 days the resulting scaling factor for  $^3\text{He}$  is  $2.38 \pm 0.20$  (Table 2.6). Although the scaling factor determined from cosmogenic  $^3\text{He}$  is strongly influenced by the atmospheric helium correction of T-01 (shifts the factor from  $1.92 \pm 0.13$  to  $2.38 \pm 0.20$ ) the use of  $^3\text{He}_{\text{cos}}$  to calculate the scaling factor is justified, as other helium sources than air are rather unlikely in synthetic quartz. Unfortunately, a reliable  $^{21}\text{Ne}$  scaling factor cannot be presented, as a non-cosmogenic neon component significantly affected the neon results of T-01. Nevertheless, the first tests have indicated that our approach has the potential to improve current production rate scaling uncertainties for cosmogenic nuclides, albeit measuring procedures have to be improved to reduce the errors. Particularly, gate times (integration time to measure ion current) and the number of repeat measurements (cycles) have to be optimized in the analytical protocol for each nuclide analysis. Comparing our experimentally determined scaling factors with the predicted value of Stone (2000), the most widely used scaling method for surface exposure dating in Antarctica, shows that Stone's (2000) value is between the scaling factors deduced from the artificial targets and agrees within error limits with our findings (Table 2.6). Also scaling factors calculated according to Dunai (2000) and Desilets et al. (2006) are with 2.46 and 2.45, respectively, close to our empirical  $^3\text{He}$  scaling factor. Whether the specific scaling factors are slightly higher than predicted by Stone (2000) as suggested from the first Antarctic targets has to be verified with measurements of the second set of Antarctic targets and is beyond the scope of this work.

In general the setup of the artificial target experiment has proven to work. Nevertheless, it is important to emphasize that the relatively low  $^{21}\text{Ne}$  production rate in quartz limits the use of artificial targets to directly measure production rate scaling factors with cosmogenic  $^{21}\text{Ne}$  to altitudes probably above  $\sim 2000$  m a.s.l., as below this elevation measured  $^{21}\text{Ne}/^{20}\text{Ne}$  and  $^{22}\text{Ne}/^{20}\text{Ne}$  ratios will be too close to blank values. Consequently, more importance should be attached to helium measurements at low altitude sites and the exposure of additional low-tritium water targets to complement the helium results from the quartz targets. Furthermore, low altitude exposure sites for artificial targets should focus on latitudes between 20 and 40 degrees because current scaling methods for low elevations differ most in this region (Fig. 2.12). Moreover, exposure sites of artificial targets should be selected where neutron monitors are installed and record the cosmic ray nucleon flux, the parameter which most published scaling procedures are based on.

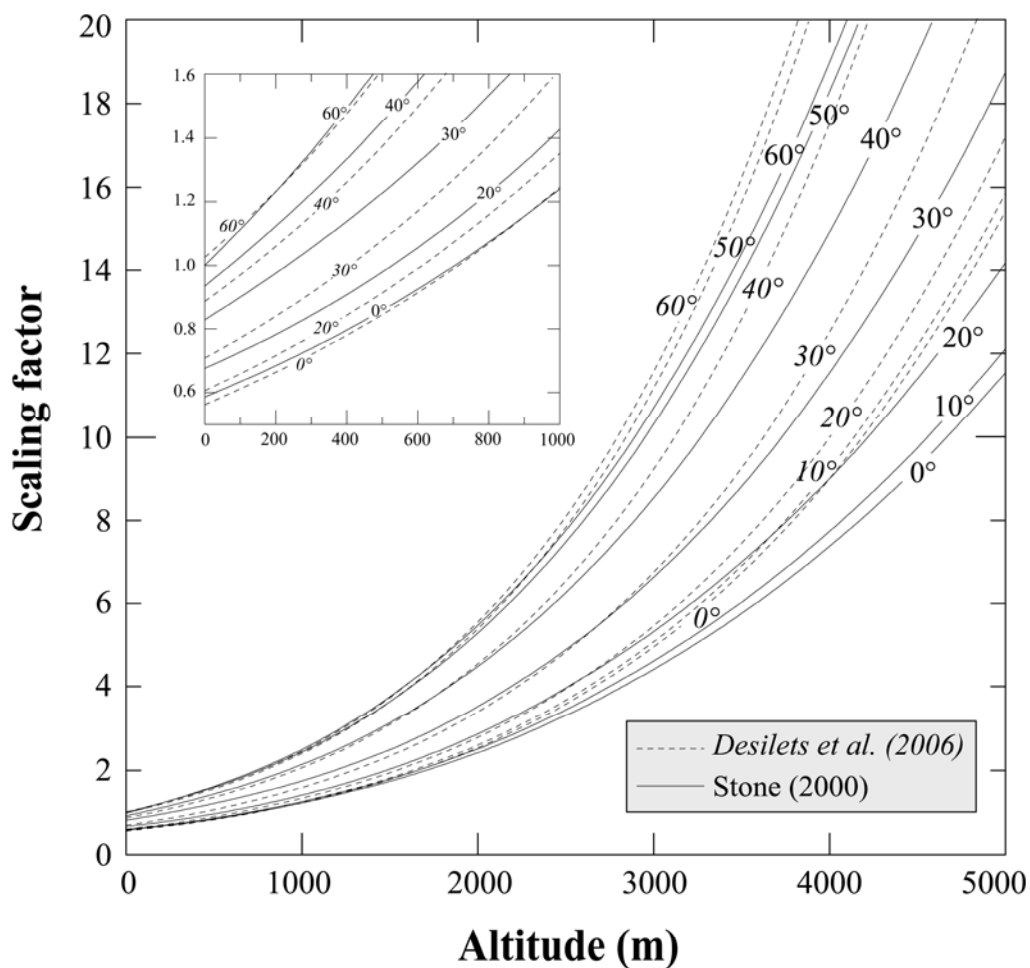


**Fig. 2.12.** Evolution lines of production rate scaling factors for cosmogenic nuclides with altitude, illustrated for selected latitudes and two different scaling models. The inset shows an enlargement of the altitude range between 0 and 1000 m a.s.l.

**Acknowledgements:** This research was supported by the Italian National Program on Antarctic Research (PNRA) and the Swiss National Science Foundation grant number: 200020-105220/1. Special thanks to H. Baur, U. Menet, A. Süssli and D. Niederer, who contributed greatly to the development of the artificial targets and to J.M. Schäfer for providing the synthetic quartz. R. Kipfer, F. Kober and P. Vermeesch are acknowledged for valuable discussions and laboratory assistance, and L. Tielin for guarding the two Tibetan targets.

## References

- BAUR, H. 1999. A Noble-Gas Mass Spectrometer Compressor Source With two Orders of Magnitude Improvement in Sensitivity. *Eos Transactions AGU*, **80**, Abstract V22B-08.
- BROOK, E.J. & KURZ, M.D. 1993. Surface-Exposure Chronology Using *in Situ* Cosmogenic  $^3\text{He}$  in Antarctic Quartz Sandstone Boulders. *Quaternary Research*, **39**, 1–10.
- BROWN, E.T., TRULL, T.W., JEAN-BAPTISTE, P., RAISBECK, G., BOURLÈS, D., YIOU, F. & MARTY, B. 2000. Determination of cosmogenic production rates of  $^{10}\text{Be}$ ,  $^3\text{He}$  and  $^3\text{H}$  in water. *Nuclear Instruments and Methods in Physics Research B*, **172**, 873–883.
- BRUNO, L.A., BAUR, H., GRAF, T., SCHLÜCHTER, C., SIGNER, P. & WIELER, R. 1997. Dating of Sirius Group tillites in the Antarctic Dry Valleys with cosmogenic  $^3\text{He}$  and  $^{21}\text{Ne}$ . *Earth and Planetary Science Letters*, **147**, 37–54.
- CERLING, T.E. & CRAIG, H. 1994. Geomorphology and in-situ cosmogenic isotopes. *Annual Review of Earth and Planetary Sciences*, **22**, 273–317.
- DESILETS, D. & ZREDA, M. 2003. Spatial and temporal distribution of secondary cosmic-ray nucleon intensities and applications to in situ cosmogenic dating. *Earth and Planetary Science Letters*, **206**, 21–42.
- DESILETS, D., ZREDA, M. & PRABU, T. 2006. Extended scaling factors for in situ cosmogenic nuclides: New measurements at low latitude. *Earth and Planetary Science Letters*, **246**, 265–276.
- DUNAI, T.J. 2000. Scaling factors for production rates of in situ produced cosmogenic nuclides: a critical reevaluation. *Earth and Planetary Science Letters*, **176**, 157–169.
- DUNAI, T.J. 2001. Influence of secular variation of the geomagnetic field on production rates of in situ produced cosmogenic nuclides. *Earth and Planetary Science Letters*, **193**, 197–212.
- GOSSE, J.C. & PHILLIPS, F.M. 2001. Terrestrial in situ cosmogenic nuclides: theory and application. *Quaternary Science Reviews*, **20**, 1475–1560.
- GRAF, T., MARTI, K. & WIENS, R.C. 1996. The  $^{21}\text{Ne}$  production rate in a Si target at mountain altitudes. *Radio-carbon*, **38**, 155–156.

- GRAHAM, I.J., BARRY, B.J., DITCHBURN, R.G. & WHITEHEAD, N.E. 2000. Validation of cosmogenic nuclide production rate scaling factors through direct measurement. *Nuclear Instruments and Methods in Physics Research B*, **172**, 802–805.
- KOBER, F. 2004. *Quantitative analysis of the topographic evolution of the Andes of Northern Chile using cosmogenic nuclides*. PhD thesis ETH No. 15858, ETH Zurich, 131 pp.
- LAL, D. 1991. Cosmic ray labeling of erosion surfaces: *in situ* nuclide production rates and erosion models. *Earth and Planetary Science Letters*, **104**, 424–439.
- LIFTON, N.A., BIEBER, J.W., CLEM, J.M., DULDIG, M.L., EVENSON, P., HUMBLE, J.E. & PYLE, R. 2005. Addressing solar modulation and long-term uncertainties in scaling secondary cosmic rays for *in situ* cosmogenic nuclide applications. *Earth and Planetary Science Letters*, **239**, 140–161.
- MASARIK, J. & REEDY, R.C. 1995. Terrestrial cosmogenic-nuclide production systematics calculated from numerical simulations. *Earth and Planetary Science Letters*, **136**, 381–395.
- MASARIK, J., FRANK, M., SCHÄFER, J.M. & WIELER, R. 2001. Correction of *in situ* cosmogenic nuclide production rates for geomagnetic field intensity variations during the past 800,000 years. *Geochimica et Cosmochimica Acta*, **65**, 2995–3003.
- NIEDERMANN, S., GRAF, T. & MARTI, K. 1993. Mass spectrometric identification of cosmic-ray-produced neon in terrestrial rocks with multiple neon components. *Earth and Planetary Science Letters*, **118**, 65–73.
- NIEDERMANN, S. 2000. The  $^{21}\text{Ne}$  production rate in quartz revisited. *Earth and Planetary Science Letters*, **183**, 361–364.
- NIEDERMANN, S. 2002. Cosmic-Ray-Produced Noble Gases in Terrestrial Rocks: Dating Tools for Surface Processes. In PORCELLI, D., BALLENTINE, C.J. & WIELER, R., eds. *Noble Gases in Geochemistry and Cosmochemistry. Reviews in Mineralogy and Geochemistry*, **47**. Washington, DC: Mineralogical Society of America, 731–784.
- NISHIZUMI, K., FINKEL, R.C., KLEIN, J. & KOHL, C.P. 1996. Cosmogenic production of  $^7\text{Be}$  and  $^{10}\text{Be}$  in water targets. *Journal of Geophysical Research B*, **101**, 22225–22232.
- PIGATI, J.S. & LIFTON, N.A. 2004. Geomagnetic effects on time-integrated cosmogenic nuclide production with emphasis on *in situ*  $^{14}\text{C}$  and  $^{10}\text{Be}$ . *Earth and Planetary Science Letters*, **226**, 193–205.
- SCHÄFER, J.M. 2000. *Reconstruction of landscape evolution and continental paleoglaciations using *in-situ* cosmogenic nuclides: Examples from Antarctica and the Tibetan Plateau*. PhD thesis ETH No. 13542, ETH Zurich, 121 pp.
- STAIGER, J., GOSSE, J., TORACINTA, R., OGLESBY, B., FASTOOK, J. & JOHNSON, J.V. 2007. Atmospheric scaling of cosmogenic nuclide production: Climate effect. *Journal of Geophysical Research B*, **112**, B02205, doi:10.1029/2005JB003811.
- STONE, J.O. 2000. Air pressure and cosmogenic isotope production. *Journal of Geophysical Research B*, **105**, 23753–23759.

## 3 ANTARCTICA

### 3.1 Introduction

---

Antarctica is the coldest, windiest, driest and iciest continent. Its two ice sheets – the larger East and smaller West Antarctic Ice Sheet (Fig. 3.1) – cover almost the entire continent. Together they hold an ice volume of 25.4 million km<sup>3</sup>, representing a sea level equivalent of 57 m (Lythe et al., 2001) and corresponding to about 80 % of the world's fresh water. This puts Antarctica into a key role for the global hydrological cycle and the response and feedbacks of its ice sheets to climate change became a major issue in climate and environmental research (Anisimov et al., 2007). Recent estimates of Antarctic Ice Sheet mass balance indicate losses of  $48 \pm 14$  km<sup>3</sup>/year from West Antarctica, and growth of  $22 \pm 23$  km<sup>3</sup>/year for East Antarctica (Rignot and Thomas, 2002). The same pattern of East Antarctic thickening (primarily from increased snowfall) and West Antarctic thinning (as a result of ocean warming and the loss of fringing ice shelves) was observed by Davis et al. (2005). Combining the East and West Antarctic numbers yields a loss of  $26 \pm 27$  km<sup>3</sup>/year for the region monitored (the negative balance of the Antarctic Peninsula was not assessed). However, competing theories over the causes of recent Antarctic Ice volume variations still limit confidence in prediction of future climate change. With the exception of the Antarctic Peninsula, where 87 % of glaciers are in retreat (Cook et al., 2005) and large ice shelves have broken up (Vaughan and Doake, 1996) due to a clear response to contemporary climate change, East and West Antarctic Ice Sheet variations cannot – a priori – be attributed to climate change, but a direct climate effect can also not be ruled out. To find out more about the response of Antarctic Ice Sheets to global climate change, reconstructing the palaeoglacial record may yield valuable information.

Among the key sites for studying former Antarctic Ice Sheet variations over space and time are the presently ice-free areas of Antarctica (~0.4 % of the continent). Glacial features of several ice sheet expansions are recorded in these regions (e.g. Denton et al., 1984; Baroni and Orombelli, 1989) and preserved over millions of years (Schäfer et al., 1999). There is supportive evidence that the East Antarctic Ice Sheet did not collapse or grow significantly over the Pliocene (Denton et al., 1993; Oberholzer et al., 2003; Staiger et al., 2006). However, there were ice sheet fluctuations of limited extent (e.g. Ackert and Kurz, 2004; Fink et al.,

2006; Mackintosh et al., 2007). But at what amplitude and when they did occur is not sufficiently answered. Also more precise dating of the expansions and contractions of the East Antarctic Ice Sheet are needed for comparison to and correlations with ice core records.

In this chapter landscape evolution and cosmogenic nuclide chronologies are presented for two palaeoglaciated sites in Victoria Land. The first study site – discussed in section 3.2 – is a nunatak at the boundary of the East Antarctic Ice Sheet. Thus, drift deposits found in this region are a direct proof of ice sheet variations. The second site presented in section 3.3 is a coastal piedmont located at the western margin of the Ross Sea where glacial features are generally related to local and outlet glaciers.

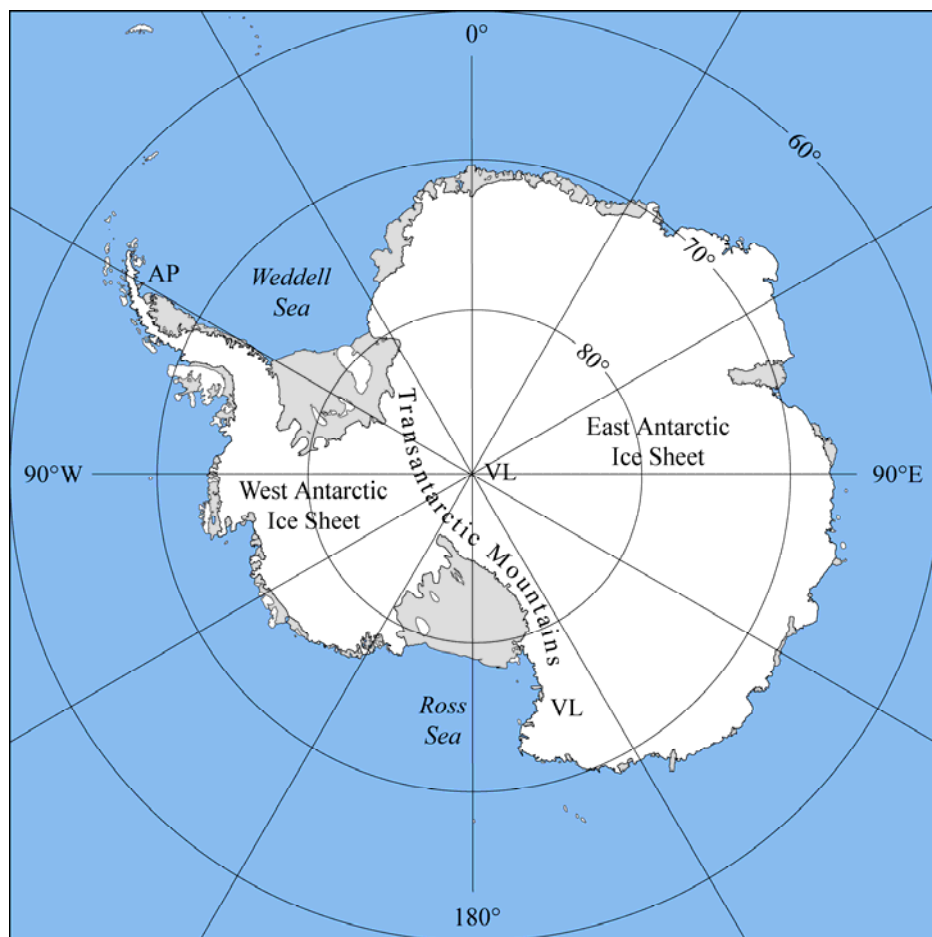


**Fig. 3.1.** Map of Antarctica showing the Transantarctic Mountains dividing East and West Antarctica. Shaded areas are ice shelves. AP: Antarctic Peninsula; VL: Victoria Land.

## 3.2 Surface exposure ages imply multiple low-amplitude Pleistocene variations in East Antarctic Ice Sheet, Ricker Hills, Victoria Land <sup>a</sup>

Stefan Strasky <sup>1\*</sup>, Luigia Di Nicola <sup>2,3</sup>, Carlo Baroni <sup>4</sup>, Maria Cristina Salvatore <sup>5</sup>, Heinrich Baur <sup>1</sup>, Peter W. Kubik <sup>6</sup>, Christian Schlüchter <sup>3</sup> and Rainer Wieler <sup>1</sup>

<sup>1</sup> *Institute of Isotope Geochemistry and Mineral Resources, ETH Zurich, 8092 Zurich, Switzerland*

<sup>2</sup> *Dipartimento di Scienze della Terra, Università degli Studi di Siena, 53100 Siena, Italy*

<sup>3</sup> *Institute of Geological Sciences, University of Bern, 3012 Bern, Switzerland*

<sup>4</sup> *Dipartimento di Scienze della Terra, Università di Pisa, e Istituto di Geoscienze e Georisorse CNR, 56126 Pisa, Italy*

<sup>5</sup> *Dipartimento di Scienze della Terra, Università degli Studi di Roma 'La Sapienza', 00185 Rome, Italy*

<sup>6</sup> *Paul Scherrer Institute, c/o Institute for Particle Physics, ETH Zurich, 8093 Zurich, Switzerland*

\*corresponding author: stefan.strasky@gmail.com

**Abstract:** One of the major issues in (palaeo-) climatology is the response of Antarctic ice sheets to global climate changes. Antarctic ice volume has varied in the past but the extent and timing of these fluctuations are not well known. In this study, we address the question of amplitude and timing of past Antarctic ice level changes by surface exposure dating using in situ produced cosmogenic nuclides (<sup>10</sup>Be and <sup>21</sup>Ne). The study area lies in the Ricker Hills, a nunatak at the boundary of the East Antarctic Ice Sheet in southern Victoria Land. By determining exposure ages of erratic boulders from glacial drifts we directly date East Antarctic Ice Sheet variations. Erosion-corrected neon and beryllium exposure ages indicate that a major ice advance reaching elevations of about 500 m above present ice levels occurred between 1.125 and 1.375 million years before present. Subsequent ice fluctuations were of lesser extent but timing is difficult as all erratic boulders from related deposits show complex exposure histories. Sample-specific erosion rates were on the order of 20–45 cm Ma<sup>-1</sup> for a quartzite and 10–65 cm Ma<sup>-1</sup> for a sandstone boulder and imply that the modern cold, arid climate has persisted since at least the early Pleistocene.

**Key words:** cosmogenic nuclides, surface exposure dating, landscape evolution, glacial drifts, erosion rates

<sup>a</sup> Published in *Antarctic Science* (2008), doi: 10.1017/S0954102008001478

### 3.2.1 Introduction

How sensitive are Antarctic ice sheets to global environmental change? When and to what extent did major Antarctic ice level variations occur in the past and will they recur in future? These are fundamental questions at the forefront of modern palaeoclimatology. As about 80 % of the world's present freshwater is stored as Antarctic ice, melting of only a small fraction of ice would result in a global sea level rise, which is of prime concern to human society (Houghton et al., 2001). Considerable effort is therefore being spent to unravel the interactions between Antarctic ice volume variations and climate excursions in the past in order to predict future climate scenarios. The Scientific Committee on Antarctic Research (SCAR) is currently coordinating these efforts in an international research initiative, called Antarctic Climate Evolution (ACE).

It is generally believed that glaciation of East Antarctica started around the Eocene/Oligocene boundary, ~34 Ma ago (Barrett, 1996), as atmospheric CO<sub>2</sub> concentrations declined (DeConto and Pollard, 2003) and the opening of the Tasmanian Gateway and Drake Passage led to the continent's "thermal isolation" (Kennett, 1977; Scher and Martin, 2006). Fluvial erosion sculpting dendritic valley systems ceased at the same time and temperate glaciers developed. Relict preglacial river valley systems that document the switch from fluvial to glacial landscape evolution – hence, the onset of ice growth – are observed in different areas of East Antarctica (e.g. Sugden and Denton, 2004; Baroni et al., 2005; Jamieson et al., 2005). From Oligocene to early Miocene times, oscillating warm-based ice existed for ~15 Ma. Naish et al. (2001) investigated offshore sediment cores and observed 46 cycles of East Antarctic glacier advance and retreat for this time period. During the middle Miocene the thermal regime of East Antarctic ice bodies changed from warm- to cold-based and a hyperarid polar climate has been established ever since (Armienti and Baroni, 1999; Sugden and Denton, 2004; Lewis et al., 2007). This last phase in the evolution of the East Antarctic Ice Sheet (EAIS) is of particular interest, because amplitude and timing of EAIS volume changes over the past million years may serve as input parameters for modelling the future climate.

High resolution data of climate and environmental parameters can be derived from Antarctic ice cores (e.g. Petit et al., 1999; EPICA community members, 2004). Their continuous records contribute significantly to the understanding of the past climate history (Wolff, 2005). However, the stratigraphy obtained from ice cores is limited to few drilling sites and at present only records the last 740 ka (EPICA community members, 2004). Furthermore,



changes in ice elevation at the ice sheet margins cannot be inferred from ice cores. Therefore, detailed glacial geological and geomorphological mapping is required to reconstruct three-dimensional palaeo-ice expansions. By dating surfaces of the mapped glacial features with in situ produced cosmogenic nuclides, information about timing of the ice fluctuations can be obtained. Glacial events ranging from Holocene to middle Miocene ages can be dated by choosing the appropriate nuclides (Gosse and Phillips, 2001). The combination of mapping and dating of the glacial record thus yields a powerful tool for palaeoclimate studies. Key sites for applying this methodological approach and investigating the glacial response to past climate change are the presently ice-free areas of Antarctica. Glacial deposits resulting from several ice sheet expansions have been recorded in these locations (e.g. Denton et al., 1984) and preserved over millions of years (Schäfer et al., 1999). Recent work has shown the potential of cosmogenic nuclide analyses to reconstruct palaeoclimate and landscape evolution in Antarctica (e.g. Oberholzer et al., 2003; Sugden et al., 2005; Fink et al., 2006; Mackintosh et al., 2007). Nevertheless, most studies focus on coastal areas, where outlet glaciers play a central role in drift deposition, and/or they concentrate on the most recent deglaciation chronologies. We consider that the extent and timing of major Antarctic ice level changes that occurred earlier, i.e. prior to the late Pleistocene, need further investigation.

Here we present surface exposure ages (using the cosmogenic nuclides  $^{10}\text{Be}$  and  $^{21}\text{Ne}$ ) from the Ricker Hills, a nunatak near the present-day margin of the EAIS in Victoria Land. By dating erratic boulders from late Pleistocene and pre-late Pleistocene glacial drifts in this area we directly date EAIS fluctuations. In addition to the glacial chronology, we determine amplitudes of the past ice level variations from detailed field surveys.

### **3.2.2 Study site**

The Ricker Hills ( $75^{\circ}41'S$ ,  $159^{\circ}10'E$ ) are located in the southwestern part of the nearly N–S striking Prince Albert Mountains, about 100 km inland from the Ross Sea coast, in southern Victoria Land (Fig. 3.2). They are an ice-free area of approximately  $70\text{ km}^2$  within the David Glacier system at the margin of the EAIS. Prevailing strong katabatic winds occur in the region and keep the nunatak ice-free. The nunatak ranges in elevation from 900 m to 1830 m above sea level (a.s.l.).



**Fig. 3.2.** Overview map of the David Glacier Basin, Victoria Land. The box in the lower left marks the location shown in Fig. 3.3a. T: Talos Dome; C: Dome C.

### *Geology of the area*

The geological basement in southern Victoria Land is made up of the late Cambrian Granite Harbour Igneous Complex that consists largely of coarse-grained granite and granodiorite and contains minor diorite and tonalite plutons and dykes (Capponi et al., 1999). During the Palaeozoic the basement was uplifted and eroded. This led to the formation of the Kukri Peneplain, which is thought to be pre-Devonian in age (Gunn and Warren, 1962). Above the peneplain the clastic sediments of the Beacon Supergroup rest unconformably on the basement. They predominantly consist of quartz-sandstones and coarse arkosic sandstones (Ricker, 1964). In the southernmost outcropping area of the Ricker Hills fossil plants indicate an early Triassic age for the Beacon sediments (Capponi et al., 1999). The highest stratigraphical unit in the area is represented by Jurassic extrusive Kirkpatrick basalts and intrusive Ferrar dolerites (Ricker, 1964). Rocks of Ferrar dolerite constitute the main outcrops of the Ricker Hills (Ricker, 1964). Sediments from the Beacon Supergroup and Kirkpatrick basalts are restricted to very rare isolated outcrops, while no occurrence of the basement is visible at the surface today (Capponi et al., 1999).

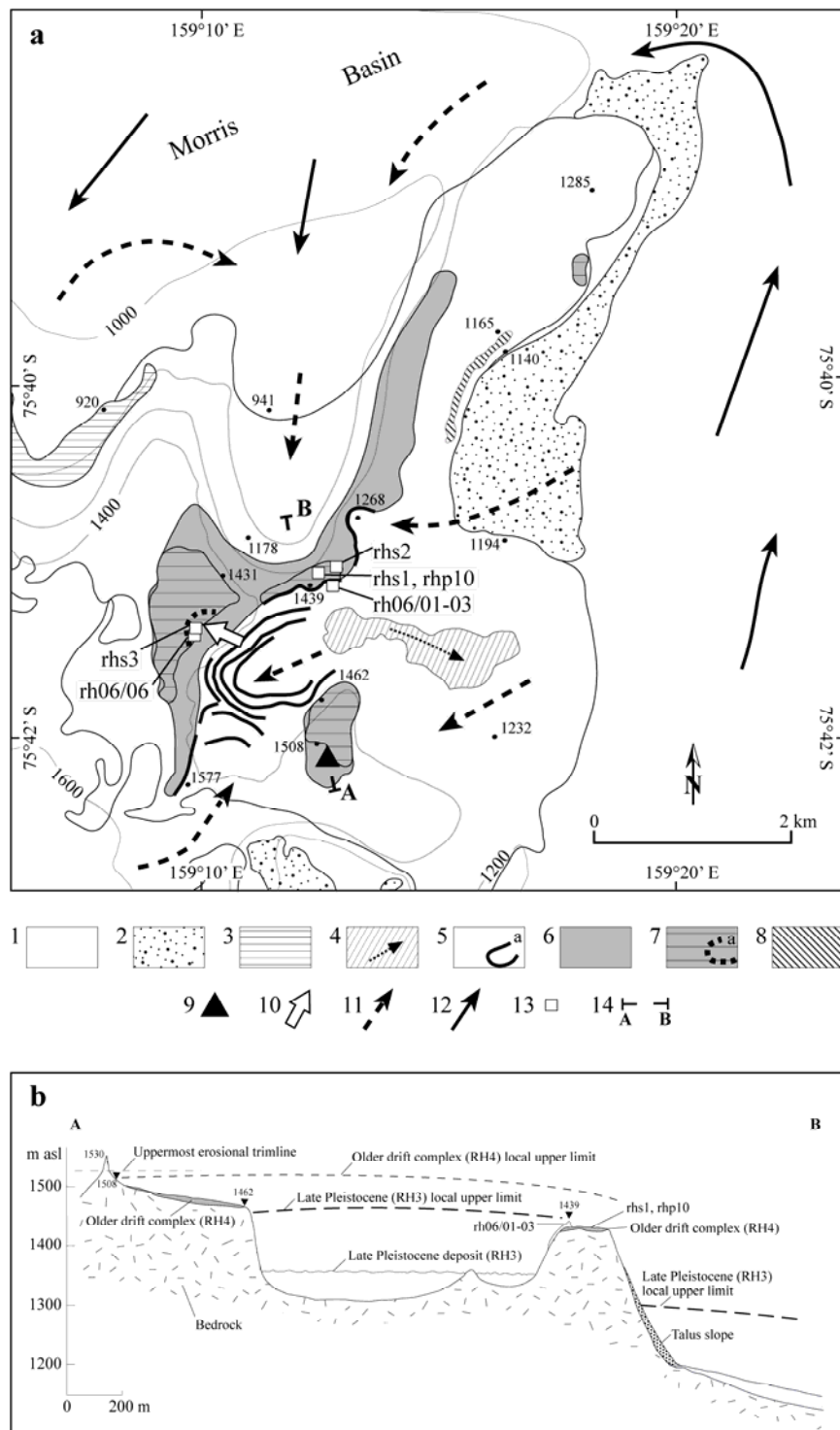


**Fig. 3.3. a.** Geomorphological map, and **b.** profile (see point 14 in a. for location) of the study area and sample positions. (1) Snow and glacier ice; (2) Supraglacial debris; (3) Holocene glacial deposit (RH1); (4) Remobilized late Pleistocene glacial deposit (Holocene; arrow = flow direction); (5) Present ice-free area overridden during late Pleistocene (RH3; a = moraine); (6) Late Pleistocene deglaciated area; (7) Older drift complex, early to middle Pleistocene (RH4; a = boulder alignment); (8) Ricker Hills Tillite, Oligocene (RH5); (9) Horn; (10) Older drift complex (RH4) ice flow direction; (11) Late Pleistocene ice flow direction; (12) Present ice flow direction; (13) Sample site; (14) Cross section. Contour lines from ADD (Antarctic Digital Database); dots with numbers: spot heights from GPS survey (elevation in metres).

*Glaciological and geomorphological settings*

The E–W flowing David Glacier is the most important outlet glacier in Victoria Land. Its floating tongue, known as the Drygalski Ice Tongue, is about 20 km wide and extends over 100 km into the Ross Sea, thus it is a distinctive element of Victoria Land’s coastline (Fig. 3.2). With an area of 214,300 km<sup>2</sup>, David Glacier is one of the large glacier systems, draining Dome C with an annual outflow of  $15.6 \pm 1$  km<sup>3</sup> (Rignot and Thomas, 2002). The drainage can be divided into a smaller flow that slopes from Talos Dome to the Ross Sea and a main flow consisting of a network of tributaries, which drain the plateau area around Dome C and converge in a huge icefall (David Cauldron) northwest of the Ricker Hills. Ice flow around the Ricker Hills is generally SW–NE, but ice flow in an opposite direction occurs in depressions at the lee side of the nunatak (Fig. 3.3). Present-day ice levels in the nunatak’s up- and downstream parts are ~1750 m and ~900 m a.s.l., respectively. Ice thicknesses vary considerably from site to site, reaching up to 1000 m in an adjacent sub-glacial valley east of the Ricker Hills (Delisle, 1997).

Higher EAIS levels in the past have left substantial imprints on the surface morphology of the Ricker Hills. Areas with distinct glacial erosional and depositional features are widespread up to a certain altitude marked by a glacial trimline. Above the trimline a weakly developed alpine topography with deep cavernous weathering forms ridges and horns. This is evidence that glaciers never overrode the highest peaks after sculpturing the alpine topography. Geomorphological and glacial geological surveys of the Ricker Hills allowed at least five glacial drifts to be distinguished, hereafter informally named RH1 to RH5 (Baroni et al., 2008). RH1 and RH2 represent the youngest glacial drifts deposited during the Holocene and Late Glacial, respectively. They are characterized by ice-cored moraines and hummocky deposits around the current ice margin (RH1) and in the area of former ice lobes, below the late Pleistocene ice limit, where ice entered the nunatak depressions. Glacial sediments related to the late Pleistocene ice level limit (RH3) occur at higher elevations up to ~300 m above the current ice stand, sometimes with well-defined moraine ridges (Figs. 3.3 and 3.4). These deposits cover broad areas of the nunatak. They are to a large part still ice-cored and can be correlated to the “Terra Nova Drift” documented in the Terra Nova Bay region by Orombelli et al. (1991). Radiocarbon ages for the “Terra Nova Drift” in the Northern Foothills (Terra Nova Bay) bracket its age between 7.5 and 25 ka before present (Orombelli et al., 1991). A fourth unit (RH4) indicates a Pleistocene drift deposit older than RH3. Yellowish-red or red staining of boulder surfaces are typical for RH4 deposits, and clearly differ from the grey colour of the

RH3 drift. Scattered erratic boulders of RH4 occur up to the top of the hills, reaching elevations of about 500 m above the present ice level. Weathering degree and occurrence of erratic boulders within this drift correspond to Orombelli et al.'s (1991) observations for the "Older Drift". The oldest unit in the relative stratigraphy of glacial deposits is the Ricker Hills Tillite (RH5). This is a semi-lithified diamicton that was deposited by a warm-based glacier most probably during Oligocene times (Baroni and Fasano, 2006; Baroni et al., 2008). Fig. 3.3 shows the different drifts and their spatial distribution in the investigated area (RH2 does not outcrop in this sector of the Ricker Hills) as well as the main geomorphological features.

### 3.2.3 Sampling

When sampling for surface exposure dating we focused on the nunatak's central part, where past ice lobes entered a depression from the northwest and distinct moraine ridges or drift boundaries are preserved. A suite of seven erratic boulders was sampled from three particular locations: RH3 moraines, and two different sites of RH4, a low-lying drift surface next to the RH3 moraines (site RH4 alpha), and a higher elevated drift surface (site RH4 beta). Sample positions are indicated on Fig. 3.3 and partly on Fig. 3.4, which shows in addition two sampled erratic boulders and gives insight into the local geomorphological situation of the area.

We collected rock material from two boulders (rh06/01 and rh06/03) from RH3 moraines that were separated only by a few metres and rest on the outermost moraine ridge delimiting the RH3 from the RH4 drift (Fig. 3.4d). Beyond the well-defined RH3 moraines, two samples (rhs1 and rhp10) were collected from a low-lying RH4 drift (site alpha) and another three (rhs2 & 3 and rh06/06) from a higher elevated RH4 drift surface (site beta). The two highest samples (rhs3 and rh06/06) derive from erratics that belong to a boulder alignment, defining the upper limit of the RH4 drift (Fig. 3.4a).

All erratic boulders sampled for surface exposure age determination are Beacon sandstones, some of which have undergone slight metamorphic transformation. In the case of rhs2, the sandstone has changed completely into quartzite. In all cases, we sampled rock material from the erratic boulders' topmost 5 cm to minimize depth corrections. We performed careful field surveys in order to collect the most representative samples from a specific drift. For each boulder, its size, weathering degree, possible snow/ice cover and the likelihood of post-

depositional movements were evaluated prior to sampling. Although the largest (0.35 to 2.15 m<sup>3</sup>) and most stable boulders were sampled, post-depositional overturning can never be completely excluded, because drifts were probably still ice-cored for a long time after deposition (the RH3 drift is to a major part still ice-cored today).

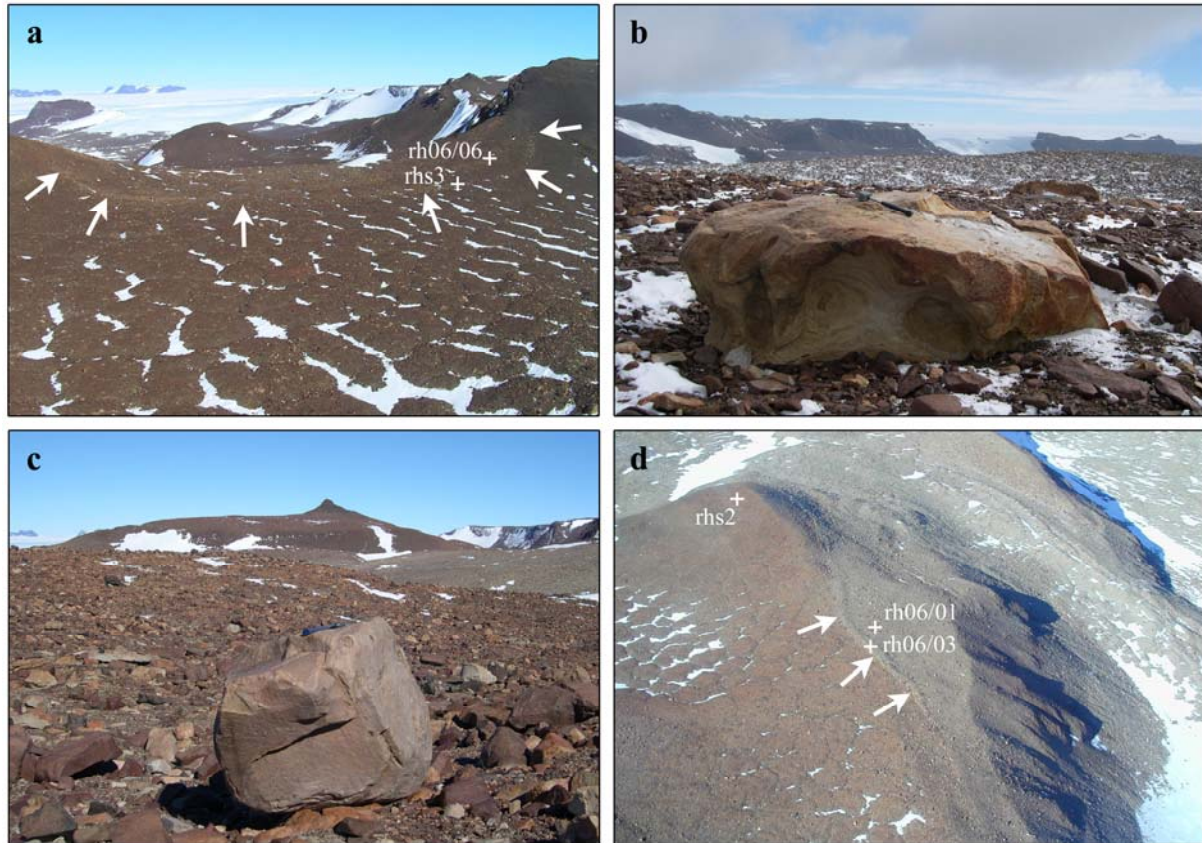


**Fig. 3.4.** **a.** Older drift lobe (RH4 site beta) with boulder alignment defining the upper limit of RH4; width of the lobe ~450 m. **b.** Sample rhs3 from the RH4 drift lobe (note the hammer for scale). **c.** Sample rhs1 on the low-lying older drift (RH4 site alpha; note the hammer for scale). In the background is the horn mapped in Fig. 3.3a. **d.** Moraine in the middle of the picture delimiting the RH3 (right side) from the RH4 drift (left side). Horizontal width of the picture is ~400 m.

### 3.2.4 Surface exposure dating

The quartz-rich sandstones we sampled are appropriate for cosmogenic nuclide analyses because quartz is relatively resistant to weathering and approved techniques allow the extraction of both cosmogenic neon (Niedermann et al., 1993) and beryllium (e.g. Kohl and Nishiizumi, 1992). Cosmogenic nuclides, induced by cosmic ray spallation reactions within mineral lattices, accumulate in surface rocks in a predictable manner over time. Measuring the cosmogenic nuclide concentrations in minerals such as quartz thus allows determining how long a rock surface has been exposed to cosmic radiation (e.g. Lal, 1991; Cerling and Craig,

1994). Coverage by, e.g., glacial till, snow or ice can, however, reduce or completely stop cosmogenic nuclide production. Beneath more than about 5 m of ice, rock surfaces are essentially completely shielded from cosmic rays (Fabel and Harbor, 1999). When studying exposure ages of erratic boulders it is generally assumed that no cosmogenic nuclides are initially present prior to deposition and accumulation of cosmogenic nuclides starts with the melt-out (~deposition) of the boulder from the ice (i.e. a “simple exposure history”). This implies that the original surfaces of the erratic boulders were either completely shielded from incoming cosmic rays or glacial erosion exceeded ~2 m (the maximum depth at which a rock experiences a sizeable secondary cosmic ray particle flux) and removed all inherited nuclides from previous exposure times (Fabel and Harbor, 1999). However, in polar regions glacial erosion might not exceed this value and after retreat of a cold-based ice body, the overridden rock surfaces or erratic boulders may still contain some cosmogenic nuclides from an exposure period prior to the last ice advance (called a “complex exposure history”). To identify such a complex exposure history scenario and check whether a surface was intermittently shielded for a substantial period (= “burial period”) a combined analysis of a stable and radioactive or two radioactive nuclides is necessary. During burial the ratio of the two nuclides changes (e.g. the  $^{21}\text{Ne}/^{10}\text{Be}$  ratio increases), due to radioactive decay.

Analysis of two independent nuclides enables us to obtain two exposure ages for each sample. Such cross-dating significantly increases our confidence in the reliability of an exposure age. Furthermore, in combination two or more different cosmogenic nuclide measurements from the same sample may yield valuable information about the sample-specific erosion rate and, as noted above, the exposure history (Lal, 1991; Gosse and Phillips, 2001). In order to determine surface exposure ages from the Ricker Hills and to benefit from the potential of multiple nuclide analyses, we extracted and measured both cosmogenic  $^{21}\text{Ne}$  and  $^{10}\text{Be}$  from the erratic boulders we sampled.

### *Sample preparation*

Rock samples were mainly processed at the Institute of Geological Sciences, University of Bern. In a first step the rocks were crushed and sieved into grain sizes between 0.25 and 0.4 mm. In a second stage magnetic separation was applied to remove magnetic minerals before the samples were put into hydrochloric and hydrofluoric acids to chemically isolate quartz according to Kohl and Nishiizumi (1992). A split of each purified quartz separate was then kept for noble gas analysis, while the rest underwent further chemical processing to

extract  $^{10}\text{Be}$  following standard procedures. The quartz splits for the  $^{21}\text{Ne}$  measurements were further crushed to grain sizes  $<0.1$  mm and cleaned in an ultrasonic bath. The suspended finest fraction was subsequently decanted.

#### *Cosmogenic nuclide measurements*

Radionuclide analyses were carried out at the accelerator mass spectrometry facility of PSI/ETH Zurich.  $^{10}\text{Be}/^9\text{Be}$  ratios were measured according to the method described by Synal et al. (1997) and used to calculate  $^{10}\text{Be}$  concentrations. Cosmogenic  $^{21}\text{Ne}$  was analysed in the noble gas laboratories of the Institute of Isotope Geochemistry and Mineral Resources at ETH Zurich. Samples of 40–60 mg quartz were measured in a non-commercial ultra-high sensitivity mass spectrometer with a special ion source (see Baur (1999) for details). Noble gases were extracted from the samples through step-wise heating at 600, 800, and 1750 °C to separate the cosmogenic from the non-cosmogenic (trapped and nucleogenic) neon components (Niedermann et al., 1993).

#### *Age calculation*

All exposure ages were calculated with CosmoCalc 1.0 (Vermeesch, 2007), using altitude and latitude production rate scaling factors defined for the Antarctic region by Stone (2000), sea level high latitude production rates for  $^{21}\text{Ne}$  and  $^{10}\text{Be}$  of 20.3 and 5.1 atoms per gram quartz per year, respectively (Niedermann, 2000; Stone, 2000), an attenuation length ( $\lambda$ ) of 157 gram per  $\text{cm}^2$  and default values for all other parameters. The  $^{21}\text{Ne}$  concentrations used in the calculations derive from the neon excesses above air ( $^{21}\text{Ne}_{\text{exc}}$ ) of the 600 °C temperature steps under the assumption of entirely atmospheric  $^{20}\text{Ne}$  concentrations. All relevant neon and beryllium isotope data for exposure age determination are shown in Table 3.1 and the neon three-isotope distribution is illustrated in Fig. 3.5. Details of the noble gas data are explained in the next section.

We corrected each date based on the slope of the sampled surface, topographic shielding by surrounding hills and mountains (Dunne et al., 1999), and for the sample thickness (Gosse and Phillips, 2001). A correction for shielding of the sampled erratic boulders by intermittent snow cover was not included in the calculations. Due to strong prevailing katabatic winds, we think it is unlikely that enough snow could accumulate to cover the erratic boulders (which have heights between 50 and 150 cm). Exposure age corrections due to past geomagnetic intensity variations that affected cosmogenic nuclide production are not required for latitudes



greater than about 60° (e.g. Cerling and Craig, 1994). However, one effect that cannot be neglected is erosion. To account for erosion we determined sample-specific neon-beryllium erosion rates from an erosion island plot (Fig. 3.6) and adopted these values to calculate erosion-corrected ages. Sample-specific information and exposure ages calculated with a range of erosion rates are listed in Table 3.2.

**Table 3.1.** Neon and beryllium isotope data.

Sample	Heating Temp. (°C); Time (min)	$^{20}\text{Ne}$ ( $10^9$ atoms $\text{g}^{-1}$ )	$^{21}\text{Ne}/^{20}\text{Ne}$ ( $10^{-3}$ )	$^{22}\text{Ne}/^{20}\text{Ne}$	$^{21}\text{Ne}_{\text{exc}}$ ( $10^6$ atoms $\text{g}^{-1}$ )	$^{21}\text{Ne}_{\text{exc}}$ released (%)	$^{10}\text{Be}$ ( $10^6$ atoms $\text{g}^{-1}$ )
rh06/01	600; 45	$9.46 \pm 0.04$	$3.64 \pm 0.06$	$0.1021 \pm 0.0007$	$6.40 \pm 0.71$	80.8	$1.11 \pm 0.06$
	800; 20	$2.52 \pm 0.06$	$3.19 \pm 0.12$	$0.1025 \pm 0.0012$	$0.59 \pm 0.51$	7.4	
	1750; 20	$1.49 \pm 0.01$	$3.59 \pm 0.17$	$0.1021 \pm 0.0021$	$0.93 \pm 0.28$	11.8	
rh06/03	600; 45	$9.04 \pm 0.05$	$4.20 \pm 0.08$	$0.1034 \pm 0.0008$	$11.19 \pm 0.91$	79.4	$2.39 \pm 0.07$
	800; 20	$2.34 \pm 0.01$	$3.33 \pm 0.09$	$0.1011 \pm 0.0010$	$0.88 \pm 0.24$	6.2	
	1750; 20	$2.55 \pm 0.01$	$3.75 \pm 0.10$	$0.1029 \pm 0.0011$	$2.02 \pm 0.30$	14.4	
rhp10	600; 45	$15.50 \pm 0.06$	$4.59 \pm 0.03$	$0.1036 \pm 0.0004$	$25.24 \pm 0.76$	95.4	$5.15 \pm 0.15$
	800; 20	$2.34 \pm 0.02$	$3.18 \pm 0.09$	$0.1020 \pm 0.0006$	$0.53 \pm 0.26$	2.0	
	1750; 20	$1.48 \pm 0.02$	$3.43 \pm 0.15$	$0.1019 \pm 0.0010$	$0.70 \pm 0.28$	2.6	
rhs1	600; 45	$15.27 \pm 0.06$	$3.48 \pm 0.03$	$0.1013 \pm 0.0004$	$7.92 \pm 0.69$	77.0	$1.54 \pm 0.05$
	800; 20	$2.61 \pm 0.01$	$3.19 \pm 0.06$	$0.1020 \pm 0.0009$	$0.61 \pm 0.19$	5.9	
	1750; 20	$2.17 \pm 0.02$	$3.77 \pm 0.10$	$0.1022 \pm 0.0010$	$1.75 \pm 0.30$	17.1	
rhs2	600; 45	$17.19 \pm 0.06$	$8.18 \pm 0.04$	$0.1073 \pm 0.0003$	$89.8 \pm 1.4$	80.0	$17.23 \pm 0.52$
	800; 20	$2.07 \pm 0.02$	$3.22 \pm 0.07$	$0.1031 \pm 0.0007$	$0.55 \pm 0.21$	0.5	
	1750; 20	$1.42 \pm 0.01$	$18.3 \pm 0.30$	$0.1013 \pm 0.0013$	$21.9 \pm 0.58$	19.5	
rhs3	600; 45	$18.83 \pm 0.07$	$6.82 \pm 0.06$	$0.1062 \pm 0.0004$	$72.8 \pm 1.6$	99.3	$14.92 \pm 0.45$
	800; 20	$2.72 \pm 0.01$	$3.06 \pm 0.06$	$0.1023 \pm 0.0010$	$0.27 \pm 0.22$	0.4	
	1750; 20	$1.68 \pm 0.02$	$3.10 \pm 0.09$	$0.1035 \pm 0.0013$	$0.24 \pm 0.21$	0.3	
rh06/06	600; 45	$21.77 \pm 0.08$	$5.88 \pm 0.05$	$0.1044 \pm 0.0002$	$63.5 \pm 1.5$	92.4	$13.17 \pm 0.40$
	800; 20	$6.54 \pm 0.03$	$3.17 \pm 0.04$	$0.1028 \pm 0.0006$	$1.42 \pm 0.34$	2.1	
	1750; 20	$2.25 \pm 0.01$	$4.64 \pm 0.13$	$0.1020 \pm 0.0010$	$3.78 \pm 0.33$	5.5	

Errors are  $1\sigma$  and include uncertainties for the variability of chemical processing for the radionuclide, and statistical, sensitivity, and mass-discrimination errors for the noble gas measurements. Absolute errors of neon abundances are not included in the noble gas data, but are about 2 % as determined with two independent air-calibrations.  $^{21}\text{Ne}_{\text{exc}}$  is the calculated  $^{21}\text{Ne}$  excess over air.

### 3.2.5 Results

Surface exposure ages of all investigated erratic boulders are compiled in Table 3.2. For each erratic boulder two independent exposure ages (neon and beryllium) are available. The apparent  $^{21}\text{Ne}$  and  $^{10}\text{Be}$  ages (assuming no erosion) range from  $70 \pm 8$  to  $951 \pm 15$  ka and from  $49 \pm 3$  to  $900 \pm 27$  ka, respectively, and show broad agreement between each other.

Only the 600 °C temperature steps were used to determine neon exposure ages, because most of the cosmogenic neon is released from quartz below this temperature and the higher temperature steps (800, 1750 °C) usually contain non-cosmogenic neon components (Niedermann et al., 1993). The cosmogenic origin of the 600 °C steps is confirmed by the positions of the associated data points in the neon three-isotope diagram (Fig. 3.5). With the exceptions of rhs1 & 2 and rh06/06 they lie within errors on the atmospheric-cosmogenic mixing line. Within two-sigma confidence limits also the rhs2 point falls on the line, while data points of the other two samples still plot below the line. The  $^{21}\text{Ne}_{\text{exc}}$  of the 600 °C steps of rhs1 and rh06/06 might therefore not consist of cosmogenic neon only but contain additional non-atmospheric neon components, leading to an overestimation of the neon exposure ages. For this reason,  $^{21}\text{Ne}$  dates for rhs1 and rh06/06 are not considered in the conclusions.

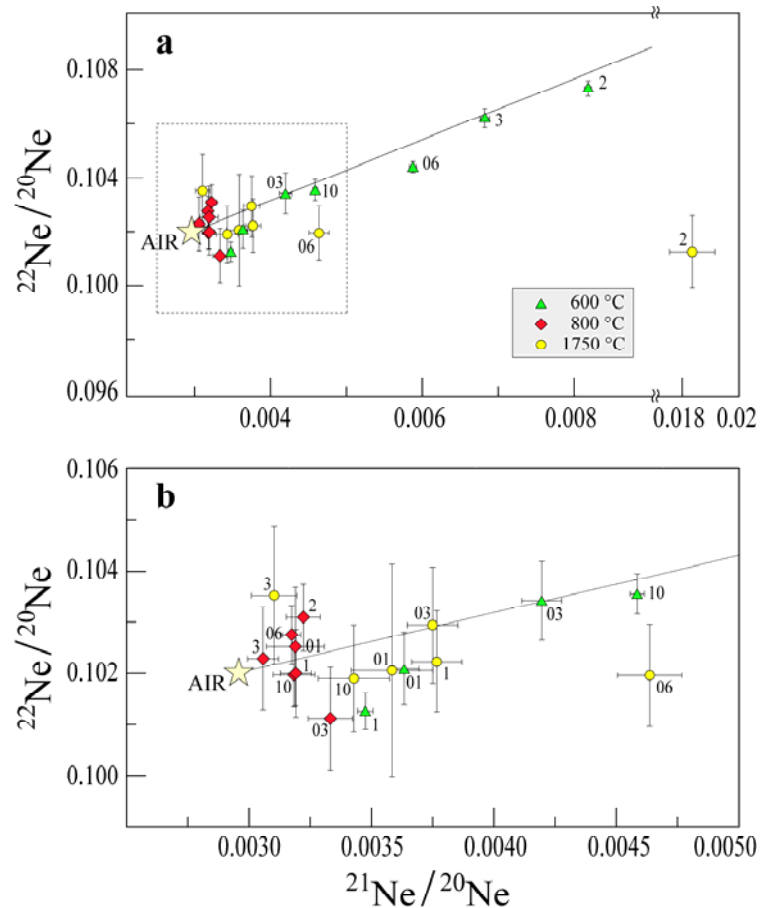
**Table 3.2.** Calculated exposure ages.

Sample	Drift	Altitude (m a.s.l.)	Correc- tion factor	Apparent $^{21}\text{Ne}$ age (ka)	Apparent $^{10}\text{Be}$ age (ka)	$^{21}\text{Ne}$ age (ka) erosion rate 35 cm Ma <sup>-1</sup>	$^{10}\text{Be}$ age (ka) erosion rate 35 cm Ma <sup>-1</sup>	$^{21}\text{Ne}$ age (ka) erosion rate 45 cm Ma <sup>-1</sup>	$^{10}\text{Be}$ age (ka) erosion rate 45 cm Ma <sup>-1</sup>
rh06/01	RH3	1438	0.958	70 ± 8	49 ± 3	71 ± 8	50 ± 3	72 ± 8	50 ± 3
rh06/03	RH3	1438	0.976	120 ± 10	106 ± 3	125 ± 10	110 ± 3	126 ± 10	111 ± 3
rhp10	RH4 α	1435	0.999	265 ± 8	230 ± 7	288 ± 9	248 ± 8	296 ± 9	254 ± 9
rhs1	RH4 α	1438	0.962	86 ± 7	69 ± 2	88 ± 8	70 ± 2	89 ± 8	71 ± 2
rhs2	RH4 β	1455	0.975	951 ± 15	900 ± 27	1396 ± 22	1423 ± 43	1686 ± 27	1892 ± 57
rhs3	RH4 β	1589	0.962	703 ± 16	678 ± 20	908 ± 20	902 ± 27	1004 ± 23	1018 ± 31
rh06/06	RH4 β	1600	0.970	603 ± 14	575 ± 19	746 ± 18	722 ± 24	807 ± 19	787 ± 26

Exposure age calculations are based on sea level high latitude production rates  $P_{10} = 5.1$  at/g/yr (Stone, 2000),  $P_{21} = 20.3$  at/g/yr (Niedermann, 2000) and the scaling model of Stone (2000). Correction factor includes geometric shielding and sample thickness (using  $A = 157$  g/cm<sup>2</sup> and  $\rho = 2.65$  g/cm<sup>3</sup>). RH4 α and RH4 β represent samples from the RH4 drift sites alpha and beta, respectively. Apparent = no erosion. Erosion-corrected ages for two reasonable erosion rates ( $\varepsilon = 35$  and  $45$  cm Ma<sup>-1</sup>, respectively) are given (see text and Fig. 3.6).

Among the total data set the oldest exposure ages (apparent  $^{10}\text{Be}$  ages from  $575 \pm 19$  to  $900 \pm 27$  ka) come from the high-elevated RH4 drift (site beta). Apparent  $^{10}\text{Be}$  dates from the two other sampling locations (Fig. 3.3) are considerably younger and range from  $69 \pm 2$  to  $230 \pm 7$  ka for the lower-lying RH4 drift (site alpha) and from  $49 \pm 3$  to  $106 \pm 3$  ka in the case of the RH3 moraines. When taking erosion into account, exposure ages are shifted towards older dates. The older a sample and/or the higher the erosion rate, the larger the shift is (Table 3.2).

**Fig. 3.5.** Neon three-isotope diagrams. The line in the graphs is the atmospheric-cosmogenic mixing line for quartz, described by Niedermann et al. (1993). **a.** Data points from this study (error limits are  $1\sigma$ ). The dashed box shows the area of the diagram shown in **b**. **b.** An enlargement of the data that have low neon ratios. Sample abbreviations: 1–3 represent samples rhs1 to 3; 10 represents sample rhp10; 01–06 represent samples rh06/01, 03 and 06.



### 3.2.6 Discussion

From the geomorphological position and weathering degree the older drift complex (RH4) is supposed to be older than late Pleistocene (Baroni et al., 2008). But when did ice retreat from these surfaces, and as a consequence, when did cosmogenic nuclide production start? As Table 3.2 reveals, the RH4 drift (apparent  $^{10}\text{Be}$  exposure ages  $69\pm 2$  ka to  $900\pm 27$  ka) generally predates the late Pleistocene, but no clear age cluster defines the timing of deglaciation. From the two investigated RH4 sites (alpha & beta) the lower lying site alpha yields much younger apparent exposure ages ( $^{10}\text{Be}$  ages  $69\pm 2$  ka and  $230\pm 7$  ka) than the higher elevated site beta ( $^{10}\text{Be}$  dates from  $575\pm 19$  ka to  $900\pm 27$  ka), which points to an unequal drift evolution. Thus, the glacial situation seems to be more complex than expected from glacial geological and geomorphological surveys and requires careful data interpretation in order to reconstruct the glacial chronology of the Ricker Hills.

Although there is broad agreement between neon and beryllium apparent ages of the analysed erratic boulders, there are small but important  $^{21}\text{Ne}$  and  $^{10}\text{Be}$  age differences (all  $^{21}\text{Ne}$  ages are older than  $^{10}\text{Be}$  ages), which reveal valuable information about drift evolution. All erratic boulders from RH3 and low-lying RH4 (site alpha) drift surfaces have  $^{21}\text{Ne}$  and  $^{10}\text{Be}$  age differences that cannot be explained by continuous exposure because in Fig. 3.6 the  $^{21}\text{Ne}/^{10}\text{Be}$  ratios plot above the erosion island in the complex exposure zone. The differences between the  $^{21}\text{Ne}$  and  $^{10}\text{Be}$  dates of these samples are most probably due to burial of the erratic boulders beneath non-erosive cold-based ice. Burial by ice plays an important role in Antarctica and limits the potential of cosmogenic nuclide dating under polar conditions (Sugden et al., 2005; Di Nicola et al., 2007). By contrast to the complex exposure histories of boulders from the low-lying surfaces, paired nuclide analyses of all erratic boulders from the high-elevated RH4 (site beta) surface indicate simple exposure histories (Fig. 3.6). This suggests that in the early Pleistocene ice levels reached the highest elevations in the Ricker Hills (up to ~500 m above present-day ice levels) and subsequent EAIS variations were of lesser extent. During the middle Pleistocene the highest areas (including RH4 site beta) were ice-free and only low elevations of RH4 (e.g. site alpha) close to RH3 deposits were intermittently ice-covered.

#### *Effect of complex exposure*

The signature of complex exposure is observed throughout the low-elevated drifts RH4 site alpha and RH3. As stated earlier, one of the major processes leading to the evolution of complex glacial surfaces is intermittent burial by ice. With a very simple scenario – assuming no erosion and a simple exposure and a subsequent burial period – we can calculate a burial age from the nuclide concentrations. For rhp10 for example this would be in the order of ~400 ka and a total exposure-burial history (burial age + apparent  $^{21}\text{Ne}$  exposure age) of ~665 ka would result. Although this scenario is far from reality it gives an idea of how much burial time is needed to accommodate a rather small age difference obtained from two nuclides. Our results suggest that cold-based ice probably covered the low-lying RH4 surfaces of the Ricker Hills for a considerable time. Such a scenario may also apply to the evolution of the RH3 drift. A similar theoretical exposure-burial quantification for rh06/01 as for rhp10 reveals a total exposure-burial history of ~1.1 Ma. Hence, the late Pleistocene ice advance probably entrained older erratic boulders and deposited them on RH3 moraines leading to deceptive old exposure ages.

On the contrary, overturning during reworking and/or rearrangements of erratic boulders after initial deposition due to melting processes in ice-cored drifts or periglacial activities can result in falsely young ages and further add to the complexity of such deposits. Continuous post-depositional movements of 1 mm per year (seasonal changes summer–winter) would be large enough to overturn a boulder during its exposure period. Putkonen et al. (2008) measured regolith degradation in the Dry Valleys of about  $2 \text{ m Ma}^{-1}$  in a soil that is presently free of ice and visible moisture and was previously considered as a stable surface.

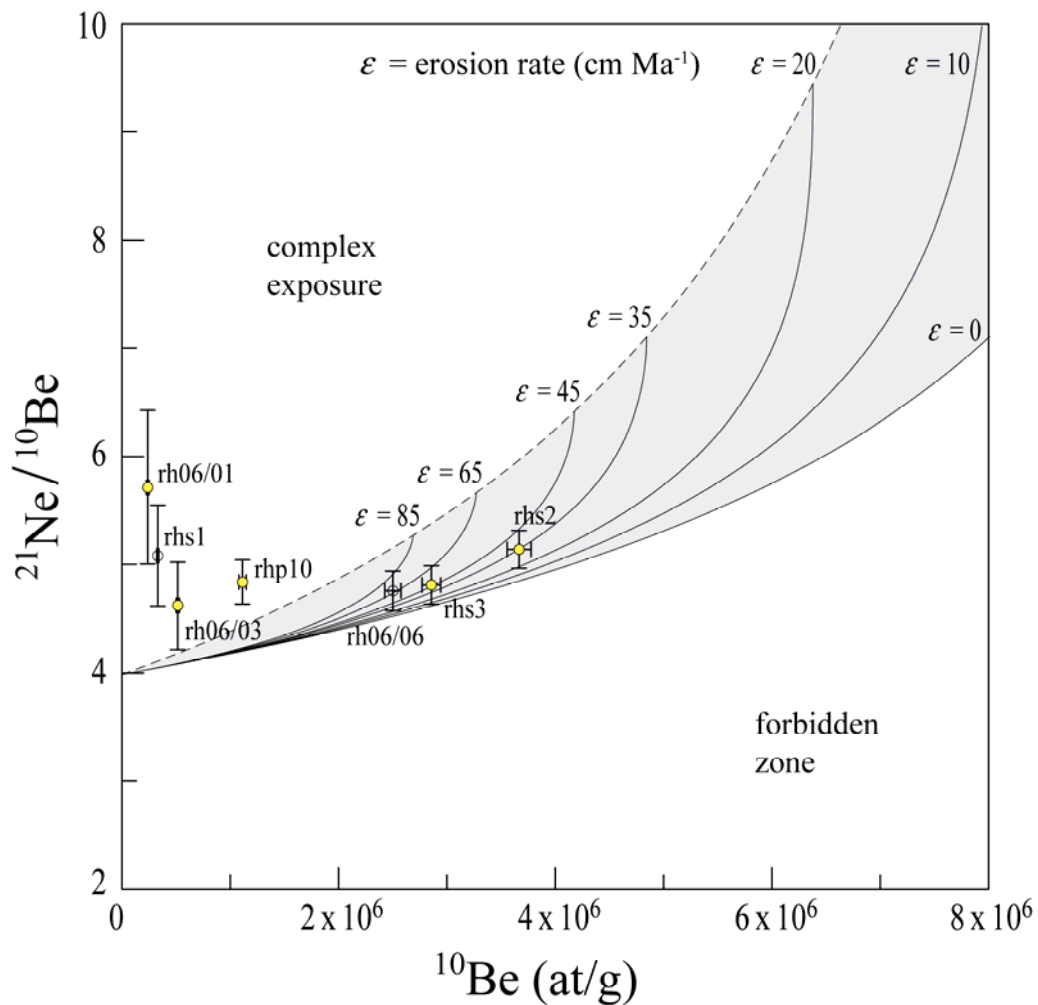


**Fig. 3.6.** Erosion island plot for all samples showing the effect of erosion on relative concentrations (normalized to sea level and high latitude) of  $^{21}\text{Ne}$  and  $^{10}\text{Be}$  for different erosion rates (solid lines). Dashed line connects steady-state erosion end points, the ratios where cosmogenic  $^{21}\text{Ne}$  does not accumulate any more due to erosion. The grey zone is known as steady-state erosion island (Lal, 1991). Samples with continuous exposure histories plot within the erosion island depending on erosion rates, whereas data plotting above indicate complex exposure. Open symbols mark the samples with possible non-cosmogenic  $^{21}\text{Ne}$  contributions (rhs1, rh06/06) and therefore might plot too high in the diagram. The graph was produced using the calculation parameters indicated in the text and caption of Table 3.2.

Burial by cold-based ice and post-depositional surface rearrangements lead to complex drift deposits that pose a challenging issue for surface exposure dating. Studying special geomorphological features like perched-boulders or pairs of erratics and glacially scoured bedrock as well as exposure histories of different surfaces (fully exposed and (partially) shielded) from the same boulder might help to address this issue in future. Furthermore, surface exposure dating with in situ produced cosmogenic  $^{14}\text{C}$  could contribute to decipher the late Pleistocene glacial chronology, due to its short half-life compared to  $^{10}\text{Be}$ . But nevertheless, the identification of complex drifts demands multiple cosmogenic nuclide analyses since single nuclide exposure ages may result in misinterpretation of the glacial geological situation.

#### *Effect of erosion*

Erosion of the sampled erratic boulders during exposure times has continuously removed cosmogenic nuclides, hence lowered the apparent exposure ages. Correcting for erosion thus shifts the dates towards older exposure ages (Table 3.2), which are more realistic as long as the adopted erosion rates reflect time-averaged local conditions. Erosion rates are generally very low in Antarctica due to the hyperarid polar climate; however, even extremely low erosion rates could significantly affect samples with apparent exposure ages in the order of several hundred thousand to million years (e.g. Schäfer et al., 1999). That erosion has to be considered in the study area is obvious from weathered boulders of RH4 deposits, which sometimes show cavernous weathering (Fig. 3.4b).

For the oldest two samples it was possible to determine erosion rates from a neon-beryllium erosion island plot (Fig. 3.6). The resulting erosion rates are 20–45  $\text{cm Ma}^{-1}$  for the quartzite rhs2 and 10–65  $\text{cm Ma}^{-1}$  for the sandstone sample rhs3 (accounting for the errors in  $^{21}\text{Ne}$  and  $^{10}\text{Be}$ ), with best-fit values of 35 and 45  $\text{cm Ma}^{-1}$ , respectively. These erosion rates are higher than previously reported for sandstone boulders (Ivy-Ochs et al., 1995; Schäfer et al., 1999) or granite bedrock (Oberholzer et al., 2003; Di Nicola et al., 2007), but are close to the values (17–41  $\text{cm Ma}^{-1}$ ) described by Oberholzer et al. (2008) for the nearby dolerite gargoyles and within the denudation range of sandstone bedrock indicated by Summerfield et al. (1999) for the Dry Valleys area (13.3–60  $\text{cm Ma}^{-1}$ ). Adopting these erosion rates increases the exposure ages of the samples for the high-elevated RH4 drift (rhs3 & 2) by roughly 45 % to ~1000 and ~1400 ka (Table 3.2).

The effect of erosion on calculated exposure ages is illustrated in Fig. 3.7 for both samples and the whole range of determined erosion rates. Fig. 3.7 shows that erosion-corrected exposure ages of rhs2 and rhs3 overlap between 1125 and 1375 ka. This concordance leads us to believe that the high-elevated RH4 drift was deposited most likely during this time period. Accepting this implies erosion rates of  $\sim 20\text{--}35\text{ cm Ma}^{-1}$  for the quartzite and  $\sim 53\text{--}65\text{ cm Ma}^{-1}$  for the sandstone boulder (Fig. 3.7). These erosion rates differ only slightly from the graphically determined best-fit values (35 and 45  $\text{cm Ma}^{-1}$ , Fig. 3.6) and seem to reflect sample-specific erosion rates most accurately for the given situation. Weathering degree and rock fragmentation of sampled boulders already suggested relatively lower erosion rates for the quartzite than for the sandstone sample in the field, which is confirmed with this finding.

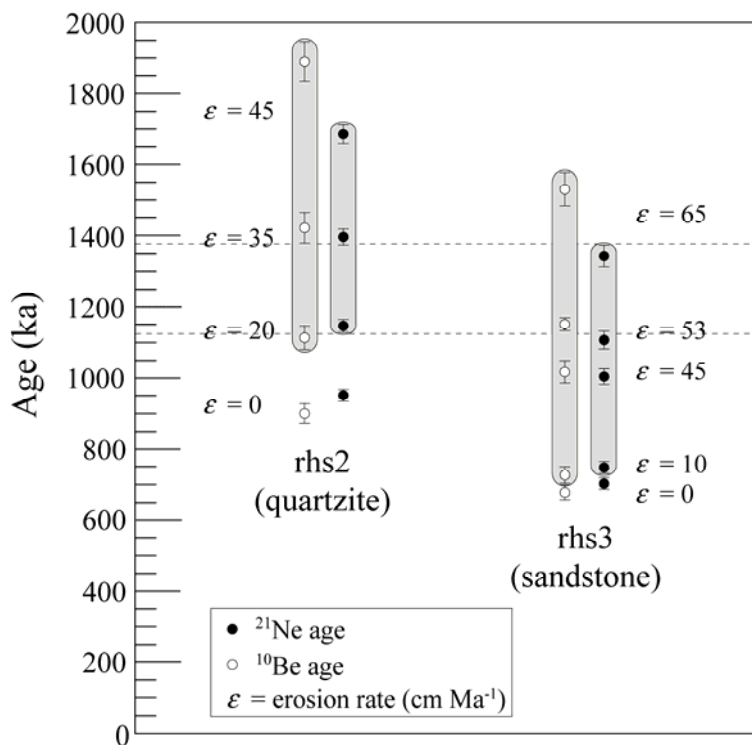


**Fig. 3.7.** Erosion-corrected exposure ages for the sample-specific range of erosion rates. The light grey horizontal band highlights the age overlap between 1125 and 1375 ka.

Erosion has a less significant effect on exposure ages of younger samples. As a consequence, erosion-corrected cosmogenic nuclide ages for the low-lying RH4 drift (site alpha) and the RH3 surfaces generally vary less than ten percent from their apparent (no erosion) ages (Table 3.2).

### 3.2.7 Conclusions

A deeply weathered glacial deposit (RH4), comparable to the “Older Drift” described in the Terra Nova Bay area by Orombelli et al. (1991), indicates a major EAIS advance in the Ricker Hills, Victoria Land, beyond the late Pleistocene drift limit. Apparent surface exposure ages based on cosmogenic  $^{21}\text{Ne}$  and  $^{10}\text{Be}$  for this older drift complex (RH4) confirms a pre-late Pleistocene age of the deposit, but at the same time suggests multiple episodes of glacial deposition. From our investigation we can divide the RH4 drift into two units, a lower (site alpha) and a higher elevated zone (site beta). The latter contains erratic boulders up to ~500 m above present-day ice levels and its ages (apparent  $^{10}\text{Be}$  ages from  $575 \pm 19$  to  $900 \pm 27$  ka) give evidence for a major early Pleistocene EAIS advance. Erosion-corrected exposure ages from this surface, including a well-defined boulder alignment from the highest outcrops of this elevated drift zone, suggest that the major ice advance occurred between 1125 and 1375 ka ago. Deposits from this glacial event seem to be only locally preserved, because subsequent ice advances possibly reworked other deposits of the same glacial phase. The range of erosion rates used to correct exposure ages were obtained from an erosion island diagram and are  $10\text{--}65 \text{ cm Ma}^{-1}$  for a sandstone and  $20\text{--}45 \text{ cm Ma}^{-1}$  for a quartzite.

The lower-lying RH4 drift unit (site alpha) represents a more complex deposit. Burial by cold-based ice seems to have played a major role in the evolution of the present surface. However, also other processes like reworking of older deposits and possibly post-depositional movements of the sub-surface could have affected the drift. Cosmogenic nuclide analyses of our samples do not allow determination of an accurate deposition age for this unit. But they indicate that the low-lying RH4 drift close to the RH3 drift was overridden by at least another Pleistocene ice advance, leaving the higher elevated surfaces unburied.

These results are important because the location of the Ricker Hills at the margin of the EAIS points to the conclusion that: 1) the nunatak has not been overridden by the EAIS during middle and late Pleistocene; 2) the position reached by the upper lobe (site beta) represents the maximum thickening of the EAIS during the entire Pleistocene; 3) glacial landforms in the Ricker Hills are older than the early Pleistocene and could date from the Pliocene or earlier, in accordance with Baroni et al. (2008); 4) the low erosion rates imply that the modern cold, arid climate has persisted since at least the early Pleistocene. This is in agreement with findings from northern Victoria Land (Oberholzer et al., 2003) and from sites further afield, like the Shackleton Range (Fogwill et al., 2004) and the Prince Charles Mountains (Fink et al., 2006).



Cosmogenic nuclide measurements for the late Pleistocene deposit (RH3) in the Ricker Hills yield exposure ages that clearly pre-date the last glacial maximum (~21 ka) and indicate a complex drift evolution. One or more processes leading to complex deposits as noted above for the low-lying RH4 drift could also explain the data scatter of the samples from the RH3 moraine. Additional samples need to be investigated with special regard to complex exposure in order to reconstruct the evolution of the RH3 drift in the Ricker Hills.

Our study of glacial deposits in the Ricker Hills showed that at least two EAIS variations occurred during the early to middle Pleistocene, and that these fluctuations were of limited amplitudes of less than ~500 m. However, multiple cold-based ice advances can pose substantial difficulties for cosmogenic nuclide chronologies. Combined nuclide analyses are therefore a prerequisite for any meaningful surface exposure dating in polar areas and are needed to further complete the picture of how the EAIS reacted to Pleistocene climate change.

**Acknowledgements:** This research was funded by the Italian National Program on Antarctic Research (PNRA) and the Swiss National Science Foundation grant number: 200020-105220/1. We gratefully acknowledge their support. Many thanks to F. Mancini for GPS survey of spot heights. We would like to thank the members of the XX and XXI Italian Antarctic Expeditions and the pilots of Helicopter New Zealand, who contributed greatly to successful sampling campaigns. Finally, we wish to thank David Marchant, Chris Fogwill and an anonymous reviewer for their helpful comments on an earlier version of this article.

## References

- ARMIENTI, P. & BARONI, C. 1999. Cenozoic climatic change in Antarctica recorded by volcanic activity and landscape evolution. *Geology*, **27**, 617–620.
- BARONI, C., NOTI, V., CICCACCI, S., RIGHINI, G. & SALVATORE, M.C. 2005. Fluvial origin of the valley system in northern Victoria Land (Antarctica) from quantitative geomorphic analysis. *Geological Society of America Bulletin*, **117**, 212–228.
- BARONI, C. & FASANO, F. 2006. Micromorphological evidence of warm-based glacier deposition from the Ricker Hills Tillite (Victoria Land, Antarctica). *Quaternary Science Reviews*, **25**, 976–992.
- BARONI, C., FASANO, F., GIORGETTI, G., SALVATORE, M.C. & RIBECAL, C. 2008. The Ricker Hills Tillite provides evidence of Oligocene warm-based glaciation in Victoria Land, Antarctica. *Global and Planetary Change*, **60**, 457–470.

- BARRETT, P.J. 1996. Antarctic palaeoenvironment through Cenozoic times - a review. *Terra Antarctica*, **3**, 103–119.
- BAUR, H. 1999. A Noble-Gas Mass Spectrometer Compressor Source With two Orders of Magnitude Improvement in Sensitivity. *Eos Transactions AGU*, **80**, Abstract V22B-08.
- CAPPONI, G., CRISPINI, L., MECCHERI, M., MUSUMECI, G., PERTUSATI, P.C., BARONI, C., DELISLE, G. & ORSI, G. 1999. *Antarctic Geological 1:250,000 map series, Mount Joyce Quadrangle (Victoria Land)*. Siena: Museo Nazionale dell'Antartide, Sez. Scienze della Terra.
- CERLING, T.E. & CRAIG, H. 1994. Geomorphology and in-situ cosmogenic isotopes. *Annual Reviews of Earth and Planetary Sciences*, **22**, 273–317.
- DECONTO, R.M. & POLLARD, D. 2003. Rapid Cenozoic glaciation of Antarctica induced by declining atmospheric CO<sub>2</sub>. *Nature*, **421**, 245–249.
- DELISLE, G. 1997. Sub-ice topography in selected areas of Victoria Land, Antarctica: Implications for its glacial erosion history. *Antarctic Research Series*, **71**, 127–135.
- DENTON, G.H., PRENTICE, M.L., KELLOGG, D.E. & KELLOGG, T.B. 1984. Late Tertiary History of the Antarctic Ice-Sheet: Evidence from the Dry Valleys. *Geology*, **12**, 263–267.
- DI NICOLA, L., STRASKY, S., SCHLÜCHTER, C., SALVATORE, M.C., KUBIK, P.W., IVY-OCHS, S., WIELER, R., AKÇAR, N. & BARONI, C. 2007. Complex exposure history of pre-LGM glacial drifts in Terra Nova Bay, Victoria Land, using a multiple cosmogenic nuclide approach. In COOPER, A.K., RAYMOND, C.R. & ISAES EDITORIAL TEAM, eds. *Antarctica: A Keystone in a Changing World - Online Proceedings of the 10th ISAES X, USGS Open-File Report 2007-1047*. Santa Barbara: U.S. Geological Survey, 4 pp.
- DUNNE, J., ELMORE, D. & MUZIKAR, P. 1999. Scaling factors for the rates of production of cosmogenic nuclides for geometric shielding and attenuation at depth on sloped surfaces. *Geomorphology*, **27**, 3–11.
- EPICA COMMUNITY MEMBERS 2004. Eight glacial cycles from an Antarctic ice core. *Nature*, **429**, 623–628.
- FABEL, D. & HARBOR, J. 1999. The use of in-situ produced cosmogenic radionuclides in glaciology and glacial geomorphology. *Annals of Glaciology*, **28**, 103–110.
- FINK, D., MCKELVEY, B., HAMBREY, M.J., FABEL, D. & BROWN, R. 2006. Pleistocene deglaciation chronology of the Amery Oasis and Radok Lake, northern Prince Charles Mountains, Antarctica. *Earth and Planetary Science Letters*, **243**, 229–243.
- FOGWILL, C.J., BENTLEY, M.J., SUGDEN, D.E., KERR, A.R. & KUBIK, P.W. 2004. Cosmogenic nuclides <sup>10</sup>Be and <sup>26</sup>Al imply limited Antarctic Ice Sheet thickening and low erosion in the Shackleton Range for >1 m.y. *Geology*, **32**, 265–268.
- GOSSE, J.C. & PHILLIPS, F.M. 2001. Terrestrial in situ cosmogenic nuclides: theory and application. *Quaternary Science Reviews*, **20**, 1475–1560.
- GUNN, B.M. & WARREN, G. 1962. Geology of Victoria Land between the Mawson and Mulock Glaciers, Antarctica. *New Zealand Geological Survey Bulletin*, **71**, 1–157.

- HOUGHTON, J.T., DING, Y., GRIGGS, D.J., NOGUER, M., VAN DEN LINDEN, P.J., DAI, X., MASKELL, K. & JOHNSON, C.A. 2001. *Climate Change 2001: Working Group I: the scientific basis*. Cambridge: Cambridge University Press, 881 pp.
- IVY-OCHS, S., SCHLÜCHTER, C., KUBIK, P.W., DITTRICH-HANNEN, B. & BEER, J. 1995. Minimum  $^{10}\text{Be}$  exposure ages of early Pliocene for the Table Mountain plateau and the Sirius Group at Mount Fleming, Dry Valleys, Antarctica. *Geology*, **23**, 1007–1010.
- JAMIESON, S.S.R., HULTON, N.R.J., SUGDEN, D.E., PAYNE, A.J. & TAYLOR, J. 2005. Cenozoic landscape evolution of the Lambert basin, East Antarctica: the relative role of rivers and ice sheets. *Global and Planetary Change*, **45**, 35–49.
- KENNETT, J.P. 1977. Cenozoic Evolution of Antarctic Glaciation, the Circum-Antarctic Ocean, and Their Impact on Global Paleooceanography. *Journal of Geophysical Research*, **82**, 3843–3860.
- KOHL, C.P. & NISHIZUMI, K. 1992. Chemical isolation of quartz for measurement of *in-situ*-produced cosmogenic nuclides. *Geochimica et Cosmochimica Acta*, **56**, 3583–3587.
- LAL, D. 1991. Cosmic ray labeling of erosion surfaces: *in situ* nuclide production rates and erosion models. *Earth and Planetary Science Letters*, **104**, 424–439.
- LEWIS, A.R., MARCHANT, D.R., ASHWORTH, A.C., HEMMING, S.R. & MACHLUS, M.L. 2007. Major middle Miocene global climate change: Evidence from East Antarctica and the Transantarctic Mountains. *Geological Society of America Bulletin*, **119**, 1449–1461.
- MACKINTOSH, A., WHITE, D., FINK, D., GORE, D.B., PICKARD, J. & FANNING, P.C. 2007. Exposure ages from mountain dipsticks in Mac. Robertson Land, East Antarctica, indicate little change in ice-sheet thickness since the Last Glacial Maximum. *Geology*, **35**, 551–554.
- NAISH, T.R., WOOLFE, K.J., BARRETT, P.J., WILSON, G.S., ATKINS, C., BOHATY, S.M., BÜCKER, C.J., CLAPS, M., DAVEY, F.J., DUNBAR, G.B., DUNN, A.G., FIELDING, C.R., FLORINDO, F., HANNAH, M.J., HARWOOD, D.M., HENRYS, S.A., KRISSEK, L.A., LAVELLE, M., VAN DER MEER, J., MCINTOSH, W.C., NIESSEN, F., PASSCHIER, S., POWELL, R.D., ROBERTS, A.P., SAGNOTTI, L., SCHERER, R.P., STRONG, C.P., TALARICO, F., VEROSUB, K.L., VILLA, G., WATKINS, D.K., WEBB, P.N. & WONIK, T. 2001. Orbitally induced oscillations in the East Antarctic ice sheet at the Oligocene/Miocene boundary. *Nature*, **413**, 719–723.
- NIEDERMANN, S., GRAF, T. & MARTI, K. 1993. Mass spectrometric identification of cosmic-ray-produced neon in terrestrial rocks with multiple neon components. *Earth and Planetary Science Letters*, **118**, 65–73.
- NIEDERMANN, S. 2000. The  $^{21}\text{Ne}$  production rate in quartz revisited. *Earth and Planetary Science Letters*, **183**, 361–364.
- OBERHOLZER, P., BARONI, C., SCHAEFER, J.M., OROMBELLI, G., IVY-OCHS, S., KUBIK, P.W., BAUR, H. & WIELER, R. 2003. Limited Pliocene/Pleistocene glaciation in Deep Freeze Range, northern Victoria Land, Antarctica, derived from *in situ* cosmogenic nuclides. *Antarctic Science*, **15**, 493–502.
- OBERHOLZER, P., BARONI, C., SALVATORE, M.C., BAUR, H. & WIELER, R. 2008. Dating late Cenozoic erosional surfaces in Victoria Land, Antarctica, with cosmogenic neon in pyroxenes. *Antarctic Science*, **20**, 89–98.

- OROMBELLI, G., BARONI, C. & DENTON, G.H. 1991. Late Cenozoic glacial history of the Terra Nova Bay region, northern Victoria Land, Antarctica. *Geografia Fisica e Dinamica Quaternaria*, **13**, 139–163.
- PETIT, J.R., JOUZEL, J., RAYNAUD, D., BARKOV, N.I., BARNOLA, J.-M., BASILE, I., BENDER, M., CHAPPELLAZ, J., DAVIS, M., DELAYGUE, G., DELMOTTE, M., KOTLYAKOV, V.M., LEGRAND, M., LIPENKOV, V.Y., LORUS, C., PÉPIN, L., RITZ, C., SALTZMAN, E. & STIEVENARD, M. 1999. Climate and atmospheric history of the past 420,000 years from the Vostok ice core, Antarctica. *Nature*, **399**, 429–436.
- PUTKONEN, J., BALCO, G. & MORGAN, D. 2008. Slow regolith degradation without creep determined by cosmogenic nuclide measurements in Arena Valley, Antarctica. *Quaternary Research*, **69**, 242–249.
- RICKER, J. 1964. Outline of the geology between Mawson and Priestley Glaciers, Victoria Land. In ADIE, R.J., ed. *Antarctic Geology*. Amsterdam: North-Holland Publishing Company, 265–275.
- RIGNOT, E. & THOMAS, R.H. 2002. Mass balance of polar ice sheets. *Science*, **297**, 1502–1506.
- SCHÄFER, J.M., IVY-OCHS, S., WIELER, R., LEYA, I., BAUR, H., DENTON, G.H. & SCHLÜCHTER, C. 1999. Cosmogenic noble gas studies in the oldest landscape on earth: surface exposure ages of the Dry Valleys, Antarctica. *Earth and Planetary Science Letters*, **167**, 215–226.
- SCHER, H.D. & MARTIN, E.E. 2006. Timing and Climatic Consequences of the Opening of Drake Passage. *Science*, **312**, 428–430.
- STONE, J.O. 2000. Air pressure and cosmogenic isotope production. *Journal of Geophysical Research B*, **105**, 23753–23759.
- SUGDEN, D. & DENTON, G. 2004. Cenozoic landscape evolution of the Convoy Range to Mackay Glacier area, Transantarctic Mountains: Onshore to offshore synthesis. *Geological Society of America Bulletin*, **116**, 840–857.
- SUGDEN, D.E., BALCO, G., COWDERY, S.G., STONE, J.O. & SASS, L.C. 2005. Selective glacial erosion and weathering zones in the coastal mountains of Marie Byrd Land, Antarctica. *Geomorphology*, **67**, 317–334.
- SUMMERFIELD, M.A., STUART, F.M., COCKBURN, H.A.P., SUGDEN, D.E., DENTON, G.H., DUNAI, T. & MARCHANT, D.R. 1999. Long-term rates of denudation in the Dry Valleys, Transantarctic Mountains, southern Victoria Land, Antarctica based on in-situ-produced cosmogenic  $^{21}\text{Ne}$ . *Geomorphology*, **27**, 113–129.
- SYNAL, H.-A., BONANI, G., DÖBELI, M., ENDER, R.M., GARTENMANN, P., KUBIK, P.W., SCHNABEL, C. & SUTER, M. 1997. Status report of the PSI/ETH AMS facility. *Nuclear Instruments and Methods in Physics Research B*, **123**, 62–68.
- VERMEESCH, P. 2007. CosmoCalc: an Excel add-in for cosmogenic nuclide calculations. *Geochemistry, Geophysics, Geosystems*, **8**, doi:10.1029/2006GC001530.
- WOLFF, E.W. 2005. Understanding the past - climate history from Antarctica. *Antarctic Science*, **17**, 487–495.

### 3.3 Multiple cosmogenic nuclides document complex Pleistocene exposure history of glacial drifts in Terra Nova Bay (northern Victoria Land, Antarctica) <sup>b</sup>

Luigia Di Nicola <sup>1,3\*</sup>, Stefan Strasky <sup>2</sup>, Christian Schlüchter <sup>3</sup>, Maria Cristina Salvatore <sup>4</sup>, Naki Akçar <sup>3</sup>, Peter W. Kubik <sup>5</sup>, Marcus Christl <sup>6</sup>, Haino Uwe Kasper <sup>7</sup>, Rainer Wieler <sup>2</sup> and Carlo Baroni <sup>8</sup>

<sup>1</sup> Scuola di Dottorato in Scienze Polari, Università di Siena, 53100 Siena, Italy

<sup>2</sup> Institute of Isotope Geochemistry and Mineral Resources, ETH Zurich, 8092 Zurich, Switzerland

<sup>3</sup> Institute of Geological Sciences, University of Bern, 3012 Bern, Switzerland

<sup>4</sup> Dipartimento di Scienze della Terra, Università 'La Sapienza' Roma, 00185 Rome, Italy

<sup>5</sup> Paul Scherrer Institute, c/o Institute for Particle Physics, ETH Zurich, 8093 Zurich, Switzerland

<sup>6</sup> Institute for Particle Physics, ETH Zurich, 8093 Zurich, Switzerland

<sup>7</sup> Department of Geology and Mineralogy, University of Cologne, 50674 Cologne, Germany

<sup>8</sup> Dipartimento di Scienze della Terra, Università di Pisa, 56126 Pisa, Italy

\*corresponding author: luigiadinicola@gmail.com

**Abstract:** Geomorphological and glacial geological surveys and multiple cosmogenic nuclide analyses (<sup>10</sup>Be, <sup>26</sup>Al, <sup>21</sup>Ne) allowed us to reconstruct the chronology of variations prior to the last glacial maximum of the East Antarctic Ice Sheet (EAIS) and valley glaciers in the Terra Nova Bay region. Glacially scoured coastal piedmonts with round-topped mountains occur below the highest local erosional trimline. They represent relict landscape features eroded by extensive ice overriding the whole coastal area before at least 6 Ma (pre-dating the build up of the Mt. Melbourne volcanic field). Since then, summit surfaces were continuously exposed and well preserved under polar condition with negligible erosion rates on the order of 17 cm Ma<sup>-1</sup>. Complex older drifts rest on deglaciated areas above the younger late-Pleistocene glacial drift and below the previously overridden summits. The combination of stable and radionuclide isotopes documents complex exposure histories with substantial periods of burial combined with minimal erosion. The areas below rounded summits were repeatedly exposed and buried by ice from local and outlet glaciers. The exposure ages of the older drift(s) indicate multiple Pleistocene glacial cycles, which did not significantly modify the pre-existing landscape.

<sup>b</sup> Published in *Quaternary Research* (2008), doi: 10.1016/j.yqres.2008.07.004

**Key words:** Antarctica, northern Victoria Land, landscape evolution, multiple cosmogenic nuclide approach, exposure ages, complex exposure history

### 3.3.1 Introduction

Antarctica has a fundamental role in moderating and forcing the earth's climate system and global sea level. The ongoing debate on climate change has engendered a growing need to understand how the ice sheet of East Antarctica will respond to increased global warming. In order to learn more about the dynamics of Antarctic ice masses, it is essential to understand the amplitude and timing of past ice volume variations. Key sites for reconstructing glacial responses to past climate change are those with extensive ice-free areas, such as the coastal region of Victoria Land, a text-book example for the study of landscape evolution.

This work focuses on ice volume variations of valley and outlet glaciers, and on coastal areas, using in situ produced cosmogenic nuclides in conjunction with detailed field mapping. This combined approach has led to recent advances in understanding the history and dynamics of ice masses by making it possible to directly date glacial landforms that previously lacked chronological control (e.g. Ivy-Ochs et al., 1995; Ackert and Kurz, 2004; Fogwill et al., 2004; Sugden et al., 2005; Bentley et al., 2006; Staiger et al., 2006; Oberholzer et al., 2008). In particular, we concentrate on Terra Nova Bay, which is situated at the margin of the East Antarctic Ice Sheet (EAIS), and today comprises extensive ice-free areas. Here, well-preserved glacial features and erosional surfaces are widespread (Orombelli et al., 1991; Baroni et al., 2005a). One of the first surface exposure dating studies in the Terra Nova Bay region (Oberholzer et al., 2003) constrained exposure ages of glacial deposits and erosion rates of glacially abraded bedrock surfaces, but additional work is required to thoroughly understand landscape evolution in this area. In this work, we present new exposure age data obtained on new samples from the Northern Foothills in the coastal area of Terra Nova Bay. We combine analyses of stable ( $^{21}\text{Ne}$ ) and radioactive ( $^{10}\text{Be}$ ,  $^{26}\text{Al}$ ) cosmogenic nuclides, together with detailed field geomorphological and glacial geological surveys, in order to date distinct glacially-derived landscape elements and draw conclusions about the climate events related to their formation.

### 3.3.2 Study area

Terra Nova Bay (Fig. 3.8) lies along the western margin of the Ross Sea and extends from the Drygalski Ice Tongue in the south to Cape Washington in the north. The bay divides Victoria Land into two regions: i) southern Victoria Land, where ice streams and outlet glaciers cross the Transantarctic Mountains and drain the EAIS (e.g. Priestley Glacier, Reeves Glacier, David Glacier); and ii) northern Victoria Land, where a dendritic network of glacial valleys has no direct relation to the EAIS but is fed by extensive ice fields and local névés (e.g. Campbell Glacier is fed by the névés of the Southern Cross Mountains and Deep Freeze Range, Orombelli, 1989).

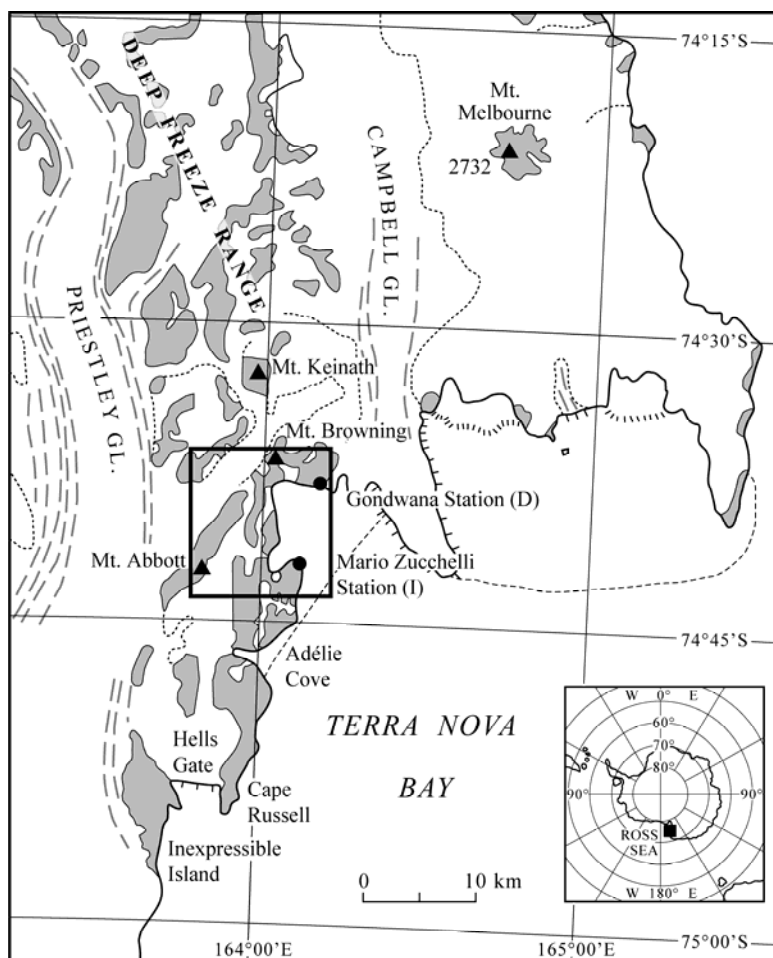


**Fig. 3.8.** Overview map of Terra Nova Bay (northern Victoria Land); grey areas are ice-free; inset shows location of Fig. 3.10.

The northern Victoria Land valley networks reflect distinctive natural basin features that can be ascribed to a fluvial origin (Baroni et al., 2005b). A shift from widespread fluvial landsculpting to temperate glacial erosion is documented in several Antarctic regions at the Eocene/Oligocene boundary (~34 Ma; Cape Roberts Science Team, 2000; Strand et al., 2003; Sugden and Denton, 2004). Wet-based glaciers subsequently occupied the relict system of fluvial valleys and the intervening mountain blocks in northern Victoria Land (Orombelli et

al., 1991; Baroni et al., 2005b). Local glaciation under temperate conditions and subsequent overriding by the EAIS characterized the first phases of glacial history in southern Victoria Land (Sugden et al. 1999; Sugden and Denton, 2004). At 13.6 Ma, a hyperarid polar climate was established in southern Victoria Land, while temperate glacial conditions ended at circa 8 Ma in northern Victoria Land (Armienti and Baroni, 1999). Cold polar glacial conditions have prevailed ever since over all Victoria Land.

Using detailed field surveys, we performed a landscape analysis in Terra Nova Bay in order to place distinct morphological features into a relative temporal sequence (Baroni and Orombelli, 1989; Orombelli et al., 1991; Armienti and Baroni, 1999). According to Orombelli et al. (1991), the process of inland erosion of valleys by outlet glaciers and adjacent alpine topography has left almost intact isolated remnants of original topography, such as relict mesas at the internal border of the Transantarctic Mountains. The maximum possible extension of ice cover since erosion of the alpine topography is marked by well-defined erosional trimlines etched into alpine ridges and spurs on the walls of outlet and valley glaciers.

At Terra Nova Bay, between the Campbell and Priestley Glaciers, relict glacial features, such as rounded-mountain tops and erratic fields, are well preserved on the Northern Foothills, a coastal north–south oriented piedmont between Cape Russell and Mt. Browning (Fig. 3.9).



**Fig. 3.9.** Overview of the Northern Foothills from NNW: Browning Pass lies in front of the rounded mountain tops; Mt. Browning is the second peak from the left, at 760 m a.s.l. and Mt. Abbott is the major right-hand peak, at 1022 m a.s.l.

The highest rounded summits are Mt. Abbott (1022 m a.s.l.) and Mt. Browning (760 m a.s.l.). These show deep weathering on the metre scale and pitting of the granitic bedrock. Neither glacial sediments nor erratic boulders are present on the tops of rounded summits, as is



documented on other rounded summits below the erosional trimline (i.e. Mt. Keinath in the Deep Freeze Range). Below the deeply weathered summits, Baroni and Orombelli (1989) and Orombelli et al. (1991) identified different glacial drifts. Scattered isolated erratic boulders, strongly oxidized and affected by deep cavernous weathering, lie at the highest elevations, from about 600 to 770 m a.s.l. on the slopes of Mt. Abbott and from 520 to 720 m a.s.l. on Mt. Browning (Terra Nova III glacial drift according to Baroni and Orombelli, 1989). Patches of complex glacial drift rest on the Northern Foothills as a thin and discontinuous sheet of strongly weathered glacial sediments between about 400 and 600 m a.s.l. at Mt. Abbott and between 400 and 520 m a.s.l. at Mt. Browning (Terra Nova II glacial drift according to Baroni and Orombelli, 1989). These are composed of massive, matrix-supported diamict with a sandy-silty matrix ranging in colour from dark greyish brown (10YR–2.5Y 4/2 of the Munsell Soil Colour Charts) to olive-grey (5Y 4/2). Clasts, from pebbles to boulders, are subangular to subrounded and composed of granitic and metamorphic rocks. Only traces of volcanic rocks are present. Clasts at the surface are deeply weathered and oxidized with yellowish-red or red staining (5YR 4/6 to 2.5YR 4/6); many show cavernous weathering. Both drifts lack perched erratic boulders and constructional morphologies. Terra Nova II and Terra Nova III glacial drifts were categorized together by Orombelli et al. (1991) and referred to as “Older Drift.” Variable concentrations of erratic blocks at different heights, an increase in weathering characteristics and changes in clast lithology with increasing altitude suggest the Older Drift may have been deposited by different glaciations (Baroni and Orombelli, 1989).

The Older Drift buries a strongly rubified palaeosol developed on bedrock or regolith characterized by a B2t horizon (red in colour, 10R 4/6) containing clay skins and resting on B3sa. Relict patches of the same soil occur up to about 700 m. This soil is comparable to the oldest Antarctic soils attributed by Campbell and Claridge (1987) to “weathering stages” 5 and 6 and considered pre-Pleistocene in age.

From sea level to an irregular upper boundary from 290 m to ~400 m a.s.l., another glacial drift mantles the eastern flanks of the Northern Foothills. This is referred to as the “Terra Nova Drift” by Orombelli et al. (1991), and corresponds to the “Younger Drift” of Denton et al. (1975). It is attributed to the late Pleistocene. It is generally a thin and discontinuous matrix-supported diamict, or simply consists of scattered clasts and erratic boulders resting directly on bedrock. The clast lithologies include gneiss, micaschist, granite, amphibolite, basalt and diorite; olivine-basalt erratic boulders of the McMurdo Volcanics are also com-

mon. Reworked marine fauna is widespread in the matrix and radiocarbon dates (Orombelli et al., 1991) provide ages from 25 to 23.5 ka BP and represent maximum ages for this deposit. Minimum dates from shells collected in marine sediments and penguin remains collected in ornithogenic soils further bracket the age of the Terra Nova Drift at 7.5 ka BP (Baroni and Orombelli, 1991; Orombelli et al., 1991; Baroni and Orombelli, 1994; Baroni and Hall, 2004).

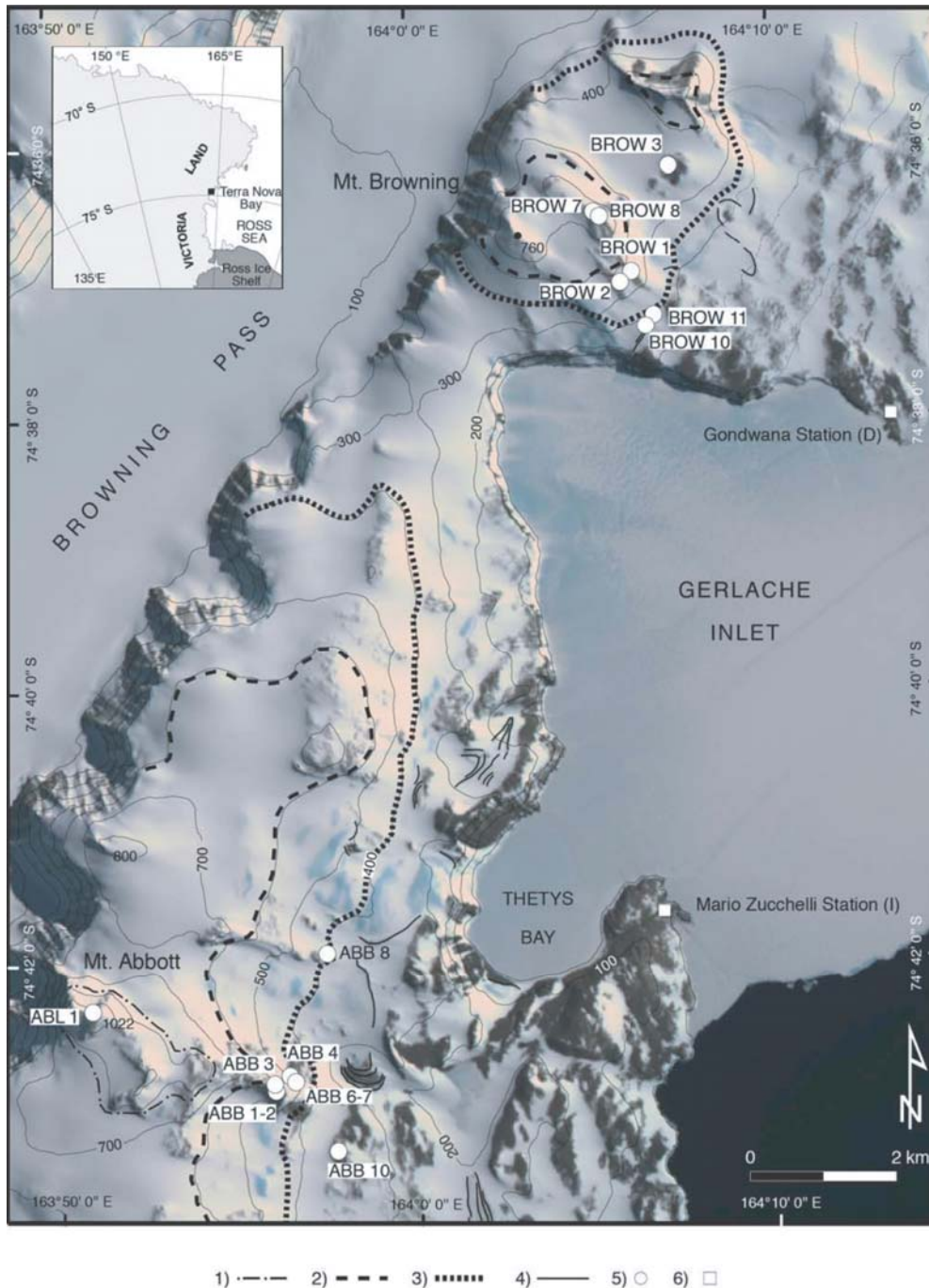


**Fig. 3.10.** Satellite image of the Northern Foothills: 1) upper limit of scattered erratic boulders (Older Drift; early–middle Pleistocene); 2) upper limit of patches of the Older Drift (early–middle Pleistocene); 3) upper limit of the Younger Drift (late Pleistocene); 4) ice-cored moraines (Holocene); 5) sample site; 6) Scientific Station. Contour interval 100 m, dotted contours are approximate (modified after Frezzotti et al., 2000).

The Terra Nova Drift is only moderately weathered, with erratic boulders displaying little weathering except for those close to the present coast. They are commonly angular and show light brown to reddish-brown staining. Perched clasts and erratic boulders, some delicately balanced, are common on the drift surface. It is often ice-cored and is characterized by ice-wedge polygons, and locally by dead-ice topography (disintegration moraines) with small conical hummocks and kettles. Constructional morphologies are lacking at the Northern Foot-hills.

Holocene moraines are widespread near the margins of outlet glaciers, ice shelves and small local glaciers. It is often possible to differentiate moraines on the basis of their weathering degree, staining colour, development of deflation pavements, lichen cover and development of patterned ground (Baroni and Orombelli, 1989; Chinn, 1991); such a Holocene moraine is well preserved in the Mt. Browning area at circa 280 m a.s.l.

### **3.3.3 Cosmogenic surface exposure dating (SED)**

#### *Sampling*

Through numerous field traverses (Baroni, 1989; Baroni et al., 2005a), detailed geomorphological and glacial geological surveys were carried out on recently ice-free areas. During the austral summers of 2004/05 and 2005/06, samples were collected from various sites (Figs. 3.10 and 3.11): the glacially abraded bedrock of the summit of Mt. Abbott below the highest trimline of the area (ABL1), glacially transported erratic boulders from the complex Older Drift(s) in the Mt. Abbott (ABB1–10) and Mt. Browning areas (BROW1–8), and the Holocene moraine at Mt. Browning (BROW10–11).

In our sampling strategy, the glacial geological and geomorphological settings of boulders and surfaces are of great importance. The lithology and size were carefully considered in order to identify the best available sample for a given locality, following the sampling strategies defined in Ivy-Ochs (1996) and Oberholzer (2004). Erratic boulders were chosen as large as possible, with wide bases to avoid the possibility of post-depositional overturning.

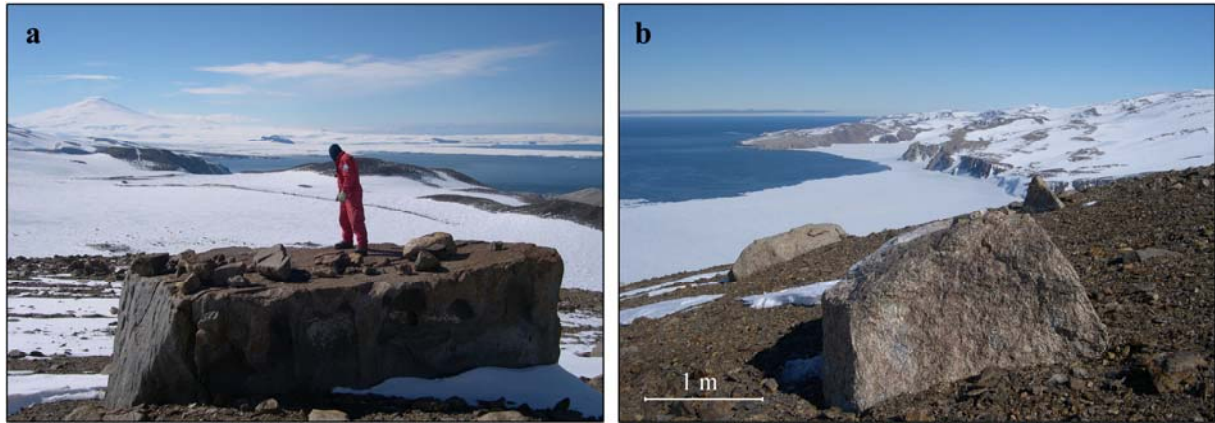


**Fig. 3.11.** Photos of sampled surfaces from erratic boulders. **a.** ABB4 from Mt. Abbott area; in the background Gerlache Inlet and Mt. Melbourne, view from SW. **b.** BROW2 from Mt. Browning area; in the background are Gerlache Inlet and Tethys Bay with the Italian scientific station (Mario Zucchelli Station) on the promontory, view from N.

Boulder heights vary from 0.45 to 3.50 m; samples were taken from the tops of boulders to reduce the likelihood of shielding, and from the centre of the block, to avoid the loss of nuclides due to neutron escape at the edges (Masarik and Wieler, 2003). We also preferred surfaces where field evidence suggested low erosion rates. In the case of evident weathering (e.g. pit holes or tafoni affecting the surface), samples were taken at a spot between depressions, at the protruding surface that retained an oxidation surface and/or rock varnish. Pure quartz (sample ABB8) and granites (all other samples) were collected, allowing a multi-nuclide approach using quartz as a target mineral for cosmogenic  $^{10}\text{Be}$ ,  $^{26}\text{Al}$  and  $^{21}\text{Ne}$ . Details of sampling sites and descriptions of samples are listed in Table 3.3. Correction and scaling factors are also reported. Correction factors for topographic shielding and dip of the surface are calculated after Dunne et al. (1999) and for sample thickness after Gosse and Phillips (2001), with a mean attenuation length of  $157\text{ g/cm}^2$  (Masarik and Reedy, 1995) and a rock density of  $2.65\text{ g/cm}^3$ . As all samples originate from latitudes above  $60^\circ$ , no corrections for geomagnetic field intensity variations are necessary (Cerling and Craig, 1994). Scaling factors for the production rates of neon, beryllium and aluminium are calculated for both altitude and latitude of sampling sites including modifications for Antarctic pressure-altitude relationships (Stone, 2000). For  $^{10}\text{Be}$  and  $^{26}\text{Al}$ , the production rates result from a combination of spallation reactions and muon capture, with fractions of spallogenic production at the surface at sea level of 0.974 and 0.978, respectively (Stone, 2000).

**Table 3.3.** Details of sampling sites.

Sample	Altitude (m a.s.l.)	Latitude (S)	Longitude (E)	Boulder height (cm)	Sample thickness (cm)	Correction factor <sup>1</sup>	Scaling factor <sup>2</sup> (Be)	Scaling factor <sup>2</sup> (Al)	Scaling factor <sup>2</sup> (Ne)
<i>Mt. Abbott area</i>									
ABL1*	1022	74°42.17'	163°50.97'	bedrock	3.0	0.96	3.29	3.29	3.33
ABB1	596	74°42.97'	163°55.97'	170	2.0	0.98	2.25	2.25	2.27
ABB2	596	74°42.97'	163°55.97'	100	4.0	0.97	2.25	2.25	2.27
ABB3	608	74°42.92'	163°56.93'	75	4.5	0.87	2.27	2.28	2.29
ABB4	520	74°42.85'	163°56.35'	300	4.5	0.87	2.09	2.09	2.11
ABB6 <sup>+</sup>	500	74°43.88'	163°57.58'	350	3.0	0.95	2.05	2.06	2.07
ABB7 <sup>+</sup>	500	74°43.88'	163°57.58'	350	3.0	0.95	2.05	2.06	2.07
ABB8	430	74°41.96'	163°57.46'	45	1.5	0.98	1.92	1.92	1.93
ABB10	393	74°43.40'	163°57.47'	330	5.0	0.95	1.85	1.86	1.87
<i>Mt. Browning area</i>									
BROW1	470	74°36.97'	164°06.20'	80	4.5	0.94	2.00	2.00	2.01
BROW2	474	74°37.03'	164°05.90'	110	3.0	0.97	2.00	2.01	2.02
BROW3	505	74°36.18'	164°07.27'	350	4.5	0.96	2.06	2.07	2.08
BROW7	674	74°36.55'	164°05.33'	120	4.5	0.96	2.41	2.42	2.44
BROW8	660	74°36.51'	164°05.16'	170	4.5	0.96	2.39	2.39	2.41
BROW10	284	74°37.36'	164°06.58'	140	3.5	0.97	1.67	1.67	1.68
BROW11	290	74°37.28'	164°06.81'	110	5.0	0.96	1.67	1.68	1.68

<sup>1</sup> calculated for topographic shielding and dip of the surface after Dunne et al. (1999) and for sample thickness after Gosse and Phillips (2001), with mean attenuation length of 157 g/cm<sup>2</sup> (Masarik and Reedy, 1995) and rock density of 2.65 g/cm<sup>3</sup>.

<sup>2</sup> calculated after Stone (2000) with fractions of spallogenic production at the surface at sea level of 0.974 for <sup>10</sup>Be and 0.978 for <sup>26</sup>Al.

\* glacially abraded bedrock sample.

<sup>+</sup> ABB6 and ABB7 belong to the same erratic boulder.

### *Sample preparation and measurements*

The surface exposure ages of 16 samples were determined using in situ produced cosmogenic <sup>10</sup>Be and <sup>21</sup>Ne; for nine of the samples <sup>26</sup>Al was also measured. Sample preparation for beryllium and aluminium was done according to a modified Kohl and Nishiizumi (1992) technique (Ivy-Ochs, 1996; Akçar, 2006) at the laboratory of the University of Bern. Samples were processed in batches of five, with each batch containing four samples and one full process blank. The average ratio of <sup>10</sup>Be/<sup>9</sup>Be of the process blanks was  $(2.57 \pm 0.14) \times 10^{-14}$ . Total aluminium was measured in aliquots of the quartz samples by inductively coupled plasma mass spectrometry (ICP-MS) at the Institute of Geology and Mineralogy at the

University of Cologne (Germany).  $^{10}\text{Be}/^9\text{Be}$  and  $^{27}\text{Al}/^{26}\text{Al}$  were measured by accelerator mass spectrometry (AMS) at the ETH/PSI tandem accelerator facility in Zurich. Noble gas concentrations were measured in ~50 mg fractions of the same quartz separates used for radionuclide analyses. Quartz was measured at the noble gas laboratories at ETH Zurich, using a non-commercial ultra-high sensitivity mass spectrometer equipped with an inverse turbo molecular-drag pump integrated into the ion source. This special compressor source concentrates the gas into a very small ionization chamber, resulting in increased sensitivity for neon by about two orders of magnitude compared to a mass spectrometer equipped with a conventional Baur-Signer source (Baur, 1999). Samples were degassed at 600, 800, and 1750 °C to separate cosmogenic from non-cosmogenic neon components. Only the 600 °C temperature steps were used for exposure age determination, as most cosmogenic neon is released from quartz below this temperature (Niedermann et al., 1993). The cosmogenic nuclide data for all 16 samples are presented in Table 3.4.

#### *Exposure age calculations*

Single nuclide exposure ages were computed from the measured concentrations of  $^{10}\text{Be}$ ,  $^{26}\text{Al}$  and  $^{21}\text{Ne}$  according to the standard models of Lal (1991) and Stone (2000) and using production rates of 5.1 at/g/yr for  $^{10}\text{Be}$  (Stone, 2000), 33.15 at/g/yr for  $^{26}\text{Al}$  (based on  $^{10}\text{Be}$  production rate and production ratio of  $6.52 \pm 0.43$  for  $^{26}\text{Al}/^{10}\text{Be}$ ; Kubik et al., 1998) and 20.33 at/g/yr for  $^{21}\text{Ne}$  (Niedermann, 2000). The cosmogenic nuclide concentration measured in a sample is a function of its exposure history. Therefore, the concentrations of more than one nuclide must be measured in order to constrain the sample history. Because  $^{21}\text{Ne}$  is stable and  $^{10}\text{Be}$  and  $^{26}\text{Al}$  decay over time with different half-lives, the ratios  $^{21}\text{Ne}/^{10}\text{Be}$  and  $^{26}\text{Al}/^{10}\text{Be}$  in long-lived samples change over time. Two-nuclide diagrams (e.g. Fig. 3.13) are useful for visualizing such ratio changes. These diagrams allow one to deduce whether a sample experienced a simple or complex exposure history (periods of exposure during which cosmogenic nuclides accumulate, and intermittent periods of burial from cosmic rays, during which radionuclide activity diminishes due to decay). In the case of continuous exposure, erosion rates can be inferred.

**Table 3.4.** Cosmogenic nuclide data.

Sample	Dissolved quartz (g)	<sup>9</sup> Be spike (mg)	<sup>10</sup> Be (10 <sup>6</sup> atoms g <sup>-1</sup> )	Al* (μg/g)	<sup>26</sup> Al (10 <sup>6</sup> atoms g <sup>-1</sup> )	<sup>26</sup> Al/ <sup>10</sup> Be	<sup>20</sup> Ne (10 <sup>9</sup> atoms g <sup>-1</sup> )	<sup>21</sup> Ne <sub>cosm</sub> (10 <sup>6</sup> atoms g <sup>-1</sup> )	<sup>21</sup> Ne/ <sup>20</sup> Ne (10 <sup>-3</sup> )	<sup>22</sup> Ne/ <sup>20</sup> Ne
<i>Mt. Abbott area</i>										
ABL1	7.91	0.3034	20.4 ± 1.9	86	102.2 ± 8.0	5.00 ± 0.86	2.36 ± 0.07	150.0 ± 5.8	66.47 ± 0.33	0.1922 ± 0.0026
ABB1	44.57	0.4023	1.58 ± 0.12				10.97 ± 0.17	15.7 ± 2.0	4.39 ± 0.11	0.1033 ± 0.0012
ABB2	52.47	0.4025	1.45 ± 0.14				6.32 ± 0.10	9.7 ± 1.3	4.48 ± 0.13	0.1045 ± 0.0015
ABB3	50.44	0.4017	1.59 ± 0.12				5.15 ± 0.05	9.0 ± 1.3	4.70 ± 0.21	0.1040 ± 0.0020
ABB4	51.53	0.4039	1.29 ± 0.10				6.27 ± 0.07	11.6 ± 0.9	4.80 ± 0.09	0.1032 ± 0.0011
ABB6	15.57	0.3048	4.98 ± 0.41	81	29.0 ± 2.3	5.82 ± 0.94	3.61 ± 0.07	46.4 ± 2.3	15.81 ± 0.43	0.1341 ± 0.0021
ABB7	30.51	0.3087	4.79 ± 0.29	106	30.1 ± 2.4	6.28 ± 0.88	2.55 ± 0.09	56.9 ± 3.1	25.32 ± 0.54	0.1591 ± 0.0029
ABB8	39.98	0.3049	1.40 ± 0.09	86	8.95 ± 0.89	6.4 ± 1.1	7.93 ± 0.08	25.2 ± 1.4	6.14 ± 0.11	0.1050 ± 0.0005
ABB10	30.38	0.3040	3.81 ± 0.23	70	17.9 ± 1.6	4.70 ± 0.70	3.76 ± 0.05	40.2 ± 1.8	13.64 ± 0.35	0.1268 ± 0.0023
<i>Mt. Browning area</i>										
BROW1	50.93	0.4025	3.15 ± 0.21				5.88 ± 0.07	19.5 ± 1.5	6.28 ± 0.20	0.1075 ± 0.0018
BROW2	52.00	0.4034	0.87 ± 0.07				7.13 ± 0.10	9.0 ± 1.1	4.22 ± 0.10	0.1044 ± 0.0015
BROW3	50.77	0.4048	5.46 ± 0.45				3.85 ± 0.10	44.2 ± 2.1	14.44 ± 0.24	0.1203 ± 0.0015
BROW7	15.18	0.3047	1.56 ± 0.12	44	11.0 ± 1.1	7.1 ± 1.3	2.95 ± 0.06	12.4 ± 1.0	7.17 ± 0.22	0.1078 ± 0.0027
BROW8	15.19	0.3042	1.46 ± 0.14				2.11 ± 0.02	6.87 ± 0.71	6.21 ± 0.29	0.1077 ± 0.0019
BROW10	34.38	0.3033	0.20 ± 0.05	171	0.99 ± 0.21	5.0 ± 2.3	2.42 ± 0.07	5.81 ± 0.73	5.36 ± 0.16	0.1025 ± 0.0009
BROW11	39.98	0.3045	0.08 ± 0.01	19	0.37 ± 0.08	4.6 ± 1.6	2.10 ± 0.06	1.14 ± 0.47	3.50 ± 0.08	0.1020 ± 0.0007

AMS Be and Al measurement errors are at 2σ level, including the statistical (counting) error and the error due to normalization to the standards and blanks; uncertainties for Ne data are 2σ and include statistical, sensitivity and mass discrimination errors.

\*Total Al measured from aliquots of whole sample of pure quartz by ICP-MS; assigned less than 3.5 % of uncertainty.

<sup>21</sup>Ne<sub>cosm</sub> is the calculated <sup>21</sup>Ne excess over air.

### 3.3.4 Results

The exposure ages calculated are referred to as “apparent exposure ages” once corrected for thickness and shielding but not erosion or uplift. If an erosion rate is taken into consideration, calculated ages increase and are then referred to as “erosion-corrected exposure ages.” When uplift is taken into consideration, exposure ages would increase, as uplift of a surface through tectonic processes during its irradiation would lead to a steady increase of the production rate (Brown et al., 1991; Brook et al., 1995). Apparent exposure ages are listed in Table 3.5.

**Table 3.5.** Apparent exposure ages of all samples.

Sample	Apparent <sup>1</sup> <sup>10</sup> Be age (ka)	Apparent <sup>1</sup> <sup>26</sup> Al age (ka)	Apparent <sup>1</sup> <sup>21</sup> Ne age (ka)
ABL1	1891 ± 261		2306 ± 88
K1*			2512 ± 226
K3*	1904 ± 283		2337 ± 138
ABB1	145 ± 11		349 ± 44
ABB2	135 ± 13		217 ± 29
ABB3	165 ± 11		222 ± 31
ABB4	144 ± 10		311 ± 23
ABB6	568 ± 51	586 ± 58	(1160 ± 58)
ABB7	543 ± 36	616 ± 62	(1424 ± 78)
ABB8	150 ± 10	154 ± 16	651 ± 35
ABB10	473 ± 30	364 ± 36	(1116 ± 51)
BROW1	358 ± 24		510 ± 39
BROW2	88.7 ± 7.7		(225 ± 28)
BROW3	619 ± 56		(1085 ± 52)
BROW7	136 ± 11	153 ± 15	260 ± 21
BROW8	128 ± 12		146 ± 15
BROW10	24.4 ± 6.5	18.7 ± 3.8	(176 ± 22)
BROW11	9.2 ± 1.5	7.0 ± 1.4	(35 ± 14)

<sup>1</sup> Apparent exposure ages are corrected for dip of rock surface, shielding of surrounding topography and sample thickness, as explained in the text; they do not include the effect of uplift of the sampled surface; ages in brackets are not taken into account for interpretation (see text); the half-lives used for calculations are 1.51 Ma for <sup>10</sup>Be (Hofmann et al., 1987) and 0.76 Ma for <sup>26</sup>Al (Samworth et al., 1972).

\* measured by Oberholzer et al. (2003), but recalculated with the parameters used in this study, as explained in the text.

Considering <sup>10</sup>Be and <sup>26</sup>Al ages, the samples generally show concordant results within error limits. The bedrock sample (ABL1) collected from the summit of Mt. Abbott has the oldest age of the group. The cosmogenic <sup>26</sup>Al inventory of ABL1 can reasonably be inferred to be in



secular equilibrium, if erosion is included. As  $^{26}\text{Al}$  has reached saturation (the concentration where production and decay are balanced), the resulting age lies at the limit of the method and is not considered in the following discussion.

The 15 samples collected from erratic boulders in the coastal belt show different populations of ages: five are older than 360 ka, seven have ages between 130 and 165 ka, one has an age of 90 ka and the remaining samples are younger than 24 ka. The two ages obtained from the same sample (ABB6/7) are concordant within error limits. In contrast, all  $^{21}\text{Ne}$  ages are older than those computed from  $^{10}\text{Be}$  and  $^{26}\text{Al}$  concentrations. This difference can be explained either by a non-cosmogenic neon component, erosion effects, or a complex exposure history. The latter two effects are discussed below. In the case of a non-cosmogenic neon component, the cosmogenic neon fraction used for exposure age calculation is overestimated; hence the real exposure age would be lower than the apparent. In order to discriminate between cosmogenic and non-cosmogenic neon components, we applied stepwise heating, an approved method in neon exposure dating studies (Niedermann, 2002). By considering the  $^{21}\text{Ne}/^{20}\text{Ne}$  and  $^{22}\text{Ne}/^{20}\text{Ne}$  ratios of different temperature steps in a neon three-isotope plot, information about various neon components can be obtained (Niedermann et al., 1993). Most of the 600 °C data points of our samples used for exposure age determination contain a mixture of atmospheric and cosmogenic neon and do not indicate any non-cosmogenic neon components; however, there are some exceptions. The data from three Mt. Browning samples (BROW2, BROW3 and BROW10) have  $^{21}\text{Ne}/^{20}\text{Ne}$  and  $^{22}\text{Ne}/^{20}\text{Ne}$  ratios that fall to the right of the atmospheric-cosmogenic mixing line described by Niedermann et al. (1993), most likely implying some nucleogenic  $^{21}\text{Ne}$  produced from  $(\alpha,n)$ -reactions on oxygen. Data from two Mt. Abbott samples (ABB6/7 and ABB10), however, plot above the atmospheric-cosmogenic mixing line, indicating significant amounts of nucleogenic  $^{22}\text{Ne}$  as a result of  $(\alpha,n)$ -reactions on fluorine (Niedermann et al., 1993).  $^{21}\text{Ne}$  exposure ages of these samples with possible nucleogenic neon components must be considered carefully and are listed in brackets in Table 3.5 as is the  $^{21}\text{Ne}$  age of BROW11, which has cosmogenic neon concentrations close to the detection limit. The neon three-isotope plots of all samples are available as supplementary data for section 3.3 in the appendix (Figs. II.1 and II.2).

### 3.3.5 Discussion

The cosmogenic nuclide data are interpreted in two steps. First, we calculate apparent single nuclide ages, which represent the simplest interpretation of the data, as they assume continuous exposure and no erosion. We then consider the three isotopes together to calculate erosion rates and eventually identify complex exposure histories. We include in this discussion two samples from Mt. Keinath published by Oberholzer et al. (2003), but recalculated with the parameters adopted here.

#### *Single nuclide exposure ages*

The exposure ages obtained by  $^{10}\text{Be}$  and  $^{26}\text{Al}$  are consistent with the relative glacial stratigraphy from the mountain top down to sea level.

- 1) The strongly weathered and rounded summit surface of Mt. Abbott shows the oldest age measured in this study. The apparent  $^{10}\text{Be}$  age is  $1.9 \pm 0.3$  Ma; when taking the sample-specific erosion rate of  $17 \pm 6$  cm  $\text{Ma}^{-1}$  into account (see next section), we get an erosion-corrected age of  $3.8 \pm 0.5$  Ma.
- 2) The intermediate  $^{10}\text{Be}$  and  $^{26}\text{Al}$  ages ranging from 90 to 620 ka come from the Older Drift and related erratic boulders found below the rounded summits. The distribution of apparent exposure ages (Fig. 3.12) shows an age cluster around 140 ka with seven samples: five erratic boulders collected from the Mt. Abbott area (ABB1, ABB2, ABB3, ABB4, ABB8) and two erratic boulders from the Mt. Browning area (BROW7, BROW8). This cluster is interpreted as a glacial event that occurred before  $\sim 120$  ka (lower  $1\sigma$  of the envelope curve). One sample (BROW2) appears to post-date this event with a  $^{10}\text{Be}$  exposure age of 90 ka. Last, the erratic boulders BROW1, ABB10, ABB6/7 and BROW3 yield the highest cosmogenic radionuclide concentrations in the landscape, corresponding to apparent  $^{10}\text{Be}$  exposure ages between about 360 and 620 ka.
- 3) The youngest ages are for BROW10 and BROW11 collected in the Mt. Browning area at a low lying moraine (284 and 289 m a.s.l., respectively). This moraine is attributed to the Holocene by Chinn (1991). One age agrees with the presumed Holocene age of this moraine (apparent  $^{10}\text{Be}$  age of  $9.4 \pm 1.5$  ka and apparent  $^{26}\text{Al}$  age of  $7.0 \pm 1.4$  ka); the other sample is older (apparent  $^{10}\text{Be}$  age of  $24.4 \pm 6.5$  ka and apparent  $^{26}\text{Al}$  age of  $18.7 \pm 3.8$  ka). Both samples show  $^{26}\text{Al}/^{10}\text{Be}$  ratios lower than expected for continuous exposure, indi-

cating inheritance due to pre-exposure. A possible scenario that explains these data is reworking of older material (Ivy-Ochs et al., 2007). The nuclide concentrations reflect a complex exposure history, indicating that the boulders of the Holocene moraine most likely originate from reworking of the older late Pleistocene glacial drift.

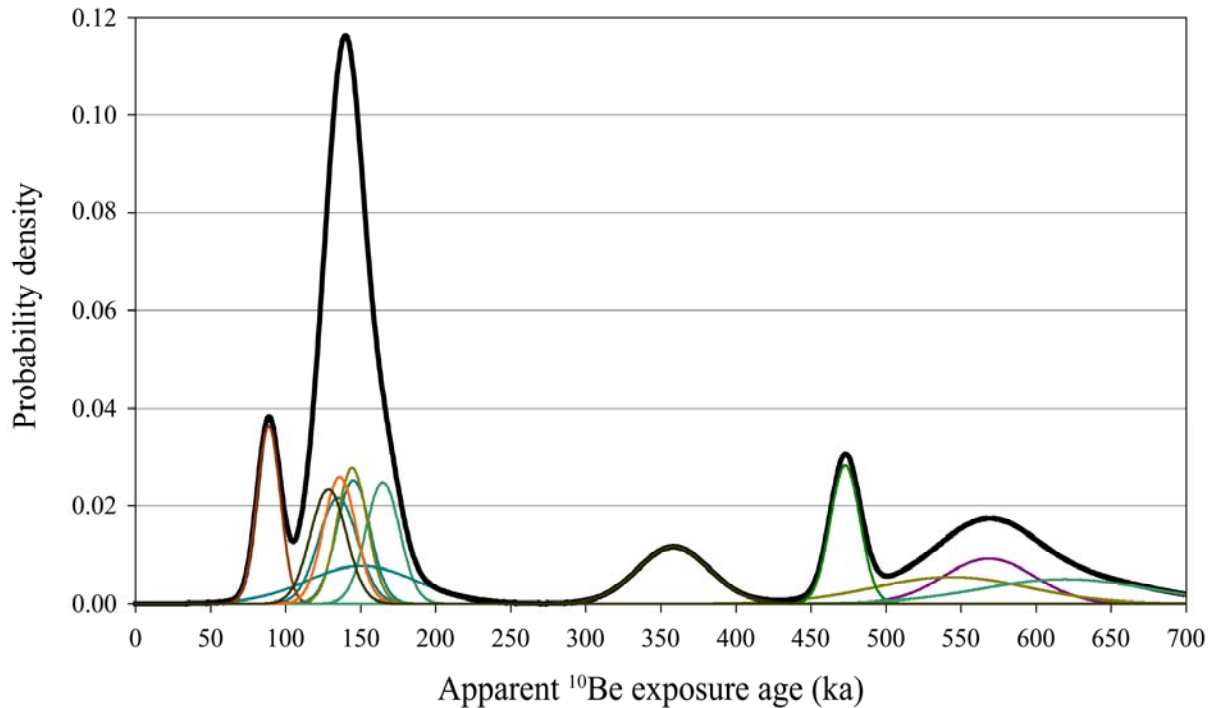


**Fig. 3.12.** Probability density plot of  $^{10}\text{Be}$  apparent exposure ages; thin lines are probability curves for individual samples; bold black line is the summed probability.

#### *Interpretations of multiple nuclide data*

The advantage of measuring multiple nuclides ( $^{10}\text{Be}$ ,  $^{26}\text{Al}$ ,  $^{21}\text{Ne}$ ) is the ability to identify and constrain erosion rates and periods of burial by looking at nuclide ratios. This analysis is carried out using “two-nuclide plots” (Lal, 1991). As pointed out above,  $^{21}\text{Ne}$  exposure ages of all erratic boulders studied here are older than the respective  $^{10}\text{Be}$  dates, resulting in high  $^{21}\text{Ne}/^{10}\text{Be}$  ratios. This can be explained by the preservation of the cosmogenic nuclide inventory from a previous exposure. Coverage by snow, sediments or ice can reduce or completely inhibit the production of cosmogenic nuclides. In the study area, it is reasonable to exclude sediment and seasonal snow cover because of the lack of sedimentary deposits thick enough to shield samples from the cosmic ray flux and because of strong winds at the sampling sites that prevent large snow accumulations, respectively. However, burial beneath ice may play an important role. Burial beneath at least 5 m of ice heavily reduces nuclide production (Fabel

and Harbor, 1999), resulting in too high  $^{21}\text{Ne}/^{10}\text{Be}$  ratios, as neon concentrations remain constant while beryllium decays over time. The  $^{21}\text{Ne}-^{10}\text{Be}$  plot leads us to the two following observations about the tops of the mountains and the complex drift(s).

- 1) A simple exposure history can explain the data from the top of Mt. Abbott, where an old glacially eroded landscape is preserved. The ratio of  $^{21}\text{Ne}/^{10}\text{Be}$  of bedrock sample ABL1 suggests a continuous history of exposure and a neon-beryllium erosion rate of  $17 \pm 6 \text{ cm Ma}^{-1}$  for ABL1 (Fig. 3.13). Recalculating the exposure data of Oberholzer et al. (2003) for Mt. Keinath with the parameters used in this study, reveals the same erosion rate for K3 as for ABL1. The erosion rate of  $17 \pm 6 \text{ cm Ma}^{-1}$  shifts the neon and beryllium exposure ages of ABL1 to  $3.8 \pm 0.5 \text{ Ma}$  and those of K3 to  $3.8 \pm 0.6 \text{ Ma}$ . Taking the upper error limit of the erosion rate into account, beryllium is in saturation and the  $^{21}\text{Ne}$  ages shift to  $5.8 \pm 0.4 \text{ Ma}$  for ABL1, and  $6.1 \pm 0.6 \text{ Ma}$  for K3.

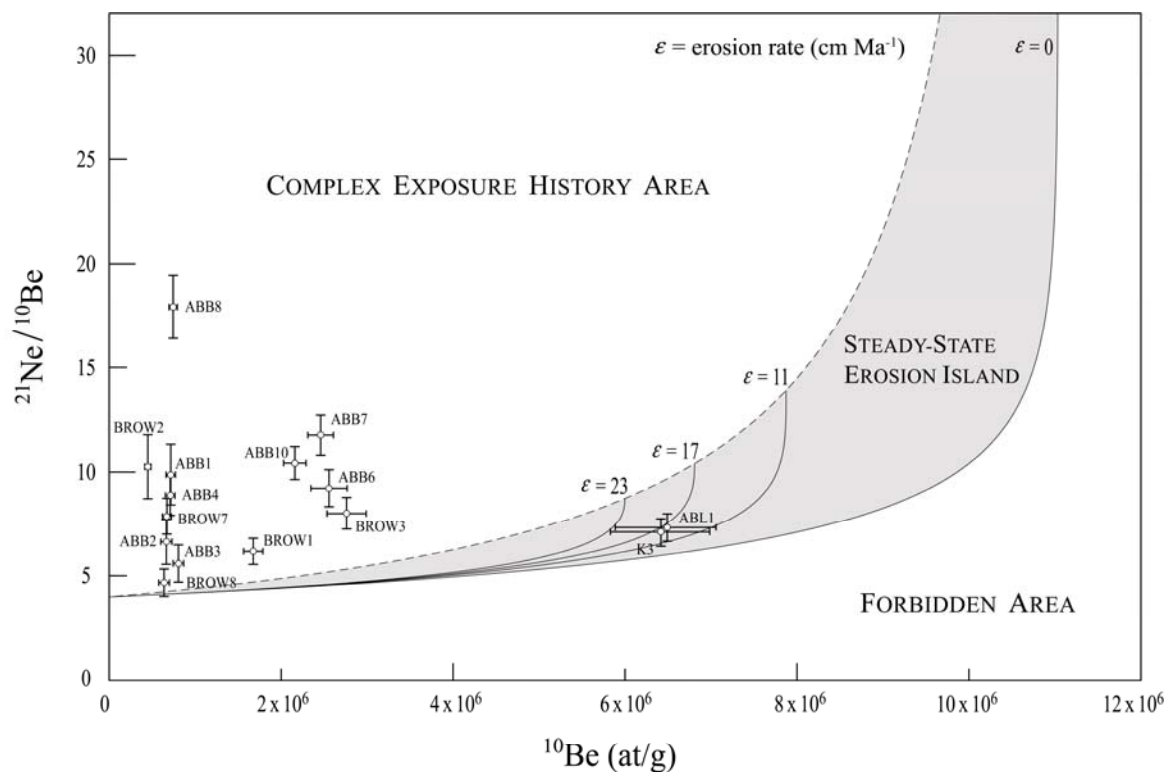


**Fig. 3.13.** Two-nuclide diagram for interpreting  $^{10}\text{Be}$  and  $^{21}\text{Ne}$  measurements. Concentrations have been normalized to sea level. The banana-shaped area is known as the steady-state erosion island (Lal, 1991). The lower boundary represents evolution with time of the  $^{21}\text{Ne}/^{10}\text{Be}$  ratio in the sample with zero erosion. The upper boundary of the erosion island (dotted line) represents steady-state ratios achieved once the rock has been eroded by at least one mean cosmic ray attenuation length at a given constant rate. Evolution lines within the island are shown for erosion rates of 11, 17, and 23  $\text{cm Ma}^{-1}$ . Samples plotting above the steady-state erosion island probably have a complex exposure history.

- 2) A different exposure history can be deduced for the erratic boulders. All the erratic boulders show  $^{21}\text{Ne}$  concentrations in excess of those expected from the  $^{10}\text{Be}$  and  $^{26}\text{Al}$  inventories. The  $^{21}\text{Ne}/^{10}\text{Be}$  ratios, ranging from 5 to 30, are significantly higher than expected for continuous exposure. All these samples experienced a complex exposure history as indicated from the positions of the data points in the diagram (Fig. 3.13). However, several complex exposure scenarios are possible (Bierman et al., 1999). The measured concentrations imply a history of multiple episodes of exposure and burial by cold-based ice, but do not allow us to reconstruct the various exposure and burial periods.

### 3.3.6 Conclusions

Surface exposure dating has proved to be a powerful tool for studying glacial chronology and identifying relevant constraints of sample histories. The key to successful SED studies lies in careful field work, which requires investigating the local (and regional) geomorphological settings, detailed field surveys, and accurate sampling; only then can SED provide reliable and meaningful results. Furthermore, compared to single nuclide data, much more information can be obtained from the multi-nuclide approach. By combining noble gas ( $^{21}\text{Ne}$ ) and radionuclide ( $^{10}\text{Be}$ ,  $^{26}\text{Al}$ ) studies, as here, it is possible to calculate erosion rates and to deduce whether the surface experienced a continuous or a complex exposure history.

Where continuous exposure is identified, results indicate the preservation of relict surfaces and very low denudation rates, as for the rounded summits of Mt. Abbott and Mt. Keinath.  $^{10}\text{Be}$ ,  $^{26}\text{Al}$  and  $^{21}\text{Ne}$  erosion-corrected exposure ages obtained from glacially scoured bedrock on the summits of Mt. Abbott and Mt. Keinath demonstrate that the highest rounded summits in the Northern Foothills and in the Boomerang Glacier area have been free of ice for at least 6 Ma (uplift is not considered). This implies that this sector of the Transantarctic Mountains has not been overridden by erosive ice (EAIS, outlet glaciers, local valley glaciers) since at least the late Miocene. Since then, erosion of outcropping granites in the coastal piedmont has been negligible, with denudation rates of  $17 \pm 6 \text{ cm Ma}^{-1}$ . Landscape features originated by glacial scouring were therefore well preserved under hyperarid polar conditions. This finding confirms that coastal piedmonts in the Terra Nova Bay are relict features of an earlier landscape, as suggested by Orombelli et al. (1991). An additional fascinating finding is that the last ice responsible for overriding the Northern Foothills and the Deep Freeze Range pre-dates

not only the build-up of the Mt. Melbourne volcano (2732 m a.s.l.), which started ~2 Ma ago (Kyle, 1990), but also the oldest effusive activity in the entire Mt. Melbourne volcanic field (2.96 Ma to present, Armienti et al., 1991; Müller et al., 1991).

The dates for erratic boulders from the area below the rounded summits display a wide range of exposure ages. The clearly distinct cluster of exposure ages from the seven erratic boulders sampled between 430 and 610 m a.s.l. on Mt. Abbott and between 600 and 670 m a.s.l. on Mt. Browning (Fig. 3.12) provides reasonable constraints for a glacial event at least before ~120 ka ago. The variability in cosmogenic nuclide abundances among the other erratic boulders sampled at elevations between 390 and 500 m indicates multiple glacial events. These findings reflect Pleistocene glacial fluctuations, confirming the hypothesis that the Older Drift was deposited by several different glaciations. Furthermore, the discrepancy between  $^{21}\text{Ne}$ ,  $^{10}\text{Be}$ , and  $^{26}\text{Al}$  exposure ages of the erratic boulders collected from the Older Drift indicates that the area below the rounded summits has been only slightly modified, surviving multiple glacial cycles with little or no erosion. The Northern Foothills have been repeatedly exposed and buried by expanding ice bodies that reached a maximum elevation of 720–770 m a.s.l. (scattered isolated erratics lie up to 770 m a.s.l. on the slopes of Mt. Abbott and up to 720 m a.s.l. on Mt. Browning). The overriding ice did not erode a sufficient thickness of rock surface to completely remove the cosmogenic nuclide inventory accumulated during previous exposure periods.

The results presented in this study demonstrate the importance of a multiple nuclide approach for interpreting exposure ages and identifying complex exposure histories and post-depositional reorganisation of sediments. We conclude that a multiple nuclide approach, together with careful field observations, is necessary to study the glacial history of Antarctica, where cold and hyperarid conditions dominate the erosion of outcropping formations, and the behaviour of cold-based glaciers controls depositional processes.

**Acknowledgements:** This work was carried out through a joint research program of the School of Polar Science of Siena, Department of Earth Sciences of Pisa, the Institutes of Geological Sciences of Bern and ETH Zurich. It was supported by the Italian National Program on Antarctic Research (PNRA) and the Swiss National Science Foundation (grant No. 200020-105220/1). The support by all Italian and Swiss colleagues of the XX and XXI

Italian Antarctic Expeditions is gratefully acknowledged. Finally, we wish to thank Samuel Niedermann for valuable discussions and suggestions and two anonymous reviewers for their comments on an earlier version of this article.

## References

- ACKERT, R.P. & KURZ, M.D. 2004. Age and uplift rates of Sirius Group sediments in the Dominion Range, Antarctica, from surface exposure dating and geomorphology. *Global and Planetary Change*, **42**, 207–225.
- AKÇAR, N. 2006. *Paleoglacial Records from the Black Sea Area of Turkey: Field and Dating Evidence*. PhD thesis, University of Bern, 187 pp.
- ARMIENTI, P., CIVETTA, L., INNOCENTI, F., MANETTI, P., TRIPODO, A., VILLARI, L. & VITA G. 1991. New petrological and geochemical data on Mt. Melbourne volcanic field, northern Victoria Land, Antarctica (II Italian Antarctic Expedition). *Memorie della Società Geologica Italiana*, **46**, 397–424.
- ARMIENTI, P. & BARONI, C. 1999. Cenozoic climatic change in Antarctica recorded by volcanic activity and landscape evolution. *Geology*, **27**, 617–620.
- BARONI, C. 1989. Geomorphological map of the Northern Foothills near the Italian Station, (Terra Nova Bay, Antarctica). *Memorie della Società Geologica Italiana*, **33**, 195–211.
- BARONI, C. & OROMBELLI, G. 1989. Glacial geology and geomorphology of Terra Nova Bay (Victoria Land, Antarctica). *Memorie della Società Geologica Italiana*, **33**, 171–193.
- BARONI, C. & OROMBELLI, G. 1991. Holocene raised beaches at Terra Nova Bay (Victoria Land, Antarctica). *Quaternary Research*, **36**, 157–177.
- BARONI, C. & OROMBELLI, G. 1994. Abandoned Penguin Rookeries as Holocene paleoclimatic indicators in Antarctica. *Geology*, **22**, 23–26.
- BARONI, C. & HALL, B.L. 2004. A new relative sea-level curve for Terra Nova Bay, Antarctica. *Journal of Quaternary Science*, **19**, 377–396.
- BARONI, C., BIASINI, A., BONDESAN, A., DENTON, G.H., FREZZOTTI, M., GRIGIONI, P., MENEGHEL, M., OROMBELLI, G., SALVATORE, M.C., DELLA VEDOVA, A.M. & VITTUARI, L. 2005a. Mount Melbourne Quadrangle, Victoria Land, Antarctica 1:250,000 (Antarctic Geomorphological and Glaciological Map Series). In HAEBERLI W., ZEMP, M., HOELZLE, M. & FRAUENFELDER, R., eds. *Fluctuations of Glaciers, 1995–2000 (Vol. VIII)*. Zürich: IAHS (ICSU)-UNEP-UNESCO, 38–40.
- BARONI, C., NOTI, V., CICCACCI, S., RIGHINI, G. & SALVATORE, M.C. 2005b. Fluvial origin of the valley system in northern Victoria Land (Antarctica) from quantitative geomorphic analysis. *Geological Society of America Bulletin*, **117**, 212–228.
- BAUR, H. 1999. A Noble-Gas Mass Spectrometer Compressor Source With two Orders of Magnitude Improvement in Sensitivity. *Eos Transactions AGU*, **80**, Abstract V22B-08.

- BENTLEY, M.J., FOGWILL, C.J., KUBIK, P.W. & SUGDEN, D.E. 2006. Geomorphological evidence and cosmogenic  $^{10}\text{Be}/^{26}\text{Al}$  exposure ages for the last glacial maximum and deglaciation of the Antarctic Peninsula Ice Sheet. *Geological Society of America Bulletin*, **118**, 1149–1159.
- BIERMAN, P.R., MARSELLA, K.A., PATTERSON, C., DAVIS, P.T. & CAFFEE, M. 1999. Mid-Pleistocene cosmogenic minimum-age limits for pre-Wisconsinan glacial surfaces in south-western Minnesota and southern Baffin Island: a multiple nuclide approach. *Geomorphology*, **27**, 25–39.
- BROOK, E.J., BROWN, E.T., KURZ, M.D., ACKERT JR., R.P., RAISBECK, G.M. & YIOU, F. 1995. Constraints on age, erosion, and uplift of Neogene glacial deposits in the Transantarctic Mountains determined from in situ cosmogenic  $^{10}\text{Be}$  and  $^{26}\text{Al}$ . *Geology*, **23**, 1063–1066.
- BROWN, E.T., EDMOND, J.M., RAISBECK, G.M., YIOU, F., KURZ, M.D. & BROOK, E.J. 1991. Examination of surface exposure ages of Antarctic moraines using in-situ produced  $^{10}\text{Be}$  and  $^{26}\text{Al}$ . *Geochimica et Cosmochimica Acta*, **55**, 2269–2283.
- CAMPBELL, I.B. & CLARIDGE, G.C. 1987. *Antarctica: soils, weathering processes and environment*. Amsterdam: Elsevier, 368 pp.
- CAPE ROBERTS SCIENCE TEAM 2000. Studies from the Cape Roberts Project, Ross Sea, Antarctica. Initial Report on CRP-3. *Terra Antartica*, **7**, 1–209.
- CERLING, T.E. & CRAIG, H. 1994. Geomorphology and in-situ cosmogenic isotopes. *Annual Reviews of Earth and Planetary Sciences*, **22**, 273–317.
- CHINN, T.J. 1991. Polar Glacier Margin and Debris Features. *Memorie della Società Geologica Italiana*, **46**, 25–44.
- DENTON, G.H., BORNES JR., H.W., GROSSWALD, M.G., STUIVER, M. & NICHOLS, R.L. 1975. Glacial History of the Ross Sea. *Antarctic Journal of the United States*, **10**, 160–164.
- DUNNE, J., ELMORE, D. & MUZIKAR, P. 1999. Scaling factors for the rates of production of cosmogenic nuclides for geometric shielding and attenuation at depth on sloped surfaces. *Geomorphology*, **27**, 3–12.
- FABEL, D. & HARBOR, J. 1999. The use of in-situ produced cosmogenic radionuclides in glaciology and glacial geomorphology. *Annals of Glaciology*, **28**, 103–110.
- FOGWILL, C.J., BENTLEY, M.J., SUGDEN, D.E., KERR, A.R. & KUBIK, P.W. 2004. Cosmogenic nuclides  $^{10}\text{Be}$  and  $^{26}\text{Al}$  imply limited Antarctic Ice Sheet thickening and low erosion in the Shackleton Range for >1 m.y. *Geology*, **32**, 265–268.
- FREZZOTTI, M., SALAVATORE, M.C., VITTUARI, L., GRIGIONI, P. & DE SILVESTRI, L. 2000. Satellite Image Map, Northern Foothills and Inexpressible Island Area (Victoria Land, Antarctica). *Terra Antartica Reports*, **6**.
- GOSSE, J.C. & PHILLIPS, F.M. 2001. Terrestrial in situ cosmogenic nuclides: theory and applications. *Quaternary Science Reviews*, **20**, 1475–1560.
- HOFMANN, H.J., BEER, J., BONANI, G., VON GUTEN, H.R., RAMAN, S., SUTER, M., WALKER, R.L., WOOFLI, W. & ZIMMERMANN, D. 1987.  $^{10}\text{Be}$ : half-life and AMS-standards. *Nuclear Instruments and Methods in Physics Research B*, **29**, 32–36.



- IVY-OCHS, S., SCHLÜCHTER, C., KUBIK, P.W., DITTRICH-HANNEN, B. & BEER, J. 1995. Minimum  $^{10}\text{Be}$  exposure ages of early Pliocene for the Table Mountain Plateau and the Sirius Group at Mount Fleming, Dry Valleys, Antarctica. *Geology*, **23**, 1007–1010.
- IVY-OCHS, S. 1996. *The dating of rock surfaces using in situ produced  $^{10}\text{Be}$ ,  $^{26}\text{Al}$  and  $^{36}\text{Cl}$ , with examples from Antarctica and the Swiss Alps*. PhD thesis ETH No. 11763, ETH Zurich, 196 pp.
- IVY-OCHS, S., KERSCHNER, H. & SCHLÜCHTER, C. 2007. Cosmogenic nuclides and the dating of Lateglacial and Early Holocene glacier variations: The Alpine perspective. *Quaternary International*, **164/165**, 53–63.
- KOHL, C.P. & NISHIZUMI, K. 1992. Chemical isolation of quartz for measurement of in-situ-produced cosmogenic nuclides. *Geochimica et Cosmochimica Acta*, **56**, 3583–3587.
- KUBIK, P.W., IVY-OCHS, S., MASARIK, J., FRANK, M. & SCHLÜCHTER, C. 1998.  $^{10}\text{Be}$  and  $^{26}\text{Al}$  production rates deduced from an instantaneous event within the dendro-calibration curve, the landslide of Köfels, Ötztal Valley, Austria. *Earth and Planetary Science Letters*, **161**, 231–241.
- KYLE, P.R. 1990. Melbourne Volcanic Province: summary. *Antarctic Research Series*, **49**, 48–52.
- LAL, D. 1991. Cosmic ray labeling of erosion surfaces: *in situ* nuclide production rates and erosion models. *Earth and Planetary Science Letters*, **104**, 424–439.
- MASARIK, J. & REEDY, R.C. 1995. Terrestrial cosmogenic-nuclide production systematics calculated from numerical simulations. *Earth and Planetary Science Letters*, **136**, 381–395.
- MASARIK, J. & WIELER, R. 2003. Production rates of cosmogenic nuclides in boulders. *Earth and Planetary Science Letters*, **216**, 201–208.
- MÜLLER, P., SCHMIDT-THOME, M., KREUZER, H., TESSENHORN, F. & VETTER, U. 1991. Cenozoic peralkaline magmatism at the western margin of the Ross Sea, Antarctica. *Memorie della Società Geologica Italiana*, **46**, 315–336.
- NIEDERMANN, S., GRAF, T. & MARTI, K. 1993. Mass spectrometric identification of cosmic-ray produced neon in terrestrial rocks with multiple neon components. *Earth and Planetary Science Letters*, **118**, 65–73.
- NIEDERMANN, S. 2000. The  $^{21}\text{Ne}$  production rate in quartz revisited. *Earth and Planetary Science Letters*, **183**, 361–364.
- NIEDERMANN, S. 2002. Cosmic-Ray-Produced Noble Gases in Terrestrial Rocks: Dating Tools for Surface Processes. In PORCELLI, D., BALLENTINE, C.J. & WIELER, R., eds. *Noble Gases in Geochemistry and Cosmochemistry. Reviews in Mineralogy and Geochemistry*, **47**. Washington, DC: Mineralogical Society of America, 731–784.
- OBERHOLZER, P., BARONI, C., SCHAEFER, J., OROMBELLI, G., IVY-OCHS, S., KUBIK, P.W., BAUR, H. & WIELER, R. 2003. Limited Pliocene/Pleistocene glaciation in Deep Freeze Range, northern Victoria Land, Antarctica, derived from *in situ* cosmogenic nuclides. *Antarctic Science*, **15**, 493–502.
- OBERHOLZER, P. 2004. *Reconstructing paleoclimate and landscape history in Antarctica and Tibet with cosmogenic nuclides*. PhD thesis ETH No. 15472, ETH Zurich, 160 pp.

- OBERHOLZER, P., BARONI, C., SALVATORE, M.C., BAUR, H. & WIELER, R. 2008. Dating late Cenozoic erosional surfaces in Victoria Land, Antarctica, with cosmogenic neon in pyroxenes. *Antarctic Science*, **20**, 89–98.
- OROMBELLI, G. 1989. Terra Nova Bay: A geographic overview. *Memorie della Società Geologica Italiana*, **33**, 69–75.
- OROMBELLI G., BARONI, C. & DENTON, G.H. 1991. Late Cenozoic glacial history of the Terra Nova Bay region, northern Victoria Land, Antarctica. *Geografia Fisica e Dinamica Quaternaria*, **13**, 139–163.
- SAMWORTH, E.A., WARBURTON, E.K. & ENGELBERTINK, G.A.P. 1972. Beta decay of the  $^{26}\text{Al}$  ground state. *Physical Review C*, **5**, 138–142.
- STAIGER, J.W., MARCHANT, D.R., SCHAEFER, J.M., OBERHOLZER, P., JOHNSON, J.V., LEWIS, A.R. & SWANGER, K.M. 2006. Plio-Pleistocene history of Ferrar Glacier, Antarctica: Implications for climate and ice sheet stability. *Earth and Planetary Science Letters*, **243**, 489–503.
- STONE, J.O. 2000. Air pressure and cosmogenic isotope production. *Journal of Geophysical Research B*, **105**, 23753–23759.
- STRAND, K., PASSCHIER, S. & NÄSI, J. 2003. Implications of quartz grain microtextures for onset Eocene/Oligocene glaciation in Prydz Bay, ODP site 1166, Antarctica. *Palaeogeography, Palaeoclimatology, Palaeoecology*, **198**, 101–111.
- SUGDEN, D.E., SUMMERFIELD, M.A., DENTON, G.H., WILCH, T.I., MCINTOSH, W.C., MARCHANT, D.R. & RUTFORD, R.H. 1999. Landscape development in the Royal Society Range, southern Victoria Land, Antarctica: Stability since the middle Miocene. *Geomorphology*, **28**, 181–200.
- SUGDEN, D.E. & DENTON, G.H. 2004. Cenozoic landscape evolution of the Convoy Range to Mackay Glacier area, Transantarctic Mountains: Onshore to offshore synthesis. *Geological Society of America Bulletin*, **116**, 840–857.
- SUGDEN, D.E., BALCO, G., COWDERY, S.G., STONE, J.O. & SASS, L.C. 2005. Selective glacial erosion and weathering zones in the coastal mountains of Marie Byrd Land, Antarctica. *Geomorphology*, **67**, 317–334.

## 4 TIBET

### 4.1 Introduction

---

The Tibetan Plateau – the largest plateau on earth with an average elevation of ~5000 m above sea level (Fielding et al., 1994) – and its bordering mountains presently have the greatest concentration of glaciers outside the polar areas. This high Asian region represents more than 80 % of the world's land surface area >4 km above sea level and influences regional and global climate by affecting atmospheric circulation (e.g. Ruddiman and Kutzbach, 1989; Molnar and England, 1990). Moreover, changes in glacial ice volume in Tibet and the bordering mountains may also have climate implications, because melting of large ice masses may affect freshwater flux to the ocean, hence modifying ocean currents, and the ice-albedo feedback of such a large high-elevated area may amplify trends in climate evolution that have globally significant consequences.

Evidence of multiple Quaternary glacier oscillations is present in the glacial geologic and geomorphologic record throughout Tibet and the bordering mountains (Lehmkuhl and Owen, 2005). However, identification and separation of some glacial deposits from sediments related to gravitational mass movements is not always trivial. Hewitt (1999) found that certain deposits previously identified as terminal moraine complexes in the Karakoram Himalaya were actually emplaced by rock avalanches. Such misinterpretations led to erroneous estimates of the palaeoglacial extent and a long controversy existed over the size of the last glacial maximum ice cover of Tibet (e.g. Zheng, 1989; Derbyshire et al., 1991; Kuhle, 1991; 1998). In the last two decades numerous publications presented evidence against Kuhle's hypothesis of an extensive ice sheet (e.g. Derbyshire et al., 1991; Lehmkuhl et al., 1998; Schäfer et al., 2002; Owen et al., 2003; Schaefer et al., 2008). Nowadays, it is generally accepted that a large ice sheet did not cover the Tibetan Plateau, at least not during the past few glacial cycles (Fig. 4.1). However, the spatial extent of regional glaciations and their temporal relationship still need to be established in some and refined in other areas. And a new controversy is coming up over the exact timing of the last glacial maximum ice advance of the Himalayan glaciers (Schäfer et al., 2002; Owen et al., 2003; 2005; Schaefer et al., 2008).

This chapter shows results from surface exposure dating studies from the southeastern margin of the Tibetan Plateau. Data from a well-defined moraine succession points to a last glacial maximum ice advance in the Garzê area during marine isotope stage 2 (section 4.2). In addition, cosmogenic nuclide ages from erratic boulders on a nearby plateau indicate a late glacial reaction of the local glacier to short-term climate change. More evidence of the abrupt climate signal of the late glacial cooling during Heinrich event 1 in the high mountain glaciers of east Asia was found in the Kangding area and is presented in section 4.3.

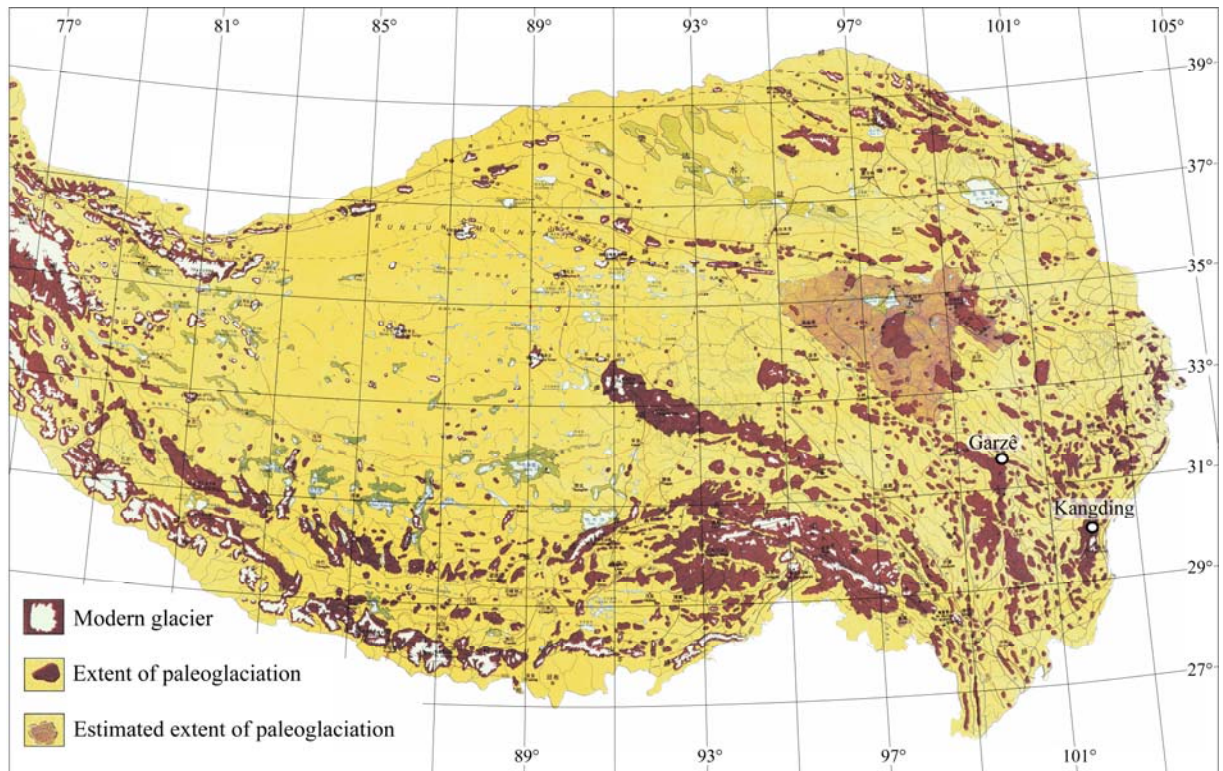


**Fig. 4.1.** Map showing the extent of glacialiation for the entire Tibetan Plateau (after Li et al., 1991). This is currently the best reconstruction available and indicates limited glacialiation in the interior of the Tibetan Plateau but expanded ice caps and valley glaciers on its margins during the last glacial cycle.

## 4.2 Glacier extension on the eastern Tibetan Plateau in response to MIS 2 cooling, with a contribution to $^{10}\text{Be}$ and $^{21}\text{Ne}$ methodology <sup>c</sup>

Angela A. Graf <sup>1\*</sup>, Stefan Strasky <sup>2</sup>, Zhizhong Zhao <sup>3</sup>, Naki Akçar <sup>1</sup>, Susan Ivy-Ochs <sup>4</sup>, Peter W. Kubik <sup>5</sup>, Marcus Christl <sup>5</sup>, Haino U. Kasper <sup>6</sup>, Rainer Wieler <sup>2</sup> and Christian Schlüchter <sup>1</sup>

<sup>1</sup> *Institute of Geological Sciences, University of Bern, 3012 Bern, Switzerland*

<sup>2</sup> *Institute of Isotope Geochemistry and Mineral Resources, ETH Zurich, 8092 Zurich, Switzerland*

<sup>3</sup> *Institute of Geomechanics, Chinese Academy of Geological Sciences, Beijing 100081, China*

<sup>4</sup> *Institute for Particle Physics, ETH Zurich, 8093 Zurich and Department of Geography, University of Zurich, 8057 Zurich, Switzerland*

<sup>5</sup> *Paul Scherrer Institute, c/o Institute for Particle Physics, ETH Zurich, 8093 Zurich, Switzerland*

<sup>6</sup> *Department of Geology and Mineralogy, University of Cologne, 50674 Cologne, Germany*

\*corresponding author: [angela.graf@bmgeng.ch](mailto:angela.graf@bmgeng.ch)

**Abstract:** The Tibetan Plateau is a key area in palaeoclimate research. It is still controversial whether glacier advances in the Himalaya occurred as a response to global cooling and synchronous to the extensions of the northern hemisphere ice sheets, or whether they were forced by an increase in moisture availability during warmer interglacial or interstadial stages. We present a multiple cosmogenic nuclide study in the Hengduan Mountains, eastern Tibetan Plateau. We dated end moraines of three outlet valley glaciers as well as erratic boulders from the granitic Chuanxi Plateau. A major ice advance occurred between  $17.5 \pm 0.7$  and  $21.6 \pm 1.0$  ka, thus synchronous to the northern hemisphere last glacial maximum (LGM). A smaller glacial event occurred between  $14.9 \pm 0.7$  and  $15.6 \pm 0.7$  ka and may correlate to the Heinrich event 1. Evidence for an older ( $>20$  ka) glaciation was found in a perched boulder with a minimum  $^{10}\text{Be}$  exposure age of  $\sim 43$  ka. While exposure ages derived from radionuclides ( $^{10}\text{Be}$ ,  $^{26}\text{Al}$ ) agree generally well within error limits, they differ considerably from neon exposure ages. This age discrepancy is rather due to an inseparable nucleogenic neon component than to major episodes of pre-exposure. The nucleogenic  $^{21}\text{Ne}$  concentrations in this study area might be used to distinguish different boulder provenances and, thus, to reconstruct palaeo-ice flow patterns over the Chuanxi Plateau.

**Key words:** cosmogenic nuclides, LGM, Tibetan Plateau, Heinrich event 1, nucleogenic/trapped neon

<sup>c</sup> Submitted to *Quaternary Geochronology*

### 4.2.1 Introduction

The assessment of climate and environmental changes since the onset of industrialisation must be based, at the global scale, on long-term climate records. To better understand ongoing changes in the climate pattern and quantitatively define human impact versus natural variations. Concentrated efforts have been made to interpret climate proxies in order to deduce forcing factors such as sea surface and atmospheric temperatures, wind intensities and oceanic circulation systems. The long-term astronomically driven oscillation patterns (precession, eccentricity, obliquity), the millennial scale Dansgaard-Oeschger oscillations and the annual variations driven by the El Niño-Southern Oscillation, have all been detected by analysis of sediment and ice cores, and more recently, stalagmites and corals. In the northern hemisphere, this apparent pacing of global climate changes by variations in insolation during the last glacial cycle is recorded as a step-wise expansion and repeated reduction of high latitude ice sheets from 115 ka to 20 ka. Ice masses reached their maximum extent around 20 ka, known as the last glacial maximum (LGM).

In continental areas from mid- to low latitudes, mountain glaciers are an important proxy for palaeoclimate studies. Due to their confined extent, they react rapidly to changes in temperature and precipitation (Kaser and Osmaston, 2002; Benn et al., 2005). Gillespie and Molnar (1995) published a comprehensive review of palaeoglacial studies discussing asynchronous behaviour of glaciers and ice sheets from different geographical locations. However, they also pointed out that the lack of precise dating weakens their conclusions.

Considerable effort has been made to improve dating methods which allow direct age determination of glacial sediments and landforms, i.e. surface exposure dating of erratic boulders or polished bedrock and optically stimulated luminescence dating of fluvio-glacial and glaciolacustrine sediments. In an effort to detect synchronous or asynchronous responses of glaciers compared to ice sheets in the northern hemisphere, surface exposure dating has been successfully applied in various mountain areas such as the Alps (Ivy-Ochs et al., 2006), Jura Mountains (Graf et al., 2007), Carpathians (Reuther et al., 2007), Kaçkar Mountains (Akçar et al., 2007; 2008), Andes (Zech et al., 2006), Himalaya (e.g. Richards et al., 2000; Zech et al., 2003) and the Tibetan Plateau (e.g. Schäfer et al., 2002; Owen et al., 2003; Tschudi et al., 2003; Owen et al., 2005; 2006; Zhou et al., 2007; Strasky et al., 2008).

As the Tibetan Plateau is a key area in palaeoclimate research, its forcing influence on regional and global climate has been discussed since the late nineteenth century. The extent and timing of ice masses during the Pleistocene, and particularly during the last glacial cycle, is debated and still subject to controversy. The concept of asynchronous glacier advances (compared to the northern hemisphere ice sheets) has been used sporadically in the literature (see Gillespie and Molnar (1995) and references therein). It implies that glaciers over most of the plateau were of rather limited extent or even absent during marine isotope stage (MIS) 2, while they reached their local LGM position during MIS 4 or 3. This asynchronous behaviour is explained by variations in the Asian summer monsoon intensity, which was strongly reduced during glacial stages.

This work focuses on the Chuanxi Plateau, which is part of the Hengduan Mountains at the eastern margin of the Tibetan Plateau. Four of the main Asian rivers have their source in the Hengduan Mountains: the Irrawaddy, Salween and Mekong rivers irrigate the coastal plains from Myanmar to Vietnam, while the Yangtze river drains towards the eastern Chinese Sea. The understanding of climate change over the Tibetan Plateau is vital in order to improve the water-based agricultural-economical development in Southeast Asia. In addition, the location of the study area within the present and last glacial limits of monsoonal precipitation makes it an ideal site to test whether glacier advances in eastern Tibet were forced by temperature minima or precipitation maxima.

#### **4.2.2 Geology and climate**

##### *Geological background*

The Hengduan Mountains constitute a series of north–south striking mountain ranges, separated by deep river gorges. From west to east, the landscape is formed by the Irrawaddy river, the Gaoligong Mountains, the Salween river, the Taniantaweng Mountains, the Mekong river, the Ningjing Mountains, the Yangtze river, the Daxue Mountains (with Minya Gongkar), the Yalong river and the Shaluli Mountains. Finally, the Dadu river drains into the Sichuan Basin. Due to their broad extent, the Hengduan Mountains form a natural rain barrier and thus a transition zone between the dry Tibetan Plateau and the wetter Sichuan Basin. From a tectonic point of view (Fig. 4.2), the Yidun Arc is located between the Songpan–Garzê Fold Belt and the Qiangtang Block (Mattauer et al., 1992; Huang et al., 2003; Reid et al., 2005). It comprises a Triassic volcanic arc built on Palaeozoic metasediments, which formed within the

Palaeotethys oceanic domain. During the closure of this palaeo-ocean, the Yidun Arc was incorporated into the Tibetan Plateau along the Jinsha Jiang and the Garzê–Litang sutures (a former subduction zone with mafic/ultramafic rocks, limestones and cherts). The eastern part of this arc is dominated by low-grade metamorphic Triassic flysch sediments, mudstones, arc-type volcanics and granodiorite intrusions. According to the  $^{40}\text{Ar}/^{39}\text{Ar}$  dating work of Reid et al. (2005) the voluminous plutons along the Garzê–Litang suture zone intruded during late Triassic (209–215 Ma), while the granite batholiths forming the Chuer Shan and the Shaluli Shan in the central part of Yidun Arc intruded during the Cretaceous (94–105 Ma). This lithological background influences the present morphology: while the low-grade metamorphic sediments are strongly overprinted by fluvial erosion leading to deep V-shaped river gorges, the valleys in the granite plutons show generally a typical U-shaped glacial morphology.

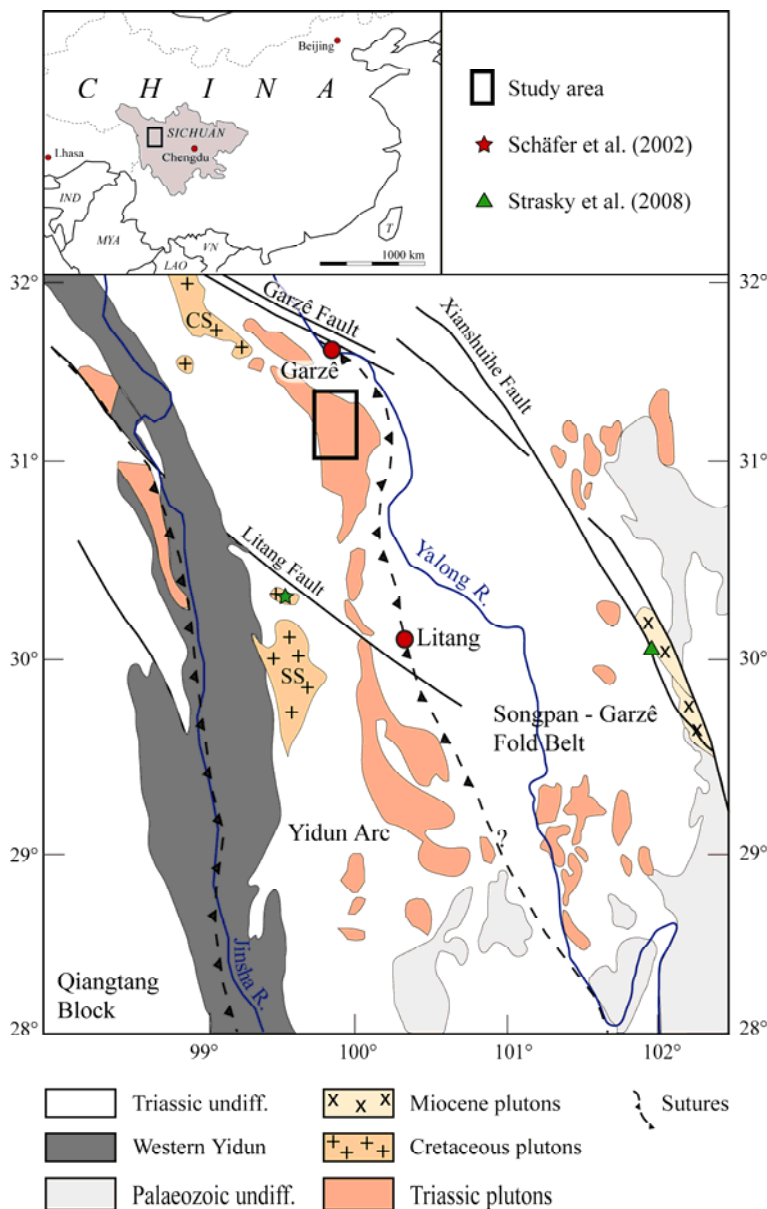


**Fig. 4.2.** Our study area on the Chuanxi Plateau lies on the eastern side of Yidun Arc, between the Jinsha Jiang and the Garzê–Litang suture zones. The asterisk indicates the sampling site of Schäfer et al. (2002), the triangle marks the sampling site of Strasky et al. (2008). CS: Chuer Shan; SS: Shaluli Shan. Modified after Reid et al. (2005).



The field area (about 25 km south of Garzê) is located in the northernmost part of the Chuanxi Plateau (Fig. 4.3). With an area of about 3300 square kilometres, it is the largest remnant of palaeoglaciation on the Tibetan Plateau. Its surface is covered by erratic boulders and contains more than 1140 lakes, probably formed by subglacial erosion. In some places on the plateau, as well as in outlet valleys, distinct end moraines are well-preserved. In the Chinese literature, the glacial relicts are attributed to three different glaciations. The most extensive glacial relicts are from the penultimate glaciation, which was followed by an intense weathering phase. Electron spin resonance ages of 560–600 ka are proposed for the penultimate glaciation by Zhou et al. (2006). The second glaciation with a prominent ice cap (3000 km<sup>2</sup>) is known as the Daocheng glaciation and is attributed to the LGM. During Late Glacial times, the ice cap was smaller (2600 km<sup>2</sup>) and a series of end moraines indicate its progressive disintegration (Zhijiu, 1958; Laixin, 1963).

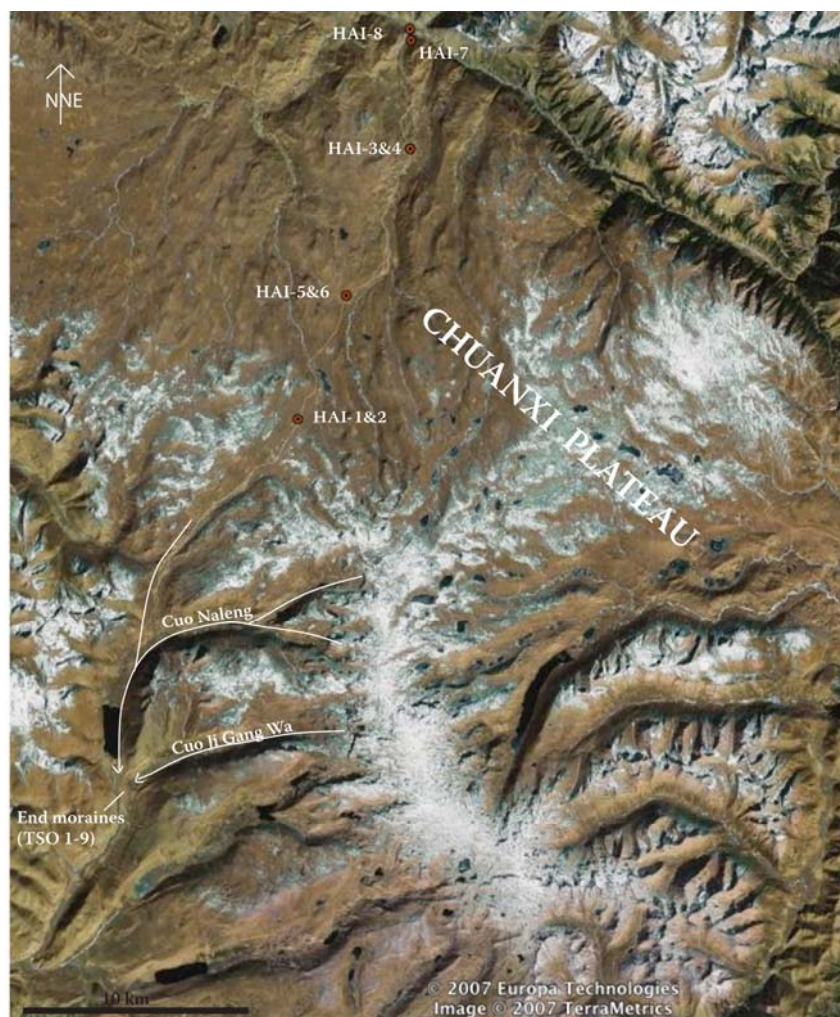


**Fig. 4.3.** Positions of the sampled erratic boulders on the Chuanxi Plateau and related outlet glacier valleys. White arrows show flow directions of the Cuo Naleng palaeoglacier and its northern tributary, as well as Cuo Ji Gang Wa palaeoglacier.

*Actual climate settings*

Our study area in today's, as well as the LGM's monsoonal precipitation zone, is characterized by cool, dry winters and warm, wet summers. In winter, the Tibetan Plateau acts as a regional refrigerator. The steep pressure gradient between the Asiatic High (over Mongolia and North China) and the Aleutian Low (over the North Pacific) results in dry continental northwestern to northeastern winds over Central and East Asia. During spring, the Tibetan Plateau warms up and pressure gradients decrease. In summer times, the Asiatic High and Aleutian Low are replaced by a low-pressure system over the Tibetan Plateau and a high pressure system over the Pacific, so that warm and humid air masses reach far into southeastern Tibet (Bohner, 2006). The Asian summer monsoon system can be divided into two subsystems: the East Asian monsoon and the Indian monsoon. Even if they develop independently of each other, the two systems seem to interact and vary on intraseasonal, interannual and interdecadal time scales, both due to internal (Eurasian snow cover, soil moisture, cloud cover) and external forcing mechanisms, such as the El Niño-Southern Oscillation, tropical sea surface temperatures (Vandenberghé et al., 2006) or movements of the intertropical convergence zone (ITCZ), while the long-term pattern seems to be linked to changes in solar activity and glacial boundary conditions (for a complete overview see Ding and Chan (2005) and Yang et al. (2007)). Recent work by Yancheva et al. (2007) shows a strong inverse correlation between the strengths of winter and summer monsoons, most probably linked to the migration of the ITCZ. When the ITCZ moves north, as it is expected during periods of northern hemisphere warming, the summer monsoons are strengthened. These studies stress the importance of northern hemisphere summer insolation and land–sea contrast, although changes in monsoon strength are not a direct and linear response to changing insolation or global ice volume, but are a product of global energy redistribution, sensitive to any process changing interhemispheric pressure gradient or moisture availability and transport (Wang et al., 2005).

The East Asian monsoon reaches the Chuanxi Plateau at the beginning of June. 70 % of the annual precipitation (640 mm per year as a mean value for 1951–1990 at Garzê meteorological station) falls during boreal summer, with a maximum of 130 mm in July (Vose et al., 1992). Only 5 % of precipitation falls during boreal winter (December–March). Towards the centre of the plateau, total precipitation decreases rapidly. Residual humidity from the Mediterranean and Caspian Sea is transported by the northern hemisphere westerlies during winter (Ono et al., 2004) to the western part of the Tibetan Plateau.

### *Palaeomonsoon*

Palaeomonsoon intensity fluctuations show a strong coupling with climate oscillations registered in Greenland ice core records (Thompson, 2000; Wang et al., 2001; Yuan et al., 2004). During the LGM, northern hemisphere ice sheets caused the intertropical convergence zone to move southwards, so that the presently weaker monsoonal areas of Tibet underwent, most probably, more drastic changes than the drier western and central parts of the plateau. As a consequence, air temperatures and therefore ocean evaporation and subsequent precipitation were generally lower. A moisture minimum occurred during the global LGM between 21.3 and 19.8 ka BP, followed by gradually rising moisture values until 17.2 ka BP (Herzschuh, 2006). In independently dated records along coastal eastern China, proxies for sea surface temperatures and for precipitation intensity suggest a synchronous change in strength of the East Asian monsoon (Wang et al., 2001; Yuan et al., 2004; Oppo and Sun, 2005).

### *Influence on glaciers and equilibrium-line altitudes*

To use glaciers as a palaeoclimate proxy, we have to consider that glaciers in monsoon-dominated regions have different mass balance characteristics than glaciers in mid- to high latitudes outside the monsoon regime. Particularly, ablation occurs over the whole year in monsoon-influenced areas, while accumulation is mainly restricted to summer months (Kaser and Osmaston, 2002). Therefore, estimates on the position of the equilibrium-line altitude, marking the boundary between the upper area of positive ice mass balance and the lower area of net mass loss, must be considered with caution (Benn et al., 2005; Wara et al., 2005). Liu et al. (2002) suggested a temperature lowering of 7–9 °C for the LGM and a precipitation decrease of 30–70 % over the Tibetan Plateau. They further showed that precipitation decreases of 50 % do not greatly affect the extent of glaciers. In contrast, other studies (e.g. Derbyshire, 1996; Owen et al., 2005) argued that low monsoon activity is responsible for the absence of glaciers or the restricted ice extents in monsoonal Tibet during cold periods like MIS 2. Towards the centre of the Tibetan Plateau, the equilibrium-line altitude increases with a very steep gradient, reflecting the dryness of the plateau's centre. For the LGM, Shi (2002) estimated an equilibrium-line altitude depression of about 400 m on Chuanxi Plateau.

### 4.2.3 Fieldwork and methods

#### *Sampling*

We chose the field area on Chuanxi Plateau to constrain the timing of both the larger and the subsequent smaller glacial extents described in the Chinese literature (Zhijiu, 1958; Laixin, 1963). The road from Garzê (3394 m a.s.l.) leads up to the Chuanxi Plateau, crossing it from north to south before reaching the town of Litang at 2560 m a.s.l. The exhumed granitic pluton forms a low relief area and is extensively covered by glacial deposits. The outlet valleys are arranged in a radial pattern from the plateau's edges. Different glaciogenic elements, such as scattered erratic boulders, small moraine ridges and polished bedrock, dominate the hummocky-like landscape of the central Chuanxi Plateau. Palaeo-ice flow directions are documented by lateral and end moraines and boulder alignments in the outlet valleys. Vegetation on the plateau is scarce and composed mainly of grass, small rhododendrons and some alpine flowers like Edelweiss (*Leontopodium alpinum*) and thistles. Along the meandering rivers and in places with reduced soil permeability (probably till cover), the soil is swampy and difficult to access.

**Table 4.1.** Geographical and geometrical information of all samples.

Sample	Altitude (m a.s.l.)	Latitude (N)	Longitude (E)	a-b-c axes <sup>a</sup> (cm)	Sample thickness (cm)	Correction factor	Geomorphological position
TSO 1	4175	31°05.4'	99°45.1'	310-380-240	3	0.955	lateral moraine
TSO 2	4138	31°05.2'	99°45.3'	570-360-450	2	0.981	outer end moraine
TSO 3	4138	31°05.2'	99°45.3'	800-320-450	2	0.981	outer end moraine
TSO 4	4150	31°05.2'	99°45.4'	850-950-350	2	0.969	middle end moraine
TSO 5	4150	31°05.3'	99°45.3'	530-340-210	2	0.981	middle end moraine
TSO 6	4150	31°05.3'	99°45.3'	620-480-250	2	0.981	middle end moraine
TSO 7	4156	31°05.4'	99°45.6'	400-500-170	2	0.964	inner end moraine
TSO 8	4161	31°05.4'	99°45.5'	500-460-270	3	0.973	inner end moraine
TSO 9	4172	31°05.6'	99°45.5'	100-120-150	4	0.954	inner end moraine
HAI 1	4453	31°13.9'	99°51.2'	200-150-95	3	0.975	resting on HAI 2
HAI 2	4453	31°13.9'	99°51.2'	600-690-200	4	0.967	resting on bedrock
HAI 3	4224	31°20.3'	99°55.1'	400-340-240	3.5	0.968	on smaller moraine ridge
HAI 4	4224	31°20.3'	99°55.1'	100-170-95	4	0.964	on smaller moraine ridge
HAI 5	4370	31°16.8'	99°52.8'	450-300-200	4	0.957	embedded in basal till
HAI 6	4370	31°16.8'	99°52.8'	300-230-120	5	0.949	embedded in basal till
HAI 7	4169	31°22.8'	99°55.8'	490-280-200	3	0.970	lowest and on plateau edge
HAI 8	4081	31°23.0'	99°55.2'	420-300-250	4	0.956	on fluvial bank

TSO samples are from the Cuo Ji Gang Wa and Cuo Naleng palaeoglaciers; HAI samples from the Chuanxi Plateau and the northern outlet glacier.

<sup>a</sup> Size of a-b-c axes for whole erratic boulder.

Our interest was focused on the plateau's interior, on the main northern outlet valley, as well as on two western outlet valleys (Fig. 4.3). The northern outlet valley at the edge of the Chuanxi Plateau is occupied by a braided river. The first western outlet valley (Cuo Naleng palaeoglacier) is crescent-shaped, ~16 km long, and has a tributary hanging valley flowing out south of the plateau. The second western outlet valley (Cuo Ji Gang Wa) is about 12 km long. Moraines and alignments of erratic boulders in the area of Lake Cuo Naleng underline the confluence of both western palaeoglaciers. At present, meandering rivers – probably following the old fluvio-glacial outwash system – occupy those valleys. The landscape of the outwash plain is characterized by a large amount of scattered erratic boulders, reworked by two active river systems. In the confluence area, lateral moraines are found at higher elevations on both valley sides.

The positions of the 17 granodiorite samples collected from the uppermost rock surfaces of large erratic boulders are shown in Fig. 4.3 and the geographical and geometrical details are given in Table 4.1. Close to the river confluence of the northern outlet valley, we sampled HAI 8 from a boulder resting on coarse sand and gravel. Sample HAI 7 (Fig. 4.4c) was collected ~90 m higher, on the orographic right side of this outlet valley. Towards the centre of the plateau, samples HAI 3 & 4 were collected on top of a ~10 m high moraine that is cut by the road (Fig. 4.4e). In the same area, boulders in delicate positions (Fig. 4.4a) and bedrock outcrops with striated surfaces characterize the glacial landscape. Samples HAI 5 & 6 derive from erratics that are embedded in basal till. We recorded a profile of this basal till on an outcrop a few metres below the sampled erratics (Fig. 4.4d). The granodiorite bedrock and some of the erratic boulders show clear evidence of hydrothermal alteration. In the centre of the plateau we sampled HAI 1, a perched boulder resting on HAI 2 (Fig. 4.4b). Further in the southwest of the HAI samples, in the former confluence area of Cuo Naleng and Cuo Ji Gang Wa palaeoglaciers, is the main region of interest of our study. In this area we sampled TSO 1 to 9. TSO 1 rests directly on the metasediment bedrock of the orographic right valley side of Cuo Naleng palaeoglacier (Fig. 4.5b), and was thus transported by the southern tributary from the centre of the Chuanxi Plateau. Erosion on the top surface of TSO 1 formed a 7 cm high quartzitic crest (see section 4.2.4). The other eight samples were collected on the ~500 m long end moraine succession of Cuo Ji Gang Wa palaeoglacier. The moraine succession is composed of three larger end moraines, separated by two smaller and patchy ones (Fig. 4.5a). TSO 2 & 3 were collected from massive boulders on the outermost moraine. TSO 4 was sampled from a prominent boulder on the intermediate moraine (Fig. 4.5c). TSO 5 & 6 were

collected from the same ridge (Fig. 4.5d). Finally, TSO 7–9 were sampled from boulders resting on the innermost moraine (Fig. 4.5e). At present, the former tongue basin of Cuo Ji Gang Wa palaeoglacier is covered with grass, while the former tongue basin of Cuo Naleng palaeoglacier is occupied by a lake.

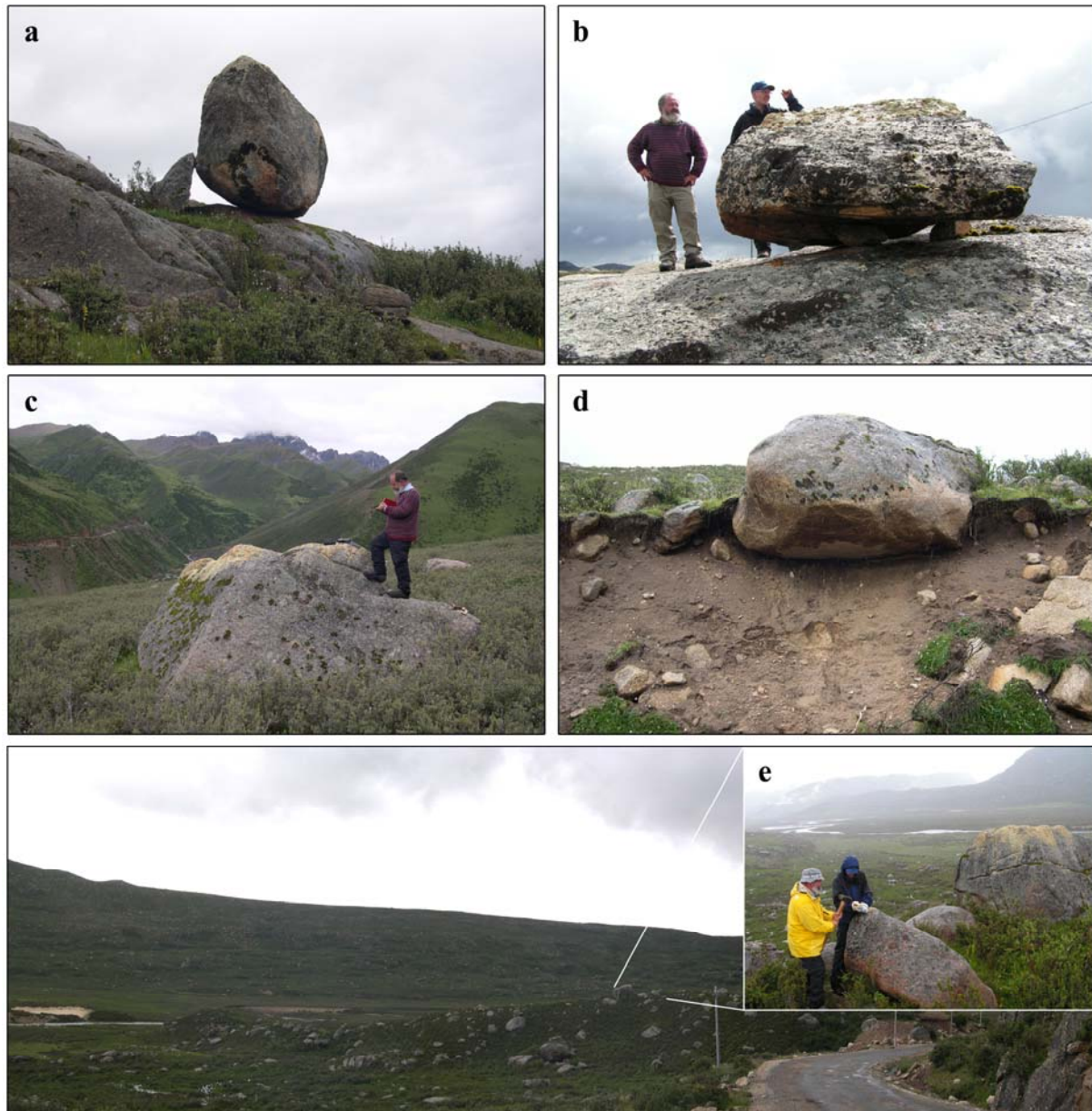


**Fig. 4.4.** Field impressions from the Chuanxi Plateau. **a.** Boulder in delicate position on glacially scoured bedrock (not sampled). **b.** HAI 1, perched boulder resting on HAI 2. **c.** HAI 7 on the orographic right side of the northern outlet glacier valley. **d.** Erratic boulder near HAI 6 & 7, embedded in basal lodgement till. **e.** Small moraine ridge with samples HAI 3 (large boulder on the right side of the picture) and HAI 4 (at sampling).

### *Multiple nuclide analyses*

Cosmogenic nuclides like  $^{10}\text{Be}$ ,  $^{21}\text{Ne}$  and  $^{26}\text{Al}$  are produced by the interaction of secondary cosmic ray particles and minerals within the topmost rock layers. Measuring the cosmogenic nuclide concentrations in minerals (quartz for this study) thus allows determining how long a rock surface has been exposed to cosmic radiation (e.g. Lal, 1991). By analyzing two or more different cosmogenic nuclides from the same sample additional information about the sample-specific erosion rate and exposure history can be obtained (Lal, 1991; Gosse and Phillips, 2001). We measured  $^{10}\text{Be}$  and  $^{21}\text{Ne}$  for all samples and  $^{26}\text{Al}$  in one sample per terminal moraine in the TSO sampling area.



**Fig. 4.5.** Samples collected in the Cuo Naleng (TSO 1) and Cuo Ji Gang Wa (TSO 2–9) palaeoglacier areas. **a.** Panoramic view of the moraine ridges with approximate sample positions. Sample abbreviations: 1–9 represent samples TSO 1 to 9. **b.** TSO 1. **c.** TSO 4, the largest sampled boulder. **d.** TSO 6 from the intermediate moraine ridge. **e.** TSO 8 from the innermost terminal moraine, in the background the tongue basin.

To control the reliability of our results, analyses of three samples were replicated in external laboratories.  $^{10}\text{Be}$  was re-extracted from purified quartz for sample TSO 7 by S. Ivy-Ochs at ETH Zurich. The neon isotopes were re-measured by S. Niedermann at the GeoForschungs-Zentrum in Potsdam for samples TSO 3 and TSO 6. External analyses are marked with asterisks in Tables 4.2 and 4.3. All cross-measurements confirm the presented ages within  $1\sigma$  errors. Additionally, TSO 3 & 4 were analysed for a second time at ETH Zurich with a more detailed degassing procedure. They are labelled TSO 3<sup>+</sup> and TSO 4<sup>+</sup>.

#### *Sample preparation and age calculation*

Depending on the shape of the sample, the uppermost 2 to 5 cm of the samples were cut, crushed and sieved. Quartz purification and  $^{10}\text{Be}$  and  $^{26}\text{Al}$  extraction were done according to a modified Kohl and Nishiizumi (1992) technique at the Institute of Geological Sciences at the University of Bern (Ivy-Ochs, 1996; Akçar, 2006; Graf, 2008). About 50 g of quartz were dissolved for each sample. Both radionuclides were measured at the ETH/PSI accelerator mass spectrometry facility at ETH Zurich (Synal et al., 1997). The  $^{27}\text{Al}$  content was determined at the Department of Geology and Mineralogy at the University of Cologne.

Neon isotopes were analyzed from 40–70 mg of the same quartz separates used for the radionuclides and crushed to grain sizes  $<0.1$  mm. The neon isotope concentrations were measured at ETH Zurich with a non-commercial ultra-high sensitivity mass spectrometer, equipped with a special compressor source. The compressor source is a combination of a sealed ion source and a molecular-drag compressor, which concentrates the gas into a small ionization volume (Baur, 1999). The compression of the gas into a small ionization chamber leads to a sensitivity increase of about two orders of magnitude for  $^{21}\text{Ne}$ , compared to the sensitivity without the special compressor source and typical for conventional instruments (Baur, 1999). Noble gases were extracted from the samples through step-wise heating at 600, 800, and 1750 °C in order to separate the cosmogenic from the non-cosmogenic (trapped and nucleogenic) neon components (Niedermann et al., 1993).

For exposure age calculations, we used the sea level high latitude production rates in quartz of  $5.1 \pm 0.3$  at/g/yr for  $^{10}\text{Be}$  and  $33.15 \pm 2.9$  at/g/yr for  $^{26}\text{Al}$  based on the  $^{10}\text{Be}$  production rate of Stone (2000) and the  $^{26}\text{Al}/^{10}\text{Be}$  production ratio of  $6.5 \pm 0.4$  of Kubik et al. (1998). A reference production rate of  $20.3 \pm 3.7$  at/g/yr was used for  $^{21}\text{Ne}$  (Niedermann, 2000). Scaling was done



after Stone (2000), calculated with CosmoCalc 1.0 (Vermeesch, 2007). Further corrections were done for sample thickness using an attenuation length ( $A$ ) of  $157 \text{ g/cm}^2$ , and a rock density ( $\rho$ ) of  $2.65 \text{ g/cm}^3$ . Dip of the sample and topographic shielding were corrected after Dunne et al. (1999). No corrections were made for snow or vegetation cover, as reliable data is missing from this area. However, strong winds are thought to prevent thick snow accumulations on the sampled large erratic boulders (Figs. 4.4 and 4.5).

Scaling of sea level high latitude production rates to sampling sites on the Tibetan Plateau is a controversial topic. We calculated and compared our data with the scaling models of Stone (2000) and Desilets et al. (2006). The latter has the advantage of taking geomagnetic field intensity variations into account, influencing production rates in mid-latitudes. Additional corrections for air pressure anomalies over Tibet are suggested by Schaefer et al. (2008) and Staiger et al. (2007). Schaefer et al. (2008) suggest a correction for a present-day air pressure anomaly over Tibet of about +12 hPa in respect to the standard atmosphere. As the production rate is inversely proportional to the thickness of the atmosphere, this anomaly lowers the production rate by 8 %. Conversely, Staiger et al. (2007) suggest corrections for compression and extension of the atmosphere due to the LGM ice cover. The presence of ice sheets compresses the atmosphere and results in a migration of its mass towards lower elevations. Integrated over the last 20 ka, this would yield production rates that are  $3 \pm 1.5 \%$  higher than the actual values used for Tibet. However, as neither one of the above cited scaling models (exposure age differences for our samples on the order of 5–10 %) nor additional corrections for the atmospheric thickness (e.g. applying Staiger et al.'s (2007) atmospheric corrections to the apparent age of TSO 1 (20.4 ka) would lower the age to 19.8 ka; applying Schaefer et al. (2008), on the other hand, would increase the age to 22.0 ka) affects the conclusions of this paper, we present the ages calculated with the “classical” scaling model of Stone (2000).

#### 4.2.4 Results

The aim of measuring multiple nuclides  $^{10}\text{Be}$ ,  $^{26}\text{Al}$  and  $^{21}\text{Ne}$  was to identify possible periods of pre-exposure. The measured cosmogenic nuclide concentrations are presented in Table 4.2 and all calculated surface exposure ages are shown in Table 4.3. As noble gas ages are systematically higher than radionuclide ages they were not used to establish glacial chronologies, but are discussed in more detail in section 4.2.5.

**Table 4.2.** Radionuclide and noble gas data.

Sample	Heating Temp. (°C); Time (min)	<sup>20</sup> Ne (10 <sup>9</sup> at g <sup>-1</sup> )	<sup>21</sup> Ne/ <sup>20</sup> Ne (10 <sup>-3</sup> )	<sup>22</sup> Ne/ <sup>20</sup> Ne	<sup>21</sup> Ne <sub>exc</sub> (10 <sup>6</sup> at g <sup>-1</sup> )	<sup>10</sup> Be (10 <sup>6</sup> at g <sup>-1</sup> )	<sup>26</sup> Al (10 <sup>6</sup> at g <sup>-1</sup> )
TSO 1	600; 45	6.11 ± 0.03	4.55 ± 0.04	0.1035 ± 0.0004	9.72 ± 0.38	1.29 ± 0.05	
	800; 20	1.93 ± 0.01	2.92 ± 0.07	0.1007 ± 0.0010	0.00 ± 0.00		
	1750; 20	1.23 ± 0.01	3.01 ± 0.05	0.1019 ± 0.0008	0.06 ± 0.11		
TSO 2	600; 45	6.43 ± 0.05	6.03 ± 0.07	0.1033 ± 0.0007	19.76 ± 0.74	1.28 ± 0.05	
	800; 20	2.06 ± 0.02	3.30 ± 0.06	0.1021 ± 0.0011	0.70 ± 0.21		
	1750; 20	1.29 ± 0.02	3.06 ± 0.08	0.0986 ± 0.0011	0.13 ± 0.17		
TSO 3	600; 45	4.22 ± 0.03	6.88 ± 0.08	0.1043 ± 0.0005	16.56 ± 0.49	1.25 ± 0.04	5.08 ± 0.24
	800; 20	1.69 ± 0.01	3.18 ± 0.07	0.1024 ± 0.0014	0.38 ± 0.17		
	1750; 20	1.00 ± 0.01	2.99 ± 0.12	0.0990 ± 0.0009	0.03 ± 0.15		
TSO 3 <sup>+</sup>	600; 45	5.08 ± 0.03	6.23 ± 0.11	0.1044 ± 0.0010	16.60 ± 0.69		
	800; 20	2.33 ± 0.02	3.07 ± 0.06	0.1009 ± 0.0009	0.26 ± 0.21		
	1750; 20	2.13 ± 0.06	3.04 ± 0.10	0.0994 ± 0.0008	0.17 ± 0.45		
TSO 3 <sup>*</sup>	400; 35	0.47 ± 0.02	15.33 ± 0.32	0.1137 ± 0.0017	5.78 ± 0.34		
	600; 30	1.48 ± 0.04	9.06 ± 0.08	0.1059 ± 0.0006	9.03 ± 0.56		
	800; 30	1.49 ± 0.05	3.46 ± 0.16	0.1024 ± 0.0011	0.75 ± 0.42		
	1200; 20	0.05 ± 0.01	3.70 ± 0.95	0.1100 ± 0.0090	0.03 ± 0.08		
TSO 4	600; 45	5.47 ± 0.03	6.28 ± 0.07	0.1037 ± 0.0004	18.19 ± 0.57	1.19 ± 0.05	
	800; 20	1.68 ± 0.01	3.26 ± 0.07	0.1026 ± 0.0007	0.51 ± 0.14		
	1750; 20	0.86 ± 0.02	2.97 ± 0.12	0.1003 ± 0.0015	0.01 ± 0.16		
TSO 4 <sup>+</sup>	200; 45	1.55 ± 0.04	3.19 ± 0.08	0.1017 ± 0.0011	0.36 ± 0.29		
	400; 45	2.27 ± 0.02	6.65 ± 0.15	0.1048 ± 0.0016	8.39 ± 0.40		
	600; 45	2.72 ± 0.01	6.37 ± 0.11	0.1065 ± 0.0006	9.28 ± 0.37		
	800; 20	2.52 ± 0.02	3.55 ± 0.10	0.1044 ± 0.0011	1.49 ± 0.32		
	1750; 20	1.91 ± 0.02	3.37 ± 0.07	0.1041 ± 0.0012	0.79 ± 0.20		
TSO 5	600; 45	5.72 ± 0.02	5.61 ± 0.05	0.1031 ± 0.0006	15.17 ± 0.38	1.08 ± 0.03	
	800; 20	1.91 ± 0.01	3.26 ± 0.07	0.1013 ± 0.0009	0.57 ± 0.16		
	1750; 20	0.89 ± 0.02	3.09 ± 0.10	0.1009 ± 0.0016	0.12 ± 0.16		
TSO 6	600; 45	6.75 ± 0.03	5.16 ± 0.05	0.1034 ± 0.0005	14.82 ± 0.50	1.15 ± 0.03	8.76 ± 0.53
	800; 20	1.78 ± 0.01	3.16 ± 0.09	0.1016 ± 0.0011	0.36 ± 0.18		
	1750; 20	1.00 ± 0.02	2.97 ± 0.07	0.1011 ± 0.0010	0.01 ± 0.13		
TSO 6 <sup>*</sup>	400; 35	0.93 ± 0.03	7.40 ± 0.16	0.1047 ± 0.0004	4.12 ± 0.34		
	800; 30	5.05 ± 0.15	4.86 ± 0.06	0.1036 ± 0.0003	9.6 ± 1.2		
	1200; 20	0.08 ± 0.01	3.60 ± 0.50	0.1100 ± 0.0055	0.05 ± 0.10		
TSO 7	600; 45	5.07 ± 0.02	5.03 ± 0.05	0.1041 ± 0.0006	10.49 ± 0.36	1.17 ± 0.05	
	800; 20	1.32 ± 0.01	5.57 ± 0.14	0.1031 ± 0.0010	3.45 ± 0.23		
	1750; 20	8.16 ± 0.02	3.61 ± 0.03	0.1027 ± 0.0006	5.31 ± 0.34		
TSO 7 <sup>*</sup>						1.08 ± 0.05	
TSO 8	600; 45	5.94 ± 0.02	5.66 ± 0.05	0.1046 ± 0.0009	16.04 ± 0.41	1.07 ± 0.03	7.06 ± 0.29
	800; 20	3.52 ± 0.03	3.22 ± 0.06	0.1025 ± 0.0005	0.93 ± 0.31		
	1750; 20	1.82 ± 0.01	3.09 ± 0.07	0.1016 ± 0.0009	0.24 ± 0.15		
TSO 9	600; 45	4.37 ± 0.03	6.71 ± 0.09	0.1046 ± 0.0005	16.41 ± 0.56	1.31 ± 0.04	
	800; 20	1.60 ± 0.02	3.57 ± 0.08	0.1014 ± 0.0011	0.97 ± 0.20		
	1750; 20	1.26 ± 0.02	3.15 ± 0.08	0.1009 ± 0.0011	0.24 ± 0.19		

**Table 4.2.** Continued.

Sample	Heating Temp. (°C); Time (min)	<sup>20</sup> Ne (10 <sup>9</sup> at g <sup>-1</sup> )	<sup>21</sup> Ne/ <sup>20</sup> Ne (10 <sup>-3</sup> )	<sup>22</sup> Ne/ <sup>20</sup> Ne	<sup>21</sup> Ne <sub>exc</sub> (10 <sup>6</sup> at g <sup>-1</sup> )	<sup>10</sup> Be (10 <sup>6</sup> at g <sup>-1</sup> )	<sup>26</sup> Al (10 <sup>6</sup> at g <sup>-1</sup> )
HAI 1	600; 45	10.53 ± 0.03	4.77 ± 0.05	0.1034 ± 0.0004	19.09 ± 0.63	3.15 ± 0.09	
	800; 20	2.49 ± 0.01	2.98 ± 0.10	0.1013 ± 0.0004	0.05 ± 0.29		
	1750; 20	0.98 ± 0.01	3.13 ± 0.07	0.0997 ± 0.0009	0.17 ± 0.12		
HAI 2	600; 45	8.11 ± 0.03	5.02 ± 0.02	0.1038 ± 0.0005	16.71 ± 0.33	2.36 ± 0.12	
	800; 20	2.77 ± 0.01	3.10 ± 0.09	0.1021 ± 0.0008	0.40 ± 0.29		
	1750; 20	1.29 ± 0.01	2.83 ± 0.09	0.1027 ± 0.0011	0.00 ± 0.00		
HAI 3	600; 45	4.12 ± 0.02	4.23 ± 0.07	0.1028 ± 0.0006	5.23 ± 0.35	0.99 ± 0.04	
	800; 20	1.44 ± 0.02	2.94 ± 0.11	0.1035 ± 0.0008	0.00 ± 0.00		
	1750; 20	0.93 ± 0.01	3.69 ± 0.14	0.1034 ± 0.0010	0.68 ± 0.17		
HAI 4	600; 45	3.29 ± 0.02	4.67 ± 0.09	0.1020 ± 0.0007	5.62 ± 0.39	0.98 ± 0.05	
	800; 20	1.45 ± 0.02	3.04 ± 0.04	0.1013 ± 0.0005	0.13 ± 0.12		
	1750; 20	1.07 ± 0.01	3.42 ± 0.11	0.1020 ± 0.0006	0.50 ± 0.18		
HAI 5	600; 45	8.76 ± 0.03	4.02 ± 0.04	0.1020 ± 0.0003	9.33 ± 0.43	1.02 ± 0.07	
	800; 20	2.95 ± 0.02	3.03 ± 0.06	0.1023 ± 0.0006	0.22 ± 0.23		
	1750; 20	1.15 ± 0.01	3.18 ± 0.09	0.1015 ± 0.0007	0.26 ± 0.15		
HAI 6	600; 45	6.59 ± 0.03	4.04 ± 0.05	0.1028 ± 0.0006	7.11 ± 0.45	0.99 ± 0.04	
	800; 20	2.52 ± 0.01	3.07 ± 0.05	0.0996 ± 0.0005	0.28 ± 0.16		
	1750; 20	1.18 ± 0.02	2.98 ± 0.06	0.1022 ± 0.0011	0.03 ± 0.13		
HAI 7	600; 45	4.43 ± 0.04	4.83 ± 0.06	0.1022 ± 0.0005	8.30 ± 0.45	1.41 ± 0.06	
	800; 20	1.59 ± 0.02	2.95 ± 0.10	0.1000 ± 0.0010	0.00 ± 0.00		
	1750; 20	1.06 ± 0.01	3.40 ± 0.10	0.0996 ± 0.0011	0.46 ± 0.16		
HAI 8	600; 45	2.12 ± 0.02	5.66 ± 0.08	0.1037 ± 0.0007	5.74 ± 0.28	0.65 ± 0.04	
	800; 20	0.91 ± 0.01	2.95 ± 0.10	0.0999 ± 0.0011	0.00 ± 0.00		
	1750; 20	1.00 ± 0.01	3.07 ± 0.07	0.1001 ± 0.0016	0.11 ± 0.13		

<sup>21</sup>Ne<sub>exc</sub> is the calculated <sup>21</sup>Ne excess over air. Error limits are 1σ.

\* external analyses by S. Niedermann (Ne) and S. Ivy-Ochs (Be).

+ repeat neon analyses at ETH Zurich.

### *Outlet glaciers (TSO 1–9)*

<sup>10</sup>Be ages from the three end moraines in the south of Chuanxi Plateau agree well with the morphostratigraphical setting. As mentioned in section 4.2.3, boulder TSO 1 has a 7 cm high outstanding quartz vein on its upper surface (Fig. 4.5b). This is our best field evidence for local erosion rates. If the boulder TSO 1 was deposited about 21 ka ago (apparent age of TSO 1 or the LGM in the northern hemisphere) we obtain an average erosion rate of 3.4 mm ka<sup>-1</sup>. This value is higher than erosion rates recorded in subarctic environments (Fabel et al., 2002; Phillips et al., 2006) but similar to erosion rates reported for the Alps (Ivy-Ochs et al., 2004; Graf et al., 2007). We use this conservatively high erosion rate of

$3.0 \pm 0.5 \text{ mm ka}^{-1}$  for our age calculation, although it does not significantly change the results (Table 4.3). The outermost moraine ridge was formed around  $21.0 \pm 1.3 \text{ ka}$  and the middle ridge around  $18.9 \pm 1.5 \text{ ka}$ . As the highest  $^{10}\text{Be}$  concentration was measured in a boulder from the innermost ridge (TSO 9 with an age of  $22.0 \pm 0.9 \text{ ka}$ ), we assume that this sample was pre-exposed, and therefore did not use it to calculate the innermost moraine's age. Thus, the innermost end moraine was formed around  $18.3 \pm 1.5 \text{ ka}$ . Except for TSO 3, the ages obtained for  $^{26}\text{Al}$  agree within  $2\sigma$  error limits with the  $^{10}\text{Be}$  ages. For TSO 3, the  $^{26}\text{Al}/^{10}\text{Be}$  ratio indicates a burial time of more than 700 ka.

**Table 4.3.** Apparent and erosion-corrected exposure ages.

Sample	Apparent $^{10}\text{Be}$ age (ka)	Erosion-corr. <sup>a</sup> $^{10}\text{Be}$ age (ka)	Apparent $^{21}\text{Ne}$ age (ka)	Erosion-corr. <sup>a</sup> $^{21}\text{Ne}$ age (ka)	Apparent $^{26}\text{Al}$ age (ka)	Erosion-corr. <sup>a</sup> $^{26}\text{Al}$ age (ka)
TSO 1	$20.4 \pm 1.0$	$21.6 \pm 1.0$	$37.8 \pm 1.5$	$42.0 \pm 1.7$		
TSO 2	$20.1 \pm 1.0$	$21.2 \pm 1.0$	$76.3 \pm 2.9$	$96.5 \pm 3.6$		
TSO 3	$19.7 \pm 0.8$	$20.7 \pm 0.9$	$64.0 \pm 1.9$	$77.3 \pm 2.3$	$12.4 \pm 0.7$	$12.7 \pm 0.7$
TSO 3 <sup>+</sup>			$64.1 \pm 2.7$	$77.5 \pm 3.2$		
TSO 3*			$60.1 \pm 3.0$	$71.7 \pm 3.6$		
TSO 4	$19.1 \pm 1.0$	$20.1 \pm 1.0$	$70.7 \pm 2.2$	$87.5 \pm 2.7$		
TSO 4 <sup>+</sup>			$70.1 \pm 2.4$	$86.5 \pm 3.0$		
TSO 5	$16.8 \pm 0.7$	$17.6 \pm 0.7$	$58.3 \pm 1.5$	$69.0 \pm 1.7$		
TSO 6	$18.0 \pm 0.7$	$18.9 \pm 0.8$	$56.9 \pm 2.0$	$67.1 \pm 2.3$	$21.3 \pm 1.4$	$22.4 \pm 1.4$
TSO 6*			$52.7 \pm 4.8$	$61.3 \pm 5.6$		
TSO 7	$18.5 \pm 0.9$	$19.5 \pm 1.0$	$54.3 \pm 1.7$	$63.5 \pm 2.0$		
TSO 7*	$17.0 \pm 0.8$	$17.8 \pm 0.9$				
TSO 8	$16.8 \pm 0.7$	$17.5 \pm 0.7$	$61.8 \pm 1.6$	$74.1 \pm 1.9$	$17.2 \pm 0.8$	$17.9 \pm 0.9$
TSO 9	$20.8 \pm 0.8$	$22.0 \pm 0.9$	$64.1 \pm 2.2$	$77.4 \pm 2.7$		
HAI 1	$42.7 \pm 1.7$	$48.2 \pm 2.6$	$63.4 \pm 2.1$	$76.5 \pm 2.5$		
HAI 2	$32.1 \pm 1.8$	$35.1 \pm 2.0$	$55.9 \pm 1.1$	$65.8 \pm 1.3$		
HAI 3	$15.0 \pm 0.7$	$15.6 \pm 0.7$	$19.6 \pm 1.3$	$20.6 \pm 1.4$		
HAI 4	$14.9 \pm 0.9$	$15.5 \pm 0.9$	$21.2 \pm 1.5$	$22.4 \pm 1.5$		
HAI 5	$14.5 \pm 1.0$	$15.1 \pm 1.1$	$32.9 \pm 1.6$	$36.0 \pm 1.7$		
HAI 6	$14.3 \pm 0.6$	$14.9 \pm 0.7$	$25.3 \pm 1.6$	$27.0 \pm 1.7$		
HAI 7	$21.9 \pm 1.1$	$23.2 \pm 1.2$	$31.9 \pm 1.7$	$34.8 \pm 1.9$		
HAI 8	$10.7 \pm 0.6$	$11.0 \pm 0.7$	$23.4 \pm 1.2$	$25.0 \pm 1.2$		

Exposure age calculations are based on sea level high latitude production rates  $P_{10} = 5.1 \text{ at/g/yr}$ ,  $P_{26} = 33.15 \text{ at/g/yr}$  (Stone, 2000; and using the  $^{26}\text{Al}/^{10}\text{Be}$  production ratio of 6.5 of Kubik et al., 1998),  $P_{21} = 20.3 \text{ at/g/yr}$  (Niedermann, 2000), an attenuation length ( $\lambda$ ) of  $157 \text{ g/cm}^2$ , a rock density ( $\rho$ ) of  $2.65 \text{ g/cm}^3$  and the scaling model of Stone (2000). Errors are  $1\sigma$  and include: AMS measurement error, uncertainties for altitudes ( $\pm 10 \text{ m}$ ), shielding- and thickness-correction errors as well as erosion rate errors ( $\pm 0.5 \text{ mm ka}^{-1}$ ). Apparent = no erosion.

<sup>a</sup> corrected for an erosion rate of  $3 \text{ mm ka}^{-1}$ .

\* external analyses by S. Niedermann (Ne) and S. Ivy-Ochs (Be).

+ repeat neon analyses at ETH Zurich.

### *Plateau glaciation (HAI 1–8)*

The eight measured samples scatter in four age groups: the perched boulder HAI 1 ( $48.2 \pm 2.6$  ka) together with HAI 2 ( $35.1 \pm 2.0$  ka) form the oldest group, followed by the sample from the northern outlet glacier HAI 7 ( $23.2 \pm 1.2$  ka). The third group is constituted by four samples (HAI 3–6) with exposure ages between  $14.9 \pm 0.7$  and  $15.6 \pm 0.7$  ka and, finally, the youngest age ( $11.0 \pm 0.7$  ka) derive from the boulder sampled on the fluvial terrace (HAI 8).

### **4.2.5 Discussion**

The increasing number of surface exposure dating studies of the last two decades has contributed significantly to our knowledge on the timing of climate events in Tibet. By comparing these results with other records, such as ice cores and stalagmites, feedback mechanisms of glacial response to global climate change are becoming better understood.

#### *A Late Glacial signal in response to 15–16 ka northern hemisphere cooling?*

The youngest ages related to glacial morphologies were obtained from boulders sampled in the centre of the Chuanxi Plateau: HAI 3 & 4 on the small moraine crest and HAI 5 & 6 embedded in basal till. The  $^{10}\text{Be}$  ages of these samples are between  $14.9 \pm 0.7$  and  $15.6 \pm 0.7$  ka. We interpret them as a response to the Late Glacial northern hemisphere cooling around 16 ka, known as Heinrich event 1 (Heinrich, 1988; Peck et al., 2006; 2007). In fact, deglaciation shows multiple steps in marine sediment and ice core records (Blunier and Brook, 2001). Similar signals were reported by Finkel et al. (2003), who dated glacial sediments in the Khumbu Himal and obtained exposure ages of  $16 \pm 2$  ka for the Periche glacial stage. For northeastern Tibet (Anyemaqen and Nianbaoyeze Mountains), Owen et al. (2003) reported moraine ages around  $16 \pm 3$  ka and  $16.5 \pm 0.3$  ka. Near Litang, ~90 km south of our sampling area (Fig. 4.2), Schäfer et al. (2002) dated a restricted valley glaciation to  $16.2 \pm 1.5$  ka (Fig. 4.2). More to the southeast of our study site, in the Kangding Pass area (Fig. 4.2), Strasky et al. (2008) found evidence of a glacial advance as a response to Heinrich event 1 cooling. Furthermore, Zhou et al. (2004) determined radiocarbon ages from a peat sequence in the Dahu Swamp ( $24^{\circ}15'\text{N}$ ;  $115^{\circ}2'\text{E}$ ) and found an interval of climate deterioration around 15.6 cal ka BP. On a global scale, glacier responses to Heinrich event 1 were dated in the Austrian Alps (Ivy-Ochs et al., 2006), in eastern New England (Kaplan,

2007) and in Argentina (Douglass et al., 2006). We thus propose that the dated moraines on Chuanxi Plateau represent most likely a Late Glacial signal related to the temperature decrease during Heinrich event 1.

#### *Glacier advance during MIS 2*

We focused our investigations on the western outlet glaciers and the well-preserved terminal moraine system. The  $^{10}\text{Be}$  ages obtained from nine erratic boulders on three distinct moraine ridges show that the Cuo Naleng and Cuo Ji Gang Wa palaeoglaciers advanced and merged before  $21.6 \pm 1.0$  ka. Then the Cuo Ji Gang Wa palaeoglacier oscillated around this position and formed three similar end moraines between  $21.6 \pm 1.0$  and  $17.5 \pm 0.7$  ka. The Cuo Naleng glacier may have followed the same pattern; however the end moraines were not preserved in the meltwater landscape. On the northern side of the Chuanxi Plateau the slightly older boulder HAI 7 ( $23.2 \pm 1.2$  ka) may represent the equivalent of this MIS 2 glacier advance. After  $17.5 \pm 0.7$  ka the western palaeoglaciers retreated well behind the end moraine positions and sedimentation began in both tongue basins. In a core taken in lake Cuo Naleng, Kramer et al. (2007) obtained a minimum age of 17.5 cal ka BP for the retreat of the Cuo Naleng palaeoglacier from its tongue basin. Two episodes of higher sedimentation were also registered in this core: the first one between 19 and 17.5 ka and the second one from 10.5 to 6 ka BP. Glacier advances in all three dated outlet glacier systems are synchronous to the MIS 2 glaciation in the northern hemisphere. A similar glacial oscillation pattern as found in the investigated valleys was observed by Schaefer et al. (2006) in the Swiss and New Zealand Alps.

The Himalaya has been intensively studied in order to decipher parameters driving glacier advances under different climate conditions. It is highly debated if the LGM on the Tibetan Plateau occurred during enhanced summer monsoon and thus interglacial or interstadial times (e.g. Benn and Owen, 1998; Owen et al., 2005), or during glacial times with enhanced westerlies and additional moisture input from the Caspian Sea (Ono et al., 2004; Yancheva et al., 2007). Ono and Irino (2004) concluded that glaciers advanced roughly synchronous during MIS 2 across most of East Asia, and thus responded to the northern hemisphere temperature forcing. However, most of these MIS 2 glacier advances represent a rather restricted ice extent instead of the maximum of the last glacial cycle. The local LGM seems to have occurred during MIS 3 or 4. A number of studies tried to shed light onto the time structure of the last glacial cycle in the broader area of our study site (e.g. Owen et al., 2003; Wei et al.,

2006; Zhou et al., 2007). Wei et al. (2006) presented thermoluminescence ages from the Gongwan Shan (25°47'–26°33'N and 102°45'–103°19'E) indicating a MIS 5d ice advance (101–104 ka), and a smaller MIS 2 advance between 17.4 and 22.7 ka. An additional glacial advance during MIS 3 was deduced from a single age of  $40 \pm 3.4$  ka. Additionally, in the southeastern Hengduan Mountains (Diancan Shan 25°34'–26°00'N and 99°57'–100°12'E) thermoluminescence ages of 58, 17–23 and  $10.8 \pm 0.8$  ka were interpreted as MIS 4 (LGM), MIS 2 and early Holocene glacier advances, respectively. Zhou et al. (2007) studied the Bodui Zangbo river valley (29°55'–30°06'N and 95°31'–95°37'E) and dated end and lateral moraines with cosmogenic  $^{10}\text{Be}$ . The Guxiang glaciation, according to their definition, occurred during MIS 6 ( $^{10}\text{Be}$  ages from  $113 \pm 17$  to  $137 \pm 16$  ka) followed by the more restricted Baiyu glaciation during MIS 2 ( $^{10}\text{Be}$  ages from  $11.1 \pm 1.9$  to  $18.5 \pm 2.2$  ka). According to Owen et al. (2003) the LGM in the Anyemaqen and Nianbaoyeze Mountains occurred during MIS 3 and subsequent glacier advances during MIS 2 and the Holocene were of lesser extent.

The data we obtained from our field and laboratory work on samples from the Chuanxi Plateau favour a glacier advance synchronous to the northern hemisphere LGM. Thus, moisture transport was still high enough to build an ice sheet with a considerable thickness on the Chuanxi Plateau during times of reduced temperature and low monsoon activity. As the Hengduan Mountains are within the last glacial limit of monsoonal precipitation, residual moisture may have been sufficient to allow ice growth.

#### *Older glaciation*

Perched boulders are an obvious document of a former glaciation (Figs. 4.4a and b). We obtained erosion-corrected  $^{10}\text{Be}$  ages of  $48.2 \pm 2.6$  ka for the perched boulder HAI 1 and  $35.1 \pm 2.0$  ka for the underlying boulder HAI 2. As boulder exhumation is a more common problem than pre-exposure (Putkonen and Swanson, 2003; Douglass et al., 2006), the relatively older boulder resting on the younger one may be explained by successive exhumation. It could thus be possible that these boulders were deposited during a pre-MIS 2 glaciation and weathered out as the moraine degraded. However, we have evidence for a MIS 2 ice advance on both sides of the Chuanxi Plateau, making it hard to believe that its centre remained ice-free. The original deposition structure of the two boulders could have only been preserved during MIS 2 if a cold-based ice sheet would have existed (Fabel et al., 2002; Staiger et al.,

2006; Briner et al., 2007). The discrepancies in nuclide concentrations could thus result from the co-existence of cold and temperate ice in the same area. A thin cold-based ice cap during MIS 2 over the Chuanxi Plateau could have preserved most of the measured nuclide concentrations and maintained the original position of the perched boulder. However, this theoretical cold-based ice cap must have become successively warm-based in order to explain the erratic-rich end and lateral moraines in its outlet valleys. It seems more likely that HAI 1 & 2 are MIS 2 reworked relicts from a previous glaciation on the Chuanxi Plateau and contain some nuclide inheritance from prior exposure periods. The oldest erratic boulders dated with in situ produced cosmogenic nuclides were found in the drier centre of the Tibetan Plateau. Their deposition age was confined to the late Pleistocene,  $169 \pm 15$  ka (Schäfer et al., 2002). The next younger, smaller ice extent occurred around  $67 \pm 6$  ka (Colgan et al., 2006). Even if the geographical distance and the differences in climate regime inhibit direct comparison, data from other areas of the Tibetan Plateau and from the Chuanxi site suggest a rather long and complex glacial history for the Tibetan Plateau.

#### *<sup>21</sup>Ne and radionuclides*

As shown in Fig. 4.6, all of the <sup>21</sup>Ne exposure ages are older than the <sup>10</sup>Be ages. This age discrepancy can be interpreted in at least two ways.

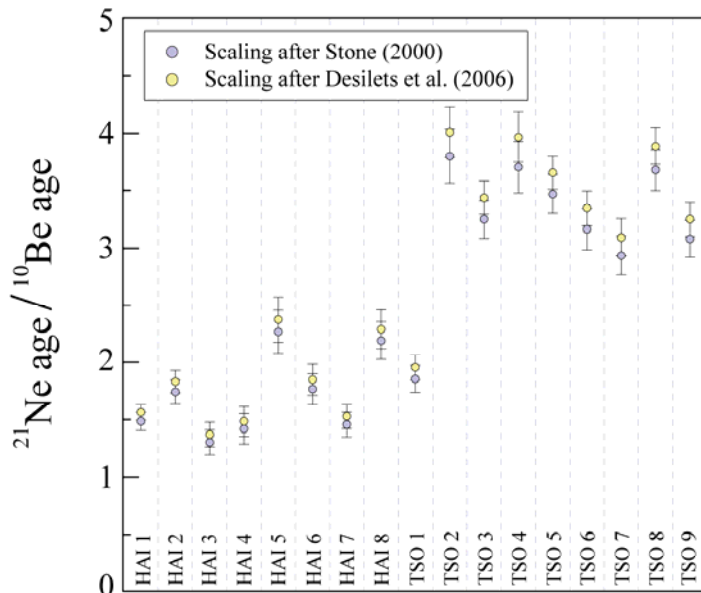


**Fig. 4.6.** <sup>21</sup>Ne/<sup>10</sup>Be age ratios of all samples. Two groups can be identified, one with <sup>21</sup>Ne/<sup>10</sup>Be age ratios around 1.5–2.5, and a second one with ratios between ~3 and 4. The first group is composed of boulders sampled on Chuanxi Plateau and TSO 1, the second group by boulders from the palaeoglacier area of Cuo Ji Gang Wa.

The *first* explanation is a complex exposure-burial history of the sampled erratic boulders. During burial the <sup>21</sup>Ne concentration in the rock surface remains constant (in the case of complete shielding) while the <sup>10</sup>Be concentration continuously decreases over time as <sup>10</sup>Be



decays with a half-life of 1.52 Ma. If the rock surface is re-exposed after the burial period, cosmogenic nuclide production resumes and adds nuclides to a certain inherited concentration. This inherited component is larger for neon and smaller for beryllium due to the decay of the radionuclide. Thus, the relatively older  $^{21}\text{Ne}$  ages of our samples might reflect such a complex exposure-burial scenario. Nevertheless, this seems rather unlikely. When calculating burial ages for the erratic boulders in an over-simplified scenario – assuming no erosion and a simple exposure and consecutive burial period – burial ages on the order of 1.2–2.8 Ma would be needed to accommodate the age differences obtained from the two nuclides. Within the given geological context, this is quite implausible. Furthermore, outside the polar areas glacial landscapes generally evolve below strongly erosive ice bodies, which remove a considerable bedrock layer. Inherited cosmogenic nuclides are therefore removed with the topmost rock layer. As field-evidence (striated surfaces, basal lodgement till) clearly indicate the presence of a former wet-based plateau glacier in the study area, we assume that glacial erosion was large enough to wipe out previously accumulated (inherited) cosmogenic nuclides.

The *second* explanation for the different  $^{21}\text{Ne}$  and  $^{10}\text{Be}$  exposure ages is an inseparable non-cosmogenic neon component that leads to overestimate the cosmogenic neon fraction and hence to erroneously old neon ages. Two sources of non-cosmogenic neon are known; nucleogenic neon (Niedermann et al., 1993) and trapped neon with a non-atmospheric composition (Hetzl et al., 2002). The latter reflects the neon composition incorporated in the minerals (mainly concentrated in fluid inclusions) during rock formation or metamorphic events. Normally, trapped neon is assumed to have an atmospheric isotopic composition but this is not always correct (Niedermann, 2002). Vacuum crushing of quartz samples from the northeastern margin of the Tibetan Plateau revealed non-atmospheric trapped neon components with  $^{21}\text{Ne}/^{20}\text{Ne}$  ratios up to 30 % higher than atmospheric values (Hetzl et al., 2002). As the amount of cosmogenic  $^{21}\text{Ne}$  used to calculate  $^{21}\text{Ne}$  exposure ages is commonly considered to be the excess over trapped air, ignoring such non-atmospheric trapped neon compositions may affect calculated  $^{21}\text{Ne}$  ages. To check the trapped neon concentration, S. Niedermann applied vacuum crushing to one sample (TSO 6) at the GeoForschungs-Zentrum Potsdam and found an atmospheric  $^{22}\text{Ne}/^{20}\text{Ne}$  ratio, and only a slightly elevated  $^{21}\text{Ne}/^{20}\text{Ne}$  ratio of  $\sim 0.00310$ . This result demonstrates that the trapped neon component in our sample is close to air and thus does not significantly influence the  $^{21}\text{Ne}$  ages.

A considerable nucleogenic  $^{21}\text{Ne}$  contribution would therefore be needed to accommodate the  $^{21}\text{Ne}$  and  $^{10}\text{Be}$  age discrepancies with non-cosmogenic neon. Nucleogenic  $^{21}\text{Ne}$  in quartz is mainly the result of the  $^{18}\text{O}(\alpha,n)^{21}\text{Ne}$  reaction. Since  $\alpha$  particles are emitted from nuclides in the U and Th decay chain, high U and Th concentrations in a rock may contribute significantly to the neon inventory in quartz. Alpha particles from U and Th decay have a range of 10–40  $\mu\text{m}$  (e.g. Ziegler, 1977) and, as a consequence, a contribution from adjacent minerals (e.g. biotite) can be neglected because etching of the quartz grains during sample preparation removes most of the affected surface layer. The relevant fraction of  $\alpha$  particles that induce  $(\alpha,n)$  reactions in quartz therefore derives from U/Th-rich inclusions like zircon. A certain nucleogenic  $^{21}\text{Ne}$  production in quartz from U/Th-rich inclusions can, thus, not be excluded and may play an important role especially in old rocks where nucleogenic neon is produced over time scales that are often orders of magnitude larger than the duration of cosmic-ray exposure (Niedermann et al., 1993). In our samples, nucleogenic neon integrated presumably over  $\sim 200$  Ma, the formation age of granite plutons in the area (Huang et al., 2003) and cosmogenic nuclides accumulated over some tens of thousands of years. When we apply the relation between U and Th decay and nucleogenic neon production according to Yatsevich and Honda (1997) and Leya and Wieler (1999) we can estimate the amount of U/Th needed to produce the observed  $^{21}\text{Ne}$  excesses in quartz over  $^{21}\text{Ne}$  concentrations corresponding to  $^{10}\text{Be}$  ages. By assuming a crystallization age of the sampled granites of  $\sim 200$  Ma, a U/Th ratio of one-third and that only nucleogenic neon is responsible for the  $^{21}\text{Ne}$  excesses, the required U concentrations in quartz would be 20–154 ppb and 195–330 ppb for the HAI 1–8 & TSO 1 and TSO 2–9 samples, respectively. These calculated U concentrations are higher than reported values between 0.7 and 4.9 ppb for chemically isolated quartz by Hetzel et al. (2002). However, we analysed one quartz sample (TSO 4) with inductively coupled plasma mass spectrometry and found 19 ppb of U and 75 ppb of Th. Although this is still lower than the required amounts for the specific sample, it is already close to explain the  $^{21}\text{Ne}$  excess of some HAI samples with in situ production of nucleogenic  $^{21}\text{Ne}$  in quartz, especially when considering the uncertainties of the nucleogenic  $^{21}\text{Ne}$  production rate of  $\sim 7\%$  (Leya and Wieler, 1999). Furthermore, quartz can have very diverse amounts of U and Th. Gamma-ray spectrometry measurements at the Paul Scherrer Institute of three commercial high-purity quartz sands revealed U concentrations of 16, 121 and 669 ppb and Thie and Ledger (1981) even found 820 ppb U in granitic quartz.

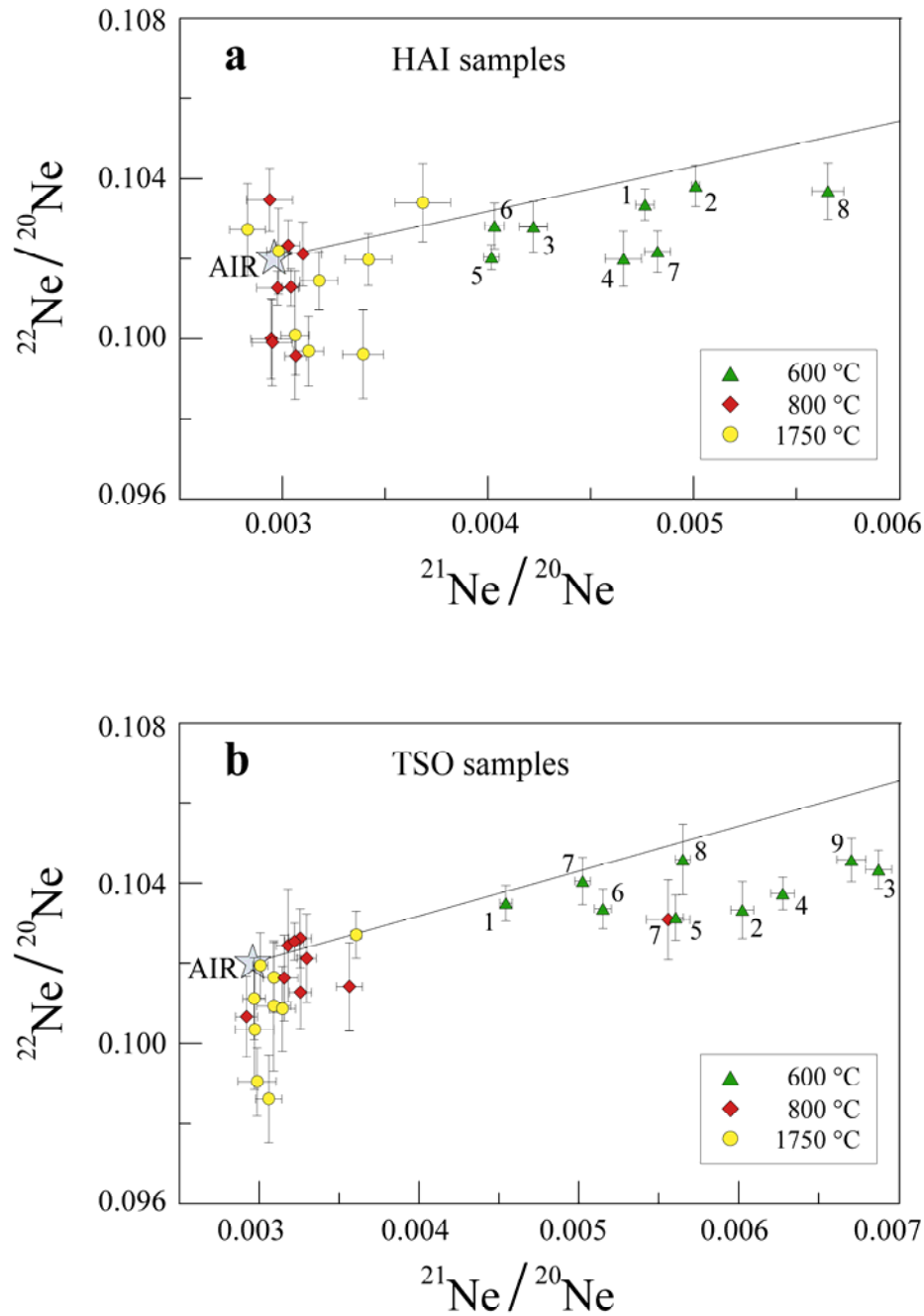


**Fig. 4.7.** Neon three-isotope diagrams. The line in the graphs is the atmospheric-cosmogenic mixing line for quartz, described by Niedermann et al. (1993). Only the relevant data used for exposure age calculations are labelled. **a.** HAI samples; 1–8 represent samples HAI 1–8. **b.** TSO samples; 1–9 represent samples TSO 1–9.

This leads us to believe that  $^{21}\text{Ne}$  production from the  $^{18}\text{O}(\alpha,n)$  reaction is the most likely reason for the  $^{10}\text{Be}$  and  $^{21}\text{Ne}$  exposure age differences. This may also be supported by the positions of the neon data in the neon three-isotope diagrams (Fig. 4.7). The data points generally fall below the atmospheric-cosmogenic mixing line, indicating a neon signature from the  $^{18}\text{O}(\alpha,n)^{21}\text{Ne}$  reaction (Niedermann et al., 1993). Also the two obvious sample

groups (HAI 1–8, TSO 1 and TSO 2–9) with clearly different  $^{21}\text{Ne}/^{10}\text{Be}$  age ratios (Fig. 4.6) may be explained by nucleogenic neon. From the glacial geological point of view erratic boulders from these two groups have different catchment areas. They may therefore vary between each other in chemical composition or even in crystallization age, that could be reflected in different nucleogenic  $^{21}\text{Ne}$  contributions. In this regard, the  $^{21}\text{Ne}/^{10}\text{Be}$  age ratios could help to trace the origin of erratic boulders on the Chuanxi Plateau and thus to identify past ice flow directions.

#### *Monsoon strength and glacier advances*

Various proxies provide information about the prevailing climate conditions on the Tibetan Plateau during MIS 2. For the last millennium oxygen isotopes measured in ice cores (Yang et al., 2007) and stalagmites (Wang et al., 2001; Dykoski et al., 2005) as well as tree ring data from Lhamcoka (one degree east of Garzê) by Brauning and Griessinger (2006), have shown that an alternation of warm and cold periods occurred in similar time intervals to the European Alps, i.e. the Medieval Warm Period (1140–1390 AD) preceded and followed by relatively cold periods until the onset of a warming trend after 1880. This suggests that the strength of the Asian monsoon is influenced by the thermal conditions on the Tibetan Plateau and the resulting pressure gradient is, in turn, coupled to the northern hemisphere cooling.

There exists a close correlation between  $\delta^{18}\text{O}$  records from cave stalagmites and ice cores throughout the Holocene (Wang et al., 2005; Fleitmann et al., 2007) and most of the last glacial cycle (Wang et al., 2001; Yuan et al., 2004). Of the four ice cores drilled on the Tibetan Plateau, only the 309 m long core from the Guliya ice cap yields continuous information about chemical and physical changes of the atmosphere during the entire last glacial cycle (Thompson et al., 1997). Because of its position on the western border of the Tibetan Plateau, the Guliya ice cap receives precipitation from the Asian monsoon in summer and from the westerlies during winter times, and thus complements the data recorded in East Asian stalagmites and Greenland ice cores. Characteristic magnitudes and shapes of most interstadial peaks and stadial troughs found in Greenland ice can also be seen in the Guliya ice core record (Figs. 4.8a and b). In both ice cores  $\delta^{18}\text{O}$  records reached minimum values during MIS 2. And after that, similarly to the Greenland record,  $\delta^{18}\text{O}$  values of the Guliya ice core increased towards the Bølling-Ållerød, with two intermittent cooling trends around

Heinrich event 1, before they dropped abruptly, indicating the Younger Dryas period. A similar  $\delta^{18}\text{O}$  evolution pattern was observed in lowland speleothem records from eastern China (Fig. 4.8c).  $\delta^{18}\text{O}$  values for both stalagmite records illustrated in Fig 4.8c (Dongge and Hulu Cave records; Dongge is 1200 km away from Hulu) replicate remarkably well for times of contemporaneous stalagmite deposition (~35 ka), indicating that variations in monsoon strength are similar over large areas (Dykoski et al., 2005). A record from Timta Cava in the western Himalaya in India further suggests that the Indian summer monsoon was closely related to the East Asian monsoon during Late Glacial times (Sinha et al., 2005). And foraminiferal shells used to derive sea surface temperatures of the southern Chinese Sea even propose a tight link between North Atlantic and East Asian climate (Oppo and Sun, 2005). Additionally to the ice core and stalagmite data, we added to Fig. 4.8 the palaeo-moisture evolution in monsoonal Central Asia (Herzschuh, 2006) and the June insolation at 30°N (Berger and Loutre, 1991) – an important regulator of the monsoon intensity (Wang et al., 2001; Dykoski et al., 2005). At the beginning of MIS 2, moisture was reduced and reached minimum values between 21.3 and 19.8 ka BP. Afterwards, climate was slightly wetter, but moisture was reduced again between 17.2 and 15.4 ka and between 13 and 11.9 ka (Herzschuh, 2006).

Erosion-corrected  $^{10}\text{Be}$  exposure ages of all measured samples are plotted in Fig. 4.8 for comparison to the above-mentioned different climate proxies of the northern hemisphere. The samples from the outlet valleys (TSO 1–8 and HAI 7) show that glaciers retreated while both insolation and moisture were increasing. The smaller ice extent registered on the Chuanxi Plateau (HAI 3–6) occurred during Heinrich event 1, as indicated by the  $\delta^{18}\text{O}$  values of the speleothem and ice core records, where moisture values were slightly higher than during MIS 2. We thus suggest that glaciers – at least on the Chuanxi Plateau – were more sensitive to temperature changes than to precipitation variations.

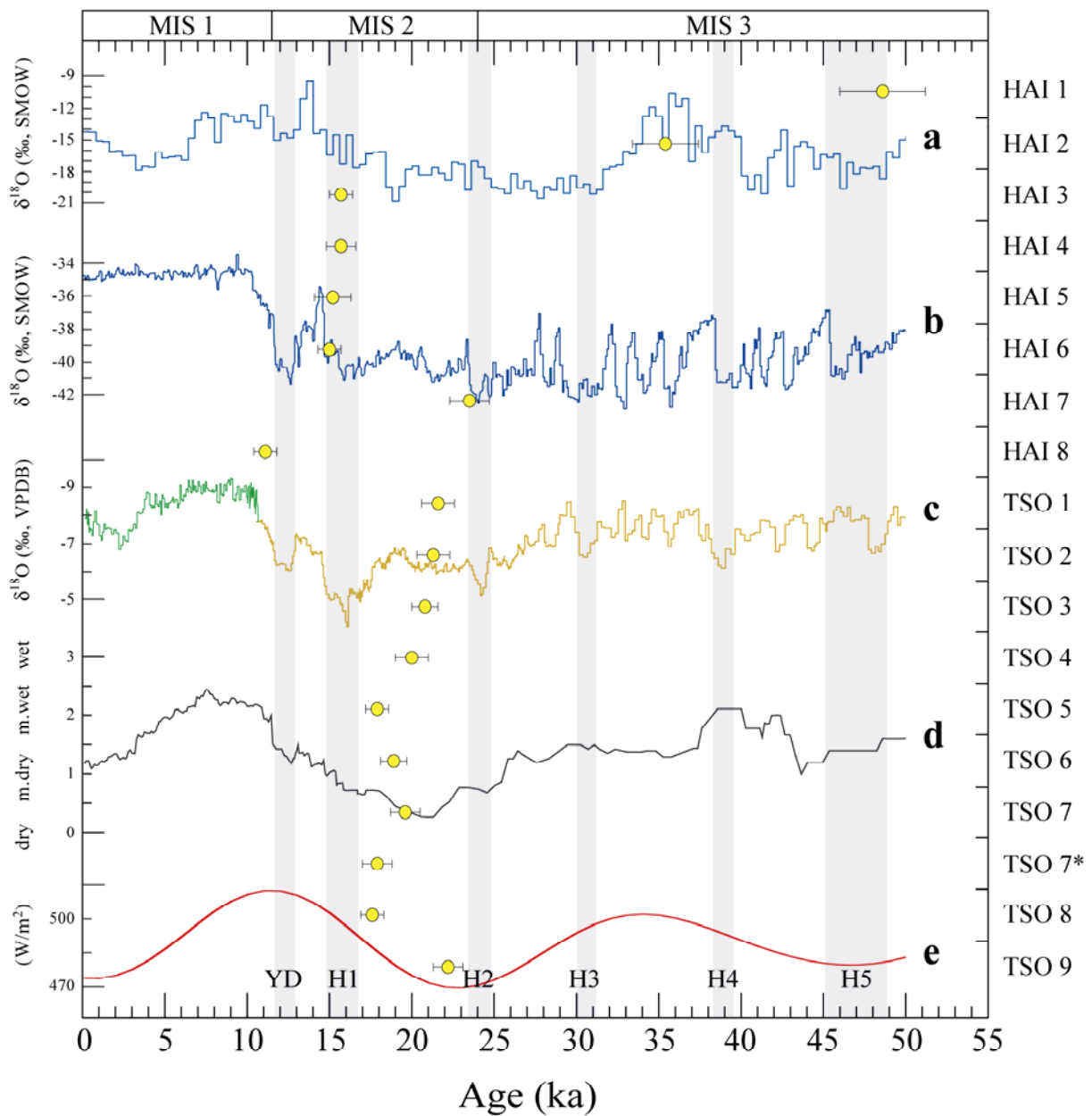


**Fig. 4.8.** Comparison between different northern hemisphere climate proxies. **a.**  $\delta^{18}\text{O}$  record from Guliya ice core (Thompson et al., 1997). **b.**  $\delta^{18}\text{O}$  record from GRIP2 (Grootes et al., 1993). **c.**  $\delta^{18}\text{O}$  from Dongge Cave (Yuan et al., 2004) and Hulu Cave (Wang et al., 2001). **d.** Mean effective moisture from the Asian monsoon margin (Herzschuh, 2006). **e.** June insolation at  $30^\circ\text{N}$  (Berger and Loutre, 1991). Chronostratigraphic position of Younger Dryas (YD) and Heinrich events (H1–5) after Bond et al. (1993) and Wang et al. (2001). Marine isotope stages (MIS) after Bassinot et al. (1994). Circles represent erosion-corrected  $^{10}\text{Be}$  ages (see Table 4.3) of the study area.

#### 4.2.6 Conclusions

From erosion-corrected ( $3 \text{ mm ka}^{-1}$ )  $^{10}\text{Be}$  exposure ages of erratic boulders from terminal moraines and from the Chuanxi Plateau in the Hengduan Mountains (eastern Tibet) we draw the following conclusions:

1. Outlet glaciers on the northern, southern and western sides of the Chuanxi Plateau stabilized in MIS 2, during an interval of weak summer monsoon activity. The ice front oscillated within a few hundred metres between  $21.2 \pm 1.0$  and  $17.5 \pm 0.7$  ka. Glaciers then retreated well behind this position and organic sedimentation started in the tongue basins.
2. A limited glacial event occurred in the centre of the Chuanxi Plateau between  $14.9 \pm 0.7$  and  $15.6 \pm 0.7$  ka. This corresponds most probably to a glacier advance during Heinrich event 1.
3. Evidence of a pre-MIS 2 glaciation was found in a perched boulder, which yielded an older age ( $48.2 \pm 2.6$  ka) than the underlying boulder ( $35.1 \pm 2.0$  ka). A simple weathering-out scenario was ruled out as the plateau must have been ice covered during MIS 2. We believe that these boulders were pre-exposed – implying multiple glaciations of the area – and reworked during MIS 2.
4. In a subset of the sampled boulders,  $^{21}\text{Ne}$  exposure ages are 1.5–4 times older than  $^{10}\text{Be}$  ages. Such discrepancies between stable and radioactive nuclides cannot be explained by pre-exposure unless we accept a minimum burial time of 1.2–2.8 Ma, which is rather unlikely. Estimates about the production of nucleogenic  $^{21}\text{Ne}$  from  $(\alpha, n)$  reactions showed that nucleogenic  $^{21}\text{Ne}$  is a more realistic explanation for the exposure age differences obtained from neon and beryllium. Future cosmogenic noble gas studies on relatively young exposure histories should, therefore, be aware of possible nucleogenic neon contributions and routinely measure the U and Th concentrations of the samples.

**Acknowledgements:** We gratefully acknowledge S. Niedermann for analyzing the trapped neon composition and measuring the noble gases in cross-control samples and P. Vermeesch and J. Eikenberg for determining U and Th concentrations. We thank the ETH/PSI facility team for technical support and the Swiss National Science Foundation (grant no. 200020-105220/1) for funding this work.

## References

- AKÇAR, N. 2006. *Paleoglacial Records from the Black Sea Area of Turkey: Field and Dating Evidence*. PhD thesis, University of Bern, 187 pp.
- AKÇAR, N., YAVUZ, V., IVY-OCHS, S., KUBIK, P.W., VARDAR, M. & SCHLÜCHTER, C. 2007. Paleoglacial records from Kavron Valley, NE Turkey: Field and cosmogenic exposure dating evidence. *Quaternary International*, **164/165**, 170–183.
- AKÇAR, N., YAVUZ, V., IVY-OCHS, S., KUBIK, P.W., VARDAR, M. & SCHLÜCHTER, C. 2008. A case for a downwasting mountain glacier during Termination I, Verçenik valley, northeastern Turkey. *Journal of Quaternary Science*, **23**, 273–285.
- BASSINOT, F.C., LABEYRIE, L.D., VINCENT, E., QUIDELLEUR, X., SHACKLETON, N.J. & LANCELOT, Y. 1994. The astronomical theory of climate and the age of the Brunhes-Matuyama magnetic reversal. *Earth and Planetary Science Letters*, **126**, 91–108.
- BAUR, H. 1999. A Noble-Gas Mass Spectrometer Compressor Source With two Orders of Magnitude Improvement in Sensitivity. *Eos Transactions AGU*, **80**, Abstract V22B-08.
- BENN, D.I. & OWEN, L.A. 1998. The role of the Indian summer monsoon and the mid-latitude westerlies in Himalayan glaciation: review and speculative discussion. *Journal of the Geological Society*, **155**, 353–363.
- BENN, D.I., OWEN, L.A., OSMASTON, H.A., SELTZER, G.O., PORTER, S.C. & MARK, B. 2005. Reconstruction of equilibrium-line altitudes for tropical and sub-tropical glaciers. *Quaternary International*, **138**, 8–21.
- BERGER, A. & LOUTRE, M.F. 1991. Insolation values for the climate of the last 10 million years. *Quaternary Science Reviews*, **10**, 297–317.
- BLUNIER, T. & BROOK, E.J. 2001. Timing of millennial-scale climate change in Antarctica and Greenland during the last glacial period. *Science*, **291**, 109–112.
- BOHNER, J. 2006. General climatic controls and topoclimatic variations in Central and High Asia. *Boreas*, **35**, 279–295.
- BOND, G., BROECKER, W., JOHNSEN, S., MCMANUS, J., LABEYRIE, L., JOUZEL, J. & BONANI, G. 1993. Correlations between climate records from North Atlantic sediments and Greenland ice. *Nature*, **365**, 143–147.
- BRAUNING, A. & GRIESSINGER, J. 2006. Late Holocene variations in monsoon intensity in the Tibetan-Himalayan region – Evidence from tree rings. *Journal of the Geological Society of India*, **68**, 485–493.
- BRINER, J.P., OVEREEM, I., MILLER, G. & FINKEL, R. 2007. The deglaciation of Clyde Inlet, northeastern Baffin Island, Arctic Canada. *Journal of Quaternary Science*, **22**, 223–232.
- COLGAN, P.M., MUNROE, J.S. & ZHOU, S.Z. 2006. Cosmogenic radionuclide evidence for the limited extent of last glacial maximum glaciers in the Tanggula Shan of the central Tibetan Plateau. *Quaternary Research*, **65**, 336–339.



- DERBYSHIRE, E. 1996. Quaternary glacial sediments, glaciation style, climate and uplift in the Karakoram and northwest Himalaya: Review and speculations. *Palaeogeography, Palaeoclimatology, Palaeoecology*, **120**, 147–157.
- DESILETS, D., ZREDA, M. & PRABU, T. 2006. Extended scaling factors for in situ cosmogenic nuclides: New measurements at low latitude. *Earth and Planetary Science Letters*, **246**, 265–276.
- DING, Y.H. & CHAN, J.C.L. 2005. The East Asian summer monsoon: an overview. *Meteorology and Atmospheric Physics*, **89**, 117–142.
- DOUGLASS, D.C., SINGER, B.S., KAPLAN, M.R., MICKELSON, D.M. & CAFFEE, M.W. 2006. Cosmogenic nuclide surface exposure dating of boulders on last-glacial and late-glacial moraines, Lago Buenos Aires, Argentina: Interpretive strategies and paleoclimate implications. *Quaternary Geochronology*, **1**, 43–58.
- DUNNE, J., ELMORE, D. & MUZIKAR, P. 1999. Scaling factors for the rates of production of cosmogenic nuclides for geometric shielding and attenuation at depth on sloped surfaces. *Geomorphology*, **27**, 3–11.
- DYKOSKI, C.A., EDWARDS, R.L., CHENG, H., YUAN, D.X., CAI, Y.J., ZHANG, M.L., LIN, Y.S., QING, J.M., AN, Z.S. & REVENAUGH, J. 2005. A high-resolution, absolute-dated Holocene and deglacial Asian monsoon record from Dongge Cave, China. *Earth and Planetary Science Letters*, **233**, 71–86.
- FABEL, D., STROEVEN, A.P., HARBOR, J., KLEMAN, J., ELMORE, D. & FINK, D. 2002. Landscape preservation under Fennoscandian ice sheets determined from in situ produced  $^{10}\text{Be}$  and  $^{26}\text{Al}$ . *Earth and Planetary Science Letters*, **201**, 397–406.
- FINKEL, R.C., OWEN, L.A., BARNARD, P.L. & CAFFEE, M.W. 2003. Beryllium-10 dating of Mount Everest moraines indicates a strong monsoon influence and glacial synchronicity throughout the Himalaya. *Geology*, **31**, 561–564.
- FLEITMANN, D., BURNS, S.J., MANGINI, A., MUDELSEE, M., KRAMERS, J., VILLA, I., NEFF, U., AL-SUBBARY, A.A., BUETTNER, A., HIPPLER, D. & MATTER, A. 2007. Holocene ITCZ and Indian monsoon dynamics recorded in stalagmites from Oman and Yemen (Socotra). *Quaternary Science Reviews*, **26**, 170–188.
- GILLESPIE, A. & MOLNAR, P. 1995. Asynchronous maximum advances of mountain and continental glaciers. *Reviews of Geophysics*, **33**, 311–364.
- GOSSE, J.C. & PHILLIPS, F.M. 2001. Terrestrial in situ cosmogenic nuclides: theory and application. *Quaternary Science Reviews*, **20**, 1475–1560.
- GRAF, A.A., STRASKY, S., IVY-OCHS, S., AKÇAR, N., KUBIK, P.W., BURKHARD, M. & SCHLÜCHTER, C. 2007. First results of cosmogenic dated pre-Last Glaciation erratics from the Montoz area, Jura Mountains, Switzerland. *Quaternary International*, **164/165**, 43–52.
- GRAF, A.A. 2008. *Surface exposure dating of LGM and pre-LGM erratic boulders: a comparison of paleoclimate records from both hemispheres*. PhD thesis, University of Bern, 215 pp.
- GROOTES, P.M., STUIVER, M., WHITE, J.W.C., JOHNSEN, S. & JOUZEL, J. 1993. Comparison of oxygen isotope records from the GISP2 and GRIP Greenland ice cores. *Nature*, **366**, 552–554.

- HEINRICH, H. 1988. Origin and Consequences of Cyclic Ice Rafting in the Northeast Atlantic Ocean during the Past 130,000 Years. *Quaternary Research*, **29**, 142–152.
- HERZSCHUH, U. 2006. Palaeo-moisture evolution in monsoonal Central Asia during the last 50,000 years. *Quaternary Science Reviews*, **25**, 163–178.
- HETZEL, R., NIEDERMANN, S., IVY-OCHS, S., KUBIK, P.W., TAO, M. & GAO, B. 2002.  $^{21}\text{Ne}$  versus  $^{10}\text{Be}$  and  $^{26}\text{Al}$  exposure ages of fluvial terraces: the influence of crustal Ne in quartz. *Earth and Planetary Science Letters*, **201**, 575–591.
- HUANG, M.H., BUICK, I.S. & HOU, L.W. 2003. Tectonometamorphic evolution of the eastern Tibetan Plateau: Evidence from the central Songpan–Garzê Orogenic Belt, western China. *Journal of Petrology*, **44**, 255–278.
- IVY-OCHS, S. 1996. *The dating of rock surfaces using in situ produced  $^{10}\text{Be}$ ,  $^{26}\text{Al}$  and  $^{36}\text{Cl}$ , with examples from Antarctica and the Swiss Alps*. PhD thesis ETH No. 11763, ETH Zurich, 196 pp.
- IVY-OCHS, S., SCHÄFER, J., KUBIK, P.W., SYNAL, H.A. & SCHLÜCHTER, C. 2004. Timing of deglaciation on the northern Alpine foreland (Switzerland). *Eclogae Geologicae Helvetiae*, **97**, 47–55.
- IVY-OCHS, S., KERSCHNER, H., KUBIK, P.W. & SCHLÜCHTER, C. 2006. Glacier response in the European Alps to Heinrich Event 1 cooling: the Gschnitz stadial. *Journal of Quaternary Science*, **21**, 115–130.
- KAPLAN, M.R. 2007. Major ice sheet response in eastern New England to a cold North Atlantic region, 16–15 cal ka BP. *Quaternary Research*, **68**, 280–283.
- KASER, G. & OSMASTON, H. 2002. *Tropical Glaciers*. Cambridge: Cambridge University Press, 207 pp.
- KOHL, C.P. & NISHIZUMI, K. 1992. Chemical isolation of quartz for measurement of *in-situ*-produced cosmogenic nuclides. *Geochimica et Cosmochimica Acta*, **56**, 3583–3587.
- KRAMER, A., HERZSCHUH, U. & MISCHKE, S. 2007. Late Quaternary changes on the southeastern margin of the Tibetan Plateau; a high resolution pollen and NPP record. In *Limnogeology: tales of an evolving Earth. Program and abstract book*. Barcelona: 4<sup>th</sup> International Limnogeology Congress.
- KUBIK, P.W., IVY-OCHS, S., MASARIK, J., FRANK, M. & SCHLÜCHTER, C. 1998.  $^{10}\text{Be}$  and  $^{26}\text{Al}$  production rates deduced from an instantaneous event within the dendro-calibration curve, the landslide of Köfels, Ötz Valley, Austria. *Earth and Planetary Science Letters*, **161**, 231–241.
- LAIXIN, L. 1963. Study on morphology of western Sichuan and northern Yunnan. *Geography collected papers*, **5**.
- LAL, D. 1991. Cosmic ray labeling of erosion surfaces: *in situ* nuclide production rates and erosion models. *Earth and Planetary Science Letters*, **104**, 424–439.
- LEYA, I. & WIELER, R. 1999. Nucleogenic production of Ne isotopes in Earth's crust and upper mantle induced by alpha particles from the decay of U and Th. *Journal of Geophysical Research B*, **104**, 15439–15450.
- LIU, T.S., ZHANG, X.S., XIONG, S.F., QIN, X.G. & YANG, X.P. 2002. Glacial environments on the Tibetan Plateau and global cooling. *Quaternary International*, **97/98**, 133–139.

- MATTAUER, M., MALAVIEILLE, J., CALASSOU, S., LANCELOT, J., ROGER, F., HAO, Z.W., XU, Z.Q. & HOU, L.W. 1992. The Songpan–Garzê Triassic belt of West Sichuan and eastern Tibet – a decollement fold belt on a passive margin. *Comptes Rendus De L'Académie Des Sciences Série II*, **314**, 619–626.
- NIEDERMANN, S., GRAF, T. & MARTI, K. 1993. Mass spectrometric identification of cosmic-ray-produced neon in terrestrial rocks with multiple neon components. *Earth and Planetary Science Letters*, **118**, 65–73.
- NIEDERMANN, S. 2000. The  $^{21}\text{Ne}$  production rate in quartz revisited. *Earth and Planetary Science Letters*, **183**, 361–364.
- NIEDERMANN, S. 2002. Cosmic-Ray-Produced Noble Gases in Terrestrial Rocks: Dating Tools for Surface Processes. In PORCELLI, D., BALLENTINE, C.J. & WIELER, R., eds. *Noble Gases in Geochemistry and Cosmochemistry. Reviews in Mineralogy and Geochemistry*, **47**. Washington, DC: Mineralogical Society of America, 731–784.
- ONO, Y. & IRINO, T. 2004. Southern migration of westerlies in the Northern Hemisphere PEP II transect during the Last Glacial Maximum. *Quaternary International*, **118/119**, 13–22.
- ONO, Y., SHULMEISTER, J., LEHMKUHL, F., ASAHI, K. & AOKI, T. 2004. Timings and causes of glacial advances across the PEP II transect (East-Asia to Antarctica) during the last glaciation cycle. *Quaternary International*, **118/119**, 55–68.
- OPPO, D.W. & SUN, Y.B. 2005. Amplitude and timing of sea-surface temperature change in the northern South China Sea: Dynamic link to the East Asian monsoon. *Geology*, **33**, 785–788.
- OWEN, L.A., FINKEL, R.C., HAIZHOU, M., SPENCER, J.Q., DERBYSHIRE, E., BARNARD, P.L. & CAFFEE, M.W. 2003. Timing and style of Late Quaternary glaciation in northeastern Tibet. *Geological Society of America Bulletin*, **115**, 1356–1364.
- OWEN, L.A., FINKEL, R.C., BARNARD, P.L., MA, H.Z., ASAHI, K., CAFFEE, M.W. & DERBYSHIRE, E. 2005. Climatic and topographic controls on the style and timing of Late Quaternary glaciation throughout Tibet and the Himalaya defined by  $^{10}\text{Be}$  cosmogenic radionuclide surface exposure dating. *Quaternary Science Reviews*, **24**, 1391–1411.
- OWEN, L.A., FINKEL, R.C., HAIZHOU, M. & BARNARD, P.L. 2006. Late Quaternary landscape evolution in the Kunlun Mountains and Qaidam Basin, Northern Tibet: A framework for examining the links between glaciation, lake level changes and alluvial fan formation. *Quaternary International*, **154**, 73–86.
- PECK, V.L., HALL, I.R., ZAHN, R., ELDERFIELD, H., GROUSSET, F., HEMMING, S.R. & SCOURSE, J.D. 2006. High resolution evidence for linkages between NW European ice sheet instability and Atlantic Meridional Overturning Circulation. *Earth and Planetary Science Letters*, **243**, 476–488.
- PECK, V.L., HALL, I.R., ZAHN, R., GROUSSET, F., HEMMING, S.R. & SCOURSE, J.D. 2007. The relationship of Heinrich events and their European precursors over the past 60 ka BP: a multi-proxy ice-rafted debris provenance study in the North East Atlantic. *Quaternary Science Reviews*, **26**, 862–875.
- PHILLIPS, W.M., HALL, A.M., MOTTRAM, R., FIFIELD, L.K. & SUGDEN, D.E. 2006. Cosmogenic  $^{10}\text{Be}$  and  $^{26}\text{Al}$  exposure ages of tors and erratics, Cairngorm Mountains, Scotland: Timescales for the development of a classic landscape of selective linear glacial erosion. *Geomorphology*, **73**, 222–245.

- PUTKONEN, J. & SWANSON, T. 2003. Accuracy of cosmogenic ages for moraines. *Quaternary Research*, **59**, 255–261.
- REID, A.J., FOWLER, A.P., PHILLIPS, D. & WILSON, C.J.L. 2005. ThermoChronology of the Yidun Arc, central eastern Tibetan Plateau: constraints from  $^{40}\text{Ar}/^{39}\text{Ar}$  K-feldspar and apatite fission track data. *Journal of Asian Earth Sciences*, **25**, 915–935.
- REUTHER, A.U., URDEA, P., GEIGER, C., IVY-OCHS, S., NILLER, H.P., KUBIK, P.W. & HEINE, K. 2007. Late Pleistocene glacial chronology of the Pietrele Valley, Retezat Mountains, Southern Carpathians constrained by  $^{10}\text{Be}$  exposure ages and pedological investigations. *Quaternary International*, **164/165**, 151–169.
- RICHARDS, B.W., OWEN, L.A. & RHODES, E.J. 2000. Timing of Late Quaternary glaciations in the Himalayas of northern Pakistan. *Journal of Quaternary Science*, **15**, 283–297.
- SCHAEFER, J.M., DENTON, G.H., BARRELL, D.J.A., IVY-OCHS, S., KUBIK, P.W., ANDERSEN, B.G., PHILLIPS, F.M., LOWELL, T.V. & SCHLÜCHTER, C. 2006. Near-Synchronous Interhemispheric Termination of the Last Glacial Maximum in Mid-Latitudes. *Science*, **312**, 1510–1513.
- SCHAEFER, J.M., OBERHOLZER, P., ZHAO, Z., IVY-OCHS, S., WIELER, R., BAUR, H., KUBIK, P.W. & SCHLÜCHTER, C. 2008. Cosmogenic beryllium-10 and neon-21 dating of late Pleistocene glaciations in Nyalam, monsoonal Himalayas. *Quaternary Science Reviews*, **27**, 295–311.
- SCHÄFER, J.M., TSCHUDI, S., ZHAO, Z., WU, X., IVY-OCHS, S., WIELER, R., BAUR, H., KUBIK, P.W. & SCHLÜCHTER, C. 2002. The limited influence of glaciations in Tibet on global climate over the past 170 000 yr. *Earth and Planetary Science Letters*, **194**, 287–297.
- SHI, Y. 2002. Characteristics of late Quaternary monsoonal glaciation on the Tibetan Plateau and in East Asia. *Quaternary International*, **97/98**, 79–91.
- SINHA, A., CANNARIATO, K.G., STOTT, L.D., LI, H.-C., YOU, C.-F., CHENG, H., EDWARDS, R.L. & SINGH, I.B. 2005. Variability of Southwest Indian summer monsoon precipitation during the Bølling-Ållerød. *Geology*, **33**, 813–816.
- STAIGER, J.W., GOSSE, J., LITTLE, E.C., UTTING, D.J., FINKEL, R., JOHNSON, J.V. & FASTOOK, J. 2006. Glacial erosion and sediment dispersion from detrital cosmogenic nuclide analyses of till. *Quaternary Geochronology*, **1**, 29–42.
- STAIGER, J., GOSSE, J., TORACINTA, R., OGLESBY, B., FASTOOK, J. & JOHNSON, J.V. 2007. Atmospheric scaling of cosmogenic nuclide production: Climate effect. *Journal of Geophysical Research B*, **112**, B02205, doi:10.1029/2005JB003811.
- STONE, J.O. 2000. Air pressure and cosmogenic isotope production. *Journal of Geophysical Research B*, **105**, 23753–23759.
- STRASKY, S., GRAF, A.A., ZHAO, Z., KUBIK, P.W., BAUR, H., SCHLÜCHTER, C. & WIELER, R. 2008. Late Glacial ice advances in southeast Tibet. *Journal of Asian Earth Sciences*, in press.

- SYNAL, H.-A., BONANI, G., DÖBELI, M., ENDER, R.M., GARTENMANN, P., KUBIK, P.W., SCHNABEL, C. & SUTER, M. 1997. Status report of the PSI/ETH AMS facility. *Nuclear Instruments and Methods in Physics Research B*, **123**, 62–68.
- THIE, T.T. & LEDGER, E.B. 1981. Fission Track Study of Uranium in Two Granites of Central Texas. *Contributions to Mineralogy and Petrology*, **76**, 12–16.
- THOMPSON, L.G., YAO, T., DAVIS, M.E., HENDERSON, K.A., MOSLEY-THOMPSON, E., LIN, P.-N., BEER, J., SYNAL, H.-A., COLE-DAI, J. & BOLZAN, J.F. 1997. Tropical Climate Instability: The Last Glacial Cycle from a Qinghai-Tibetan Ice Core. *Science*, **276**, 1821–1825.
- THOMPSON, L.G. 2000. Ice core evidence for climate change in the Tropics: implications for our future. *Quaternary Science Reviews*, **19**, 19–35.
- TSCHUDI, S., SCHÄFER, J.M., ZHAO, Z., WU, X., IVY-OCHS, S., KUBIK, P.W. & SCHLÜCHTER, C. 2003. Glacial advances in Tibet during the Younger Dryas? Evidence from cosmogenic  $^{10}\text{Be}$ ,  $^{26}\text{Al}$ , and  $^{21}\text{Ne}$ . *Journal of Asian Earth Sciences*, **22**, 301–306.
- VANDENBERGHE, J., RENNSSEN, H., VAN HUISSTEDEN, K., NUGTEREN, G., KONERT, M., LU, H.Y., DODONOV, A. & BUYLAERT, J.P. 2006. Penetration of Atlantic westerly winds into Central and East Asia. *Quaternary Science Reviews*, **25**, 2380–2389.
- VERMEESCH, P. 2007. CosmoCalc: an Excel add-in for cosmogenic nuclide calculations. *Geochemistry, Geophysics, Geosystems*, **8**, doi:10.1029/2006GC001530.
- VOSE, R.S., SCHMOYER, R.L., STEURER, P.M., PETERSON, T.C., HEIM, R., KARL, T.R. & EISCHEID, J. 1992. *The Global Historical Climatology Network: long-term monthly temperature, precipitation, sea level pressure, and station pressure data*. Carbon Dioxide Information Analysis Center, Oak Ridge National Laboratory, ORNL/CDIAC-53, NDP-041, pp. 1–325 [Also available online at: <http://iridl.ldeo.columbia.edu/SOURCES/.NOAA/.NCDC/.GHCN/>].
- WANG, Y.J., CHENG, H., EDWARDS, R.L., AN, Z.S., WU, J.Y., SHEN, C.-C. & DORALE, J.A. 2001. A High-Resolution Absolute-Dated Late Pleistocene Monsoon Record from Hulu Cave, China. *Science*, **294**, 2345–2348.
- WANG, P.X., CLEMENS, S., BEAUFORT, L., BRACONNOT, P., GANSEN, G., JIAN, Z.M., KERSHAW, P. & SARNTHEIN, M. 2005. Evolution and variability of the Asian monsoon system: state of the art and outstanding issues. *Quaternary Science Reviews*, **24**, 595–629.
- WARA, M.W., RAVELO, A.C. & DELANEY, M.L. 2005. Permanent El Niño-like conditions during the Pliocene warm period. *Science*, **309**, 758–761.
- WEI, Z., ZHIJIU, C. & YONGHUA, L. 2006. Review of the timing and extent of glaciers during the last glacial cycle in the bordering mountains of Tibet and in East Asia. *Quaternary International*, **154/155**, 32–43.
- YANCHEVA, G., NOWACZYK, N.R., MINGRAM, J., DULSKI, P., SCHETTLER, G., NEGENDANK, J.F.W., LIU, J.Q., SIGMAN, D.M., PETERSON, L.C. & HAUG, G.H. 2007. Influence of the intertropical convergence zone on the East Asian monsoon. *Nature*, **445**, 74–77.

- YANG, X.L., ZHANG, P.Z., CHEN, F.H., HUH, C.A., LI, H.C., CHENG, H., JOHNSON, K.R., LIU, J.H. & AN, C.L. 2007. Modern stalagmite oxygen isotopic composition and its implications of climatic change from a high-elevation cave in the eastern Qinghai-Tibet Plateau over the past 50 years. *Chinese Science Bulletin*, **52**, 1238–1247.
- YATSEVICH, I. & HONDA, M. 1997. Production of nucleogenic neon in the Earth from natural radioactive decay. *Journal of Geophysical Research B*, **102**, 10291–10298.
- YUAN, D.X., CHENG, H., EDWARDS, R.L., DYKOSKI, C.A., KELLY, M.J., ZHANG, M.L., QING, J.M., LIN, Y.S., WANG, Y.J., WU, J.Y., DORALE, J.A., AN, Z.S. & CAI, Y.J. 2004. Timing, Duration, and Transitions of the Last Interglacial Asian Monsoon. *Science*, **304**, 575–578.
- ZECH, W., GLASER, B., ABRAMOWSKI, U., DITTMAR, C. & KUBIK, P.W. 2003. Reconstruction of the Late Quaternary Glaciation of the Macha Khola valley (Gorkha Himal, Nepal) using relative and absolute ( $^{14}\text{C}$ ,  $^{10}\text{Be}$ , dendrochronology) dating techniques. *Quaternary Science Reviews*, **22**, 2253–2265.
- ZECH, R., KULL, C. & VEIT, H. 2006. Late Quaternary glacial history in the Encierro Valley, northern Chile (29 degrees S), deduced from  $^{10}\text{Be}$  surface exposure dating. *Palaeogeography, Palaeoclimatology, Palaeoecology*, **234**, 277–286.
- ZHIJU, C. 1958. Initial observation of modern glacier in Gongga mountain. *Acta Geographica Sinica*, **24**.
- ZHOU, W.J., YU, X.F., JULL, A.J.T., BURR, G., XIAO, J.Y., LU, X.F. & XIAN, F. 2004. High-resolution evidence from southern China of an early Holocene optimum and a mid-Holocene dry event during the past 18,000 years. *Quaternary Research*, **62**, 39–48.
- ZHOU, S.Z., WANG, X., WANG, J. & XU, L. 2006. A preliminary study on timing of the oldest Pleistocene glaciation in Qinghai–Tibetan Plateau. *Quaternary International*, **154/155**, 44–51.
- ZHOU, S.Z., XU, L.B., COLGAN, P.M., MICKELSON, D.M., WANG, X.L., WANG, J. & ZHONG, W. 2007. Cosmogenic  $^{10}\text{Be}$  dating of Guxiang and Baiyu glaciations. *Chinese Science Bulletin*, **52**, 1387–1393.
- ZIEGLER, J.F. 1977. *Helium: Stopping powers and ranges in all elemental matter*. New York: Pergamon Press, 367 pp.

### 4.3 Late Glacial ice advances in southeast Tibet <sup>d</sup>

---

Stefan Strasky <sup>1\*</sup>, Angela A. Graf <sup>2</sup>, Zhizhong Zhao <sup>3</sup>, Peter W. Kubik <sup>4</sup>, Heinrich Baur <sup>1</sup>, Christian Schlüchter <sup>2</sup> and Rainer Wieler <sup>1</sup>

<sup>1</sup> *Institute of Isotope Geochemistry and Mineral Resources, ETH Zurich, 8092 Zurich, Switzerland*

<sup>2</sup> *Institute of Geological Sciences, University of Bern, 3012 Bern, Switzerland*

<sup>3</sup> *Institute of Geomechanics, Chinese Academy of Geological Sciences, Beijing 100081, China*

<sup>4</sup> *Paul Scherrer Institute, c/o Institute for Particle Physics, ETH Zurich, 8093 Zurich, Switzerland*

\* *corresponding author: stefan.strasky@gmail.com*

---

**Abstract:** The sensitivity of Tibetan glacial systems to North Atlantic climate forcing is a major issue in palaeoclimatology. In this study, we present surface exposure ages of erratic boulders from a valley system in the Hengduan Mountains, southeastern Tibet, showing evidence of an ice advance during Heinrich event 1. Cosmogenic nuclide analyses (<sup>10</sup>Be and <sup>21</sup>Ne) revealed consistent exposure ages, indicating no major periods of burial or pre-exposure. Erosion-corrected (3 mm ka<sup>-1</sup>) <sup>10</sup>Be exposure ages range from 13.4 to 16.3 ka. This is in agreement with recalculated exposure ages from the same valley system by Tschudi et al. (2003). Thus this indicates that local glaciers advanced in the investigated area as a response to Heinrich event 1 cooling and periglacial surface adjustments during the Younger Dryas overprinted the glacial morphology, leading to deceptively young exposure ages of certain erratic boulders.

**Key words:** cosmogenic nuclides; exposure age; Late Glacial; Heinrich event; Tibet

#### 4.3.1 Introduction

Abrupt climate change has a direct impact on terrestrial geo-ecosystems and can lead to environmental changes at global scales. Such abrupt and strong shifts in climate occur during both glacial and interglacial periods (Bond et al., 1997). The most prominent of these rapid warm–cold oscillations are the Dansgaard–Oeschger cycles, documented by Johnsen et al. (1992) and Dansgaard et al. (1993) in Greenland ice cores. A sudden North Atlantic surface temperature increase of  $\geq 5$  °C in less than 40 years, followed by a gradual cooling to stadial values over several hundred to thousand years characterize the short-term climate fluctuations during

---

<sup>d</sup> In press *Journal of Asian Earth Sciences* (2008)

the last deglaciation (Lehman and Keigwin, 1992) and probably reflect period and amplitude of most Dansgaard–Oeschger cycles. Bundled Dansgaard–Oeschger cycles, each defined by a succession of progressively cooler interstadials followed by a particularly warm Dansgaard–Oeschger cycle, show longer-term cooling cycles, lasting on average 10 to 15 ka (Bond et al., 1993). Associated to these longer-term cycles are major episodes of ice rafting, the so-called Heinrich events (Heinrich, 1988; Broecker et al., 1992). They occur during the final stages of the cycles in prolonged cold periods with ice-sheet instability and massive calving. Throughout the last glacial period, six exceptionally large discharges of icebergs (Heinrich events) led to characteristic layers of ice-rafted debris and detrital carbonate, which were recorded in deep-sea sediment cores from the North Atlantic (Heinrich, 1988; Broecker et al., 1992).

Although the key sites for Dansgaard–Oeschger cycles and Heinrich events lie in Greenland and the North Atlantic, there is evidence that both cycles/events have a global signature (e.g. Lowell et al., 1995; Leuschner and Sirocko, 2000; Rahmstorf, 2002; Voelker and workshop participants, 2002). In east Asia, this imprint can be found in few terrestrial climate proxies. Porter and An (1995) and Chen et al. (1997) investigated loess sequences and discovered a correlation between rapid climate events in the North Atlantic and the central and western Chinese loess plateaus, respectively. Similarly, oxygen isotope records of stalagmites from southwestern China resemble the general pattern of oxygen isotope records from Greenland ice cores (Wang et al., 2001; Zhang et al., 2004). However, while Chinese loess profiles and stalagmites suggest a climatic teleconnection between the North Atlantic region and east Asia, such evidence is missing in the Guliya ice core record from the Tibetan Plateau (Thompson et al., 1997). Thus, whether glacial activity on the Tibetan Plateau and its bordering mountains is sensitive to Dansgaard–Oeschger cycles or Heinrich events remains an open question. Tschudi et al. (2003) report a synchronous response of a Tibetan valley glacier to the abrupt climate signal of the Younger Dryas, although previous studies suggested a rather asynchronous behaviour of high Asian glaciers compared to worldwide glacial chronologies (e.g. Gillespie and Molnar, 1995; Benn and Owen, 1998; Phillips et al., 2000; Owen et al., 2001; 2002). According to Benn and Owen (1998) and Shi (2002) glacier fluctuations in the Himalayan region are controlled by variations in the south Asian monsoon and the mid-latitude westerlies. Owen et al. (2005) support this view and associate the corresponding cooling to Heinrich events. Nevertheless, only few absolutely dated glacial records document an ice build-up around the youngest Heinrich event (H1, ~16 ka) in the broad Himalayan–Tibetan region (Schäfer et al., 2002; Finkel et al., 2003; Owen et al., 2003a; 2003b; 2005; Schaefer et



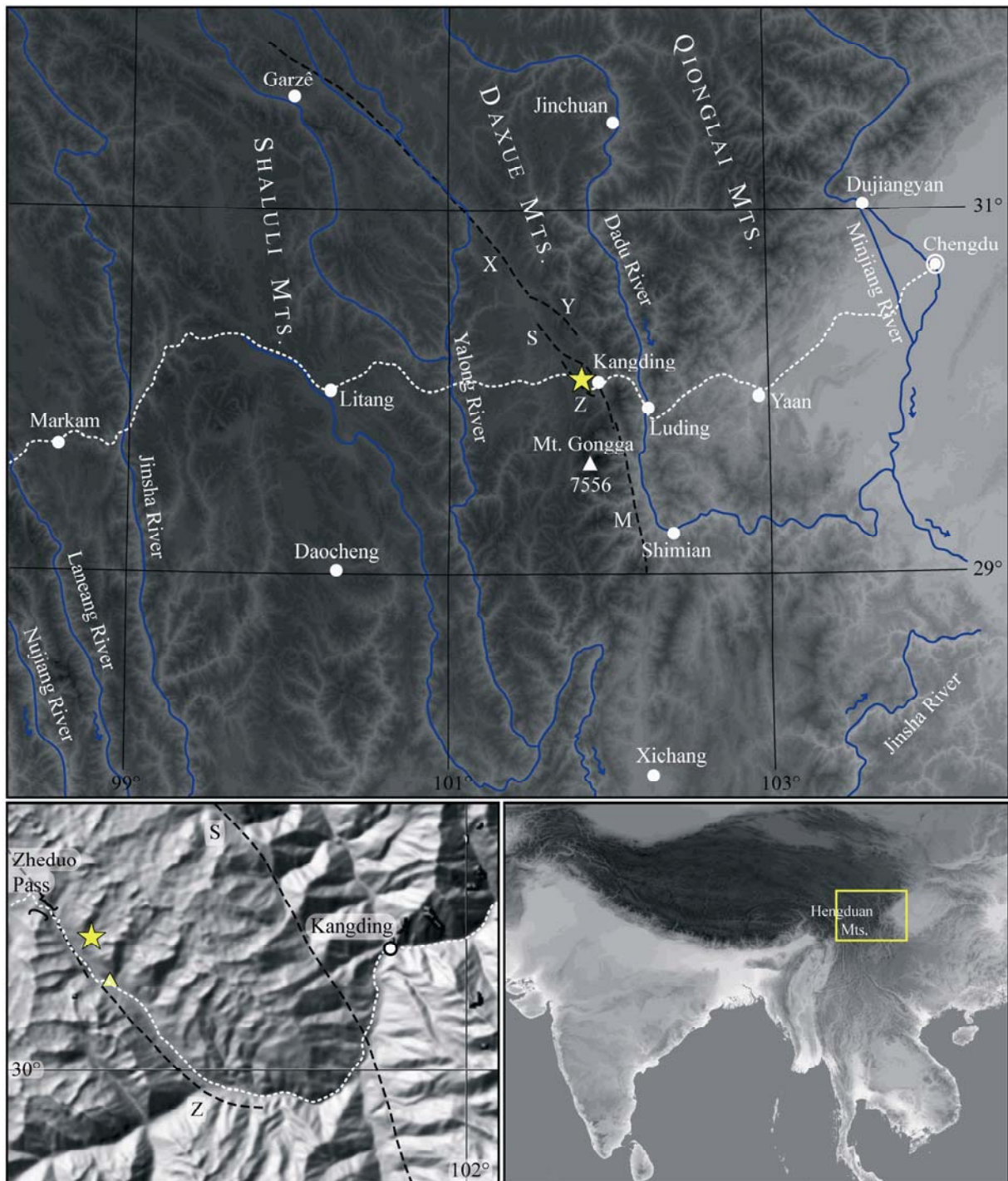


**Fig. 4.9.** Overview map of the eastern Hengduan Mountains showing major rivers and cities. The inset at the lower right locates the geographic setting within southeast Asia. In the lower left is a DEM of the Kangding area, showing Zheduo valley. The light dotted line marks the Sichuan-Tibet highway and the asterisks in the upper and lower left pictures indicate the study area. The dark broken lines represent the five segments of the Xianshuihe fault zone (after Allen et al., 1991): X = restricted Xianshuihe fault, Y = Yalahe fault, S = Selaha (Kangding) fault, Z = Zheduo tang fault, M = Moxi fault. The triangle in the DEM locates the southernmost till outcrop described in the text. Source: SRTM 30 and SRTM 90.

al., 2008). In this study we present surface exposure ages from a highly glaciated valley at the eastern margin of the Tibetan Plateau, with evidence for an ice advance during H1. The field area lies within the valley system investigated by Tschudi et al. (2003) and was found to be suitable to check glacial response to abrupt climate change (Tschudi et al., 2003). Thus by adding new data and revising the published exposure ages of Tschudi et al. (2003) we supply another piece of information needed to complete the picture of how east Asian glaciers reacted to Late Glacial abrupt climate changes.

### 4.3.2 Study area

The study area is located near Kangding in the Daxue Mountains (Fig. 4.9). This NNW–SSE striking mountain range is part of the Hengduan Mountains, making up the eastern margin of the Qinghai-Tibetan Plateau. Mountains reach elevations well over 4000 m above sea level (a.s.l.), with summits exceeding 6000 m a.s.l. The highest peak in the Hengduan Mountains is Gongga Mountain (Minya Gongkar, 7556 m a.s.l.), south of Kangding. An early survey and mapping of the area was carried out by Imhof (1974) and his expedition team. The climate of the region is relatively warm and humid, strongly influenced by the southwest monsoon that provides most of the annual precipitation of typically more than 1000 mm (Shi, 2002). Contemporary glaciers only exist around the highest summits, and permanent snow occurs above 4500 m a.s.l.

The city of Kangding marks the gateway to Tibet. It is nestled in a steep river valley at 2610 m a.s.l., on the southern route of the Sichuan-Tibet highway (Chengdu–Lhasa). The mean annual temperature in Kangding is 7.8 °C and annual precipitation is 810 mm, 64 % of which fall in the summer season from June to September (Vose et al., 1992). From Kangding the Sichuan-Tibet highway continues westwards in a valley along a river towards Zheduo Pass (Fig. 4.9). In the following, Zheduo valley refers to this main valley between Kangding and Zheduo Pass. The surrounding mountains in this area generally consist of biotite-muscovite granite that intruded 16–13 Ma ago (Roger et al., 1995). Tectonically important is the Zheduo fault, running through the Zheduo Valley (Fig. 4.9). It is one of five segments of the Xianshuihe fault zone, which is one of the most active fault systems in the world (Allen et al., 1991). Quaternary sediments, such as till, slope deposits and periglacially reactivated tills, dominate the landscape in the upper part of Zheduo valley. The southernmost till outcrop found along the Sichuan-Tibet highway (Fig. 4.9; 30°02.45'N, 101°50.17'E) shows glacial till

with sheared clasts and distorted shales. This is evidence that a considerable valley glacier occupied at least the upper part of Zheduo valley during the last glaciation. However, the till outcrop indicates only a minimum ice extent, the real ice front during the last glacial maximum reached most likely further down-valley. How far is not obvious; but from the geomorphological situation we believe that the ice front didn't reach as far as 30°00'N and therefore was in-between the till outcrop and the latitude of 30°N.

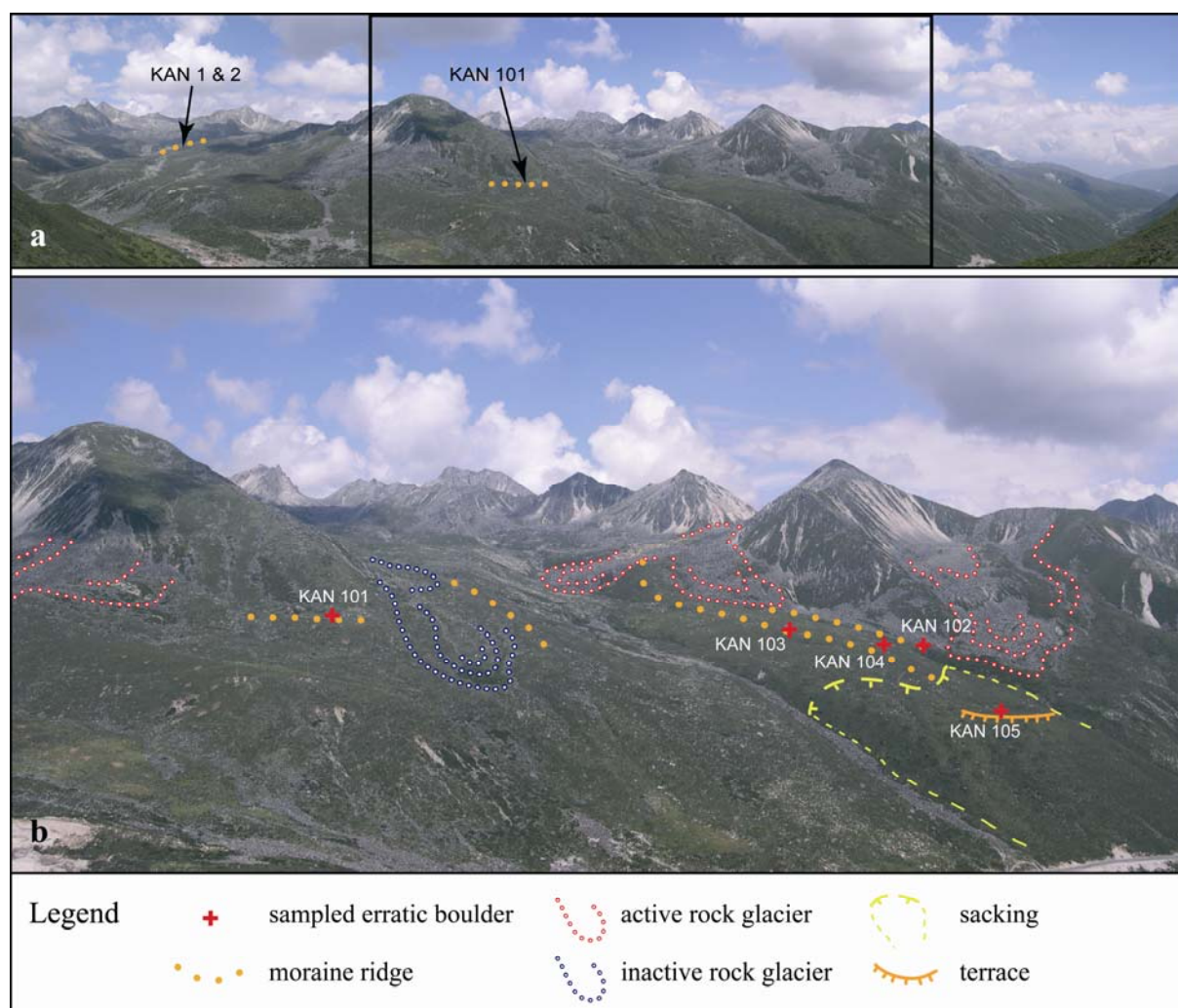


**Fig. 4.10. a.** Panorama picture of Zheduo valley (view northeast) with sampling sites of KAN 1 & 2 (Tschudi et al., 2003) and KAN 101 (this study) for comparison. KAN 1 & 2 are higher elevated than KAN 101, the differences in altitude are 171 and 191 m, respectively. The box shows location of **b.**, the region of this study. Schematic representation of geomorphological features in the study area and sample positions. Note the road (Sichuan-Tibet highway) in the lower right of the picture for scale.

In the uppermost parts of Zheduo valley, glacial features and morphologies become widespread. This is the area of interest for our study. About two kilometres up-valley from the above-mentioned till outcrop are the sampling sites. They are located between 3990 m and 4070 m a.s.l. in the upper part of the Zheduo valley system (30°03'N, 101°49'E) about 13 km

west of Kangding, where a tributary valley enters the main valley from the left side (Figs. 4.9 and 4.10). No modern glacier exists in the catchment areas as the main surface lies below the current snowline. Several active and inactive rock glaciers as well as moraine ridges characterize the valley morphologies. In addition, distinct periglacial and meltwater processes – most likely active very shortly after deglaciation and during the Younger Dryas – led to substantial surface arrangements, like stone lines, active and inactive periglacial lobes at metre to decametre scales, boulder pavement in depressions and the formation of stone rivers. Under periglacial conditions, such processes are still active, to some extent, today.

### 4.3.3 Cosmogenic nuclide exposure ages

#### *Sampling and sample preparation*

Five erratic boulders were sampled for surface exposure dating with in situ produced cosmogenic nuclides ( $^{10}\text{Be}$  and  $^{21}\text{Ne}$ ). The largest boulders, located in stable positions on moraine ridges, were chosen in order to avoid the possibility of post-depositional overturning. With hammer and chisel we collected for each sample 1.5 to 2 kg of rock material of the erratic boulders' topmost 5 cm to reduce self-shielding. Where possible we sampled the central part of the top surface, as cosmic ray neutrons are more easily lost from near the edges than from the centre of a boulder (Masarik and Wieler, 2003). Shielding from surrounding mountains was determined with an inclinometer for each locality and was used together with the sample thickness to calculate the correction factor, reported in Table 4.4. All collected samples were of similar granitic composition and reflect the characteristic rock type of the area. Locations of all samples are indicated in Fig. 4.10 and specific information is given in Table 4.4.

**Table 4.4.** Site details.

Sample	Latitude (N)	Longitude (E)	Elevation (m a.s.l.)	a-b-c axes <sup>a</sup> (m)	Correction factor
KAN 101	30°03.77'	101°49.28'	4069	3.0–2.0–1.2	0.947
KAN 102	30°03.50'	101°49.67'	4061	5.8–1.7–1.2	0.946
KAN 103	30°03.55'	101°49.58'	4071	3.2–2.0–1.6	0.976
KAN 104	30°03.47'	101°49.55'	4058	10.0–4.0–2.9	0.968
KAN 105	30°03.38'	101°49.42'	3993	6.7–3.3–1.3	0.960

<sup>a</sup> Size of a-b-c axes for whole erratic boulder.

One of the sampled erratic boulders (KAN 101) derives from a left lateral moraine ridge of Zheduo valley, marking an ice contact of the main valley glacier. A continuation of this lateral moraine cannot be found further down-valley. The other erratic blocks are related to palaeoglacial deposits of a local glacier that originated in the tributary valley. KAN 102 is from a very prominent ridge of the outermost left lateral moraine that merges down-slope into a rock glacier (Fig. 4.11a). This distinct morphology might reflect a confluence ridge of the palaeoglacier and the adjacent rock glacier. Post-depositional movements of KAN 102 cannot be ruled out by field evidence. KAN 103 and 104 are very stable boulders from the main left lateral moraine, which is about 100 m broad (Fig. 4.11b). Further down-valley, this moraine ridge is affected by gravitational mass movements. On a small terrace within this instability area (sacking), before the slope drop-off to Zheduo valley, we sampled KAN 105.

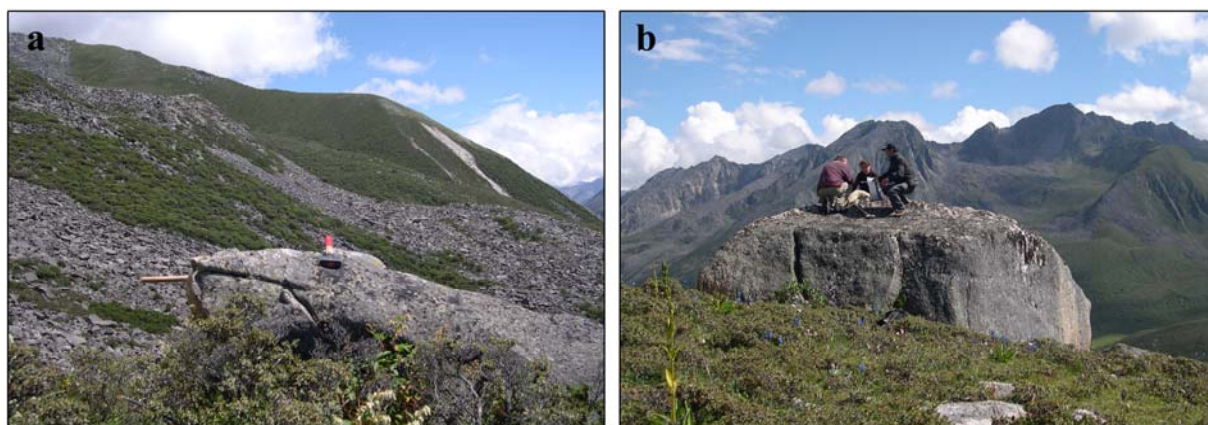


**Fig. 4.11.** Photographs of sampled erratic boulders. **a.** Sample KAN 102 (note the hammer for scale). In the background is the active rock glacier mapped in Fig. 4.10b. **b.** Sampling of KAN 104. With a volume of about  $116 \text{ m}^3$  (above ground) is KAN 104 the largest investigated erratic boulder of the area.

Sample preparation was done at the Institute of Geological Sciences in Bern according to the standard procedure of Kohl and Nishiizumi (1992). A split of each quartz separate was then kept for noble gas analyses, while the rest underwent further procedural steps following Ochs and Ivy-Ochs (1997) for beryllium extraction.

#### *Analyses and exposure age determination*

Radionuclide measurements were carried out at the accelerator mass spectrometry facility of PSI/ETH Zurich (Synal et al., 1997). Noble gas concentrations were measured in 50–60 mg quartz at the noble gas laboratories at ETH Zurich, using a unique non-commercial ultra-high sensitivity mass spectrometer equipped with an inverse molecular-drag pump compressing the

gas into the ion source (Baur, 1999). Samples were degassed at 600, 800, and 1750 °C to separate the cosmogenic from the non-cosmogenic neon components.

Calculations of surface exposure ages were done with CosmoCalc 1.0 (Vermeesch, 2007), using scaling factors according to Dunai (2000), Stone (2000), and Desilets et al. (2006) and default values for all parameters with exception of the attenuation length ( $\lambda$ ) of 157 gram per cm<sup>2</sup> and the average sea level high latitude <sup>10</sup>Be production rate of 5.1 at/g/yr used to calculate exposure ages after Stone's (2000) scaling method. To determine exposure ages based on Lifton et al.'s (2005) scaling model, we used the Microsoft Excel® spreadsheet given by Lifton et al. (2005) and adopted a sea level high latitude production rate in quartz of 5.37 at/g/yr for cosmogenic <sup>10</sup>Be. This production rate was obtained by scaling the reference sample concentrations of Nishiizumi et al. (1989) to sea level high latitudes according to Lifton et al. (2005) and using an exposure time of the reference samples of 13 ka (Clark et al., 1995). At present day, still no consensus exists on using a common set of scaling factors. We used Dunai's (2000) scaling method in this work to discuss our data. The ages calculated by Stone (2000), Lifton et al. (2005), and Desilets et al. (2006) are meant to show the fluctuation range of exposure ages due to varying scaling factors.

Corrections due to sample thickness and geometric shielding are less than six percent. The exact correction factor for each sample is reported in Table 4.4. Shielding of the sampled surface because of intermittent snow cover was neglected in the calculations, as the cold season is relatively dry and temperatures hardly ever drop below 0 °C in the wet season. Tschudi et al. (2003) expect rarely more than 50 cm snow cover in the sampling area. To correct erosion of the rock surface during exposure, we have used an erosion rate of 3 mm ka<sup>-1</sup>. This was found to be a good estimate for rocks of granitic composition in an alpine environment (Ivy-Ochs et al., 2006).

### *Results*

Neon and beryllium isotope data are shown in Table 4.5 and surface exposure ages are given in Table 4.6. All errors reported in the tables are within 1 $\sigma$  confidence levels. They include errors for the variability of chemical processing for the radionuclide, and statistical, sensitivity, and mass-discrimination errors for the noble gas measurements.

**Table 4.5.** Neon and beryllium isotope data.

Sample	Heating Temp. (°C); Time (min)	$^{20}\text{Ne}$	$^{21}\text{Ne}/^{20}\text{Ne}$	$^{22}\text{Ne}/^{20}\text{Ne}$	$^{21}\text{Ne}_{\text{cosmogenic}}$	$^{10}\text{Be}$
		( $10^9$ atoms $\text{g}^{-1}$ )	( $10^{-3}$ )		( $10^6$ atoms $\text{g}^{-1}$ )	( $10^5$ atoms $\text{g}^{-1}$ )
KAN 101	600; 45	$2.20 \pm 0.01$	$4.52 \pm 0.04$	$0.1018 \pm 0.0002$	$3.34 \pm 0.11$	$9.03 \pm 0.38$
	800; 20	$1.00 \pm 0.01$	$3.02 \pm 0.05$	$0.1002 \pm 0.0007$	$0.02 \pm 0.09$	
	1750; 20	$0.87 \pm 0.01$	$2.95 \pm 0.03$	$0.0999 \pm 0.0006$	$-0.04 \pm 0.07$	
KAN 102	600; 45	$7.86 \pm 0.04$	$3.43 \pm 0.02$	$0.1012 \pm 0.0002$	$3.36 \pm 0.31$	$7.59 \pm 0.31$
	800; 20	$1.63 \pm 0.01$	$3.07 \pm 0.02$	$0.1015 \pm 0.0004$	$0.11 \pm 0.06$	
	1750; 20	$1.05 \pm 0.01$	$3.14 \pm 0.04$	$0.1008 \pm 0.0004$	$0.14 \pm 0.10$	
KAN 103	600; 45	$1.43 \pm 0.01$	$4.83 \pm 0.07$	$0.1022 \pm 0.0004$	$2.62 \pm 0.13$	$8.51 \pm 0.38$
	800; 20	$0.76 \pm 0.01$	$2.87 \pm 0.04$	$0.1004 \pm 0.0004$	$-0.10 \pm 0.06$	
	1750; 20	$0.87 \pm 0.01$	$3.00 \pm 0.04$	$0.1000 \pm 0.0005$	$0.00 \pm 0.06$	
KAN 104	600; 45	$2.28 \pm 0.01$	$4.38 \pm 0.04$	$0.1025 \pm 0.0003$	$3.14 \pm 0.12$	$8.26 \pm 0.43$
	800; 20	$0.84 \pm 0.01$	$3.02 \pm 0.04$	$0.1006 \pm 0.0005$	$0.01 \pm 0.08$	
	1750; 20	$0.86 \pm 0.01$	$3.02 \pm 0.02$	$0.1008 \pm 0.0005$	$0.01 \pm 0.03$	
KAN 105	600; 45	$2.29 \pm 0.02$	$4.24 \pm 0.03$	$0.1026 \pm 0.0003$	$2.83 \pm 0.18$	$7.27 \pm 0.36$
	800; 20	$1.04 \pm 0.02$	$2.90 \pm 0.04$	$0.1004 \pm 0.0004$	$-0.10 \pm 0.12$	
	1750; 20	$0.93 \pm 0.01$	$3.04 \pm 0.04$	$0.0998 \pm 0.0004$	$0.03 \pm 0.09$	

The erosion-corrected ( $3 \text{ mm ka}^{-1}$ )  $^{10}\text{Be}$  exposure ages range from  $16.3 \pm 0.7$  to  $13.4 \pm 0.6$  ka. Similarly, surface exposure ages determined with  $^{21}\text{Ne}$  are between  $16.1 \pm 1.5$  and  $12.0 \pm 0.6$  ka. The noble gas data are in accordance with the radionuclide results, indicating single exposure histories for the sampled erratic boulders.

**Table 4.6.** Beryllium and neon surface exposure ages.

Sample	Dunai Apparent		Dunai $\varepsilon = 3 \text{ mm ka}^{-1}$		Stone $\varepsilon = 3 \text{ mm ka}^{-1}$	Lifton et al. $\varepsilon = 3 \text{ mm ka}^{-1}$	Desilets et al. $\varepsilon = 3 \text{ mm ka}^{-1}$
	$^{10}\text{Be}$ age (ka)	$^{21}\text{Ne}$ age (ka)	$^{10}\text{Be}$ age (ka)	$^{21}\text{Ne}$ age (ka)	$^{10}\text{Be}$ age (ka)	$^{10}\text{Be}$ age (ka)	$^{10}\text{Be}$ age (ka)
KAN 101	$15.7 \pm 0.7$	$15.3 \pm 0.5$	$16.3 \pm 0.7$	$15.9 \pm 0.5$	$16.3 \pm 0.7$	$15.7 \pm 0.7$	$15.4 \pm 0.6$
KAN 102	$13.3 \pm 0.5$	$15.5 \pm 1.5$	$13.7 \pm 0.5$	$16.1 \pm 1.5$	$13.7 \pm 0.5$	$13.4 \pm 0.6$	$13.0 \pm 0.5$
KAN 103	$14.3 \pm 0.6$	$11.7 \pm 0.6$	$14.9 \pm 0.6$	$12.0 \pm 0.6$	$14.9 \pm 0.6$	$14.5 \pm 0.7$	$14.0 \pm 0.6$
KAN 104	$14.1 \pm 0.7$	$14.2 \pm 0.6$	$14.6 \pm 0.7$	$14.7 \pm 0.6$	$14.6 \pm 0.7$	$14.3 \pm 0.7$	$13.8 \pm 0.7$
KAN 105	$13.0 \pm 0.6$	$13.4 \pm 0.8$	$13.4 \pm 0.6$	$13.8 \pm 0.8$	$13.4 \pm 0.6$	$13.2 \pm 0.7$	$12.7 \pm 0.6$

Apparent = no erosion;  $\varepsilon$  = erosion rate; Dunai (2000), Stone (2000), Lifton et al. (2005), Desilets et al. (2006)

However, the noble gas data have to be interpreted carefully, because cosmogenic neon concentrations are close to the detection limit with  $^{21}\text{Ne}/^{20}\text{Ne}$  ratios  $<0.005$  (Fig. 4.12). Furthermore, blank values of the noble gas mass spectrometer differed slightly from atmospheric composition. This is due to solar wind measurements from another experiment that caused a solar wind memory in the system. We corrected this memory effect by determining a composition of non-cosmogenic neon of 0.003002 ( $^{21}\text{Ne}/^{20}\text{Ne}$ ) and 0.100432 ( $^{22}\text{Ne}/^{20}\text{Ne}$ ) from the data points of the 800 and 1750 °C temperature steps, which was then used to calculate the cosmogenic  $^{21}\text{Ne}$  concentrations. Thus, the mixing line towards cosmogenic neon used here is parallel to that determined by Niedermann et al. (1993) but passes through a lower  $^{22}\text{Ne}/^{20}\text{Ne}$  ratio (Fig. 4.12). Although there is substantial agreement between the radionuclide and noble gas data, the neon exposure ages are used here only to rule out major episodes of pre-exposure, while the discussion and conclusions are mainly based on the beryllium exposure ages, which are more accurate in the age range of this study.

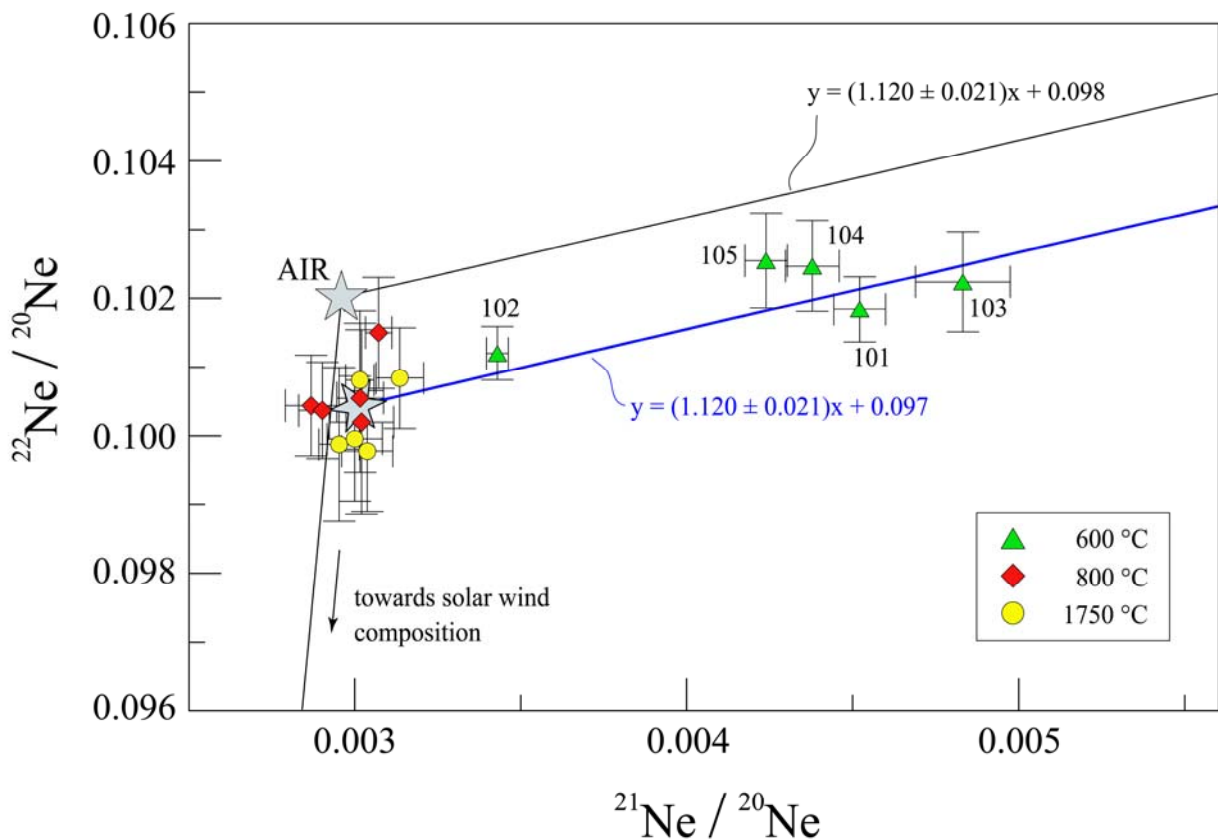


**Fig. 4.12.** Neon three-isotope diagram for KAN samples 101 to 105. The upper line with a positive slope is the atmospheric-cosmogenic mixing line (Niedermann et al., 1993). The lower one is the mixing line corrected for a non-atmospheric neon component (represented by a star, being the average of the 800 and 1750 °C temperature steps). Data points shown in the figure are not blank-corrected.  $^{20}\text{Ne}$  concentrations in blanks were in the same range as in samples. Only the 600 °C temperature steps were used for exposure age determination.



#### 4.3.4 Discussion

The signature of abrupt climate change is found in climate archives around the globe. Is this imprint also visible in the glacial record of a monsoon-dominated area in southeast Tibet? Our data affirm this question, showing evidence of glacier response to short-term cooling during the time period of H1.

As expected from the geomorphological situation, the oldest erratic boulder in the study area (KAN 101) is from the left lateral moraine of the main Zheduo valley glacier with an erosion-corrected exposure age of  $16.3 \pm 0.7$  ka. A similar age was anticipated for KAN 102, the boulder from the stratigraphically oldest preserved moraine in the tributary valley. However, this boulder yields a younger age and seems to have been exposed to cosmic rays for an even shorter time than the two boulders from the main moraine of the local glacier. The controversial age of KAN 102 is probably due to boulder instability that also affected KAN 105. The latter boulder was obviously moved after initial deposition, hence yields a too low cosmogenic nuclide concentration. A reliable age for the main lateral moraine of the local glacier from the tributary valley is obtained from KAN 103 and 104. Erosion-corrected ages are  $14.9 \pm 0.6$  and  $14.6 \pm 0.7$  ka, respectively. These results – together with missing evidence of prominent moraines in the main Zheduo valley – imply that the ice mass of the main Zheduo valley glacier decayed fast after the last glacial maximum and ice masses were reduced to the cirque areas in Late Glacial times, hence, allowing the relatively small glaciers to react to the abruptly cooler climate conditions that characterized the time range between 17 and 15 ka ago (e.g. Hemming, 2004), leading to ice accumulations in the feeder cirques and readvances for a few kilometres with moraine stabilization around 15 ka ago. With the start of the Bølling interstadial, 14.7 ka before present, deglaciation began and the present periglacial landscape evolved. Note that neither different scaling methods (Table 4.6) nor erosion rates of  $10 \text{ mm ka}^{-1}$  (this would shift the age of KAN 103 from  $14.9 \pm 0.6$  to  $16.4 \pm 0.6$  ka) could call into question the above-mentioned scenario. Our finding is thus supporting the view of a synchronous deglaciation after the last glacial maximum and a less extensive Late Glacial advance, at least in the northern hemisphere, as proposed by Schaefer et al. (2006). However, the sensitivity of our record still lacks the precision to allow a direct correlation to one of the short-term (~200-year)  $\delta^{18}\text{O}$  oscillations, observed in the Guliya ice core (Thompson et al., 1997). Nevertheless, surface exposure ages are important as they reflect the maximum stages of glacial climate evolution, which might be difficult to identify in a high-resolution record.

Tschudi et al. (2003) suggest a glacial advance during the Younger Dryas, only about one and a half kilometres main valley upwards from our sampling sites (Fig. 4.10a). But recalculating the data presented by Tschudi et al. (2003) yields  $^{10}\text{Be}$  exposure ages (scaled after Dunai (2000) and corrected for  $3 \text{ mm ka}^{-1}$  erosion) of  $14.2 \pm 0.9$  and  $12.0 \pm 0.8 \text{ ka}$  for KAN 1 and 2, respectively (Fig. 4.13), slightly higher than originally reported and in very good agreement with our results. Since significant pre-exposure or burial periods can be excluded for Tschudi et al.'s (2003) samples, the oldest boulder age, rather than the average age, best represents the moraine's age (Putkonen and Swanson, 2003). Thus we believe that the glacial event dated by Tschudi et al. (2003) does not reflect an advance during the Younger Dryas, but documents the same Late Glacial advance found in this study.

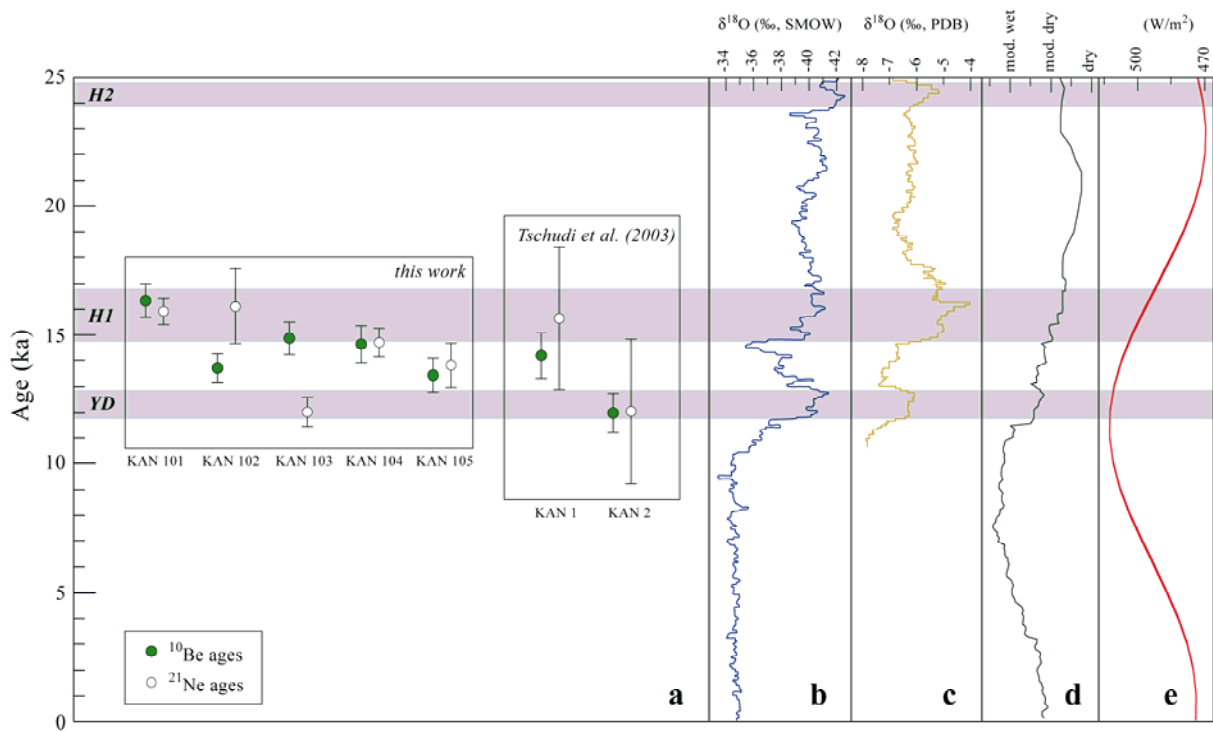


**Fig. 4.13.** Surface exposure ages in comparison with different climate proxies. **a.** Beryllium and neon exposure ages from this work and recalculated data from Tschudi et al. (2003). Presented exposure ages are based on Dunai's (2000) scaling method and an erosion rate of  $3 \text{ mm ka}^{-1}$ . YD = Younger Dryas; H1 = Heinrich event 1; H2 = Heinrich event 2. **b.** Greenland Ice Sheet Project 2 oxygen isotope record (Groottes et al., 1993). **c.**  $\delta^{18}\text{O}$  of Hulu Cave stalagmites (Wang et al., 2001). **d.** Mean effective moisture from the Asian monsoon margin (Herzschuh, 2006). **e.** June insolation at  $30^\circ\text{N}$  (Berger and Loutre, 1991).

During the Younger Dryas cooling event, distinct periglacial surface adjustments probably overprinted glacial morphologies. In particular, post-depositional overturning of erratic boulders and amplified frost wedging are likely for this time period. Unfortunately, these processes can be hardly recognized in the field and sampling of moved and/or frost shattered boulders can lead to falsely young surface exposure ages.

#### **4.3.5 Conclusions**

Surface exposure ages from the Kangding area provide evidence of a glacier advance during the period of Heinrich event 1. After Litang (Schäfer et al., 2002) it is the second site in the Hengduan Mountains where cosmogenic nuclide analyses of erratic boulders reveal a glacial event in this stage of the Late Glacial. Although an abrupt climate signal was recorded in these two locations, far more data is needed for the Hengduan Mountains in order to depict glacial response to H1 cooling in the monsoon-influenced region of southeast Tibet. Only then comparisons between H1 glacial advances from this area and from around the northern hemisphere (e.g. Licciardi et al., 2004; Ivy-Ochs et al., 2006) can be made and climatic implications can be inferred.

When working with in situ produced cosmogenic nuclides, one should be aware of periglacial surface adjustments, which seem to have played a major role during the Younger Dryas. Careful fieldwork and evaluation of potential erratic boulders for surface exposure dating is, therefore, a prerequisite for any meaningful sampling in this region. Nevertheless the promising results from the first studies should encourage future work in this area to check the proposed tight link between North Atlantic and east Asian glacial climate as suggested by Ruth et al. (2007) and to verify the abrupt climate signal of H1 in glacial records of a broader area in southeast Tibet.

**Acknowledgements:** The research on which this article is based was funded by the Swiss National Science Foundation grant number: 200020-105220/1. We gratefully acknowledge this support. Many thanks to the Chinese Academy of Geological Sciences and the Ministry of Geology and Mineral Resources for their support during the field campaign and to two anonymous reviewers for their helpful comments.

## References

- ALLEN, C.R., ZHUOLI, L., HONG, Q., XUEZE, W., HUAWEI, Z. & WEISHI, H. 1991. Field study of a highly active fault zone: The Xianshuihe fault of southwestern China. *Geological Society of America Bulletin*, **103**, 1178–1199.
- BAUR, H. 1999. A Noble-Gas Mass Spectrometer Compressor Source With two Orders of Magnitude Improvement in Sensitivity. *Eos Transactions AGU*, **80**, Abstract V22B-08.
- BENN, D.I. & OWEN, L.A. 1998. The role of the Indian summer monsoon and the mid-latitude westerlies in Himalayan glaciation: review and speculative discussion. *Journal of the Geological Society*, **155**, 353–363.
- BERGER, A. & LOUTRE, M.F. 1991. Insolation values for the climate of the last 10 million years. *Quaternary Science Reviews*, **10**, 297–317.
- BOND, G., BROECKER, W., JOHNSEN, S., MCMANUS, J., LABEYRIE, L., JOUZEL, J. & BONANI, G. 1993. Correlations between climate records from North Atlantic sediments and Greenland ice. *Nature*, **365**, 143–147.
- BOND, G., SHOWERS, W., CHESEBY, M., LOTTI, R., ALMASI, P., DEMENOCAL, P., PRIORE, P., CULLEN, H., HAJDAS, I. & BONANI, G. 1997. A Pervasive Millennial-Scale Cycle in North Atlantic Holocene and Glacial Climates. *Science*, **278**, 1257–1266.
- BROECKER, W., BOND, G., KLAS, M., CLARK, E. & MCMANUS, J. 1992. Origin of the northern Atlantic's Heinrich events. *Climate Dynamics*, **6**, 265–273.
- CHEN, F.H., BLOEMENDAL, J., WANG, J.M., LI, J.J. & OLDFIELD, F. 1997. High-resolution multi-proxy climate records from Chinese loess: evidence for rapid climatic changes over the last 75 kyr. *Palaeogeography, Palaeoclimatology, Palaeoecology*, **130**, 323–335.
- CLARK, D.H., BIERMAN, P.R. & LARSEN, P. 1995. Improving *in Situ* Cosmogenic Chronometers. *Quaternary Research*, **44**, 367–377.
- DANSGAARD, W., JOHNSEN, S.J., CLAUSEN, H.B., DAHL-JENSEN, D., GUNDESTRUP, N.S., HAMMER, C.U., HVIDBERG, C.S., STEFFENSEN, J.P., SVEINBJÖRNSDÓTTIR, A.E., JOUZEL, J. & BOND, G. 1993. Evidence for general instability of past climate from a 250-kyr ice-core record. *Nature*, **364**, 218–220.
- DESILETS, D., ZREDA, M. & PRABU, T. 2006. Extended scaling factors for *in situ* cosmogenic nuclides: New measurements at low latitude. *Earth and Planetary Science Letters*, **246**, 265–276.
- DUNAI, T.J. 2000. Scaling factors for production rates of *in situ* produced cosmogenic nuclides: a critical reevaluation. *Earth and Planetary Science Letters*, **176**, 157–169.
- FINKEL, R.C., OWEN, L.A., BARNARD, P.L. & CAFFEE, M.W. 2003. Beryllium-10 dating of Mount Everest moraines indicates a strong monsoon influence and glacial synchronicity throughout the Himalaya. *Geology*, **31**, 561–564.
- GILLESPIE, A. & MOLNAR, P. 1995. Asynchronous Maximum Advances of Mountain and Continental Glaciers. *Reviews of Geophysics*, **33**, 311–364.

- GROOTES, P.M., STUIVER, M., WHITE, J.W.C., JOHNSEN, S. & JOUZEL, J. 1993. Comparison of oxygen isotope records from the GISP2 and GRIP Greenland ice cores. *Nature*, **366**, 552–554.
- HEINRICH, H. 1988. Origin and Consequences of Cyclic Ice Rafting in the Northeast Atlantic Ocean during the Past 130,000 Years. *Quaternary Research*, **29**, 142–152.
- HEMMING, S.R. 2004. Heinrich events: Massive Late Pleistocene detritus layers of the North Atlantic and their global climate imprint. *Reviews of Geophysics*, **42**, 1–43.
- HERZSCHUH, U. 2006. Palaeo-moisture evolution in monsoonal Central Asia during the last 50,000 years. *Quaternary Science Reviews*, **25**, 163–178.
- IMHOF, E. 1974. *Die Grossen Kalten Berge von Szetschuan: Erlebnisse, Forschungen und Kartierungen im Minya-Konka-Gebirge*. Zurich: Orell Füssli, 227 pp.
- IVY-OCHS, S., KERSCHNER, H., KUBIK, P.W. & SCHLÜCHTER, C. 2006. Glacier response in the European Alps to Heinrich Event 1 cooling: the Gschnitz stadial. *Journal of Quaternary Science*, **21**, 115–130.
- JOHNSEN, S.J., CLAUSEN, H.B., DANSGAARD, W., FUHRER, K., GUNDESTRUP, N., HAMMER, C.U., IVERSEN, P., JOUZEL, J., STAUFFER, B. & STEFFENSEN, J.P. 1992. Irregular glacial interstadials recorded in a new Greenland ice core. *Nature*, **359**, 311–313.
- KOHL, C.P. & NISHIZUMI, K. 1992. Chemical isolation of quartz for measurement of *in-situ*-produced cosmogenic nuclides. *Geochimica et Cosmochimica Acta*, **56**, 3583–3587.
- LEHMAN, S.J. & KEIGWIN, L.D. 1992. Sudden changes in North Atlantic circulation during the last deglaciation. *Nature*, **356**, 757–762.
- LEUSCHNER, D.C. & SIROCKO, F. 2000. The low-latitude monsoon climate during Dansgaard-Oeschger cycles and Heinrich Events. *Quaternary Science Reviews*, **19**, 243–254.
- LICCIARDI, J.M., CLARK, P.U., BROOK, E.J., ELMORE, D. & SHARMA, P. 2004. Variable responses of western U.S. glaciers during the last deglaciation. *Geology*, **32**, 81–84.
- LIFTON, N.A., BIEBER, J.W., CLEM, J.M., DULDIG, M.L., EVENSON, P., HUMBLE, J.E. & PYLE, R. 2005. Addressing solar modulation and long-term uncertainties in scaling secondary cosmic rays for in situ cosmogenic nuclide applications. *Earth and Planetary Science Letters*, **239**, 140–161.
- LOWELL, T.V., HEUSSER, C.J., ANDERSEN, B.G., MORENO, P.I., HAUSER, A., HEUSSER, L.E., SCHLÜCHTER, C., MARCHANT, D.R. & DENTON, G.H. 1995. Interhemispheric Correlation of Late Pleistocene Glacial Events. *Science*, **269**, 1541–1549.
- MASARIK, J. & WIELER, R. 2003. Production rates of cosmogenic nuclides in boulders. *Earth and Planetary Science Letters*, **216**, 201–208.
- NIEDERMANN, S., GRAF, T. & MARTI, K. 1993. Mass spectrometric identification of cosmic-ray-produced neon in terrestrial rocks with multiple neon components. *Earth and Planetary Science Letters*, **118**, 65–73.
- NISHIZUMI, K., WINTERER, E.L., KOHL, C.P., KLEIN, J., MIDDLETON, R., LAL, D. & ARNOLD, J.R. 1989. Cosmic Ray Production Rates of  $^{10}\text{Be}$  and  $^{26}\text{Al}$  in Quartz From Glacially Polished Rocks. *Journal of Geophysical Research B*, **94**, 17907–17915.

- OCHS, M. & IVY-OCHS, S. 1997. The chemical behavior of Be, Al, Fe, Ca and Mg during AMS target preparation from terrestrial silicates modeled with chemical speciation calculations. *Nuclear Instruments and Methods in Physics Research B*, **123**, 235–240.
- OWEN, L.A., GUALTIERI, L., FINKEL, R.C., CAFFEE, M.W., BENN, D.I. & SHARMA, M.C. 2001. Cosmogenic radionuclide dating of glacial landforms in the Lahul Himalaya, northern India: defining the timing of Late Quaternary glaciation. *Journal of Quaternary Science*, **16**, 555–563.
- OWEN, L.A., FINKEL, R.C. & CAFFEE, M.W. 2002. A note on the extent of glaciation throughout the Himalaya during the global Last Glacial Maximum. *Quaternary Science Reviews*, **21**, 147–157.
- OWEN, L.A., HAIZHOU, M., DERBYSHIRE, E., SPENCER, J.Q., BARNARD, P.L., NIAN, Z.Y., FINKEL, R.C. & CAFFEE, M.W. 2003a. The timing and style of Late Quaternary glaciation in the La Ji Mountains, NE Tibet: Evidence for restricted glaciation during the latter part of the last glacial. *Zeitschrift für Geomorphologie*, **130**, 263–276.
- OWEN, L.A., FINKEL, R.C., HAIZHOU, M., SPENCER, J.Y., DERBYSHIRE, E., BARNARD, P.L. & CAFFEE, M.W. 2003b. Timing and style of Late Quaternary glaciation in northeastern Tibet. *Geological Society of America Bulletin*, **115**, 1356–1364.
- OWEN, L.A., FINKEL, R.C., BARNARD, P.L., HAIZHOU, M., ASAHI, K., CAFFEE, M.W. & DERBYSHIRE, E. 2005. Climatic and topographic controls on the style and timing of Late Quaternary glaciation throughout Tibet and the Himalaya defined by <sup>10</sup>Be cosmogenic radionuclide surface exposure dating. *Quaternary Science Reviews*, **24**, 1391–1411.
- PHILLIPS, W.M., SLOAN, V.F., SHRODER JR., J.F., SHARMA, P., CLARKE, M.L. & RENDELL, H.M. 2000. Asynchronous glaciation at Nanga Parbat, northwestern Himalaya Mountains, Pakistan. *Geology*, **28**, 431–434.
- PORTER, S.C. & AN, Z.S. 1995. Correlation between climate events in the North Atlantic and China during the last glaciation. *Nature*, **375**, 305–308.
- PUTKONEN, J. & SWANSON, T. 2003. Accuracy of cosmogenic ages for moraines. *Quaternary Research*, **59**, 255–261.
- RAHMSTORE, S. 2002. Ocean circulation and climate during the past 120,000 years. *Nature*, **419**, 207–214.
- ROGER, F., CALASSOU, S., LANCELOT, J., MALAVIEILLE, J., MATTAUER, M., XU, Z.Q., HAO, Z.W. & HOU, L.W. 1995. Miocene emplacement and deformation of the Konga Shan granite (Xianshui He fault zone, west Sichuan, China): Geodynamic implications. *Earth and Planetary Science Letters*, **130**, 201–216.
- RUTH, U., BIGLER, M., RÖTHLISBERGER, R., SIGGAARD-ANDERSEN, M.-L., KIPFSTUHL, S., GOTO-AZUMA, K., HANSSON, M.E., JOHNSEN, S.J., LU, H.Y. & STEFFENSEN, J.P. 2007. Ice core evidence for a very tight link between North Atlantic and east Asian glacial climate. *Geophysical Research Letters*, **34**, doi:10.1029/2006GL027876.
- SCHAEFER, J.M., DENTON, G.H., BARRELL, D.J.A., IVY-OCHS, S., KUBIK, P.W., ANDERSEN, B.G., PHILLIPS, F.M., LOWELL, T.V. & SCHLÜCHTER, C. 2006. Near-Synchronous Interhemispheric Termination of the Last Glacial Maximum in Mid-Latitudes. *Science*, **312**, 1510–1513.

- SCHAEFER, J.M., OBERHOLZER, P., ZHAO, Z., IVY-OCHS, S., WIELER, R., BAUR, H., KUBIK, P.W. & SCHLÜCHTER, C. 2008. Cosmogenic beryllium-10 and neon-21 dating of late Pleistocene glaciations in Nyalam, monsoonal Himalayas. *Quaternary Science Reviews*, **27**, 295–311.
- SCHÄFER, J.M., TSCHUDI, S., ZHAO, Z., WU, X., IVY-OCHS, S., WIELER, R., BAUR, H., KUBIK, P.W. & SCHLÜCHTER, C. 2002. The limited influence of glaciations in Tibet on global climate over the past 170 000 yr. *Earth and Planetary Science Letters*, **194**, 287–297.
- SHI, Y. 2002. Characteristics of late Quaternary monsoonal glaciation on the Tibetan Plateau and in East Asia. *Quaternary International*, **97/98**, 79–91.
- STONE, J.O. 2000. Air pressure and cosmogenic isotope production. *Journal of Geophysical Research B*, **105**, 23753–23759.
- SYNAL, H.-A., BONANI, G., DÖBELI, M., ENDER, R.M., GARTENMANN, P., KUBIK, P.W., SCHNABEL, C. & SUTER, M. 1997. Status report of the PSI/ETH AMS facility. *Nuclear Instruments and Methods in Physics Research B*, **123**, 62–68.
- THOMPSON, L.G., YAO, T., DAVIS, M.E., HENDERSON, K.A., MOSLEY-THOMPSON, E., LIN, P.-N., BEER, J., SYNAL, H.-A., COLE-DAI, J. & BOLZAN, J.F. 1997. Tropical Climate Instability: The Last Glacial Cycle from a Qinghai-Tibetan Ice Core. *Science*, **276**, 1821–1825.
- TSCHUDI, S., SCHÄFER, J.M., ZHAO, Z., WU, X., IVY-OCHS, S., KUBIK, P.W. & SCHLÜCHTER, C. 2003. Glacial advances in Tibet during the Younger Dryas? Evidence from cosmogenic  $^{10}\text{Be}$ ,  $^{26}\text{Al}$ , and  $^{21}\text{Ne}$ . *Journal of Asian Earth Sciences*, **22**, 301–306.
- VERMEESCH, P. 2007. CosmoCalc: an Excel add-in for cosmogenic nuclide calculations. *Geochemistry, Geophysics, Geosystems*, **8**, doi:10.1029/2006GC001530.
- VOELKER, A.H.L. & WORKSHOP PARTICIPANTS 2002. Global distribution of centennial-scale records for Marine Isotope Stage (MIS) 3: a database. *Quaternary Science Reviews*, **21**, 1185–1212.
- VOSE, R.S., SCHMOYER, R.L., STEURER, P.M., PETERSON, T.C., HEIM, R., KARL, T.R. & EISCHEID, J. 1992. *The Global Historical Climatology Network: long-term monthly temperature, precipitation, sea level pressure, and station pressure data*. Carbon Dioxide Information Analysis Center, Oak Ridge National Laboratory, ORNL/CDIAC-53, NDP-041, pp. 1–325 [Also available online at: <http://iridl.ldeo.columbia.edu/SOURCES/.NOAA/.NCDC/.GHCN/>].
- WANG, Y.J., CHENG, H., EDWARDS, R.L., AN, Z.S., WU, J.Y., SHEN, C.-C. & DORALE, J.A. 2001. A High-Resolution Absolute-Dated Late Pleistocene Monsoon Record from Hulu Cave, China. *Science*, **294**, 2345–2348.
- ZHANG, M.L., CHENG, H., YUAN, D.X., LIN, Y.S., QIN, J.M., WANG, H., FENG, Y.M., TU, L.L. & ZHANG, H.L. 2004. High-resolution climate records from two stalagmites in Qixin Cave, southern Guizhou, and Heinrich events during the last glacial period. *Episodes*, **27**, 112–118.





## 5 EUROPE

### 5.1 Introduction

---

Europe plays a historical role in Quaternary glacial geology. It's the place of birth of the ice age theory and location of many pioneer studies in Quaternary sciences. De Saussure (1779) was the first who wondered about the presence of large granitic boulders in the valleys: "Les granites ne se forment pas dans la terre comme des truffes, et ne croissent pas comme des sapins sur les roches calcaires". However, de Saussure (1779) related the erratic boulders to the diluvium and did not consider anything else than liquid water as transport medium to explain their position in the landscape. It was at the beginning of the nineteenth century when Jean-Pierre Perraudin recognized the glacial origin of the erratic boulders and concluded that glacier extent in the Valais (Switzerland) must have been much larger during earlier times. Ignaz Venetz and Jean de Charpentier continued the work of Perraudin and collected evidence of a former glaciation throughout the Rhône Valley up to the Jura mountains (de Charpentier, 1841). Although Agassiz held his famous "Discours sur les glaciers" already in 1837 and published his article before de Charpentier (Agassiz, 1840), he is not considered as the founder of the ice age theory, as his work was mainly based on observations and studies from others. Therefore, Venetz and de Charpentier are regarded as the real founders of the glacial theory in the Alps.

The next major advance in glacial geology was the establishment of relative stratigraphies of different glacial episodes and the description of the "glaciale Serie" (Penck and Brückner, 1909). The original four glaciations recognized by Penck and Brückner (1909) were later expanded to seven glaciations (e.g. Schaefer, 1953) in the type area of the Iller-Lech Platte, southern Germany. In the northern alpine foreland of Switzerland Schlüchter and Kelly (2000) found evidence of at least 15 individual ice advances. Although a lot of work was carried out in the twentieth century and a unique density of Quaternary data is available for Europe (Ehlers and Gibbard, 2004), correlation of individual units from one site to another is still contentious (e.g. Litt, 2007). This is mainly due to the lack of absolute chronologies. With the exception of the last glacial maximum and subsequent late glacial ice fluctuations (e.g. Tschudi et al., 2000; Preusser, 2004; Ivy-Ochs et al., 2006b; Rinterknecht et al., 2006) the time structure of former Quaternary glaciations remains largely unknown. Of particular

interest is the timing of the most extensive glaciation (Schlüchter, 2004), the Riss Glaciation sensu Penck and Brückner (1909).

So far two studies have dated erratic boulders from the most extensive glaciation with cosmogenic nuclides, but each one was limited to only one single boulder (Oberholzer, 2004; Ivy-Ochs et al., 2006a). In this chapter surface exposure ages of additional erratic boulders attributed to the most extensive glaciation in Europe are presented. In section 5.2 the maximum extent of the Fennoscandian Ice Sheet in Northern Germany was investigated by re-dating the boulder analysed by Oberholzer (2004) and further determining a surface exposure age for a sister-boulder. A similar approach was used to date the most extensive alpine glaciation in section 5.3, where cosmogenic nuclide ages of erratic boulders from the southernmost chain of the Swiss Jura Mountains confirm the published exposure age by Ivy-Ochs et al. (2006a) and enlarge the number of numerical datings.

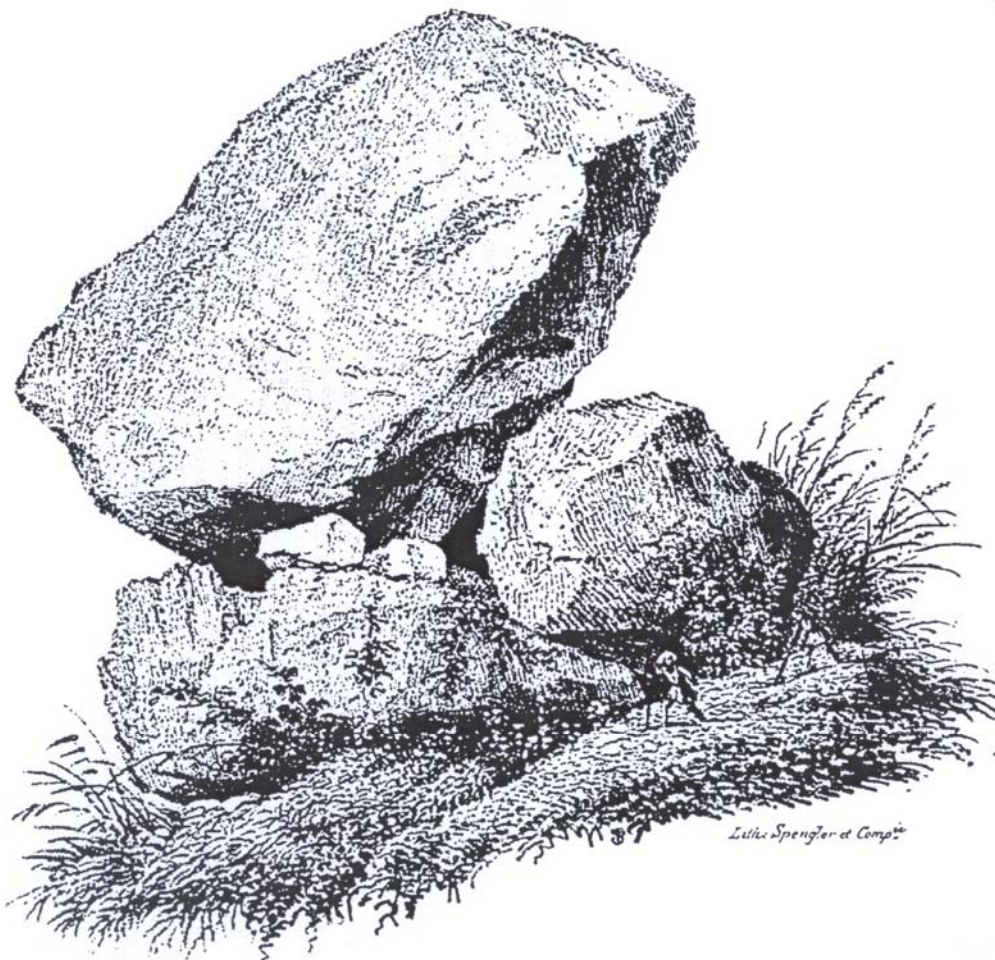


**Fig. 5.1.** Pierre à Dzo (from de Charpentier, 1841). Perched erratic boulder in the area of Monthey, Valais.

## 5.2 Oberflächenalter zweier Findlinge aus Niedersachsen – Zeugen einer alten fennoskandischen Vergletscherung in Norddeutschland <sup>e</sup>

### Surface exposure dating of two erratic boulders from Niedersachsen – evidence of an old Fennoscandian Ice Sheet advance in Northern Germany

Stefan Strasky <sup>1\*</sup>, Peter Oberholzer <sup>1</sup>, Klaus-Dieter Meyer <sup>2</sup>, Heinrich Baur <sup>1</sup>, Susan Ivy-Ochs <sup>3</sup>, Peter W. Kubik <sup>4</sup>, Rainer Wieler <sup>1</sup> and Christian Schlüchter <sup>5</sup>

<sup>1</sup> *Institut für Isotopengeologie und Mineralische Rohstoffe, ETH Zürich, 8092 Zürich, Schweiz*

<sup>2</sup> *Engenser Weg 5, 30938 Burgwedel, Deutschland (vormals Niedersächsisches Landesamt für Bodenforschung, 30631 Hannover, Deutschland)*

<sup>3</sup> *Geographisches Institut, Universität Zürich, 8057 Zürich, Schweiz*

<sup>4</sup> *Paul Scherrer Institut, c/o Institut für Teilchenphysik, ETH Zürich, 8093 Zürich, Schweiz*

<sup>5</sup> *Institut für Geologie, Universität Bern, 3012 Bern, Schweiz*

\* *corresponding author: stefan.strasky@gmail.com*

**Abstract:** Major advances of the Fennoscandian Ice Sheet reached at least three times as far south as Northern Germany during the Pleistocene. While the extent of Fennoscandian ice in northern Europe is fairly well mapped, the exact timing remains contentious. This study tries to shed light onto the time structure of the Fennoscandian Ice Sheet advances into Northern Germany with surface exposure dating by cosmogenic nuclides (<sup>21</sup>Ne und <sup>10</sup>Be). Two erratic boulders were sampled in Niedersachsen: The Giebichenstein and an erratic boulder from Ventschau. Both are beyond the Weichselian, the erratic from Ventschau is located on a younger Saalian (Warthe) surface and the Giebichenstein lies on an older Saalian (Drenthe) basal lodgement till surface. The minimum exposure ages for the Giebichenstein and the erratic boulder from Ventschau are 103'000±8'000 years and 193'000±32'000 years, respectively. Therefore the erratic boulders were most probably deposited in a Fennoscandian ice advance during marine isotope stage 6.

**Key words:** surface exposure dating, cosmogenic nuclides, glacial erratic boulder

<sup>e</sup> Published in *Archiv für Geschichtskunde*, 5 (2006), 283–292

**Zusammenfassung:** Der fennoskandische Eisschild stiess während des Pleistozän mindestens dreimal bis in den Norden Deutschlands vor und bedeckte grosse Gebiete mit mächtigen Eismassen. Während die räumliche Ausdehnung des fennoskandischen Eises in Nordeuropa gut dokumentiert ist, herrscht über den absoluten zeitlichen Ablauf Ungewissheit. Die vorliegende Arbeit versucht anhand von Oberflächendatierungen mit kosmogenen Nukliden ( $^{21}\text{Ne}$  und  $^{10}\text{Be}$ ) zu einem besseren Verständnis der Glazial-Chronologie Norddeutschlands beizutragen. Beprobte worden sind zwei Findlinge aus Niedersachsen: der Giebichenstein und der Findling von Ventschau. Die erratischen Blöcke befinden sich ausserhalb der letzteiszeitlichen Weichsel-Vergletscherung; der Findling von Ventschau liegt innerhalb des Warthe-Stadiums, der Giebichenstein auf einer Drenthe-zeitlichen Grundmoränenfläche. Die minimalen Oberflächenalter betragen für den Giebichenstein  $103'000 \pm 8'000$  Jahre, für den Ventschau-Findling  $193'000 \pm 32'000$  Jahre. Angesichts dessen sind die Findlinge vermutlich von einem Eisvorstoss abgelagert worden, der in das marine Isotopen-Stadium 6 zu stellen ist.

**Schlüsselwörter:** Oberflächendatierung, kosmogene Nuklide, Findling, Grossgeschiebe, Bl. der TK 25 (3321 Nienburg, 2731 Neuhaus/Elbe)

### 5.2.1 Einführung

Eine der grössten Inlandeismassen der Welt bedeckte während des Pleistozän mehrere Male riesige Gebiete von Nord-Eurasien. Eis, das sich über dem fennoskandischen Festland gebildet hatte, floss in den Kaltzeiten radial nach aussen und stiess bis in den Norden Deutschlands vor. Bei der Maximalausdehnung erreichte der Rand des fennoskandischen Eisschildes in Deutschland den 51. nördlichen Breitengrad. Niedersachsen und Sachsen-Anhalt waren fast gänzlich von Eis bedeckt, Nordrhein-Westfalen und Sachsen ungefähr zur Hälfte. Spuren dieser grössten nordischen Vergletscherung – und auch der kleineren Eisvorstösse aus Fennoskandia – finden sich in glazialen und fluvioglazialen Ablagerungen wie Moränen, Findlingen und Sandern wieder. Detaillierte Untersuchungen dieser eiszeitlichen Zeugen und Befunde in marinen Sedimenten ermöglichten die Rekonstruktion der Eisrandpositionen des fennoskandischen Eisschildes (Ehlers et al., 2004; Svendsen et al., 2004). In Nordwest-Europa sind heute drei Hauptvereisungsphasen bekannt; in der relativen Chronologie von der Ältesten zur Jüngsten sind dies die Elster-, die Saale- und die Weichsel-Vereisung. Die Saale-Vereisung wird in Norddeutschland in einen älteren (Drenthe) und einen jüngeren (Warthe) Eisvorstoss unterteilt (Woldstedt, 1954; Lüttig, 1958; Eissmann, 1975). Während die räumliche Aus-

dehnung der einzelnen Vereisungen sowohl für die letzteiszeitliche Weichsel-Vergletscherung als auch für die beiden älteren Glaziale gut dokumentiert ist, bleibt der absolute zeitliche Ablauf umstritten (Geyh und Müller, 2005). Abgesehen von wenigen Altersbestimmungen für die Weichsel-Vereisung gibt es keine gesicherten Datierungen der pleistozänen nordischen Vereisungen.

In der vorliegenden Arbeit wird versucht, einen ersten Schritt in die absolute zeitliche Dimension der oszillierenden fennoskandischen Eismassen vor der letzten Vereisung vorzudringen. Wir präsentieren hierzu Oberflächenaltersbestimmungen mit kosmogenen Nukliden ( $^{21}\text{Ne}$  und  $^{10}\text{Be}$ ) zweier Findlinge, dem Giebichenstein bei Stöckse und dem Findling von Ventschau. Beide erratischen Blöcke liegen in Niedersachsen, ausserhalb des letzteiszeitlichen Maximums des Weichsel-Eisvorstosses (Abb. 5.2).

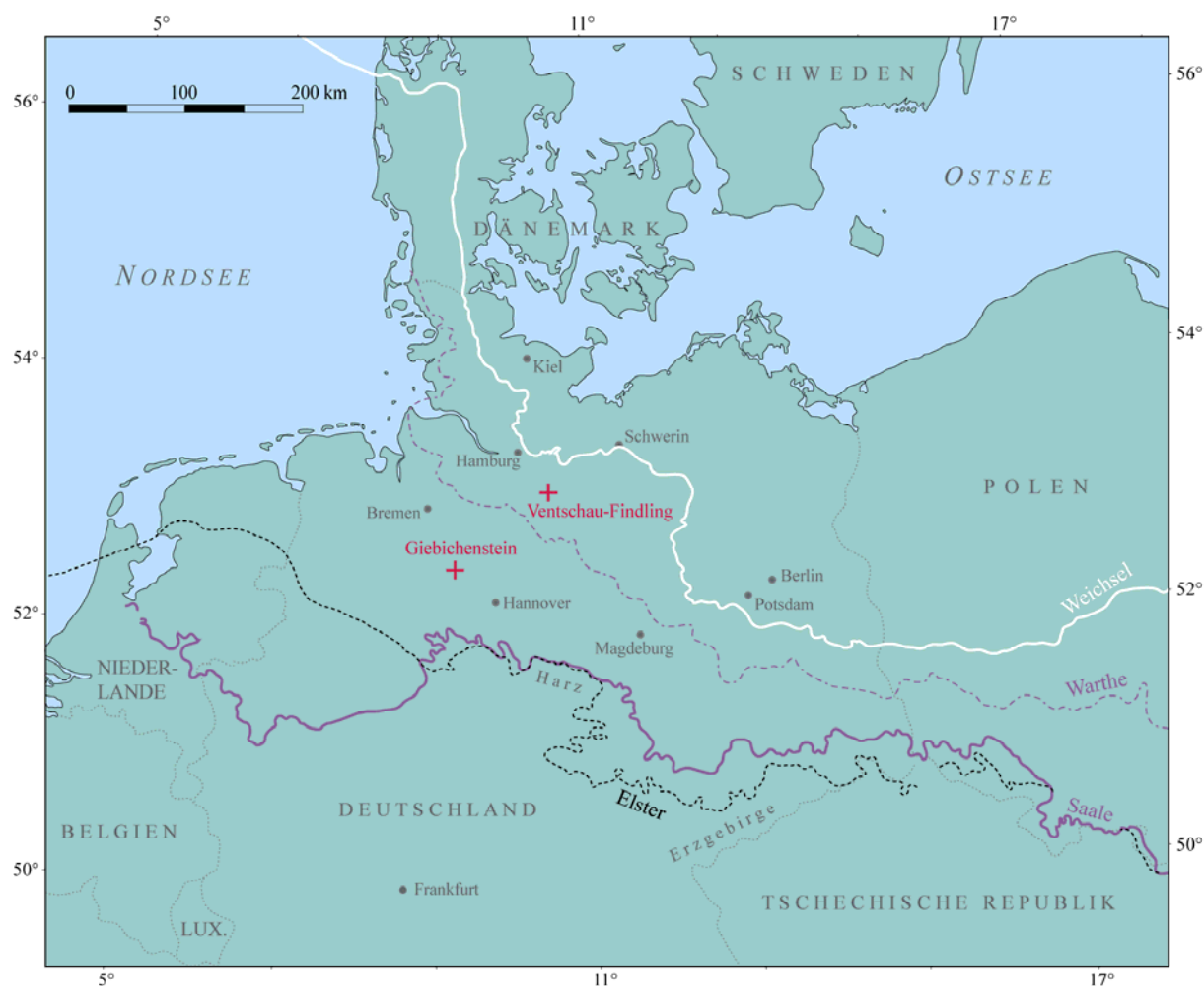


**Abb. 5.2.** Maximale Eisrandpositionen des fennoskandischen Eisschildes: Ausgezogene Linien zeigen die Eisränder der Weichsel- beziehungsweise der Saale-Vereisung, gestrichelte Linien diejenigen der Warthe- und der Elster-Vergletscherung (nach Ehlers et al., 2004). Kreuze markieren die Probenlokalitäten.

### 5.2.2 Probenlokalitäten und Probennahme

**A** - Der Giebichenstein ist mit 7.5 m Länge, 4.5 m Breite und 2.75 m Höhe der grösste Findling Niedersachsens (Abb. 5.3). Er befindet sich im Staatsforst auf einer Höhe von 50 m ü.M., südwestlich der Gemeinde Stöckse, im Osten von Nienburg ( $52^{\circ}38'N$ ,  $9^{\circ}19'E$ , Bl. 3321 Nienburg der TK 25). Nach Meyer (1999) liegt der Giebichenstein auf einer Drenthe-zeitlichen Grundmoränenfläche. Die Basis des grössten Erratikers Niedersachsens befindet sich 0.9–0.95 m unter Waldboden. Prähistorische Funde von Feuersteingeräten aus dem Jungpaläolithikum an der Sohle des Giebichensteins lassen darauf schliessen, dass der Findling vor 13'000 Jahren bis zu seiner Grundfläche freigelegt haben muss (Nowothnig, 1979).



Abb. 5.3. Probennahme am Giebichenstein.



Abb. 5.4. Findling von Ventschau.

**B** - Ungefähr 110 km in nordöstlicher Richtung vom Giebichenstein entfernt, nördlich von Ventschau, befindet sich der erratische Block von Ventschau ( $53^{\circ}12'N$ ,  $10^{\circ}51'E$ , Bl. 2731 Neuhaus a. d. Elbe der TK 25). Dieser Findling liegt innerhalb des Verbreitungsgebietes des Warthe-Stadiums. Er ist 4 m lang, 3 m breit und 3 m hoch und kaum im Boden eingebettet (Meyer, 1999). Wie der Giebichenstein liegt der Erratiker von Ventschau heute in einem mitteldichten Laubwald auf 50 m ü.M. (Abb. 5.4).

Für Oberflächenaltersbestimmungen wurden Gesteinsproben dem Giebichenstein (GIE) und dem Findling von Ventschau (VEN) entnommen. Mit Hammer und Meissel wurden an der höchsten Stelle der Blöcke die obersten zwei bis fünf Zentimeter beprobt. Beim Giebichenstein lassen Bohrlöcher an der Findlingsoberfläche erkennen, dass in historischer Zeit versucht worden war, den Gesteinsblock zum Zweck der Rohstoffgewinnung zu sprengen (Nowothnig, 1979). Die Probe GIE stammt aber von einer alten intakten Oberfläche, die keine

künstliche Spaltfläche ist (Abb. 5.3). Die Gesteinszusammensetzungen der Findlinge sind ähnlich. Quarz und Feldspat sind die dominanten Phasen, der Hauptunterschied liegt im Glimmeranteil. Während der Block von Ventschau einen bedeutenden Dunkelglimmeranteil aufweist (Biotit führender Granit), ist im Giebichenstein nur ein geringer Anteil Hellglimmer vorhanden. Die granitische Zusammensetzung des Giebichensteins ist zudem leicht metamorph überprägt worden, weshalb von einem Gneisgranit gesprochen werden kann (Meyer, 1999).

### 5.2.3 Die Methode der Oberflächenaltersbestimmung mit kosmogenen Nukliden

Die Oberflächenaltersbestimmung mit in situ produzierten terrestrischen kosmogenen Nukliden ist eine Methode, die seit 20 Jahren erfolgreich in diversen erdwissenschaftlichen Gebieten angewendet wird. Absolute Datierungen quartärer Vergletscherungen ausserhalb des Radiokarbonbereiches ( $>40'000$  J.) sind erst dank der Oberflächenaltersbestimmungsmethode möglich geworden. Die Methode basiert auf der Messung der Konzentration von Nukliden, die durch die kosmische Strahlung in gewissen Mineralien (beispielsweise Quarz) in Oberflächengesteinen produziert werden. Daraus ergibt sich ein Alter, das aussagt, wie lange eine Fläche der kosmischen Strahlung ausgesetzt gewesen ist. Im Fall eines Findlings wird damit der Moment des Ausschmelzens aus dem Eis datiert. Theorie und Anwendung der Oberflächenaltersbestimmung mit kosmogenen Nukliden sind in den neusten Reviews von Gosse und Phillips (2001) und Niedermann (2002) ausführlich beschrieben.

Die erratischen Blöcke aus Norddeutschland wurden auf das kosmogene Edelgas  $^{21}\text{Ne}$  und das Radionuklid  $^{10}\text{Be}$  untersucht; die  $^{10}\text{Be}$ -Analyse für den Findling von Ventschau ist noch ausstehend. Alle Messungen fanden an hochreinen Quarz-Separaten statt, die für VEN durch physikalische Methoden (Dichtentrennung, Magnetseparation, Auslese von Hand), für GIE mittels selektiver chemischer Auflösung nach Kohl und Nishiizumi (1992) aus dem Gesamtgestein gewonnen wurden. Die Beryllium-Extraktion folgte dem Standardverfahren von Ochs und Ivy-Ochs (1997); die  $^{10}\text{Be}/^9\text{Be}$ -Verhältnisse wurden nach Synal et al. (1997) und mittels Beschleuniger-Massenspektrometrie an der ETH/PSI Tandem-Beschleuniger-Anlage in Zürich gemessen.

Die Edelgas-Messungen erfolgten an zirka 60 mg Quarz (Korngrösse  $<100\ \mu\text{m}$ ) in einem nicht-kommerziellen, ultra-hoch empfindlichen Edelgasmassenspektrometer ausgestattet mit

einer Kompressor-Quelle (Baur, 1999) am Institut für Isotopengeologie und Mineralische Rohstoffe der ETH Zürich. Zur Unterscheidung des kosmogenen vom nicht-kosmogenen Neon wurden die Edelgase in unterschiedlichen Temperaturschritten extrahiert. Im Idealfall können auf diese Weise drei verschiedene Arten von Neon voneinander getrennt werden: das kosmogene, das eingefangene und das nukleogene Neon. Nach Niedermann et al. (1993) entgast kosmogenes Neon bei niedrigeren Temperaturen (90 % bis 600 °C) als eingefangenes Neon, das bei der Gesteinsbildung (meist in Form von Einschlüssen) eingebaut worden ist. Dennoch kann das bei der Gesteinsgenese eingefangene Neon nicht immer eindeutig durch stufenweises Entgasen vom kosmogenen getrennt werden, da sich der Temperaturbereich zur Freisetzung von eingefangenen Neon (450–800 °C) mit jenem des kosmogenen Neons überschneidet. Unter der Annahme, dass die eingefangene Neon-Komponente eine atmosphärische Neon-Zusammensetzung aufweist, kann das kosmogene Neon trotzdem für den eingefangenen Neon-Anteil korrigiert werden. Die Freisetzung von nukleogenem Neon (Neon, das durch Kernreaktionen mit  $\alpha$ -Teilchen oder Neutronen aus radioaktivem Zerfall beziehungsweise aus spontanen Spaltreaktionen hervorgeht) kann nach Niedermann et al. (1994) bereits bei Temperaturen bis 600 °C erfolgen, aber unter Umständen auch erst bei höheren Temperaturen ( $>800$  °C). Erste Messungen für den Giebichenstein zeigten ein unklares Entgasungsmuster (Oberholzer, 2004). Aufgrund der Befunde in Oberholzer (2004) erweiterten wir die Edelgas-Extraktion auf fünf Temperaturschritte (400, 600, 800, 1000 und 1750 °C).

Zur Berechnung der Oberflächenalter wurden Produktionsraten in Quarz für Meereshöhe und hohe Breitengrade von 5.1 Atomen pro Gramm pro Jahr für  $^{10}\text{Be}$  (Stone, 2000) und von 20.3 Atomen pro Gramm pro Jahr für  $^{21}\text{Ne}$  (Niedermann, 2000) verwendet. Die Skalierung der Produktionsraten auf die geographische Breite und Höhe der Probenlokalitäten erfolgte nach Stone (2000). Abschirmungskorrekturen für die Umgebungstopographie mussten keine gemacht werden; einzig für die Probe VEN, die eine Oberflächenneigung von 42° aufwies, wurde ein Korrekturfaktor für die Eigenabschirmung von 0.9357 nach Dunne et al. (1999) berechnet. Die Abschirmung durch die Vegetation wird für beide Probenlokalitäten als vernachlässigbar erachtet, weil während eines Grossteils der Liegezeiten der Findlinge das Baumwachstum eingeschränkt war und die Landschaft einer Grassteppe mit spärlichem Baumbestand glich. Korrekturen für Veränderungen der paläomagnetischen Intensität wurden keine gemacht.



### 5.2.4 Resultate

Die Neon-Daten des Giebichensteins und des Findlings von Ventschau sind in Tabelle 5.1, die für die Altersbestimmung relevanten Nuklid-Konzentrationen und die  $^{21}\text{Ne}$ - und  $^{10}\text{Be}$ -Oberflächenalter in Tabelle 5.2 dargestellt. Messunsicherheiten sind für alle Messwerte mit  $2\sigma$ -Fehlern angegeben. Die Fehlerangaben der Beryllium-Daten beinhalten eine Schwankung von fünf Prozent in der chemischen Probenaufbereitung (Ivy-Ochs, 1996). In den Neon-Messunsicherheiten sind statistische Fehler, Empfindlichkeits- und Massendiskriminierungsfehler enthalten.

**Tabelle 5.1.** Neon-Isotopen-Daten.

Probe	Heiz- Temperatur (°C); Dauer (min)	$^{20}\text{Ne}$ ( $10^9$ Atome $\text{g}^{-1}$ )	$^{21}\text{Ne}/^{20}\text{Ne}$ ( $10^{-3}$ )	$^{22}\text{Ne}/^{20}\text{Ne}$
GIE	400; 45	$1.32 \pm 0.04$	$8.80 \pm 0.27$	$0.1030 \pm 0.0027$
GIE	600; 45	$1.47 \pm 0.07$	$8.62 \pm 0.40$	$0.1056 \pm 0.0024$
GIE	800; 30	$1.11 \pm 0.03$	$3.20 \pm 0.24$	$0.0997 \pm 0.0036$
GIE	1000; 30	$0.69 \pm 0.25$	$3.51 \pm 0.15$	$0.1020 \pm 0.0042$
GIE	1750; 15	$0.75 \pm 0.26$	$4.74 \pm 0.17$	$0.1034 \pm 0.0030$
VEN	400; 45	$1.53 \pm 0.02$	$3.34 \pm 0.25$	$0.1019 \pm 0.0020$
VEN	600; 45	$6.28 \pm 0.06$	$3.96 \pm 0.07$	$0.1041 \pm 0.0011$
VEN	800; 30	$3.19 \pm 0.04$	$3.30 \pm 0.10$	$0.1038 \pm 0.0014$
VEN	1000; 30	$0.99 \pm 0.02$	$3.25 \pm 0.16$	$0.1031 \pm 0.0027$
VEN	1750; 15	$1.14 \pm 0.02$	$3.45 \pm 0.19$	$0.1022 \pm 0.0024$

GIE = Giebichenstein bei Stöckse; VEN = Findling von Ventschau.

Der Unterschied zwischen dem Radionuklid- und dem Edelgasoberflächenalter des Giebichensteins ist sehr gross. Der Grund für diese Diskrepanz liegt in einer nicht-kosmogenen Neon-Komponente, die das  $^{21}\text{Ne}$ -Oberflächenalter verfälscht. Das Neon-Isotopen-Diagramm des Giebichensteins (Abb. 5.5a) zeigt, dass die Datenpunkte der beiden niedrigen Temperaturschritte, die gewöhnlich für Oberflächenaltersbestimmungen verwendet werden (400 und 600 °C), deutlich unterhalb der atmosphärisch-kosmogenen Mischgerade liegen. Sie enthalten also Neon, das nicht kosmogenen Ursprungs ist. Nach Niedermann et al. (1993) sind es vorwiegend ( $\alpha, n$ )-Reaktionen im Sauerstoff, die zu einer relativen Anreicherung von  $^{21}\text{Ne}$  gegenüber  $^{22}\text{Ne}$  führen. Das auf diese Weise produzierte nukleogene Neon wird zum Problem, wenn es sich – wie im Falle des Giebichensteins –während langer Zeit hat ansammeln können (alte Kratongesteine) und vergleichsweise wenig kosmogenes Neon gebildet worden ist (kurze Expositionszeit, geringe Produktionsrate). Eine Auftrennung der unterschiedlichen

Neon-Komponenten ist für die Probe GIE nicht möglich; folglich sind auch die  $^{21}\text{Ne}$ -Oberflächenaltersangaben für den Giebichenstein nicht weiter verwendbar. Wann der Giebichenstein aus dem skandinavischen Eis schmolz, kann somit einzig über das  $^{10}\text{Be}$ -Oberflächenalter beantwortet werden. Das berechnete minimale  $^{10}\text{Be}$ -Oberflächenalter für den Giebichenstein liegt bei  $103'000 \pm 8'000$  Jahren vor heute.

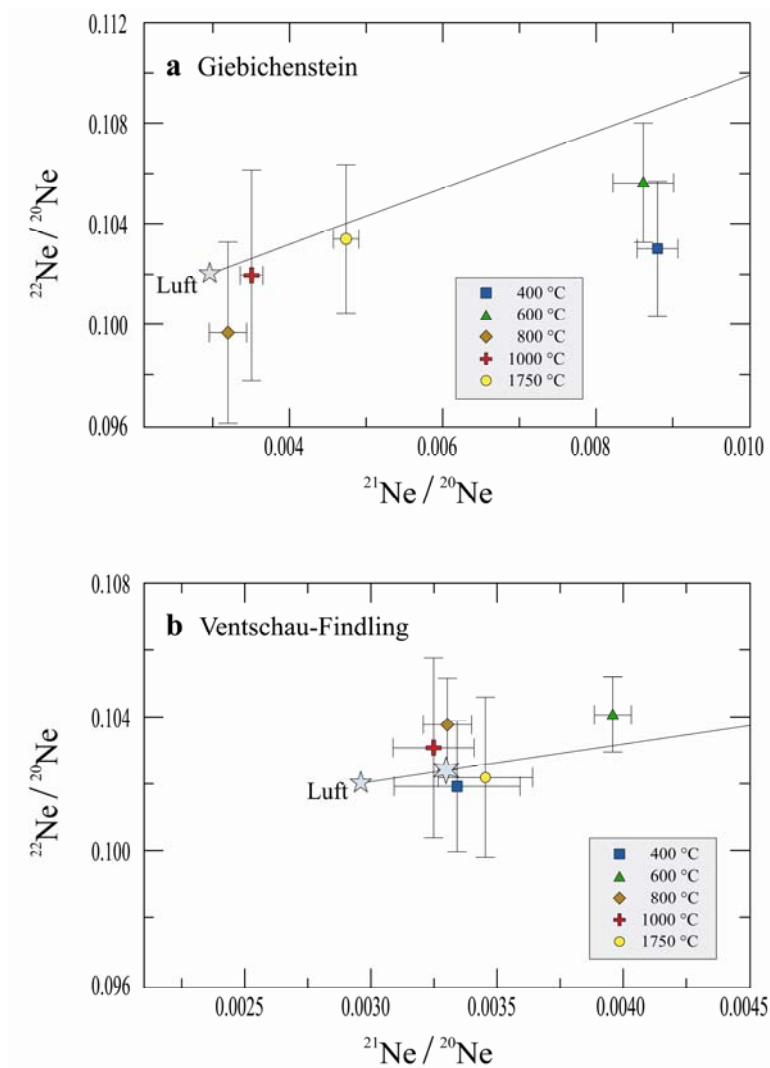


**Abb. 5.5.** Neon-Isotopen-Diagramme für den Giebichenstein (a) und den Findling von Ventschau (b). Die Gerade ( $y = (1.120 \pm 0.021)x + 0.098$ ) in den Diagrammen ist die atmosphärisch-kosmogene Mischgerade für Quarz (Niedermann et al., 1993). Der fünfzackige Stern repräsentiert jeweils die atmosphärische Neon-Zusammensetzung, der sechszackige Stern im Diagramm b) eine eingefangene Neon-Komponente mit einem  $^{21}\text{Ne}/^{20}\text{Ne}$ -Verhältnis von 0.00329.

Anders als beim Giebichenstein liegen im Neon-Isotopen-Diagramm vom Ventschau-Findling (Abb. 5.5b) sowohl der 400 °C- als auch der 600 °C-Temperaturschritt innerhalb der Fehler auf der atmosphärisch-kosmogenen Mischgerade. Der 600 °C-Temperaturschritt zeigt als einziger einen klaren kosmogenen Neon-Überschuss. Die restlichen Datenpunkte gruppieren sich alle um eine leicht über dem atmosphärischen Wert liegende Neon-Zusammensetzung. Dies spricht dafür, dass das bei der Gesteinsbildung eingefangene Neon keine atmosphärische, sondern eine leicht vom Luftwert abweichende Zusammensetzung aufgewiesen

hat, wie dies Hetzel et al. (2002) auch in Quarzproben von Tibet beobachtet haben. Aus den Datenpunkten der 400 °C-, 800 °C- und 1000 °C-Temperaturschritte errechneten wir eine eingefangene Neon-Komponente mit einem  $^{21}\text{Ne}/^{20}\text{Ne}$ -Verhältnis von 0.00329 (sechszackiger Stern in Abb. 5.5b). Diese liegt im Bereich der in Hetzel et al. (2002) angegebenen eingefangenen Neon-Komponenten mit nicht-atmosphärischen  $^{21}\text{Ne}/^{20}\text{Ne}$ -Verhältnissen von 0.00299–0.00398. Für die Berechnung des Oberflächenalters wurde der  $^{21}\text{Ne}$ -Überschuss über die eingefangene Neon-Komponente verwendet. Daraus resultiert ein  $^{21}\text{Ne}$ -Oberflächenalter für den Ventschau-Findling von  $193'000 \pm 32'000$  Jahren. Um das  $^{21}\text{Ne}$ -Oberflächenalter des Findlings von Ventschau zu bestätigen, sind eine Messung der genauen Zusammensetzung des eingefangenen Neons und die  $^{10}\text{Be}$ -Analyse notwendig.

**Tabelle 5.2.**  $^{21}\text{Ne}$ - und  $^{10}\text{Be}$ -Oberflächenalter.

Probe	Heiz-Temp. (°C); Dauer (min)	$^{21}\text{Ne}_{\text{Übers.}}^{\text{a}}$ ( $10^6$ Atome $\text{g}^{-1}$ )	$^{21}\text{Ne}_{\text{Übers.}}^{\text{b}}$ ( $10^6$ Atome $\text{g}^{-1}$ )	$^{21}\text{Ne}$ minimum Alter (in 1000 J.)	$^{10}\text{Be}$ ( $10^4$ Atome $\text{g}^{-1}$ )	$^{10}\text{Be}$ minimum Alter (in 1000 J.)
GIE	400; 45	$7.71 \pm 0.62$	-	$337 \pm 27$	-	-
GIE	600; 45	$8.3 \pm 1.1$	-	$364 \pm 47$	-	-
GIE	800; 30	$0.26 \pm 0.37$	-	$12 \pm 16$	-	-
GIE	1000; 30	$0.4 \pm 1.6$	-	$16 \pm 70$	-	-
GIE	1750; 15	$1.3 \pm 2.0$	-	$58 \pm 88$	-	-
GIE	-	-	-	-	$59.2 \pm 4.0$	$103 \pm 8$
VEN	400; 45	$0.58 \pm 0.43$	$0.07 \pm 0.43$	$3 \pm 20$	-	-
VEN	600; 45	$6.28 \pm 0.70$	$4.15 \pm 0.69$	$193 \pm 32$	-	-
VEN	800; 30	$1.10 \pm 0.45$	$0.02 \pm 0.45$	$1 \pm 21$	-	-
VEN	1000; 30	$0.29 \pm 0.24$	$0 \pm 0$	$0 \pm 0$	-	-
VEN	1750; 15	$0.56 \pm 0.27$	$0.18 \pm 0.27$	$8 \pm 12$	-	-

<sup>a</sup>  $^{21}\text{Ne}$  Überschuss über Luft, berechnet aus dem atmosphärischen  $^{21}\text{Ne}/^{20}\text{Ne}$  Verhältnis.

<sup>b</sup>  $^{21}\text{Ne}$  Überschuss über eine eingefangene Neon Komponente mit einem  $^{21}\text{Ne}/^{20}\text{Ne}$  Verhältnis von 0.00329.

GIE = Giebichenstein bei Stöckse; VEN = Findling von Ventschau.

### 5.2.5 Schlussfolgerungen

Die vorliegenden Untersuchungen zeigen, dass die beprobten norddeutschen Findlinge Zeugen einer alten Vergletscherung sind und seit mehr als 100'000 Jahren am heutigen Ort liegen. Der Eisvorstoss, der die erratischen Blöcke abgelagert hat, ist vermutlich in das marine Isotopen-Stadium 6 zu stellen (Abb. 5.6 und Geyh und Müller, 2005) beziehungsweise kann nicht jünger sein als ein Gletschervorstoss in dieser Zeit. Beweise einer vergleichbaren alpinen Vergletscherung um die 100'000 Jahre vor heute liefern Graf et al. (2007) mit Ober-

flächendatierungen von Findlingen aus dem Schweizer Jura. Anders als beim Giebichenstein stimmen im Jura die  $^{21}\text{Ne}$ - und die  $^{10}\text{Be}$ -Oberflächenalter überein. Möglicherweise sind in Nordeuropa die Produktionsraten für kosmogenes Neon – aufgrund der geringen Höhe über Meer – zu niedrig, damit ein klares kosmogenes Signal nukleogene und eingefangene Neon-Komponenten in alten skandinavischen Kratongesteinen überwiegen könnte. Für künftige Studien in diesem Gebiet sind deshalb Beryllium-Oberflächenaltersbestimmungen den Edelgas-Analysen vorzuziehen.

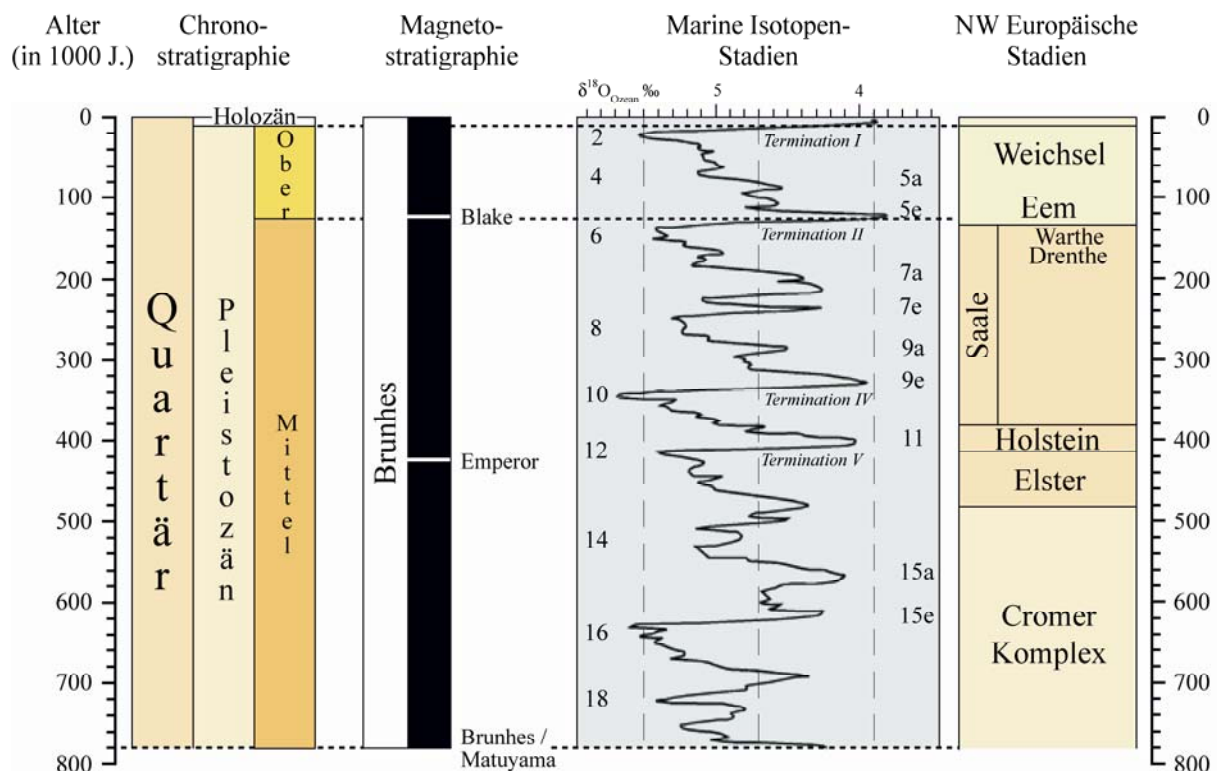


Abb. 5.6. Chronostratigraphische Korrelationstabelle der letzten 780'000 Jahre (nach Gibbard et al., 2005).

Auch wenn die vorliegenden Untersuchungen die Ansicht stützen, dass Drenthe- und Warthe-Stadium in Norddeutschland nicht durch eine Warmzeit getrennt sind, sondern beide in das marine Isotopen-Stadium 6 gehören, so wäre es doch wünschenswert, die Altersstellung der verschiedenen Stadien der Saale- (und Elster-) Vereisung durch Oberflächenaltersbestimmungen weiter zu präzisieren.

Zusätzliche Oberflächendatierungen werden nötig sein, um die vorliegenden Daten zu bestätigen und eine absolute, lokale Chronologie der fennoskandischen Vergletscherungen in Norddeutschland zu erstellen.

## Literaturverzeichnis

- BAUR, H. 1999. A Noble-Gas Mass Spectrometer Compressor Source With two Orders of Magnitude Improvement in Sensitivity. *Eos Transactions AGU*, **80**, Abstract V22B-08.
- DUNNE, J., ELMORE, D. & MUZIKAR, P. 1999. Scaling factors for the rates of production of cosmogenic nuclides for geometric shielding and attenuation at depth on sloped surfaces. *Geomorphology*, **27**, 3–11.
- EHLERS, J., EISSMANN, L., LIPPSTREU, L., STEPHAN, H.-J. & WANSA, S. 2004. Pleistocene glaciations of Northern Germany. In EHLERS, J. & GIBBARD, P.L., eds. *Quaternary Glaciations – Extent and Chronology; Part I: Europe. Developments in Quaternary Science*, **2**. Amsterdam: Elsevier, 135–146.
- EISSMANN, L. 1975. *Das Quartär der Leipziger Tieflandsbucht und angrenzender Gebiete um Saale und Elbe: Modell einer Landschaftsentwicklung am Rand der europäischen Kontinentalvereisung*. Berlin: Akademie-Verlag, 263 pp.
- GEYH, M. A. & MÜLLER, H. 2005. Numerical  $^{230}\text{Th}/\text{U}$  dating and a palynological review of the Holsteinian/Hoxnian Interglacial. *Quaternary Science Reviews*, **24**, 1861–1872.
- GIBBARD, P.L., SMITH, A.G., ZALASIEWICZ, J.A., BARRY, T.L., CANTRILL, D., COE, A.L., COPE, J.C.W., GALE, A.S., GREGORY, F.J., POWELL, J.H., RAWSON, P.F., STONE, P. & WATERS, C.N. 2005. What status for the Quaternary? *Boreas*, **34**, 1–6.
- GOSSE, J.C. & PHILLIPS, F.M. 2001. Terrestrial in situ cosmogenic nuclides: theory and application. *Quaternary Science Reviews*, **20**, 1475–1560.
- GRAF, A.A., STRASKY, S., IVY-OCHS, S., AKÇAR, N., KUBIK, P.W., BURKHARD, M. & SCHLÜCHTER, C. 2007. First results of cosmogenic dated pre-Last Glaciation erratics from the Montoz area, Jura Mountains, Switzerland. *Quaternary International*, **164/165**, 43–52.
- HETZEL, R., NIEDERMANN, S., IVY-OCHS, S., KUBIK, P.W., TAO, M. & GAO, B. 2002.  $^{21}\text{Ne}$  versus  $^{10}\text{Be}$  and  $^{26}\text{Al}$  exposure ages of fluvial terraces: the influence of crustal Ne in quartz. *Earth and Planetary Science Letters*, **201**, 575–591.
- IVY-OCHS, S. 1996. *The dating of rock surfaces using in situ produced  $^{10}\text{Be}$ ,  $^{26}\text{Al}$  and  $^{36}\text{Cl}$ , with examples from Antarctica and the Swiss Alps*. PhD thesis ETH No. 11763, ETH Zurich, 196 pp.
- KOHL, C.P. & NISHIZUMI, K. 1992. Chemical isolation of quartz for measurement of *in-situ*-produced cosmogenic nuclides. *Geochimica et Cosmochimica Acta*, **56**, 3583–3587.
- LÜTTIG, G. 1958. Methodische Fragen der Geschiebeforschung. *Geologisches Jahrbuch*, **75**, 361–418.
- MEYER, K.-D. 1999. Die grössten Findlinge in Niedersachsen. *Geschiebekunde aktuell, Sonderheft*, **5**, 36 pp.
- NIEDERMANN, S., GRAF, T. & MARTI, K. 1993. Mass spectrometric identification of cosmic-ray-produced neon in terrestrial rocks with multiple neon components. *Earth and Planetary Science Letters*, **118**, 65–73.
- NIEDERMANN, S., GRAF, T., KIM, J.S., KOHL, C.P., MARTI, K. & NISHIZUMI, K. 1994. Cosmic-ray-produced  $^{21}\text{Ne}$  in terrestrial quartz: the neon inventory of Sierra Nevada quartz separates. *Earth and Planetary Science Letters*, **125**, 341–355.

- NIEDERMANN, S. 2000. The  $^{21}\text{Ne}$  production rate in quartz revisited. *Earth and Planetary Science Letters*, **183**, 361–364.
- NIEDERMANN, S. 2002. Cosmic-Ray-Produced Noble Gases in Terrestrial Rocks: Dating Tools for Surface Processes. In PORCELLI, D., BALLENTINE, C.J. & WIELER, R., eds. *Noble Gases in Geochemistry and Cosmochemistry. Reviews in Mineralogy and Geochemistry*, **47**. Washington, DC: Mineralogical Society of America, 731–784.
- NOWOTHNIG, W. 1979. Der archäologische Wanderweg am Giebichenstein bei Stöckse, Kr. Nienburg/Weser – Vom Rentierjäger zum Bauern. *Wegweiser zur Vor- und Frühgeschichte Niedersachsens*, **6**, 44 pp.
- OBERHOLZER, P. 2004. *Reconstructing paleoclimate and landscape history in Antarctica and Tibet with cosmogenic nuclides*. PhD thesis ETH No. 15472, ETH Zurich, 160 pp.
- OCHS, M. & IVY-OCHS, S. 1997. The chemical behavior of Be, Al, Fe, Ca and Mg during AMS target preparation from terrestrial silicates modeled with chemical speciation calculations. *Nuclear Instruments and Methods in Physics Research B*, **123**, 235–240.
- STONE, J.O. 2000. Air pressure and cosmogenic isotope production. *Journal of Geophysical Research B*, **105**, 23753–23759.
- SVENDSEN, J.I., ALEXANDERSON, H., ASTAKHOV, V.I., DEMIDOV, I., DOWDESWELL, J.A., FUNDER, S., GATAULLIN, V., HENRIKSEN, M., HJORT, C., HOUMARK-NIELSEN, M., HUBBERTEN, H.W., INGÓLFSSON, Ó., JAKOBSSON, M., KJÆR, K.H., LARSEN, E., LOKRANTZ, H., LUNKKA, J.P., LYSÅ, A., MANGERUD, J., MATIOUCHKOV, A., MURRAY, A., MÖLLER, P., NIESSEN, F., NIKOLSKAYA, O., POLYAK, L., SAARNISTO, M., SIEGERT, C., SIEGERT, M.J., SPIELHAGEN, R.F. & STEIN, R. 2004. Late Quaternary ice sheet history of northern Eurasia. *Quaternary Science Reviews*, **23**, 1229–1271.
- SYNAL, H.-A., BONANI, G., DÖBELI, M., ENDER, R.M., GARTENMANN, P., KUBIK, P.W., SCHNABEL, C. & SUTER, M. 1997. Status report of the PSI/ETH AMS facility. *Nuclear Instruments and Methods in Physics Research B*, **123**, 62–68.
- WOLDSTEDT, P. 1954. Saaleeiszeit, Warthestadium und Weichseleiszeit in Norddeutschland. *Eiszeitalter und Gegenwart*, **4/5**, 34–48.

### 5.3 First results of cosmogenic dated pre-last glaciation erratics from the Montoz area, Jura Mountains, Switzerland <sup>f</sup>

---

Angela A. Graf <sup>1\*</sup>, Stefan Strasky <sup>2</sup>, Susan Ivy-Ochs <sup>3</sup>, Naki Akçar <sup>1</sup>, Peter W. Kubik <sup>4</sup>, Martin Burkhard <sup>5, †</sup> and Christian Schlüchter <sup>1</sup>

<sup>1</sup> *Institute of Geological Sciences, University of Bern, 3012 Bern, Switzerland*

<sup>2</sup> *Institute of Isotope Geochemistry and Mineral Resources, ETH Zurich, 8092 Zurich, Switzerland*

<sup>3</sup> *Institute for Particle Physics, ETH Zurich, 8093 Zurich, Switzerland*

<sup>4</sup> *Paul Scherrer Institute, c/o Institute for Particle Physics, ETH Zurich, 8093 Zurich, Switzerland*

<sup>5</sup> *Institut de Géologie et d'Hydrogéologie, University of Neuchâtel, 2009 Neuchâtel, Switzerland*

\* *corresponding author: angela.graf@bmgeng.ch*

† *deceased in August 2006*

---

**Abstract:** The Jura Mountains are a peri-Alpine chain bending from the SW to the NW of Switzerland. Alpine ice reached only marginal areas of this chain during the last glacial maximum (LGM) but remaining erratic boulders of Alpine origin beyond the LGM ice limit indicate older glaciations of unknown age, tentatively correlated either with the classical Rissian or with the most extensive glaciation. Here we present first results of four pre-LGM erratic boulders, dated with in situ produced cosmogenic nuclides (<sup>10</sup>Be and <sup>21</sup>Ne). Both data sets are in good agreement within error limits, with radionuclide apparent exposure ages ranging from 60 to 107 ka, and noble gas apparent ages from 73 to 123 ka. Taking the effect of erosion into account, these dates are shifted towards older ages and correspond most probably to a boulder deposition during marine isotope stage 6. These results are promising for further exposure dating studies on pre-LGM erratic boulders in mid-latitudes.

#### 5.3.1 Introduction

The peri-Alpine chain of the Jura Mountains is not only linked to the Alps by the tectonic history (Labhart, 1992), but was also repeatedly influenced by huge ice masses flowing out of the inner Alpine valleys during the Quaternary (Schlüchter, 2004). In comparison to the Alps and the Swiss Midlands, the chronology of glaciations in the Jura Mountains is poorly constrained, as dating was limited to deposits of the last glacial maximum (LGM) (Buoncristiani and Campy, 2004a; Vannières et al., 2004; Heiri and Millet, 2005). However, relict glacial

---

<sup>f</sup> Published in *Quaternary International*, 164/165 (2007), 43–52

deposits, e.g. erratic boulders of Alpine origin, are found beyond the LGM ice extent. Without age control, these deposits have tentatively been attributed either to the classical Rissian as defined by Penck and Brückner (1909) or to the most extensive glaciation (MEG), expected to be older than 700 ka (Schluchter and Kelly, 2000).

In order to develop a better understanding of the glacial chronology of the Jura Mountains we initiated a project where we absolutely date pre-LGM erratic boulders from the tops of Jura anticlines with in situ produced cosmogenic nuclides. In this work we present exposure ages from erratic boulders from the Montoz anticline, far beyond the LGM ice extent. By combining the radionuclide  $^{10}\text{Be}$  and the noble gas  $^{21}\text{Ne}$  it was possible to rule out pre-exposure, a process which can have a significant effect on exposure ages and thus can lead to misinterpretations. Combined  $^{10}\text{Be}$  and  $^{21}\text{Ne}$  analyses have proven to be suitable to cross-check exposure ages in Antarctica (e.g. Oberholzer et al., 2003), Tibet (e.g. Schäfer et al., 2002) and the Swiss Midlands (Ivy-Ochs et al., 2004).

### 5.3.2 Evidence for glaciation of the Jura Mountains

At the southern slope of the first Jura Mountain anticline, e.g. Mont Suchet and Mont Tendre, some 50 km from the outlet of the Rhône valley, the LGM Alpine ice of the Rhône glacier reached an altitude of at least 1200 m a.s.l. (Jäckli, 1962). From this point, the Rhône ice body split into two lobes sloping down to 400 m a.s.l. to the southwest of Genève and to 600 m a.s.l. to the northeast of Solothurn (Fig. 5.7). However, erratic boulders of quite fresh appearance are found at higher altitudes (1395 m a.s.l. on Mt d'Amin, west of Chasseral) and far over the Doubs river to the Loue valley near Ornans, France (Hantke, 1978). These boulders clearly indicate that a higher and much more extensive glaciation overrode most of the Jura Mountains, including high plateaus (> 1000 m a.s.l.) such as the Franches Montagnes (Vuille, 1965). The snowline of this “larger than LGM” glaciation dropped down to 700–800 m a.s.l. (Nussbaum and Gygax, 1935; Trümpy, 1980).

The ice extent within the western Jura (mainly France) is relatively well constrained. Ice fronts of the pre-LGM glaciation, the so-called “external moraine complex”, extended from Ornans to Bourg-en-Bresse and reached Lyon, where the ice lobe descended to 300 m a.s.l. (Penck and Brückner, 1909; Nussbaum and Gygax, 1935; Hantke, 1978; Campy and Arn, 1991; Campy, 1992; Buoncristiani and Campy, 2004b). On the other hand, the LGM “internal



moraine complex” is ~10–40 km inwards of the “external moraine complex” and extends over more than 100 km. North of Pontarlier, the ice reached an altitude of 850–950 m a.s.l. (Campy and Arn, 1991) and up to 550 m a.s.l. in the west of Champagnole. It extended to Bourg-en-Bresse (Moscariello et al., 1998), and ended some 20 km before Lyon.

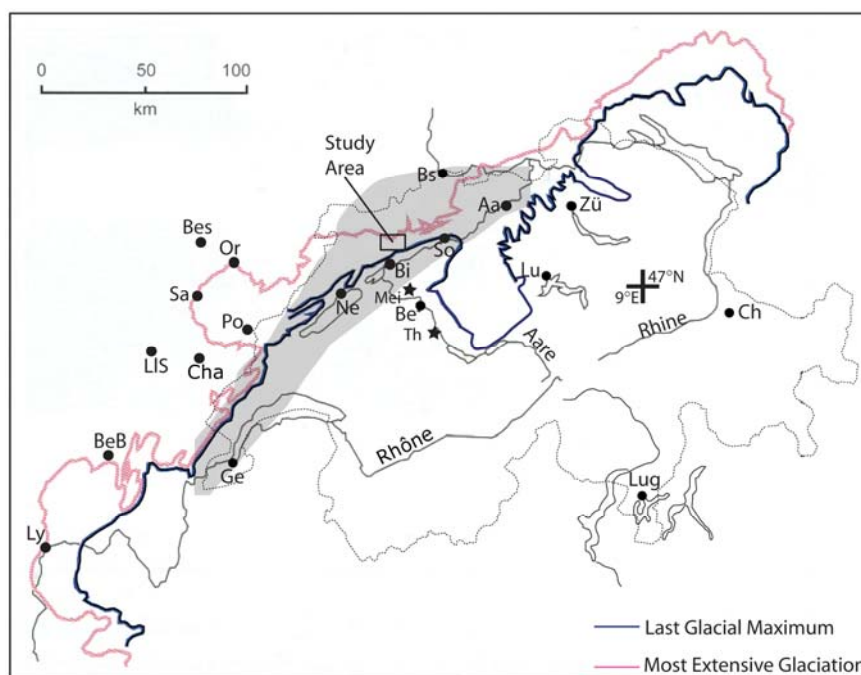


**Fig. 5.7.** Extension of the LGM and the MEG in Switzerland (outline shown) and France. The study area is indicated north of Biel. The grey area corresponds to the extent of Fig. 5.8 (from Genève to Basel). Aa: Aarau; Be: Bern; BeB: Bourg-en-Bresse; Bes: Besançon; Bi: Biel; Bs: Basel; Ch: Chur; Cha: Champagnole; Ge: Genève; LIS: Lons-le-Saunier; Lu: Luzern; Lug: Lugano; Ly: Lyon; Mei: Meikirch; Ne: Neuchâtel; Or: Orbe; Po: Pontarlier; Sa: Salins-les-Bains; So: Solothurn; Th: Thalgut; Zü: Zürich.

Agassiz (1843) and later Nussbaum and Gygax (1935) proposed a local ice cap covering the central part of the Jura Mountain chain, further complicating the reconstruction of glacial chronology. Studies by Aubert (1938; 1965), Arn and Aubert (1984), Campy (1992), Badoux (1995) and Buoncristiani and Campy (2004a; b) tend to constrain the extent of this local ice cap during the last two glaciations. They mostly argued on the distribution and composition of lodgement till, outcropping along the southernmost slopes of the central Jura Mountains. In these areas, lodgement tills containing exclusively limestone clasts from the Jura Mountains are found over Alpine lodgement tills. From this, as well as from striaes indicating ice flow directions, the above-mentioned authors concluded that local ice has accumulated in the Joux valley (Fig. 5.8), filling up the depression and finally overflowed the passes north- and southward, preventing the Alpine Rhône glacier from penetrating into most of the central Jura

Mountains. During the LGM, local ice has extended to the northeast into the Vallorbe and Vaultion valleys (leaving Dent de Vaultion as a nunatak) and to the north, reaching Pontarlier. It is more difficult to constrain the ice cap during the pre-LGM glaciation, but the absence of any Alpine material in the “external moraine complex” suggests that both, thickness and extension of the ice, were larger in pre-LGM times than during the LGM and that the pre-LGM ice cap culminated at about 2000 m a.s.l. (Campy, 1992).

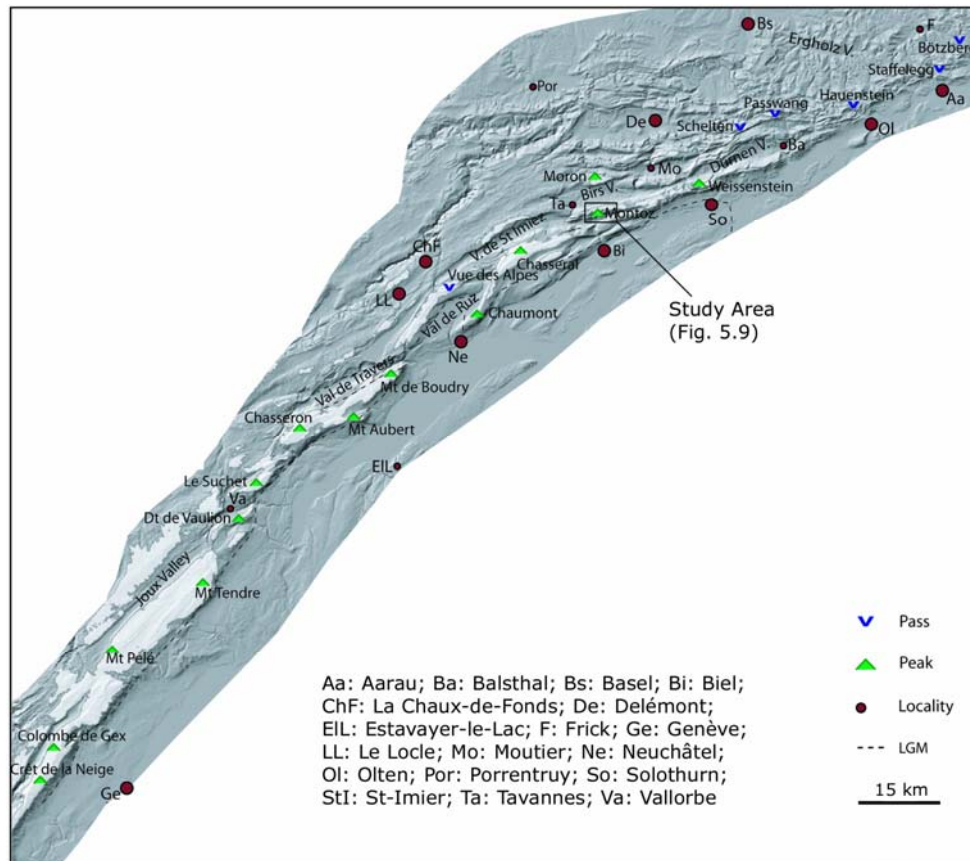


**Fig. 5.8.** The morphology of the Jura Mountain chain. White shading indicates areas above 1200 m a.s.l., thus above the generally recognized LGM ice extent. Vertical exaggeration 3x.

The eastern part of the Jura Mountains (east of the décrochement Vallorbe–Pontarlier) is characterized by generally lower elevations. This, and the absence of an extended local ice cap, allowed the pre-LGM Rhône glacier to penetrate deeper into the ranges, reaching a maximum elevation of 1420 m a.s.l. on Montagne de Boudry (compared to 1080–1180 m a.s.l. during the LGM). North and northeast of Neuchâtel the Alpine ice flowed into the Val de Travers and the Val de Ruz, across the Vue des Alpes pass, towards La Chaux-de-Fonds, Le Locle and Pontarlier, to end up some 16 km southeast of Besançon.

In the study area, the LGM Rhône glacier settled near Solothurn and the ice did not override the border chain except for a few valley floors. However, pre-LGM Alpine ice flowed from the Val de Ruz into the Vallon de St-Imier which is still covered by pre-LGM till (Bourquin et al., 1946). Further to the east, the glacier penetrated valleys above Biel, then flowing west of Montoz into the upper Birs valley, where it was diluted by local ice (Hantke, 1978). Ice further flowed through the Balsthal Water Gap and filled up the Dünnerg valley and also ended up in the Birs valley. Finally, north of Olten and Aarau, only pre-LGM ice is reported that flowed over various smaller passes, to end about 20 km southeast of Basel (Hantke, 1978). Further to the east, Rhône ice joined the piedmont glacier of the western Reuss–Rhein system.

### 5.3.3 Distribution of the erratic boulders

As noted before, the main argument to attribute a moraine or an erratic boulder to a pre-LGM glaciation is its geographical location beyond the generally accepted limits of the LGM (Jäckli, 1962; Schlüchter, 2004). We therefore focus on boulders located above 1200 m a.s.l. on the border chain, and/or beyond the second anticline. The area between La Chaux-de-Fonds and Le Locle is quite rich in pre-LGM material (Bourquin et al., 1946), like the French side along the Doubs river, around Pontarlier and as far as the Vallée de la Loue (Hantke, 1978). The easternmost erratic boulder was found in Anwil near Basel (Heim, 1919).

Unfortunately, the modern distribution of erratic boulders is only a relict of the original one. Most of the blocks were destroyed by human activities (Agassiz, 1836; Heim, 1919; de Saussure *in* Aubert, 1986). From the remaining boulders, the majority originate from the southern part of the Aar Massif (present Rhône, Fiesch and Aletsch glaciers) but a surprisingly high amount is also attributable to the Mont Blanc Massif. From this area only two relatively small tributary glaciers (Trient and Val d'Entremont) flowed into the Rhône valley. However, difficulties in distinguishing between Aar and Mont Blanc granites (both are whitish but the latter should be porphyritic and coarser grained) were first pointed out by Heim (1919), and confirmed by Spring (2004). The Penninic Nappes to the south of the east–west oriented part of the Rhône valley provide an abundance of metamorphic boulders, including a series of index erratics, mostly gabbros and eclogites from the Zermatt–Saas-Fee zone and Arolla gneisses from the Dent-Blanche Nappe. The sampled erratic boulders from the Montoz area are pale-greenish rocks, with whitish feldspar–quartz lenses in an oriented matrix composed of muscovite, epidote, and chlorite, with zircon and opaque minerals as

accessories. Thin sections have been compared to the descriptions by Aeberhard (1987), Burri et al. (1999) and Abbühl (2004), and according to these, the investigated boulders are attributed to the Arolla gneisses. Kelly et al. (2004) reconstructed the LGM ice surface geometry of the Rhône valley and suggested that ice from its southern part dominated the Rhône ice flow, pushing the glacier towards the northern valley side. This would explain how boulders from the Zermatt–Saas-Fee area have been integrated into the ice, transported to the northern valley side and finally deposited in the eastern Jura Mountains.

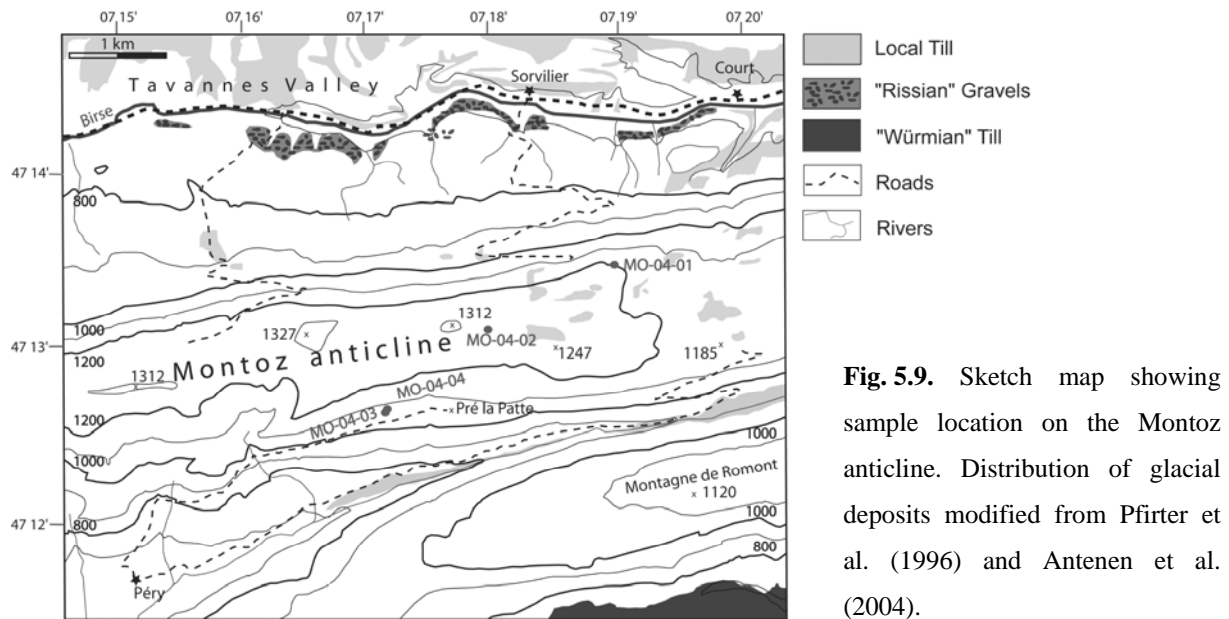


**Fig. 5.9.** Sketch map showing sample location on the Montoz anticline. Distribution of glacial deposits modified from Pfirter et al. (1996) and Antenen et al. (2004).

### 5.3.4 Cosmogenic dating

#### *Sampling*

The Montoz anticline is situated behind the southern border chain of the Jura Mountains. In the area, pre-LGM gravels are mapped on both flanks of the anticline (Fig. 5.9), while no indication for LGM Alpine tills has been found so far. However, local tills attributed to the last glacial cycle are covering the valley floors between Montoz and Delémont (Pfirter et al., 1996). Samples were collected from four different erratic boulders distributed on both sides of the anticline. MO-04-01 was found on the northern slope, MO-04-02 is located almost on the top, and MO-04-03 & -04 lie on the southern slope. Sampling of maximum 2 cm thick rock chips was done with hammer and chisel (geometrical and geographical details of the samples are given in Table 5.3 and boulders are shown in Fig. 5.10). On the rock surfaces, preferential erosion (quartz grains standing 5 mm above other grains) and pitting, with a maximum depth of 1.5 cm, was observed.

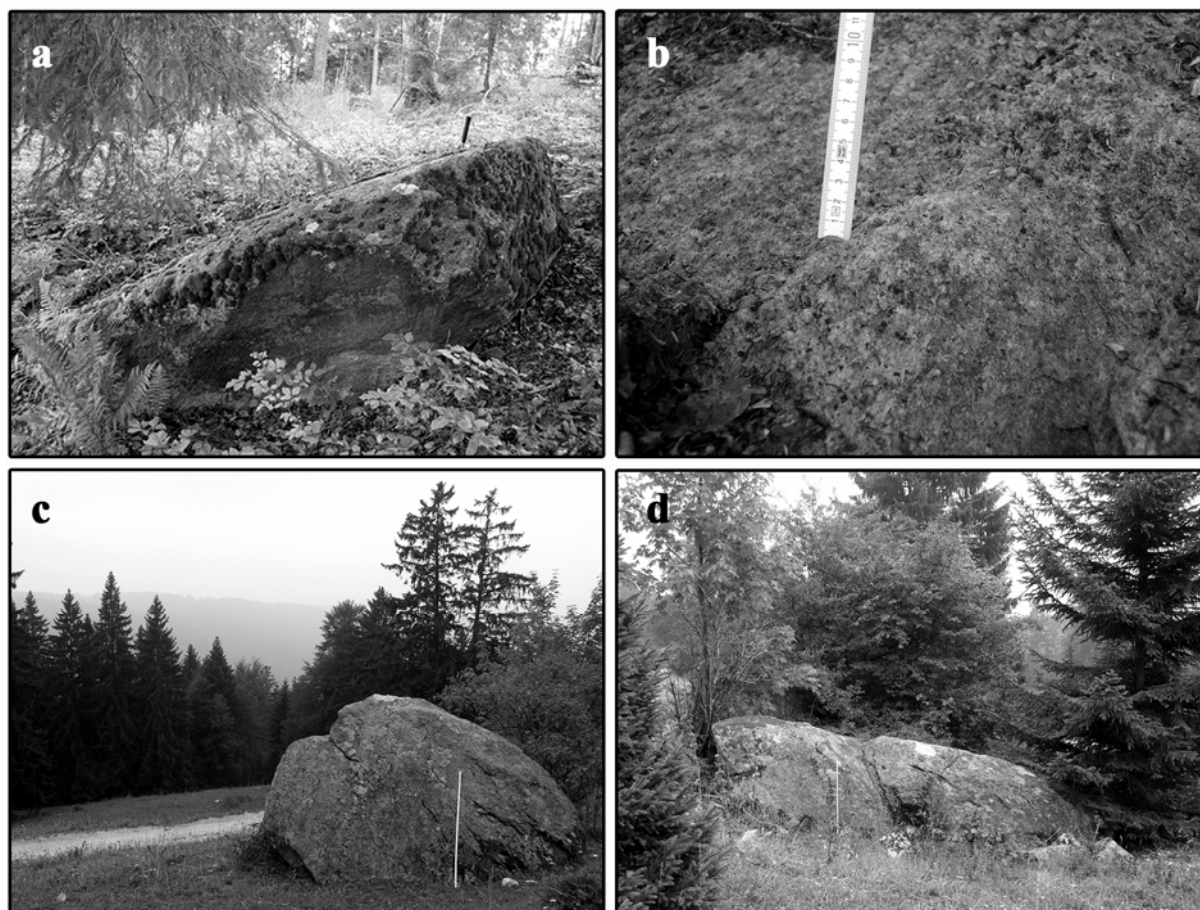


**Fig. 5.10.** Sampled erratic boulders. **a.** MO-04-01. **b.** surface detail of MO-04-01. **c.** MO-04-03, scale is a metre. **d.** MO-04-04, scale is a metre.

### *Cosmogenic radionuclides*

The samples were prepared at the Clean Lab of the Institute of Geological Sciences, University of Bern. They were crushed and sieved to grain sizes between 0.25 and 0.4 mm. Quartz was physically isolated with a Frantz magnetic separator and then chemically treated by selective mineral dissolution with hydrochloric and hydrofluoric acids (Kohl and Nishiizumi, 1992; Bierman et al., 2002). The four samples were treated and measured together with a procedure blank.  $^{10}\text{Be}$  was extracted from dissolved pure quartz following the procedure established by Ochs and Ivy-Ochs (1997). Measurements of the beryllium ratio ( $^{10}\text{Be}/^9\text{Be}$ ) were carried out by accelerator mass spectrometry at the ETH/PSI tandem facility in Zurich-Hönggerberg after Synal et al. (1997).

**Table 5.3.** Geographical information and boulder geometry of the Montoz samples.

Sample	Latitude (N)	Altitude (m a.s.l.)	a-b-c axes <sup>1</sup> (cm)	Boulder height (cm)	Surface inclination (inclination; azimuth)	Correction factor <sup>2</sup>
MO-04-01	47°13.50'	1200	220-380-75	50	26; 50	0.9857
MO-04-02	47°13.08'	1260	160-220-50	50	0; 0	0.9972
MO-04-03	47°12.54'	1050	280-220-180	180	0; 0	0.9742
MO-04-04	47°12.60'	1060	800-450-170	130	40; 270	0.9283

<sup>1</sup> Size of a-b-c axes for whole erratic boulder.

<sup>2</sup> Applied corrections are calculated for surrounding topographic shielding and surface geometry.

### *Cosmogenic noble gas*

Neon isotopes were analyzed in ~50 mg sized fractions of the same quartz separates used for radionuclide analyses. The quartz was further crushed to a grain size smaller than 0.1 mm and measured in a non-commercial ultra-high sensitivity noble gas mass spectrometer, at the Institute of Isotope Geochemistry and Mineral Resources at ETH Zurich (Baur, 1999). Noble gases were extracted in three temperature steps at 600, 800 and 1750 °C, in order to separate the cosmogenic from the non-cosmogenic gas fraction. As derived from the neon three-isotope diagram (Fig. 5.11), data of all low-temperature steps (600 °C) lie on the atmospheric–cosmogenic mixing line, indicating no nucleogenic neon component. Data from the high-temperature steps (800, 1750 °C) scatter around atmospheric composition and are not considered for age determination. Cosmogenic neon excess ( $^{21}\text{Ne}_{\text{exc}}$ ) was calculated as excess over air. Uncertainties for the neon data are  $1\sigma$  and include statistical, sensitivity and mass discrimination errors.

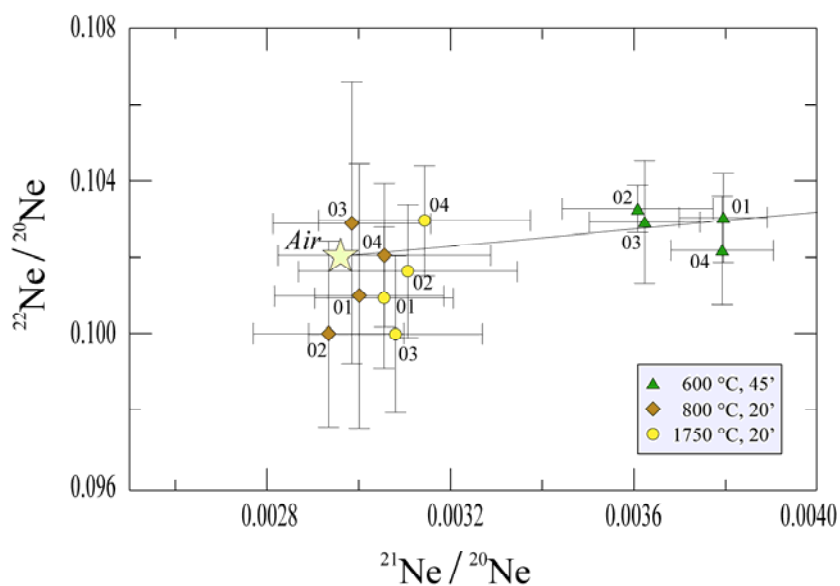


**Fig. 5.11.** Neon three-isotope plot of all samples. The line in the panel is the atmospheric-cosmogenic mixing line for quartz,  $y = (1.120 \pm 0.021)x + 0.098$ , reported by Niedermann et al. (1993). Sample abbreviations: 01–04 represent samples MO-04-01 to -04.

### Age calculations

To calculate surface exposure ages, we used the sea level high latitude production rates of 5.1 and 20.3 at/g/yr for  $^{10}\text{Be}$  and  $^{21}\text{Ne}$ , respectively (Niedermann, 2000; Stone, 2000; Gosse and Stone, 2001). Production rates were scaled to latitude and altitude after Stone (2000). Changes in palaeomagnetic intensity and non-dipole effects have not been considered and sea level changes are not yet integrated. Local production rates were further corrected for topographic shielding and dip of the sampled surfaces (between 0 and 40°) after Dunne et al. (1999), and for sample thickness after Gosse and Phillips (2001), using an effective attenuation length of 157 g/cm<sup>2</sup> and a rock density of 2.65 g/cm<sup>3</sup>. Snow corrected ages were obtained by assuming an over-the-year cover of 7 cm of snow (Atlas der Schweiz 2.0 © swisstopo) with a density of 0.4 g/cm<sup>3</sup>. Together with a vegetation coverage of 5 cm (density of 0.2 g/cm<sup>3</sup>; Tschudi, 2000), we obtained a rock equivalent layer of 1.01 cm.

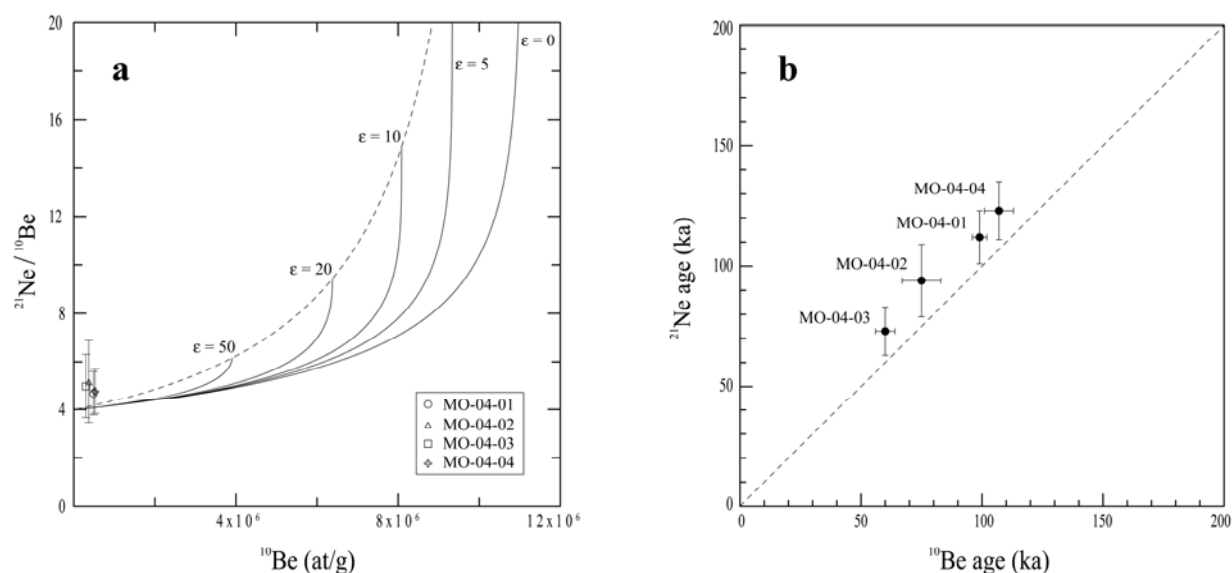


**Fig. 5.12.a.** Two-isotope erosion island plot, which allows the determination of long-term erosion rates of the sampled surfaces. As our data points fall into the range where all erosion curves converge, we could not determine the erosion rate for the Montoz samples.  $\epsilon$  = erosion rate in cm Ma<sup>-1</sup>. **b.** Two-isotope plot, showing the good correlation between  $^{21}\text{Ne}$  and  $^{10}\text{Be}$  apparent ages within 1 $\sigma$  errors. However,  $^{21}\text{Ne}$  ages are systematically slightly older.

Erosion rate varies in space and time and is, thus, the most challenging correction factor in surface exposure dating. Multiple nuclide studies in Switzerland (Ivy-Ochs et al., 2004; 2006a) showed that a conservative rate of 3 mm ka<sup>-1</sup> might be a good estimate between steady state erosion and rock slab split-off for LGM boulders. In order to constrain the erosion rate for the pre-LGM boulders, we plotted the two nuclides in an erosion island plot (Fig. 5.12a).

Unfortunately, all data points fall in the convergence zone of the erosion curves and no additional information about site-specific erosion rates could be obtained. As seen in Fig. 5.12b, the  $^{10}\text{Be}$  and  $^{21}\text{Ne}$  concentrations from the four boulders show good agreement between each other and support the hypothesis of continuous single-stage exposure. Therefore, we present our ages as apparent ages, as well as corrected for conservative erosion rates of  $1 \pm 0.5$  and  $3 \pm 0.5 \text{ mm ka}^{-1}$ .

### Results

Radionuclide ages are given in Table 5.4 and noble gas ages in Table 5.5. For the two larger boulders, we obtained apparent exposure ages of  $99 \pm 3 \text{ ka}$  ( $^{10}\text{Be}$ ) and  $112 \pm 11 \text{ ka}$  ( $^{21}\text{Ne}$ ) for MO-04-01 and  $107 \pm 6 \text{ ka}$  ( $^{10}\text{Be}$ ) and  $123 \pm 12 \text{ ka}$  ( $^{21}\text{Ne}$ ) for MO-04-04. With the exposure ages of MO-04-01 we confirmed the results obtained for a different sample of the same boulder by Ivy-Ochs et al. (2006b). The two smaller boulders are considerably younger with apparent ages of  $75 \pm 8 \text{ ka}$  ( $^{10}\text{Be}$ ) and  $94 \pm 15 \text{ ka}$  ( $^{21}\text{Ne}$ ) for MO-04-02 and  $60 \pm 4 \text{ ka}$  ( $^{10}\text{Be}$ ) and  $73 \pm 10 \text{ ka}$  ( $^{21}\text{Ne}$ ) for MO-04-03. By applying a conservative erosion rate of  $3 \pm 0.5 \text{ mm ka}^{-1}$ , the radionuclide ages increase to  $143 \pm 17 \text{ ka}$  ( $^{10}\text{Be}$ ) and  $166 \pm 16 \text{ ka}$  ( $^{21}\text{Ne}$ ) for MO-04-01;  $163 \pm 21 \text{ ka}$  ( $^{10}\text{Be}$ ) and  $193 \pm 18 \text{ ka}$  for MO-04-04;  $98 \pm 11 \text{ ka}$  ( $^{10}\text{Be}$ ) and  $128 \pm 20 \text{ ka}$  ( $^{21}\text{Ne}$ ) for MO-04-02; and  $74 \pm 6 \text{ ka}$  ( $^{10}\text{Be}$ ) and  $91 \pm 12 \text{ ka}$  ( $^{21}\text{Ne}$ ) for MO-04-03.

**Table 5.4.** Accelerator mass spectrometry results of the samples and resulting ages.

Sample	$^{10}\text{Be}$ ( $10^6 \text{ atoms g}^{-1}$ )	Apparent $^{10}\text{Be}$ age (ka)	$^{10}\text{Be}$ age (ka) $\epsilon = 1 \text{ mm ka}^{-1}$	$^{10}\text{Be}$ age (ka) $\epsilon = 3 \text{ mm ka}^{-1}$
MO-04-01	$1.35 \pm 0.04$	$99 \pm 3$	$111 \pm 11$	$143 \pm 17$
MO-04-02	$1.09 \pm 0.11$	$75 \pm 8$	$82 \pm 9$	$98 \pm 11$
MO-04-03	$0.73 \pm 0.05$	$60 \pm 4$	$65 \pm 5$	$74 \pm 6$
MO-04-04	$1.23 \pm 0.06$	$107 \pm 6$	$121 \pm 13$	$163 \pm 21$

Apparent ages are corrected for thickness and shielding, the erosion-corrected ages also contain corrections for snow and vegetation cover, see text for details. Error limits are  $1\sigma$  (systematic production rate errors are not included).

As all boulders are of the same lithology from a quite narrow location, we do not expect them to have been deposited by different glacial events. However, a purely downwasting ice body cannot explain the age differences of the four boulders, because, if so, we would expect the more elevated one to be the oldest. Although boulder MO-04-02 lies almost on the summit of the anticline, its age is quite young.



In surface exposure dating, only pre-exposure would explain age overestimates (ruled out in this study by applying both noble gases and radionuclides), while several processes can lead to younger ages. One of them would be post-depositional overturning of a boulder. In fact, based only on field evidence, we cannot exclude post depositional movements of the tabular shaped bloc MO-04-02, e.g. by farming activities. Assuming that the sampled top surface was once the boulders' bottom, we recalculated the production rate for a depth of 50 cm, and obtained a  $^{10}\text{Be}$  apparent age of  $172 \pm 10$  ka. As agricultural activity began in the Neolithic (Brombacher, 1997), overturning of the boulder by farmers could only explain age differences of a few thousand years. Boulders MO-04-03 and MO-04-04 are part of a small block field on a  $24^\circ$  slope, the latter about 10 m above the first. Soil creep could have slid the smaller rock for some metres, but rotation would likely induce more dynamic movements towards the valley. Alternatively, a younger age of a boulder within a sample set can be explained by post-depositional coverage of the boulder's surface, e.g. with sediments (Putkonen and Swanson, 2003). Nevertheless, we exclude coverage of MO-04-03 because of the above described sample site characteristics. However, it can be reasonably assumed that the 0.5 m tall boulder MO-04-02 was buried under a sediment layer after glacier retreat. Finally, as most of the cosmogenic nuclides accumulate in the uppermost 20 cm, periodical split-off of rock slabs sets the cosmogenic clock back for thousands of years. As shown in Fig. 5.10c, a bit from the upper left part of boulder MO-04-03 seems to be missing. For MO-04-02 such a process can be excluded because of its regular and flat top surface.

**Table 5.5.** Neon data and corresponding neon exposure ages.

Sample	Heating Temp. ( $^\circ\text{C}$ ); Time (min)	$^{20}\text{Ne}$ ( $10^9$ at $\text{g}^{-1}$ )	$^{21}\text{Ne}/^{20}\text{Ne}$ ( $10^{-3}$ )	$^{22}\text{Ne}/^{20}\text{Ne}$	$^{21}\text{Ne}_{\text{exc}}$ ( $10^6$ at $\text{g}^{-1}$ )	$^{21}\text{Ne}$ age (ka)		
						erosion 0 mm $\text{ka}^{-1}$	erosion 1 mm $\text{ka}^{-1}$	erosion 3 mm $\text{ka}^{-1}$
MO-04-01	600; 45	$7.58 \pm 0.12$	$3.79 \pm 0.10$	$0.1030 \pm 0.0012$	$6.3 \pm 1.2$	$112 \pm 11$	$124 \pm 12$	$166 \pm 16$
	800; 20	$1.57 \pm 0.02$	$3.00 \pm 0.18$	$0.1010 \pm 0.0035$	$0.07 \pm 0.36$			
	1750; 20	$2.88 \pm 0.06$	$3.06 \pm 0.15$	$0.1009 \pm 0.0019$	$0.28 \pm 0.66$			
MO-04-02	600; 45	$8.68 \pm 0.10$	$3.61 \pm 0.16$	$0.1033 \pm 0.0006$	$5.6 \pm 1.8$	$94 \pm 15$	$103 \pm 16$	$128 \pm 20$
	800; 20	$1.91 \pm 0.06$	$2.93 \pm 0.16$	$0.1000 \pm 0.0024$	$0.00 \pm 0.00$			
	1750; 20	$2.95 \pm 0.03$	$3.11 \pm 0.24$	$0.1016 \pm 0.0017$	$0.44 \pm 0.80$			
MO-04-03	600; 45	$5.47 \pm 0.07$	$3.62 \pm 0.12$	$0.1029 \pm 0.0016$	$3.64 \pm 0.94$	$73 \pm 10$	$78 \pm 10$	$91 \pm 12$
	800; 20	$1.26 \pm 0.03$	$2.99 \pm 0.17$	$0.1029 \pm 0.0037$	$0.03 \pm 0.34$			
	1750; 20	$2.10 \pm 0.03$	$3.08 \pm 0.19$	$0.1000 \pm 0.0021$	$0.26 \pm 0.50$			
MO-04-04	600; 45	$7.05 \pm 0.09$	$3.79 \pm 0.11$	$0.1022 \pm 0.0014$	$5.9 \pm 1.1$	$123 \pm 12$	$138 \pm 13$	$193 \pm 18$
	800; 20	$1.19 \pm 0.04$	$3.06 \pm 0.23$	$0.1020 \pm 0.0019$	$0.12 \pm 0.40$			
	1750; 20	$1.86 \pm 0.06$	$3.14 \pm 0.23$	$0.1030 \pm 0.0015$	$0.34 \pm 0.66$			

Uncertainties for the neon data are  $1\sigma$  and include statistical, sensitivity and mass discrimination errors.

For the reasons explained above, our larger blocks certainly better represent deposition time because we avoid substantial post-depositional coverage. In addition, it has been statistically shown by Putkonen and Swanson (2003) that in many cases older ages from a data set are more representative of the true deposition age than younger ones. According to this, the boulders were deposited on the Montoz anticline between 126 and 184 ka (accounting for the errors in erosion-corrected ( $\varepsilon = 3 \text{ mm ka}^{-1}$ )  $^{10}\text{Be}$  ages of the two largest boulders), a time span corresponding to marine isotope stage (MIS) 6.

### 5.3.5 Discussion

How then does the timing of a MIS 6 glaciation presented in this work relate to the events in the Swiss Midlands? Beside the maximum of the last glaciation dated near Solothurn by Ivy-Ochs et al. (2004), some evidence for pre-LGM glaciations has been documented in the Swiss Midlands, joining the complexity of the pollen profiles of Gondiswil (Wegmüller, 1992), Füramoos in southern Germany (Müller et al., 2003), Les Echets near Lyon (de Beaulieu and Reille, 1984) and La Grande Pile in the Vosges (de Beaulieu and Reille, 1992). For example, evidence for early late Pleistocene glaciations, i.e. MIS 5d/b and MIS 4, has been found in Gossau (near Zurich), Finsterhennen (south of Lake Biel), and Thalgut (south of Bern) (Preusser et al., 2003; Preusser, 2004; Preusser and Schlüchter, 2004; Preusser et al., 2007), as well as from Grandson (Badoux, 1995) and Les Tuilleries (Jayet and Portmann, 1960; 1966).

However, only few pre-Eemian sediment records have been found until now. The Thalgut gravel pit mentioned above presents a very complete sediment succession described in detail in Schlüchter (1989a; b). The lowermost part of the profile is formed by a till followed concordantly by lacustrine silts (Jaberg-Seetone). These lacustrine silts were correlated to the Holsteinian period by Welten (1982; 1988), based on the pollen assemblage of *Pterocarya* and dominance of *Fagus*. They are overlain by a prograding delta (progressively more glacigenic and with a coarsening-upward sequence), which is itself conformably overlain by a waterlain till and a 4 m thick sandy–silty varve succession. These older sediments are cut by a broad erosional unconformity that was preceded by an important pedogenic event. Above the erosional surface, up to 30 m thick, are delta gravels (Kirchdorf-Deltaschotter) with fore-sets dipping towards the present-day Aare river. The presence of a glacier is inferred from this different hydrological control, even if the gravels and sands contain only local reworked material. The concordantly overlying Thalgut-Seetone, also dipping towards the present day

river, were interpreted as basin accumulation during the last interglacial (Welten, 1982; 1988). These silts are followed by up to 30 m of the Upper Münsingen gravels (braided river system), divided into two units by an erosional surface. The lower unit was dated and correlated to MIS 5d (Preusser and Schlüchter, 2004). The upper unit is overlain by a 6 m thick LGM lodgement till. If the Thalgut-Seetone are interglacial MIS 5e in age, the delta gravels (Kirchdorf-Deltaschotter) under these silts were most probably deposited at the same time as the Montoz erratic boulders, or slightly later, before climate amelioration led to re-vegetation and deposition of the Eemian silts in a lacustrine environment.

The second long sediment record discussed here was drilled near Meikirch, in the northwest of Bern. The laminated sands and silts of the Meikirch complex represent three warm periods and four stadial periods, preceded and followed by sediments deposited during full glacial times. Preusser et al. (2005) have completely re-interpreted the pollen analyses and partly also the sediment analyses presented in Welten (1982; 1988). They proposed a correlation of the Meikirch complex with MIS 7. Above the laminated sands and silts of the Meikirch complex are about 39 m of coarse glacial outwash, representing at least two independent ice advances. Three samples from silty-sand layers within the basal part of the coarse-grained glacial outwash yielded luminescence ages between 186 and 206 ka, indicating a pre-Eemian glacial advance in this area (Preusser et al., 2005).

### 5.3.6 Conclusions

In this study we successfully applied surface exposure dating to pre-LGM erratic boulders in mid-latitudes.  $^{10}\text{Be}$  and  $^{21}\text{Ne}$  results are in good agreement with each other and are promising for further studies. The dated boulders from the Montoz anticline show pre-Eemian ages between 126 and 184 ka, and we propose a correlation with MIS 6. This implies (i) the larger than LGM glaciation responsible for the deposition of the erratic boulders on the Montoz anticline correlates most probably to the Rissian as defined by Penck and Brückner (1909), (ii) the early late Pleistocene glaciations (i.e. MIS 5d, 5b and 4) were of lesser extent than those during MIS 6 and MIS 2 (LGM), (iii) such an important ice advance and associated high erosive activity can easily explain the scarcity of pre-Eemian sediment records in the narrow Swiss Midlands.

**Acknowledgements:** We thank F. Preusser, P. Häuselmann and C. Buoncristiani for critical reviews, D. Rieke-Zapp for GIS support, as well as the ETH-PSI facility at Zurich-Hönggerberg for technical support. The Zurich AMS facility is jointly operated by the Swiss Federal Institute of Technology, Zurich and the Paul Scherrer Institute, Villigen, Switzerland. This work was funded by the Swiss National Science Foundation grant number: 200020-105220/1.

## References

- ABBÜHL, L.M. 2004. *A zero-exposure-time experiment on a sub-recent erratic boulder: the problem of pre-exposure in dating with cosmogenic nuclides*. Unpublished diploma thesis, ETH Zurich, 89 pp.
- AEBERHARD, T. 1987. Verzeichnis der geschützten geologischen Objekte des Kantons Bern. In NATURSCHUTZINSPEKTORAT DES KANTONS BERN, ed. *Bericht 1986. Mitteilungen der Naturforschenden Gesellschaft Bern*, **44**. Bern: Naturhistorisches Museum.
- AGASSIZ, L. 1836. Distribution des blocs erratiques sur les pentes du Jura. *Bulletin de la Société Géologique de France*, **1**.
- AGASSIZ, L. 1843. Le Jura a eu ses glaciers propres. *Actes de la Société Helvétique des Sciences Naturelles*, 28<sup>e</sup> session, Lausanne.
- ANTENEN M., KELLERHALS, P. & TRÖHLER, B. 2004. Blatt 1126 “Büren a.A.”. *Geologischer Atlas der Schweiz, 1:25 000*, **109**. Wabern: Bundesamt für Landestopografie.
- ARN, R. & AUBERT, D. 1984. Les formations quaternaires de l'Orbe et du Nozon, au pied du Jura. *Bulletin de Géologie (Lausanne)*, **275**, 17–42.
- AUBERT, D. 1938. Les glaciers quaternaires d'un bassin fermé: la vallée de Joux (Canton de Vaud). *Bulletin de Géologie (Lausanne)*, **62**, 1–14.
- AUBERT, D. 1965. Calotte glaciaire et morphologie jurassienne. *Eclogae Geologicae Helvetiae*, **58**, 555–578.
- AUBERT, D. 1986. La récurrence des glaciers jurassiens entre la Venoge et l'Aubonne. *Bulletin de Géologie (Lausanne)*, **285**, 21–46.
- BADOUX, H. 1995. Le glacier du Rhône au Pléistocène. *Bulletin de Géologie (Lausanne)*, **329**, 245–292.
- BAUR, H. 1999. A Noble-Gas Mass Spectrometer Compressor Source With two Orders of Magnitude Improvement in Sensitivity. *Eos Transactions AGU*, **80**, Abstract V22B-08.
- BIERMAN, P.R., CAFFEE, M.W., DAVIS, P.T., MARSELLA, K., PAVICH, M., COLGAN, P., MICKELSON, D. & LARSEN, J. 2002. Rates and Timing of Earth Surface Processes From *In Situ*-Produced Cosmogenic Be-10. In GREW, E.S., ed. *Beryllium: Mineralogy, Petrology, and Geochemistry. Reviews in Mineralogy and Geochemistry*, **50**. Washington DC: Mineralogical Society of America, 147–205.

- BOURQUIN, P., SUTER, H. & FALLOT, P. 1946. Blätter 114 “Biaufond”, 115 “Les Bois”, 116 “La Ferrière” und 117 “St-Imier” mit angrenzenden Teilen der Blätter 83 “Le Locle” und 130 “La Chaux-de-Fonds” und der französischen Seite des Doubstaes. *Geologischer Atlas der Schweiz, 1:25 000*, **15**. Wabern: Bundesamt für Landestopografie.
- BROMBACHER, C. 1997. Archeobotanical investigations of late neolithic lakeshore settlements (lake Biel, Switzerland). *Vegetation History and Archeobotany*, **6**, 167–186.
- BUONCRISTIANI, J.F. & CAMPY, M. 2004a. Expansion and retreat of the Jura ice sheet (France) during the last glacial maximum. *Sedimentary Geology*, **165**, 253–264.
- BUONCRISTIANI, J.F. & CAMPY, M. 2004b. The paleogeography of the last two glacial episodes in France: the Alps and Jura. In EHLERS, J. & GIBBARD, P.L., eds. *Quaternary Glaciations – Extent and Chronology, Part I: Europe. Developments in Quaternary Science*, **2**. Amsterdam: Elsevier, 101–112.
- BURRI, M., DAL PIAZ, G.V., DELLA VALLE, G., GOUFFON, Y. & GUERMANI, A. 1999. Blatt 1346 “Chanrion” mit N-Anteil von Blatt 1366 “Mont Vélán”. *Geologischer Atlas der Schweiz, 1:25 000*, **101**. Wabern: Bundesamt für Landestopografie.
- CAMPY, M. & ARN, R. 1991. The Jura glaciers: palaeogeography in the Würmian circum-Alpine zone. *Boreas*, **20**, 17–27.
- CAMPY, M. 1992. Paleogeographical relationships between Alpine and Jura glaciers during the two last Pleistocene glaciations. *Palaeogeography, Palaeoclimatology, Palaeoecology*, **93**, 1–12.
- DE BEAULIEU, J.-L. & REILLE, M. 1984. A long Upper Pleistocene pollen record from Les Echets, near Lyon, France. *Boreas*, **13**, 111–132.
- DE BEAULIEU, J.-L. & REILLE, M. 1992. The last climatic cycle at La Grande Pile (Vosges, France): a new pollen profile. *Quaternary Science Reviews*, **11**, 431–438.
- DUNNE, J., ELMORE, D. & MUZIKAR, P. 1999. Scaling factors for the rates of production of cosmogenic nuclides for geometric shielding and attenuation at depth on sloped surfaces. *Geomorphology*, **27**, 3–11.
- GOSSE, J.C. & PHILLIPS, F.M. 2001. Terrestrial in situ cosmogenic nuclides: theory and application. *Quaternary Science Reviews*, **20**, 1475–1560.
- GOSSE, J.C. & STONE, J.O. 2001. Terrestrial cosmogenic nuclide methods passing milestones toward paleo-altimetry. *Eos Transactions AGU*, **82**.
- HANTKE, R. 1978. *Eiszeitalter: die jüngste Erdgeschichte der Schweiz und ihrer Nachbargebiete*, **I**. Thun: Ott Verlag, 468 pp.
- HEIM, A. 1919. *Geologie der Schweiz*, **I & II**. Leipzig: Tauchnitz, 704 & 1018 pp.
- HEIRI, O. & MILLET, L. 2005. Reconstruction of Late Glacial summer temperatures from chironomid assemblages in Lac Lautrey (Jura, France). *Journal of Quaternary Science*, **20**, 33–44.
- IVY-OCHS, S., SCHÄFER, J.M., KUBIK, P.W., SYNAL, H.-A. & SCHLÜCHTER, C. 2004. Timing of deglaciation on the northern Alpine foreland (Switzerland). *Eclogae Geologicae Helvetiae*, **97**, 47–55.

- IVY-OCHS, S., KERSCHNER, H., KUBIK, P.W. & SCHLÜCHTER, C. 2006a. Glacier response in the European Alps to Heinrich Event 1 cooling: the Gschnitz stadial. *Journal of Quaternary Science*, **21**, 115–130.
- IVY-OCHS, S., KERSCHNER, H., REUTHER, A., MAISCH, M., SAILER, R., SCHAEFER, J., KUBIK, P.W., SYNAL, H.-A. & SCHLÜCHTER, C. 2006b. The timing of glacier advances in the northern European Alps based on surface exposure dating with cosmogenic  $^{10}\text{Be}$ ,  $^{26}\text{Al}$ ,  $^{36}\text{Cl}$ , and  $^{21}\text{Ne}$ . In SIAME, L.L., BOURLÈS, D.L. & BROWN, E.T., eds. *In Situ-Produced Cosmogenic Nuclides and Quantification of Geological Processes. Geological Society of America Special Paper*, **415**. Boulder: Geological Society of America, 43–60.
- JÄCKLI, H. 1962. Die Vergletscherung der Schweiz im Würmmaximum. *Eclogae Geologicae Helveticae*, **55**, 185–294.
- JAYET, A. & PORTMANN, J.-P. 1960. Deux gisements interglaciaires nouveaux aux environs d'Yverdon (Vaud, Suisse). *Eclogae Geologicae Helveticae*, **53**, 640–645.
- JAYET, A. & PORTMANN, J.-P. 1966. Sur la présence de moraines rissiennes profondes dans le gisement quaternaire des Tuilleries près d'Yverdon (Vaud, Suisse). *Eclogae Geologicae Helveticae*, **59**, 960–964.
- KELLY, M., BUONCRISTIANI, J.F. & SCHLÜCHTER, C. 2004. A reconstruction of the last glacial maximum (LGM) ice-surface geometry in the western Swiss Alps and contiguous Alpine regions in Italy and France. *Eclogae Geologicae Helveticae*, **97**, 57–75.
- KOHL, C.P. & NISHIZUMI, K. 1992. Chemical isolation of quartz for measurement of *in-situ*-produced cosmogenic nuclides. *Geochimica et Cosmochimica Acta*, **56**, 3583–3587.
- LABHART, T.P. 1992. *Geologie der Schweiz*. Thun: Ott Verlag, 211 pp.
- MOSCARIELLO, A., PUGIN, A., WILDI, W., BECK, C., CHAPRON, E., DE BATIST, M., GIRARD-CLOS, S., IVY-OCHS, S., RACHOUD-SCHNEIDER, A.-M., SIGNER, C. & VAN CAUWENBERGHE, T. 1998. Déglaciation würmienne dans des conditions lacustres à la terminaison occidentale du bassin lémanique (Suisse occidentale et France). *Eclogae Geologicae Helveticae*, **91**, 185–201.
- MÜLLER, U.C., PROSS, J. & BIBUS, E. 2003. Vegetation response to rapid climate change in central Europe during the past 140,000 yr based on evidence from the Füramoos pollen record. *Quaternary Research*, **59**, 235–245.
- NIEDERMANN, S., GRAF, T. & MARTI, K. 1993. Mass spectrometric identification of cosmic-ray-produced neon in terrestrial rocks with multiple neon components. *Earth and Planetary Science Letters*, **118**, 65–73.
- NIEDERMANN, S. 2000. The  $^{21}\text{Ne}$  production rate in quartz revisited. *Earth and Planetary Science Letters*, **183**, 361–364.
- NUSSBAUM, F. & GYGAX, F. 1935. Zur Ausdehnung des risszeitlichen Rhonegletschers im französischen Jura. *Eclogae Geologicae Helveticae*, **28**, 659–665.
- OBERHOLZER, P., BARONI, C., SCHAEFER, J.M., OROMBELLI, G., IVY-OCHS, S., KUBIK, P.W., BAUR, H. & WIELER, R. 2003. Limited Pliocene/Pleistocene glaciation in Deep Freeze Range, northern Victoria Land, Antarctica, derived from *in situ* cosmogenic nuclides. *Antarctic Science*, **15**, 493–502.

- OCHS, M. & IVY-OCHS, S. 1997. The chemical behavior of Be, Al, Fe, Ca and Mg during AMS target preparation from terrestrial silicates modeled with chemical speciation calculations. *Nuclear Instruments and Methods in Physics Research B*, **123**, 235–240.
- PENCK, A. & BRÜCKNER, E. 1909. *Die Alpen im Eiszeitalter, I-III*. Leipzig: Tauchnitz, 1199 pp.
- PFIRTER, U., ANTENEN M., HECKENDORN, W., BURKHALTER, R.M., GÜRLER, B. & KREBS, D. 1996. Blatt 1106 “Moutier”. *Geologischer Atlas der Schweiz, 1:25 000*, **96**. Wabern: Bundesamt für Landestopografie.
- PREUSSER, F., GEYH, M.A. & SCHLÜCHTER, C. 2003. Timing of Late Pleistocene climate change in lowland Switzerland. *Quaternary Science Reviews*, **22**, 1435–1445.
- PREUSSER, F. 2004. Towards a chronology of the Late Pleistocene in the northern Alpine Foreland. *Boreas*, **33**, 195–210.
- PREUSSER, F. & SCHLÜCHTER, C. 2004. Dates from an important early Late Pleistocene ice advance in the Aare valley, Switzerland. *Eclogae Geologicae Helveticae*, **97**, 245–253.
- PREUSSER, F., DRESCHER-SCHNEIDER, R., FIEBIG, M. & SCHLÜCHTER, C. 2005. Re-interpretation of the Meikirch pollen record, Swiss Alpine Foreland, and implications for Middle Pleistocene chronostratigraphy. *Journal of Quaternary Science*, **20**, 607–620.
- PREUSSER, F., BLEI, A., GRAF, H.-R. & SCHLÜCHTER, C. 2007. Luminescence dating of Würmian (Weichselian) proglacial sediments from Switzerland: methodological aspects and stratigraphical conclusions. *Boreas*, **36**, 130–142.
- PUTKONEN, J. & SWANSON, T. 2003. Accuracy of cosmogenic ages for moraines. *Quaternary Research*, **59**, 255–261.
- SCHÄFER, J.M., TSCHUDI, S., ZHAO, Z., WU, X., IVY-OCHS, S., WIELER, R., BAUR, H., KUBIK, P.W. & SCHLÜCHTER, C. 2002. The limited influence of glaciations in Tibet on global climate over the past 170 000 yr. *Earth and Planetary Science Letters*, **194**, 287–297.
- SCHLÜCHTER, C. 1989a. The most complete Quaternary record of the Swiss Alpine foreland. *Palaeogeography, Palaeoclimatology, Palaeoecology*, **72**, 141–146.
- SCHLÜCHTER, C. 1989b. Thalgut: ein umfassendes eiszeitstratigraphisches Referenzprofil im nördlichen Alpenvorland. *Eclogae Geologicae Helveticae*, **82**, 277–284.
- SCHLÜCHTER, C. & KELLY, M. 2000. *Das Eiszeitalter in der Schweiz – eine schematische Zusammenfassung*. Uttigen: Stiftung Landschaft und Kies, 4 pp.
- SCHLÜCHTER, C. 2004. The Swiss glacial record – a schematic summary. In EHLERS, J. & GIBBARD, P.L., eds. *Quaternary Glaciations – Extent and Chronology, Part I: Europe. Developments in Quaternary Science*, **2**. Amsterdam: Elsevier, 413–418.
- SPRING, J. 2004. *Les blocs erratiques granitiques de l'ancien glacier du Rhône*. Unpublished diploma thesis, University of Neuchâtel, 138 pp.
- STONE, J.O. 2000. Air pressure and cosmogenic isotope production. *Journal of Geophysical Research B*, **105**, 23753–23759.

- SYNAL, H.-A., BONANI, G., DÖBELI, M., ENDER, R.M., GARTENMANN, P., KUBIK, P.W., SCHNABEL, C. & SUTER, M. 1997. Status report of the PSI/ETH AMS facility. *Nuclear Instruments and Methods in Physics Research B*, **123**, 62–68.
- TRÜMPY, R. 1980. *Geology of Switzerland*. **A & B**. Basel: Wepf & Co., 104 & 334 pp.
- TSCHUDI, S. 2000. *Surface exposure dating: A geologist's view with examples from both hemispheres*. PhD thesis, University of Bern, 125 pp.
- VANNIÈRES, B., BOSSUET, G., WALTER-SIMONNET, A.-V., RUFFALDI, P., ADDATTE, T., ROSSY, M. & MAGNY, M. 2004. High-resolution record of environmental changes and tephrochronological markers of the Last Glacial-Holocene transition at Lake Lautrey (Jura, France). *Journal of Quaternary Science*, **19**, 797–808.
- VUILLE, A. 1965. Extension du glacier du Rhône dans les montagnes neuchâtelaises à l'époque rissienne. *Bulletin de la Société Neuchâteloise de Géographie*, **LIII**, 45–66.
- WEGMÜLLER, S. 1992. Vegetationsgeschichtliche und stratigraphische Untersuchungen an Schieferkohlen des nördlichen Alpenvorlandes. *Denkschriften der Schweizerischen Akademie der Naturwissenschaften*, **102**, 82 pp.
- WELTEN, M. 1982. Pollenanalytische Untersuchungen im Jüngeren Quartär des nördlichen Alpenvorlandes der Schweiz. *Beiträge zur Geologischen Karte der Schweiz NF*, **156**, 174 pp.
- WELTEN, M. 1988. Neue pollenanalytische Ergebnisse über das jüngere Quartär des nördlichen Alpenvorlandes der Schweiz (Mittel- und Jungpleistozän). *Beiträge zur Geologischen Karte der Schweiz NF*, **162**, 40 pp.



## 6 CONCLUSIONS AND OUTLOOK

Cosmogenic nuclide chronologies from six local glacial systems, two each in Antarctica, Tibet and Europe, were established within the framework and with financial support of the Swiss National Science Foundation project “LGM and pre-LGM paleoclimates of high and low latitudes: absolute chronologies in key regions for the global climate system” grant number: 200020-105220/1. Surface exposure ages ( $^{21}\text{Ne}$ ,  $^{10}\text{Be}$ ,  $^{26}\text{Al}$ ) of glacially eroded bedrock and erratic boulders on moraines or drift deposits revealed the following facts:

### **Antarctica**

The investigated section in the Transantarctic Mountains in Victoria Land has not been overridden by erosive ice since 4–6 Ma. However, multiple East Antarctic Ice Sheet variations occurred in Victoria Land throughout the Pleistocene and probably also during much of the Pliocene, but these fluctuations were of limited amplitudes. Reworking of Pliocene/Pleistocene deposits led to complex exposure histories and does not (yet) allow an unambiguous reconstruction of the timing of individual glacial episodes with cosmogenic nuclides.

### **Tibet**

Ice build-up of two Tibetan valley glaciers was synchronous with regard to ice growth elsewhere on the northern hemisphere during the last glacial cycle. Exposure ages of distinct glacial features around 20 and 15 ka suggest glacier advances during marine isotope stage (MIS) 2 and the Late Glacial, respectively. A discrepancy between  $^{21}\text{Ne}$  and  $^{10}\text{Be}$  exposure ages from one study area raised a methodological question about non-cosmogenic neon and needs further research.

### **Europe**

Alpine glaciers and the Fennoscandian Ice Sheet reached their maximum extent in the Quaternary most probably during MIS 6. This is indicated from erratic boulders deposited on top of the Swiss Jura Mountains and in Northern Germany. However, so far only limited data is available and more surface exposure ages are required for a better age control of the most extensive glaciation in Europe.

Surface exposure dating was successfully applied to reconstruct glacial landscape evolution in different regions of the world. However, in several cases accurate dating of glacial landforms was constrained by methodological limits. Multiple episodes of exposure followed by burial (e.g. beneath cold-based ice) can be identified with analyses of more than one cosmogenic nuclide but can currently not be resolved in time. Furthermore, non-cosmogenic neon may play an important role for samples with low local production rates and/or relatively short exposure times, but separation between cosmogenic and non-cosmogenic neon is not always possible. More fundamental research is needed – not only to better understand the non-cosmogenic neon inventory in rocks – but also more generally, for example, to improve production rate systematics of cosmogenic nuclides and, thus, to increase the potential of surface exposure dating.

It is in this respect that an experiment was set up to measure cosmogenic nuclide production rates at different geographical positions in artificial quartz targets. First tests revealed promising results and showed that the quartz targets are suitable for refining currently available altitude and latitude scaling routines. Members of the CRONUS research team now use the artificial quartz targets for an extended experiment. A number of targets are already exposed at an altitudinal transect and will be measured soon and hopefully contribute to further improve the method of surface exposure dating with in situ produced cosmogenic nuclides on earth.

## I REFERENCES

This bibliography includes references of chapter 1 and all introductory sections; all other references are listed at the end of the individual sections.

- ABBÜHL, L.M., AKÇAR, N., STRASKY, S., GRAF, A., IVY-OCHS, S. & SCHLÜCHTER, C. 2008. A zero-exposure time test on an erratic boulder: evaluating the problem of pre-exposure in Surface Exposure Dating. *Quaternary Science Journal (Eiszeitalter und Gegenwart)*, submitted.
- ACKERT, R.P. & KURZ, M.D. 2004. Age and uplift rates of Sirius Group sediments in the Dominion Range, Antarctica, from surface exposure dating and geomorphology. *Global and Planetary Change*, **42**, 207–225.
- AGASSIZ, L. 1840. *Études sur les glaciers*. Neuchâtel et Soleure: Nicolet et Jent & Gassmann, 346 pp.
- AKÇAR, N. 2006. *Paleoglacial Records from the Black Sea Area of Turkey: Field and Dating Evidence*. PhD thesis, University of Bern, 187 pp.
- ANISIMOV, O.A., VAUGHAN, D.G., CALLAGHAN, T.V., FURGAL, C., MARCHANT, H., PROWSE, T.D., VILHJÁLMSSON, H. & WALSH, J.E. 2007. Polar regions (Arctic and Antarctic). In PARRY, M.L., CANZIANI, O.F., PALUTIKOF, J.P., VON DER LINDEN, P.J. & HANSON, C.E., eds. *Climate Change 2007: Impacts, Adaptation and Vulnerability. Contribution of Working Group II to the Fourth Assessment Report of the Intergovernmental Panel on Climate Change*. Cambridge: Cambridge University Press, 653–685.
- BARONI, C. & OROMBELLI, G. 1989. Glacial geology and geomorphology of Terra Nova Bay (Victoria Land, Antarctica). *Memorie della Società Geologica Italiana*, **33**, 171–193.
- BIERMAN, P.R., CAFFEE, M.W., DAVIS, P.T., MARSELLA, K., PAVICH, M., COLGAN, P., MICKELSON, D. & LARSEN, J. 2002. Rates and Timing of Earth Surface Processes From *In Situ*-Produced Cosmogenic Be-10. In GREW, E.S., ed. *Beryllium: Mineralogy, Petrology, and Geochemistry. Reviews in Mineralogy and Geochemistry*, **50**. Washington DC: Mineralogical Society of America, 147–205.
- BRUNO, L.A. 1995. *Datierung von Moränen und glazial überprägten Oberflächen in der Antarktis mit in situ produzierten kosmogenen Edelgasen*. PhD thesis ETH No. 11256, ETH Zurich, 140 pp.
- CERLING, T.E. & CRAIG, H. 1994. Geomorphology and in-situ cosmogenic isotopes. *Annual Review of Earth and Planetary Sciences*, **22**, 273–317.
- COOK, A.J., FOX, A.J., VAUGHAN, D.G. & FERRIGNO, J.G. 2005. Retreating Glacier Fronts on the Antarctic Peninsula over the Past Half-Century. *Science*, **308**, 541–544.
- DAVIS, P.T., BIERMAN, P.R., MARSELLA, K.A., CAFFEE, M.W. & SOUTON, J.R. 1999. Cosmogenic analysis of glacial terrains in the eastern Canadian Arctic: a test for inherited nuclides and the effectiveness of glacial erosion. *Annals of Glaciology*, **28**, 181–188.

## I REFERENCES

- DAVIS, C.H., LI, Y., MCCONNELL, J.R., FREY, M.M. & HANNA, E. 2005. Snowfall-Driven Growth in East Antarctic Ice Sheet Mitigates Recent Sea-Level Rise. *Science*, **308**, 1898–1901.
- DE CHARPENTIER, J. 1841. *Essai sur les glaciers et sur le terrain erratique du bassin du Rhône*. Lausanne: Marc Ducloux, 363 pp.
- DENTON, G.H., PRENTICE, M.L., KELLOGG, D.E. & KELLOGG, T.B. 1984. Late Tertiary History of the Antarctic Ice-Sheet: Evidence from the Dry Valleys. *Geology*, **12**, 263–267.
- DENTON, G.H., SUGDEN, D.E., MARCHANT, D.R., HALL, B.L. & WILCH, T.I. 1993. East Antarctic Ice Sheet Sensitivity to Pliocene Climatic Change from a Dry Valleys Perspective. *Geografiska Annaler A*, **75**, 155–204.
- DERBYSHIRE, E., YAFENG, S., JIJUN, L., BENXING, Z., SHIJIE, L. & JINGTAI, W. 1991. Quaternary Glaciation of Tibet: The Geological Evidence. *Quaternary Science Reviews*, **10**, 485–510.
- DE SAUSSURE, H.-B. 1779. *Voyages dans les Alpes, précédés d'un essai sur l'histoire naturelle des environs de Genève*, **1**. Neuchâtel: Samuel Fauche, 540 pp.
- DESILETS, D. & ZREDA, M. 2003. Spatial and temporal distribution of secondary cosmic-ray nucleon intensities and applications to in situ cosmogenic dating. *Earth and Planetary Science Letters*, **206**, 21–42.
- DESILETS, D., ZREDA, M. & PRABU, T. 2006. Extended scaling factors for in situ cosmogenic nuclides: New measurements at low latitude. *Earth and Planetary Science Letters*, **246**, 265–276.
- DUNAI, T.J. 2000. Scaling factors for production rates of in situ produced cosmogenic nuclides: a critical reevaluation. *Earth and Planetary Science Letters*, **176**, 157–169.
- DUNAI, T.J. 2001. Influence of secular variation of the geomagnetic field on production rates of in situ produced cosmogenic nuclides. *Earth and Planetary Science Letters*, **193**, 197–212.
- EHLERS, J. & GIBBARD, P.L., eds. 2004. Quaternary Glaciations – Extent and Chronology, Part I: Europe. *Developments in Quaternary Science*, **2**. Amsterdam: Elsevier, 475 pp.
- FABEL, D. & HARBOR, J. 1999. The use of in-situ produced cosmogenic radionuclides in glaciology and glacial geomorphology. *Annals of Glaciology*, **28**, 103–110.
- FABEL, D., STROEVEN, A.P., HARBOR, J., KLEMAN, J., ELMORE, D. & FINK, D. 2002. Landscape preservation under Fennoscandian ice sheets determined from in situ produced  $^{10}\text{Be}$  and  $^{26}\text{Al}$ . *Earth and Planetary Science Letters*, **201**, 397–406.
- FIELDING, E., ISACKS, B., BARAZANGI, M. & DUNCAN, C. 1994. How flat is Tibet? *Geology*, **22**, 163–167.
- FINK, D., MCKELVEY, B., HAMBREY, M.J., FABEL, D. & BROWN, R. 2006. Pleistocene deglaciation chronology of the Amery Oasis and Radok Lake, northern Prince Charles Mountains, Antarctica. *Earth and Planetary Science Letters*, **243**, 229–243.
- GAISSER, T.K. 1990. *Cosmic Rays and Particle Physics*. Cambridge: Cambridge University Press, 279 pp.
- GILLESPIE, A. & MOLNAR, P. 1995. Asynchronous Maximum Advances of Mountain and Continental Glaciers. *Reviews of Geophysics*, **33**, 311–364.

- GOSSE, J.C. & PHILLIPS, F.M. 2001. Terrestrial in situ cosmogenic nuclides: theory and application. *Quaternary Science Reviews*, **20**, 1475–1560.
- HEWITT, K. 1999. Quaternary Moraines vs Catastrophic Rock Avalanches in the Karakoram Himalaya, Northern Pakistan. *Quaternary Research*, **51**, 220–237.
- IVY-OCHS, S. 1996. *The dating of rock surfaces using in situ produced  $^{10}\text{Be}$ ,  $^{26}\text{Al}$  and  $^{36}\text{Cl}$ , with examples from Antarctica and the Swiss Alps*. PhD thesis ETH No. 11763, ETH Zurich, 196 pp.
- IVY-OCHS, S., SCHLÜCHTER, C., KUBIK, P.W. & DENTON, G.H. 1999. Moraine exposure dates imply synchronous Younger Dryas glacier advances in the European Alps and in the Southern Alps of New Zealand. *Geografiska Annaler A*, **81**, 313–323.
- IVY-OCHS, S., KERSCHNER, H., REUTHER, A., MAISCH, M., SAILER, R., SCHAEFER, J., KUBIK, P.W., SYNAL, H.-A. & SCHLÜCHTER, C. 2006a. The timing of glacier advances in the northern European Alps based on surface exposure dating with cosmogenic  $^{10}\text{Be}$ ,  $^{26}\text{Al}$ ,  $^{36}\text{Cl}$ , and  $^{21}\text{Ne}$ . In SIAME, L.L., BOURLÈS, D.L. & BROWN, E.T., eds. *In Situ-Produced Cosmogenic Nuclides and Quantification of Geological Processes*. Geological Society of America Special Paper, **415**. Boulder: Geological Society of America, 43–60.
- IVY-OCHS, S., KERSCHNER, H., KUBIK, P.W. & SCHLÜCHTER, C. 2006b. Glacier response in the European Alps to Heinrich Event 1 cooling: the Gschnitz stadial. *Journal of Quaternary Science*, **21**, 115–130.
- KAPLAN, M.R., DOUGLASS, D.C., SINGER, B.S., ACKERT, R.P. & CAFFEE, M.W. 2005. Cosmogenic nuclide chronology of pre-last glacial maximum moraines at Lago Buenos Aires, 46°S, Argentina. *Quaternary Research*, **63**, 301–315.
- KELLY, M.A. 2003. *The late Würmian Age in the western Swiss Alps - last glacial maximum (LGM) ice-surface reconstruction and  $^{10}\text{Be}$  dating of late-glacial features*. PhD thesis, University of Bern, 105 pp.
- KOBER, F. 2004. *Quantitative analysis of the topographic evolution of the Andes of Northern Chile using cosmogenic nuclides*. PhD thesis ETH No. 15858, ETH Zurich, 131 pp.
- KUHLE, M. 1991. Observations supporting the Pleistocene inland glaciation of High Asia. *GeoJournal*, **25**, 133–231.
- KUHLE, M. 1998. Reconstruction of the 2.4 Million km<sup>2</sup> late Pleistocene ice sheet on the Tibetan Plateau and its impact on the global climate. *Quaternary International*, **45/46**, 71–108.
- KURZ, M.D. & BROOK, E.J. 1994. Surface exposure dating with cosmogenic nuclides. In BECK, C., ed. *Dating in Exposed and Surface Contexts*. Albuquerque: University of New Mexico Press, 139–159.
- LAL, D. & PETERS, B. 1967. Cosmic ray produced radioactivity on the earth. In *Handbuch der Physik*, **46/2**, Berlin: Springer, 551–612.
- LAL, D. 1988. In situ-produced cosmogenic isotopes in terrestrial rocks. *Annual Review of Earth and Planetary Sciences*, **16**, 355–388.
- LAL, D. 1991. Cosmic ray labeling of erosion surfaces: *in situ* nuclide production rates and erosion models. *Earth and Planetary Science Letters*, **104**, 424–439.

## REFERENCES

- LEHMKUHL, F., OWEN, L.A. & DERBYSHIRE, E. 1998. Late Quaternary Glacial History of Northeast Tibet. *In* OWEN, L.A., ed. *Mountain Glaciation. Quaternary Proceedings*, **6**. Chichester: John Wiley & Sons Ltd., 121–142.
- LEHMKUHL, F. & OWEN, L.A. 2005. Late Quaternary glaciation of Tibet and the bordering mountains: a review. *Boreas*, **34**, 87–100.
- LEMKE, P., REN, J., ALLEY, R.B., ALLISON, I., CARRASCO, J., FLATO, G., FUJII, Y., KASER, G., MOTE, P., THOMAS, R.H. & ZHANG, T. 2007. Observations: Changes in Snow, Ice and Frozen Ground. *In* SOLOMON, S., QIN, D., MANNING, M., CHEN, Z., MARQUIS, M., AVERYT, K.B., TIGNOR, M. & MILLER, H.L., eds. *Climate Change 2007: The Physical Science Basis. Contribution of Working Group I to the Fourth Assessment Report of the Intergovernmental Panel on Climate Change*. Cambridge: Cambridge University Press, 337–383.
- LI, B., LI, J., CUI, Z., ZHENG, B., ZHANG, Q., WANG, F., ZHOU, S., SHI, Z., JIAO, K. & KANG, J., eds. 1991. Quaternary Glacial Distribution Map of Qinghai-Xizang (Tibet) Plateau 1:3,000,000. *Scientific Advisor*: SHI, Y. Quaternary Glacier & Environment Research Center, Lanzhou University. Beijing: Science Press.
- LIFTON, N.A., BIEBER, J.W., CLEM, J.M., DULDIG, M.L., EVENSON, P., HUMBLE, J.E. & PYLE, R. 2005. Addressing solar modulation and long-term uncertainties in scaling secondary cosmic rays for in situ cosmogenic nuclide applications. *Earth and Planetary Science Letters*, **239**, 140–161.
- LITT, T., ed. 2007. Stratigraphie von Deutschland – Quartär (im Auftrag der Deutschen Stratigraphischen Kommission). *Quaternary Science Journal (Eiszeitalter und Gegenwart)*, **56** (special issue). Stuttgart: E. Schweizerbart'sche Verlagsbuchhandlung, 138 pp.
- LYTHE, M.B., VAUGHAN, D.G. & BEDMAP CONSORTIUM 2001. BEDMAP: A new ice thickness and subglacial topographic model of Antarctica. *Journal of Geophysical Research B*, **106**, 11,335–11,351.
- MACKINTOSH, A., WHITE, D., FINK, D., GORE, D.B., PICKARD, J. & FANNING, P.C. 2007. Exposure ages from mountain dipsticks in Mac. Robertson Land, East Antarctica, indicate little change in ice-sheet thickness since the Last Glacial Maximum. *Geology*, **35**, 551–554.
- MASARIK, J., FRANK, M., SCHÄFER, J.M. & WIELER, R. 2001. Correction of in situ cosmogenic nuclide production rates for geomagnetic field intensity variations during the past 800,000 years. *Geochimica et Cosmochimica Acta*, **65**, 2995–3003.
- MOLNAR, P. & ENGLAND, P. 1990. Late Cenozoic uplift of mountain ranges and global climate change: chicken or egg? *Nature*, **346**, 29–34.
- NIEDERMANN, S. 2002. Cosmic-Ray-Produced Noble Gases in Terrestrial Rocks: Dating Tools for Surface Processes. *In* PORCELLI, D., BALLENTINE, C.J. & WIELER, R., eds. *Noble Gases in Geochemistry and Cosmochemistry. Reviews in Mineralogy and Geochemistry*, **47**. Washington, DC: Mineralogical Society of America, 731–784.

- OBERHOLZER, P., BARONI, C., SCHAEFER, J., OROMBELLI, G., IVY-OCHS, S., KUBIK, P.W., BAUR, H. & WIELER, R. 2003. Limited Pliocene/Pleistocene glaciation in Deep Freeze Range, northern Victoria Land, Antarctica, derived from *in situ* cosmogenic nuclides. *Antarctic Science*, **15**, 493–502.
- OBERHOLZER, P. 2004. *Reconstructing paleoclimate and landscape history in Antarctica and Tibet with cosmogenic nuclides*. PhD thesis ETH No. 15472, ETH Zurich, 160 pp.
- OERLEMANS, J. 1994. Quantifying Global Warming from the Retreat of Glaciers. *Science*, **264**, 243–245.
- OERLEMANS, J. 2001. *Glaciers and Climate Change*. Lisse: A.A. Balkema Publishers, 148 pp.
- OWEN, L.A., FINKEL, R.C., HAIZHOU, M., SPENCER, J.Y., DERBYSHIRE, E., BARNARD, P.L. & CAFFEE, M.W. 2003. Timing and style of Late Quaternary glaciation in northeastern Tibet. *Geological Society of America Bulletin*, **115**, 1356–1364.
- OWEN, L.A., FINKEL, R.C., BARNARD, P.L., HAIZHOU, M., ASAHI, K., CAFFEE, M.W. & DERBYSHIRE, E. 2005. Climatic and topographic controls on the style and timing of Late Quaternary glaciation throughout Tibet and the Himalaya defined by  $^{10}\text{Be}$  cosmogenic radionuclide surface exposure dating. *Quaternary Science Reviews*, **24**, 1391–1411.
- PATERSON, W.S.B. 1994. *The Physics of Glaciers*. Oxford: Pergamon, 480 pp.
- PENCK, A. & BRÜCKNER, E. 1909. *Die Alpen im Eiszeitalter, I-III*. Leipzig: Tauchnitz, 1199 pp.
- PIGATI, J.S. & LIFTON, N.A. 2004. Geomagnetic effects on time-integrated cosmogenic nuclide production with emphasis on *in situ*  $^{14}\text{C}$  and  $^{10}\text{Be}$ . *Earth and Planetary Science Letters*, **226**, 193–205.
- PREUSSER, F. 2004. Towards a chronology of the Late Pleistocene in the northern Alpine Foreland. *Boreas*, **33**, 195–210.
- PUTKONEN, J. & SWANSON, T. 2003. Accuracy of cosmogenic ages for moraines. *Quaternary Research*, **59**, 255–261.
- RIGNOT, E. & THOMAS, R.H. 2002. Mass balance of polar ice sheets. *Science*, **297**, 1502–1506.
- RINTERKNECHT, V.R., CLARK, P.U., RAISBECK, G.M., YIOU, F., BITINAS, A., BROOK, E.J., MARKS, L., ZELCS, V., LUNKKA, J.P., PAVLOVSKAYA, I.E., PIOTROWSKI, J.A. & RAUKAS, A. 2006. The last deglaciation of the southeastern sector of the Scandinavian Ice Sheet. *Science*, **311**, 1449–1452.
- RUDDIMAN, W.F. & KUTZBACH, J.E. 1989. Forcing of late Cenozoic Northern Hemisphere climate by plateau uplift in southern Asia and the American west. *Journal of Geophysical Research D*, **94**, 18,409–18,427.
- SCHAEFER, I. 1953. Die donau eiszeitlichen Ablagerungen an Lech und Wertach. *Geologica Bavarica*, **19**, 13–64.
- SCHAEFER, J.M., DENTON, G.H., BARRELL, D.J.A., IVY-OCHS, S., KUBIK, P.W., ANDERSEN, B.G., PHILLIPS, F.M., LOWELL, T.V. & SCHLÜCHTER, C. 2006. Near-Synchronous Interhemispheric Termination of the Last Glacial Maximum in Mid-Latitudes. *Science*, **312**, 1510–1513.
- SCHAEFER, J.M., OBERHOLZER, P., ZHAO, Z., IVY-OCHS, S., WIELER, R., BAUR, H., KUBIK, P.W. & SCHLÜCHTER, C. 2008. Cosmogenic beryllium-10 and neon-21 dating of late Pleistocene glaciations in Nyalam, monsoonal Himalayas. *Quaternary Science Reviews*, **27**, 295–311.

## I REFERENCES

- SCHÄFER, J.M., IVY-OCHS, S., WIELER, R., LEYA, I., BAUR, H., DENTON, G.H. & SCHLÜCHTER, C. 1999. Cosmogenic noble gas studies in the oldest landscape on earth: surface exposure ages of the Dry Valleys, Antarctica. *Earth and Planetary Science Letters*, **167**, 215–226.
- SCHÄFER, J.M. 2000. *Reconstruction of landscape evolution and continental paleoglaciations using in-situ cosmogenic nuclides: Examples from Antarctica and the Tibetan Plateau*. PhD thesis ETH No. 13542, ETH Zurich, 121 pp.
- SCHÄFER, J.M., TSCHUDI, S., ZHAO, Z., WU, X., IVY-OCHS, S., WIELER, R., BAUR, H., KUBIK, P.W. & SCHLÜCHTER, C. 2002. The limited influence of glaciations in Tibet on global climate over the past 170 000 yr. *Earth and Planetary Science Letters*, **194**, 287–297.
- SCHLÜCHTER, C. & KELLY, M. 2000. *Das Eiszeitalter in der Schweiz – eine schematische Zusammenfassung*. Uttigen: Stiftung Landschaft und Kies, 4 pp.
- SCHLÜCHTER, C. 2004. The Swiss glacial record – a schematic summary. In EHLERS, J. & GIBBARD, P.L., eds. *Quaternary Glaciations – Extent and Chronology, Part I: Europe. Developments in Quaternary Science*, **2**. Amsterdam: Elsevier, 413–418.
- SHEA, M.A., SMART, D.F. & GENTILE, L.C. 1987. Estimating cosmic ray vertical cutoff rigidities as a function of the McIlwain L-parameter for different epochs of the geomagnetic field. *Physics of the Earth and Planetary Interiors*, **48**, 200–205.
- STAIGER, J.W., MARCHANT, D.R., SCHAEFER, J.M., OBERHOLZER, P., JOHNSON, J.V., LEWIS, A.R. & SWANGER, K.M. 2006. Plio-Pleistocene history of Ferrar Glacier, Antarctica: Implications for climate and ice sheet stability. *Earth and Planetary Science Letters*, **243**, 489–503.
- STAIGER, J., GOSSE, J., TORACINTA, R., OGLESBY, B., FASTOOK, J. & JOHNSON, J.V. 2007. Atmospheric scaling of cosmogenic nuclide production: Climate effect. *Journal of Geophysical Research B*, **112**, B02205, doi:10.1029/2005JB003811.
- STONE, J.O. 2000. Air pressure and cosmogenic isotope production. *Journal of Geophysical Research B*, **105**, 23753–23759.
- SUGDEN, D.E., BALCO, G., COWDERY, S.G., STONE, J.O. & SASS, L.C. 2005. Selective glacial erosion and weathering zones in the coastal mountains of Marie Byrd Land, Antarctica. *Geomorphology*, **67**, 317–334.
- TSCHUDI, S. 2000. *Surface exposure dating: A geologist's view with examples from both hemispheres*. PhD thesis, University of Bern, 125 pp.
- TSCHUDI, S., IVY-OCHS, S., SCHLÜCHTER, C., KUBIK, P. & RAINIO, H. 2000. <sup>10</sup>Be dating of Younger Dryas Salpausselkä I formation in Finland. *Boreas*, **29**, 287–293.
- VAUGHAN, D.G. & DOAKE, C.S.M. 1996. Recent atmospheric warming and retreat of ice shelves on the Antarctic Peninsula. *Nature*, **379**, 328–331.
- ZHENG, B.X. 1989. Controversy Regarding the Existence of a Large Ice Sheet on the Qinghai-Xizang (Tibetan) Plateau during the Quaternary Period. *Quaternary Research*, **32**, 121–123.



## II APPENDIX

The appendix includes supplementary neon data of all samples presented in section 3.3 as well as a compilation of additionally analyzed samples not discussed within this work.

Neon concentrations were generally measured in samples of 40–80 mg pure mineral separates (quartz, if nothing else is indicated). Neon and beryllium results reported in the Tables are given within two-sigma errors. The errors include uncertainties for the variability of chemical processing for the radionuclide, and statistical, sensitivity, and mass-discrimination errors for the noble gas measurements. Absolute errors of neon abundances are not included in the noble gas data, but are about 2 % as determined with two independent air-calibrations. Exposure ages of quartz samples were calculated with CosmoCalc 1.0 (Vermeesch 2007: *CosmoCalc: an Excel add-in for cosmogenic nuclide calculations. Geochemistry, Geophysics, Geosystems*, **8**, doi: 10.1029/2006GC001530.), using altitude and latitude production rate scaling factors defined by Stone (2000: *Air pressure and cosmogenic isotope production. Journal of Geophysical Research B*, **105**, 23753–23759) and default values for all parameters. Exposure ages of amphibole and pyroxene samples were calculated using the same scaling method and elemental production rates according to Kober et al. (2005: *In situ cosmogenic <sup>10</sup>Be and <sup>21</sup>Ne in sanidine and in situ cosmogenic <sup>3</sup>He in Fe-Ti-oxide minerals. Earth and Planetary Science Letters*, **236**, 404–418). The <sup>21</sup>Ne concentrations used in the calculations derive from the neon excesses above air (<sup>21</sup>Ne<sub>exc</sub>) of the relevant temperature steps under the assumption of entirely atmospheric <sup>20</sup>Ne concentrations.

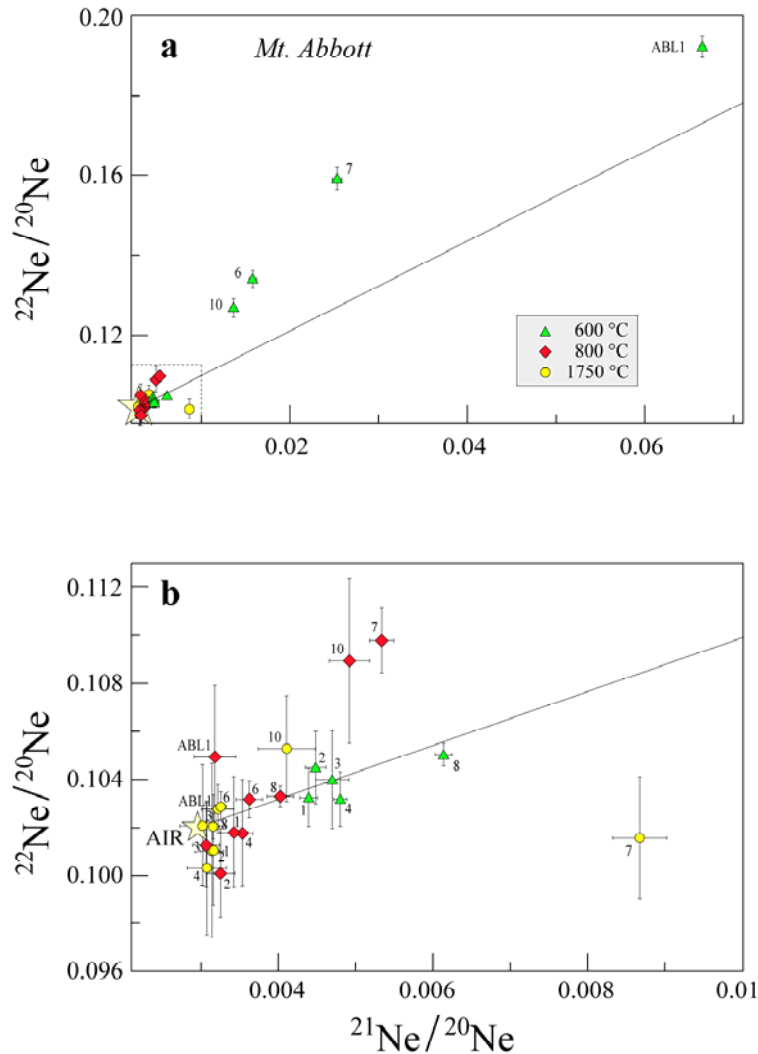
## Supplementary data for section 3.3

Table II.1. Complete neon data of all samples presented in section 3.3.

Sample	Heating temperature (°C); time (min)	$^{20}\text{Ne}$ ( $10^9$ atoms $\text{g}^{-1}$ )	$^{21}\text{Ne}/^{20}\text{Ne}$ ( $10^{-3}$ )	$^{22}\text{Ne}/^{20}\text{Ne}$	$^{21}\text{Ne}_{\text{exc}}$ ( $10^6$ atoms $\text{g}^{-1}$ )
<i>Mt. Abbott area</i>					
ABL 1	600; 45	$2.36 \pm 0.07$	$66.47 \pm 0.33$	$0.1922 \pm 0.0026$	$150.0 \pm 5.8$
	800; 20	$1.39 \pm 0.03$	$3.18 \pm 0.27$	$0.1050 \pm 0.0030$	$0.31 \pm 0.46$
	1750; 20	$3.29 \pm 0.05$	$3.22 \pm 0.21$	$0.1028 \pm 0.0010$	$0.86 \pm 0.86$
ABB 1	600; 45	$10.97 \pm 0.17$	$4.39 \pm 0.11$	$0.1033 \pm 0.0012$	$15.7 \pm 2.0$
	800; 20	$3.09 \pm 0.07$	$3.43 \pm 0.18$	$0.1018 \pm 0.0023$	$1.45 \pm 0.84$
	1750; 20	$2.01 \pm 0.04$	$3.16 \pm 0.07$	$0.1011 \pm 0.0023$	$0.41 \pm 0.31$
ABB 2	600; 45	$6.32 \pm 0.10$	$4.48 \pm 0.13$	$0.1045 \pm 0.0015$	$9.6 \pm 1.3$
	800; 20	$1.30 \pm 0.03$	$3.25 \pm 0.19$	$0.1001 \pm 0.0019$	$0.38 \pm 0.36$
	1750; 20	$0.86 \pm 0.02$	$3.14 \pm 0.15$	$0.1010 \pm 0.0036$	$0.16 \pm 0.22$
ABB 3	600; 45	$5.15 \pm 0.05$	$4.70 \pm 0.21$	$0.1040 \pm 0.0020$	$9.0 \pm 1.3$
	800; 20	$1.32 \pm 0.03$	$3.07 \pm 0.17$	$0.1013 \pm 0.0018$	$0.15 \pm 0.32$
	1750; 20	$1.26 \pm 0.04$	$3.02 \pm 0.29$	$0.1021 \pm 0.0025$	$0.08 \pm 0.49$
ABB 4	600; 45	$6.27 \pm 0.07$	$4.80 \pm 0.09$	$0.1032 \pm 0.0011$	$11.55 \pm 0.86$
	800; 20	$1.28 \pm 0.02$	$3.54 \pm 0.14$	$0.1018 \pm 0.0022$	$0.74 \pm 0.27$
	1750; 20	$0.98 \pm 0.03$	$3.08 \pm 0.25$	$0.1003 \pm 0.0028$	$0.12 \pm 0.36$
ABB 6	600; 45	$3.61 \pm 0.07$	$15.81 \pm 0.43$	$0.1341 \pm 0.0021$	$46.4 \pm 2.3$
	800; 20	$1.75 \pm 0.08$	$3.63 \pm 0.17$	$0.1032 \pm 0.0008$	$1.17 \pm 0.66$
	1750; 20	$1.94 \pm 0.06$	$3.26 \pm 0.07$	$0.1029 \pm 0.0006$	$0.58 \pm 0.41$
ABB 7	600; 45	$2.55 \pm 0.09$	$25.32 \pm 0.54$	$0.1591 \pm 0.0028$	$56.9 \pm 3.1$
	800; 20	$0.98 \pm 0.03$	$5.34 \pm 0.16$	$0.1098 \pm 0.0013$	$2.33 \pm 0.30$
	1750; 20	$0.92 \pm 0.06$	$8.67 \pm 0.35$	$0.1016 \pm 0.0026$	$5.28 \pm 0.83$
ABB 8	600; 45	$7.93 \pm 0.08$	$6.14 \pm 0.11$	$0.1050 \pm 0.0005$	$25.2 \pm 1.3$
	800; 20	$2.59 \pm 0.07$	$4.03 \pm 0.17$	$0.1033 \pm 0.0004$	$2.77 \pm 0.74$
	1750; 20	$2.02 \pm 0.06$	$3.16 \pm 0.08$	$0.1021 \pm 0.0005$	$0.40 \pm 0.41$
ABB 10	600; 45	$3.76 \pm 0.05$	$13.64 \pm 0.35$	$0.1268 \pm 0.0023$	$40.2 \pm 1.8$
	800; 20	$1.05 \pm 0.01$	$4.92 \pm 0.26$	$0.1089 \pm 0.0034$	$2.07 \pm 0.32$
	1750; 20	$0.93 \pm 0.01$	$4.11 \pm 0.37$	$0.1053 \pm 0.0022$	$1.07 \pm 0.39$
<i>Mt. Browning area</i>					
BROW 1	600; 45	$5.88 \pm 0.07$	$6.28 \pm 0.20$	$0.1075 \pm 0.0018$	$19.5 \pm 1.5$
	800; 20	$1.83 \pm 0.02$	$3.20 \pm 0.11$	$0.1022 \pm 0.0020$	$0.44 \pm 0.27$
	1750; 20	$1.61 \pm 0.03$	$5.88 \pm 0.23$	$0.1028 \pm 0.0027$	$4.71 \pm 0.50$
BROW 2	600; 45	$7.13 \pm 0.10$	$4.22 \pm 0.10$	$0.1044 \pm 0.0015$	$9.0 \pm 1.1$
	800; 20	$1.39 \pm 0.06$	$2.98 \pm 0.20$	$0.1013 \pm 0.0036$	$0.03 \pm 0.50$
	1750; 20	$1.34 \pm 0.07$	$13.56 \pm 0.53$	$0.1079 \pm 0.0026$	$14.2 \pm 1.4$
BROW 3	600; 45	$3.85 \pm 0.10$	$14.44 \pm 0.24$	$0.1203 \pm 0.0015$	$44.2 \pm 2.1$
	800; 20	$1.03 \pm 0.05$	$5.12 \pm 0.29$	$0.1056 \pm 0.0038$	$2.23 \pm 0.57$
	1750; 20	$1.13 \pm 0.05$	$14.65 \pm 0.88$	$0.1067 \pm 0.0015$	$13.2 \pm 1.4$

**Table II.1.** Continued.

Sample	Heating temperature (°C); time (min)	$^{20}\text{Ne}$ ( $10^9$ atoms $\text{g}^{-1}$ )	$^{21}\text{Ne}/^{20}\text{Ne}$ ( $10^{-3}$ )	$^{22}\text{Ne}/^{20}\text{Ne}$	$^{21}\text{Ne}_{\text{exc}}$ ( $10^6$ atoms $\text{g}^{-1}$ )
BROW 7	600; 45	$2.95 \pm 0.06$	$7.17 \pm 0.22$	$0.1078 \pm 0.0027$	$12.4 \pm 1.0$
	800; 20	$1.50 \pm 0.03$	$3.60 \pm 0.17$	$0.1020 \pm 0.0036$	$0.97 \pm 0.37$
	1750; 20	$2.73 \pm 0.07$	$5.11 \pm 0.28$	$0.1043 \pm 0.0031$	$5.9 \pm 1.0$
BROW 8	600; 45	$2.11 \pm 0.02$	$6.21 \pm 0.29$	$0.1077 \pm 0.0019$	$6.87 \pm 0.71$
	800; 20	$0.79 \pm 0.02$	$3.14 \pm 0.21$	$0.1027 \pm 0.0037$	$0.15 \pm 0.25$
	1750; 20	$1.70 \pm 0.04$	$2.90 \pm 0.15$	$0.1043 \pm 0.0024$	$0.0 \pm 0.0$
BROW 10	600; 45	$2.42 \pm 0.07$	$5.36 \pm 0.16$	$0.1025 \pm 0.0009$	$5.81 \pm 0.73$
	800; 20	$1.62 \pm 0.05$	$3.13 \pm 0.06$	$0.1012 \pm 0.0006$	$0.28 \pm 0.36$
	1750; 20	$1.83 \pm 0.04$	$3.54 \pm 0.09$	$0.1020 \pm 0.0010$	$1.07 \pm 0.34$
BROW 11	600; 45	$2.10 \pm 0.06$	$3.50 \pm 0.08$	$0.1020 \pm 0.0007$	$1.14 \pm 0.47$
	800; 20	$1.53 \pm 0.05$	$2.95 \pm 0.06$	$0.1018 \pm 0.0008$	$0.0 \pm 0.0$
	1750; 20	$1.47 \pm 0.06$	$3.13 \pm 0.07$	$0.1018 \pm 0.0008$	$0.25 \pm 0.41$



**Fig. II.1.** Neon three-isotope diagrams of Mt. Abbott samples. The line in the graphs is the atmospheric-cosmogenic mixing line for quartz. **a.** Data points from all Mt. Abbott samples (error limits are  $2\sigma$ ). The dashed box shows the area of the diagram shown in **b.** **b.** An enlargement of the data that have low neon ratios. Sample abbreviations: 1–10 represent samples ABB1, 2, 3, 4, 6, 7, 8 and 10.

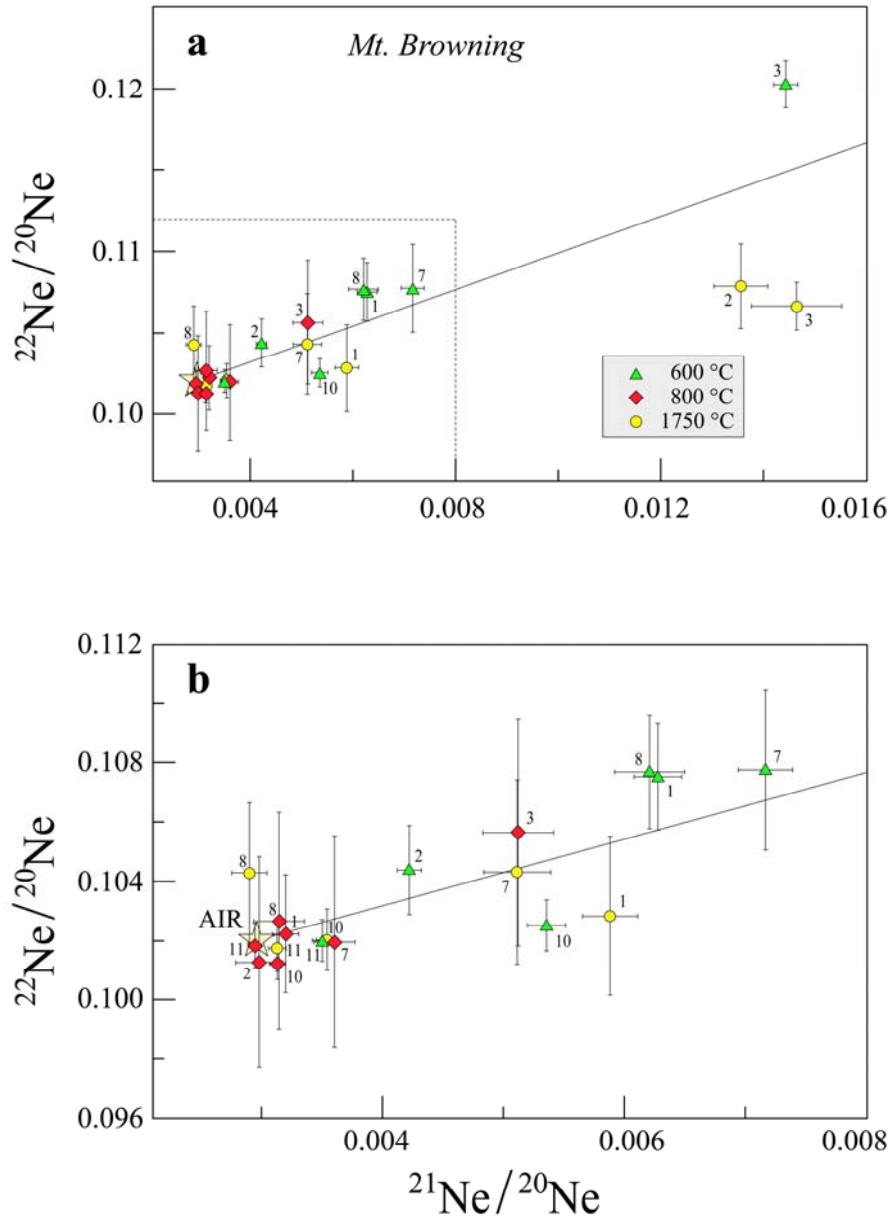


**Fig. II.2.** Neon three-isotope diagrams of Mt. Browning samples. The line in the graphs is the atmospheric-cosmogenic mixing line for quartz. **a.** Data points from all Mt. Browning samples (error limits are  $2\sigma$ ). The dashed box shows the area of the diagram shown in **b.** **b.** An enlargement of the data that have low neon ratios. Sample abbreviations: 1–11 represent samples BROW1, 2, 3, 7, 8, 10 and 11.

## Additional data

### Antarctica

**Table II.2.** Site details and exposure ages of all additional Antarctic samples.

Sample	Location	Altitude (m a.s.l.)	Corr. factor <sup>a</sup>	<sup>21</sup> Ne <sub>exc</sub> (10 <sup>6</sup> at g <sup>-1</sup> )	<sup>10</sup> Be <sup>b</sup> (10 <sup>6</sup> at g <sup>-1</sup> )	Apparent <sup>21</sup> Ne age (ka)	Apparent <sup>10</sup> Be age <sup>b</sup> (ka)
ANL 1	Andersson Ridge	298	0.930	5.53 ± 0.68	0.5 ± 0	(172 ± 21)	61 ± 6
ANL 2	Andersson Ridge	298	0.918	3.51 ± 0.40	0.4 ± 0	(110 ± 13)	45 ± 4
ARC 1	Archambault Ridge	2726	0.983	828 ± 32	109 ± 7	3525 ± 136	4322 ± 730
BELL 1	Mt. Bellingshausen	910	0.946	86.0 ± 3.6	11 ± 1	1484 ± 63	933 ± 56
BR 1	Black Ridge	915	0.950	9.0 ± 1.1	2.2 ± 0.1	146 ± 18	144 ± 10
BR 2	Black Ridge	937	0.976	17.0 ± 2.2	4.1 ± 0.2	271 ± 35	285 ± 15
CR 1	Mt. Crummer	888	0.963	103.1 ± 3.0	16 ± 1	1781 ± 53	1574 ± 129
EMI 1	Mt. Emison	1622	0.976	4.07 ± 0.55	1.2 ± 0.1	38 ± 5	45 ± 4
EMI 2 <sup>1</sup>	Mt. Emison	1625	-	35.2 ± 3.4	-	265 ± 26	-
EMI 3	Mt. Emison	1615	0.952	65.6 ± 2.0	13 ± 1	628 ± 19	585 ± 38
EMI 4 <sup>1</sup>	Mt. Emison	1614	-	109.5 ± 5.7	-	794 ± 42	-
EMI 5	Mt. Emison	1614	0.959	84.4 ± 2.9	16 ± 1	802 ± 28	742 ± 50
GER 1	Mt. Gerlache	810	0.959	55.3 ± 2.0	6.8 ± 0.4	1027 ± 37	576 ± 4
GERL 1	Mt. Gerlache	360	0.959	3.9 ± 1.2	0.1 ± 0	(109 ± 33)	7 ± 2
GERL 7B	Mt. Gerlache	29	0.677	9.5 ± 1.0	0.3 ± 0	(539 ± 58)	60 ± 5
GERL 8	Mt. Gerlache	558	0.979	20.5 ± 2.0	2.6 ± 0.2	472 ± 47	244 ± 16
LH 1	Lichen Hills	1979	0.891	10.4 ± 0.9	0.2 ± 0.1	(81 ± 7)	7 ± 1
POL 2	Mt. Pollock	2640	0.924	850 ± 26	92 ± 6	4065 ± 124	3692 ± 491
POL 3	Mt. Pollock	2640	0.943	956 ± 24	90 ± 5	4478 ± 111	3355 ± 390
RHS 4 <sup>2</sup>	Ricker Hills	1589	-	48.9 ± 3.1	-	(363 ± 23)	-
971210.01	Andersson Ridge	420	0.983	75.6 ± 3.1	0.1 ± 0	(1972 ± 82)	10 ± 0
971210.02	Andersson Ridge	420	0.959	6.1 ± 1.2	0.6 ± 0.1	(164 ± 32)	70 ± 7
971210.10	Black Ridge	1000	0.959	3.2 ± 0.4	0.8 ± 0.1	48 ± 5	46 ± 6
1000202.04 <sup>2</sup>	Ford Peak	1880	-	443 ± 12	-	(2521 ± 68)	-
1000202.04 <sup>2*</sup>	Ford Peak	1880	-	986 ± 39	-	4391 ± 175	-
1000202.05 <sup>2</sup>	Ford Peak	1880	-	376 ± 13	-	(2182 ± 73)	-
1000202.06 <sup>2</sup>	Ford Peak	1880	-	351 ± 11	-	(1988 ± 61)	-

<sup>21</sup>Ne ages in brackets have to be handled with care (nucleogenic neon; concentrations close to blank values; plagioclase contamination in pyroxene samples).

<sup>a</sup> Applied corrections are calculated for topographic shielding, surface geometry and sample thickness.

<sup>b</sup> Determined by L. Di Nicola.

<sup>1</sup> Amphibole sample.

<sup>2</sup> Pyroxene sample (probably contaminated with plagioclase).

\* Same sample as 1000202.04, but different mineral phase.

**Table II.3.** Neon isotope data of all additional Antarctic samples.

Sample	Heating temperature (°C); time (min)	$^{20}\text{Ne}$ ( $10^9$ atoms $\text{g}^{-1}$ )	$^{21}\text{Ne}/^{20}\text{Ne}$ ( $10^{-3}$ )	$^{22}\text{Ne}/^{20}\text{Ne}$	$^{21}\text{Ne}_{\text{exc}}$ ( $10^6$ atoms $\text{g}^{-1}$ )
ANL 1	600; 45	$10.98 \pm 0.04$	$3.46 \pm 0.05$	$0.1027 \pm 0.0003$	$5.53 \pm 0.68$
	800; 20	$2.65 \pm 0.03$	$3.08 \pm 0.05$	$0.1027 \pm 0.0005$	$0.31 \pm 0.26$
	1750; 20	$1.64 \pm 0.04$	$3.07 \pm 0.07$	$0.1020 \pm 0.0005$	$0.18 \pm 0.31$
ANL 2	600; 45	$3.62 \pm 0.03$	$3.93 \pm 0.08$	$0.1033 \pm 0.0008$	$3.51 \pm 0.40$
	800; 20	$2.21 \pm 0.05$	$3.53 \pm 0.07$	$0.1027 \pm 0.0008$	$1.26 \pm 0.38$
	1750; 20	$1.35 \pm 0.04$	$3.62 \pm 0.12$	$0.1023 \pm 0.0013$	$0.90 \pm 0.36$
ARC 1	600; 45	$3.94 \pm 0.10$	$213.0 \pm 4.3$	$0.3438 \pm 0.0054$	$828 \pm 32$
	800; 20	$2.03 \pm 0.06$	$3.29 \pm 0.08$	$0.1020 \pm 0.0008$	$0.67 \pm 0.41$
	1750; 20	$1.93 \pm 0.06$	$3.22 \pm 0.08$	$0.1011 \pm 0.0007$	$0.50 \pm 0.41$
BELL 1	600; 45	$11.17 \pm 0.14$	$10.66 \pm 0.21$	$0.1116 \pm 0.0010$	$86.0 \pm 3.6$
	800; 20	$3.92 \pm 0.03$	$5.01 \pm 0.17$	$0.1053 \pm 0.0021$	$8.03 \pm 0.81$
	1750; 20	$1.91 \pm 0.07$	$3.98 \pm 0.23$	$0.1040 \pm 0.0029$	$1.95 \pm 0.72$
BR 1	600; 45	$4.02 \pm 0.09$	$5.19 \pm 0.16$	$0.1038 \pm 0.0004$	$9.0 \pm 1.1$
	800; 20	$1.93 \pm 0.09$	$2.95 \pm 0.06$	$0.1021 \pm 0.0007$	$0.0 \pm 0.0$
	1750; 20	$1.86 \pm 0.07$	$3.23 \pm 0.03$	$0.1021 \pm 0.0007$	$0.50 \pm 0.41$
BR 2	600; 45	$2.07 \pm 0.14$	$11.17 \pm 0.40$	$0.1106 \pm 0.0018$	$17.0 \pm 2.2$
	800; 20	$1.43 \pm 0.02$	$3.01 \pm 0.24$	$0.1051 \pm 0.0040$	$0.08 \pm 0.42$
	1750; 20	$3.79 \pm 0.08$	$2.87 \pm 0.18$	$0.1030 \pm 0.0024$	$0.0 \pm 0.0$
CR 1	600; 45	$2.42 \pm 0.04$	$45.55 \pm 0.49$	$0.1516 \pm 0.0028$	$103.1 \pm 3.0$
	800; 20	$1.09 \pm 0.04$	$3.75 \pm 0.25$	$0.1022 \pm 0.0016$	$0.86 \pm 0.42$
	1750; 20	$3.23 \pm 0.09$	$2.97 \pm 0.16$	$0.1035 \pm 0.0016$	$0.03 \pm 0.82$
EMI 1	600; 45	$2.24 \pm 0.05$	$4.77 \pm 0.14$	$0.1029 \pm 0.0008$	$4.07 \pm 0.55$
	800; 20	$1.78 \pm 0.07$	$2.95 \pm 0.06$	$0.1022 \pm 0.0006$	$0.0 \pm 0.0$
	1750; 20	$1.84 \pm 0.05$	$2.85 \pm 0.06$	$0.1027 \pm 0.0010$	$0.0 \pm 0.0$
EMI 2 <sup>1</sup>	850; 45	$6.81 \pm 0.42$	$3.50 \pm 0.11$	$0.1014 \pm 0.0007$	$3.7 \pm 2.9$
	1500; 15	$4.54 \pm 0.08$	$9.90 \pm 0.26$	$0.1107 \pm 0.0015$	$31.5 \pm 1.8$
	1750; 15	$2.20 \pm 0.08$	$2.89 \pm 0.16$	$0.0972 \pm 0.0012$	$0.0 \pm 0.0$
EMI 3	600; 45	$2.86 \pm 0.04$	$25.91 \pm 0.38$	$0.1275 \pm 0.0030$	$65.6 \pm 2.0$
	800; 20	$1.44 \pm 0.05$	$3.70 \pm 0.19$	$0.0998 \pm 0.0028$	$1.07 \pm 0.46$
	1750; 20	$1.72 \pm 0.02$	$10.23 \pm 0.47$	$0.1016 \pm 0.0023$	$12.49 \pm 0.94$
EMI 4 <sup>1</sup>	850; 45	$11.03 \pm 0.35$	$3.84 \pm 0.11$	$0.1009 \pm 0.0003$	$9.7 \pm 2.8$
	1500; 15	$5.52 \pm 0.16$	$21.04 \pm 0.44$	$0.1242 \pm 0.0011$	$99.8 \pm 5.0$
	1750; 15	$2.55 \pm 0.10$	$2.95 \pm 0.06$	$0.1014 \pm 0.0008$	$0.0 \pm 0.0$
EMI 5	600; 45	$3.04 \pm 0.06$	$30.70 \pm 0.40$	$0.1326 \pm 0.0018$	$84.4 \pm 2.9$
	800; 20	$1.25 \pm 0.05$	$3.13 \pm 0.07$	$0.1013 \pm 0.0009$	$0.21 \pm 0.35$
	1750; 20	$1.17 \pm 0.04$	$6.27 \pm 0.28$	$0.1025 \pm 0.0009$	$3.88 \pm 0.51$
GER 1	600; 45	$8.44 \pm 0.08$	$9.50 \pm 0.15$	$0.1098 \pm 0.0011$	$55.3 \pm 2.0$
	800; 20	$1.87 \pm 0.04$	$4.88 \pm 0.19$	$0.1045 \pm 0.0020$	$3.59 \pm 0.51$
	1750; 20	$0.99 \pm 0.04$	$3.78 \pm 0.27$	$0.1021 \pm 0.0033$	$0.81 \pm 0.41$
GERL 1	600; 45	$7.79 \pm 0.12$	$3.45 \pm 0.09$	$0.1026 \pm 0.0016$	$3.9 \pm 1.2$
	800; 20	$2.39 \pm 0.03$	$3.09 \pm 0.24$	$0.1026 \pm 0.0032$	$0.32 \pm 0.65$
	1750; 20	$3.09 \pm 0.11$	$4.03 \pm 0.19$	$0.1024 \pm 0.0022$	$3.3 \pm 1.0$

<sup>1</sup> Amphibole sample.

Table II.3. Continued.

Sample	Heating temperature (°C); time (min)	$^{20}\text{Ne}$ ( $10^9$ atoms $\text{g}^{-1}$ )	$^{21}\text{Ne}/^{20}\text{Ne}$ ( $10^{-3}$ )	$^{22}\text{Ne}/^{20}\text{Ne}$	$^{21}\text{Ne}_{\text{exc}}$ ( $10^6$ atoms $\text{g}^{-1}$ )
GERL 7B	600; 45	$3.01 \pm 0.08$	$6.12 \pm 0.19$	$0.1080 \pm 0.0032$	$9.5 \pm 1.0$
	800; 20	$1.62 \pm 0.02$	$3.93 \pm 0.23$	$0.1034 \pm 0.0021$	$1.57 \pm 0.44$
	1750; 20	$2.55 \pm 0.02$	$2.97 \pm 0.13$	$0.1029 \pm 0.0016$	$0.03 \pm 0.40$
GERL 8	600; 45	$3.61 \pm 0.10$	$8.64 \pm 0.40$	$0.1077 \pm 0.0025$	$20.5 \pm 2.0$
	800; 20	$1.93 \pm 0.03$	$3.53 \pm 0.24$	$0.1028 \pm 0.0032$	$1.09 \pm 0.55$
	1750; 20	$3.54 \pm 0.06$	$3.04 \pm 0.20$	$0.1013 \pm 0.0026$	$0.27 \pm 0.92$
LH 1	600; 45	$2.76 \pm 0.09$	$6.71 \pm 0.08$	$0.1022 \pm 0.0003$	$10.36 \pm 0.90$
	800; 20	$2.05 \pm 0.07$	$2.97 \pm 0.05$	$0.1013 \pm 0.0004$	$0.02 \pm 0.46$
	1750; 20	$1.98 \pm 0.06$	$2.94 \pm 0.08$	$0.1016 \pm 0.0007$	$0.0 \pm 0.0$
POL 2	600; 45	$3.11 \pm 0.06$	$275.9 \pm 3.2$	$0.4213 \pm 0.0058$	$850 \pm 26$
	800; 20	$1.00 \pm 0.04$	$3.18 \pm 0.35$	$0.0997 \pm 0.0020$	$0.22 \pm 0.51$
	1750; 20	$1.19 \pm 0.06$	$3.29 \pm 0.29$	$0.1005 \pm 0.0020$	$0.39 \pm 0.55$
POL 3	600; 45	$4.14 \pm 0.05$	$233.9 \pm 1.6$	$0.3741 \pm 0.0031$	$956 \pm 24$
	800; 20	$0.98 \pm 0.02$	$2.82 \pm 0.27$	$0.1007 \pm 0.0028$	$0.0 \pm 0.0$
	1750; 20	$1.05 \pm 0.03$	$3.47 \pm 0.25$	$0.0999 \pm 0.0024$	$0.54 \pm 0.39$
RHS 4 <sup>2</sup>	850; 45	$15.21 \pm 0.16$	$3.64 \pm 0.09$	$0.1032 \pm 0.0011$	$10.3 \pm 1.9$
	1500; 15	$6.25 \pm 0.10$	$9.13 \pm 0.28$	$0.1061 \pm 0.0022$	$38.6 \pm 2.4$
	1750; 15	$3.92 \pm 0.16$	$2.97 \pm 0.07$	$0.1026 \pm 0.0012$	$0.04 \pm 0.99$
971210.01	600; 45	$23.78 \pm 0.17$	$6.14 \pm 0.08$	$0.1061 \pm 0.0006$	$75.6 \pm 3.1$
	800; 20	$4.24 \pm 0.06$	$5.59 \pm 0.19$	$0.1055 \pm 0.0018$	$11.1 \pm 1.1$
	1750; 20	$1.82 \pm 0.04$	$4.63 \pm 0.26$	$0.1041 \pm 0.0023$	$3.04 \pm 0.64$
971210.02	600; 45	$10.34 \pm 0.06$	$3.55 \pm 0.09$	$0.1030 \pm 0.0012$	$6.1 \pm 1.2$
	800; 20	$2.29 \pm 0.03$	$3.21 \pm 0.13$	$0.1040 \pm 0.0013$	$0.57 \pm 0.42$
	1750; 20	$1.12 \pm 0.05$	$2.98 \pm 0.25$	$0.1037 \pm 0.0025$	$0.02 \pm 0.48$
971210.10	600; 45	$2.89 \pm 0.03$	$4.05 \pm 0.09$	$0.1022 \pm 0.0005$	$3.16 \pm 0.36$
	800; 20	$2.06 \pm 0.06$	$3.02 \pm 0.07$	$0.1021 \pm 0.0008$	$0.12 \pm 0.39$
	1750; 20	$1.16 \pm 0.04$	$3.05 \pm 0.06$	$0.1018 \pm 0.0012$	$0.10 \pm 0.28$
1000202.04 <sup>2</sup>	850; 45	$24.26 \pm 0.16$	$21.08 \pm 0.28$	$0.1284 \pm 0.0012$	$440 \pm 12$
	1500; 15	$3.05 \pm 0.14$	$3.93 \pm 0.12$	$0.1036 \pm 0.0021$	$3.0 \pm 1.1$
	1750; 15	$0.79 \pm 0.03$	$3.08 \pm 0.30$	$0.1017 \pm 0.0047$	$0.09 \pm 0.33$
1000202.04 <sup>2*</sup>	850; 45	$3.02 \pm 0.05$	$45.67 \pm 0.71$	$0.1486 \pm 0.0035$	$129.0 \pm 4.3$
	1500; 15	$2.46 \pm 0.10$	$351.6 \pm 3.9$	$0.4722 \pm 0.0107$	$857 \pm 39$
	1750; 15	$0.87 \pm 0.01$	$4.25 \pm 0.44$	$0.0990 \pm 0.0034$	$1.13 \pm 0.43$
1000202.05 <sup>2</sup>	850; 45	$10.79 \pm 0.19$	$37.73 \pm 0.58$	$0.1513 \pm 0.0031$	$375 \pm 13$
	1500; 15	$2.38 \pm 0.04$	$3.45 \pm 0.37$	$0.1001 \pm 0.0057$	$1.2 \pm 1.0$
	1750; 15	$2.06 \pm 0.03$	$2.99 \pm 0.35$	$0.1031 \pm 0.0037$	$0.06 \pm 0.81$
1000202.06 <sup>2</sup>	850; 45	$10.71 \pm 0.14$	$35.62 \pm 0.56$	$0.1517 \pm 0.0022$	$350 \pm 11$
	1500; 15	$2.37 \pm 0.04$	$3.41 \pm 0.14$	$0.1004 \pm 0.0014$	$1.07 \pm 0.48$
	1750; 15	$1.76 \pm 0.14$	$2.84 \pm 0.19$	$0.0978 \pm 0.0027$	$0.0 \pm 0.0$

<sup>2</sup> Pyroxene sample (probably contaminated with plagioclase).

\* Same sample as 1000202.04, but different mineral phase.

**Table II.4.** Helium isotope data of Antarctic amphibole and pyroxene samples.

Sample	Heating temperature (°C); time (min)	<sup>4</sup> He (10 <sup>12</sup> atoms g <sup>-1</sup> )	<sup>3</sup> He (10 <sup>6</sup> atoms g <sup>-1</sup> )	<sup>3</sup> He / <sup>4</sup> He (10 <sup>-6</sup> )	R / R <sub>a</sub>
EMI 2 <sup>1</sup>	850; 45	1787.5 ± 1.7	456 ± 10	0.26 ± 0.01	0.18
	1500; 15	18.50 ± 0.02	0.35 ± 0.80	0.02 ± 0.04	0.01
EMI 4 <sup>1</sup>	850; 45	3832.5 ± 3.4	1636 ± 21	0.43 ± 0.01	0.31
	1500; 15	38.79 ± 0.04	3.3 ± 1.3	0.09 ± 0.03	0.06
RHS 4 <sup>2</sup>	850; 45	268.65 ± 0.56	122.3 ± 6.9	0.46 ± 0.03	0.33
	1500; 15	30.14 ± 0.03	7.4 ± 1.4	0.24 ± 0.05	0.18
1000202.04 <sup>2</sup>	850; 45	1.41 ± 0.02	22.9 ± 1.9	16.3 ± 1.4	11.8
	1500; 15	0.22 ± 0.01	1705 ± 75	7834 ± 383	5660
1000202.04 <sup>2*</sup>	850; 45	59.79 ± 0.78	3564 ± 142	59.6 ± 2.5	43.1
1000202.05 <sup>2</sup>	850; 45	2.50 ± 0.06	10.1 ± 2.5	4.1 ± 1.0	2.93
	1500; 15	0.40 ± 0.01	0.77 ± 0.45	1.9 ± 1.1	1.40
1000202.06 <sup>2</sup>	850; 45	1.38 ± 0.03	5.5 ± 1.1	3.96 ± 0.81	2.86
	1500; 15	0.31 ± 0.01	0.56 ± 0.43	1.8 ± 1.4	1.29

R<sub>a</sub> is the atmospheric <sup>3</sup>He / <sup>4</sup>He ratio.

<sup>1</sup> Amphibole sample.

<sup>2</sup> Pyroxene sample (probably contaminated with plagioclase).

\* Same sample as 1000202.04, but different mineral phase.

**Table II.5.** Relative concentrations of elements that produce cosmogenic <sup>21</sup>Ne, measured by ICP-AES at CNRS-CRPG, Vandoeuvre, France (<http://cprg.cnrs-nancy.fr/SARM>).

Sample	Al (weight %)	Ca (weight %)	Fe (weight %)	Mg (weight %)	Na (weight %)	Si (weight %)	O (weight %)
EMI 2	5.0	8.6	16.2	5.0	0.8	19.6	40.8
EMI 4	4.1	8.8	14.3	5.8	0.6	21.3	41.5
RHS 4	1.2	8.8	17.1	6.7	0.2	22.9	42.5
1000202.04	14.2	8.5	0.6	0.1	2.6	25.3	46.0
1000202.04 <sup>*</sup>	0.8	7.1	11.7	11.2	0.1	24.7	44.2
1000202.05	14.0	8.4	0.5	0.1	2.4	25.5	46.0
1000202.06	14.6	8.7	0.6	0.0	2.5	25.3	46.5

\* same sample as 1000202.04, but different mineral phase.



## Greenland

**Table II.6.** Site details and exposure ages of Greenland samples.

Sample	Location	Altitude (m a.s.l.)	$^{21}\text{Ne}_{\text{exc}}$ ( $10^6$ atoms $\text{g}^{-1}$ )	$^{10}\text{Be}^{\text{a}}$ ( $10^5$ atoms $\text{g}^{-1}$ )	Apparent $^{21}\text{Ne}$ age <sup>b</sup> (ka)	Apparent $^{10}\text{Be}$ age <sup>a</sup> (ka)
001	Store Koldewey	630	$1.5 \pm 1.0$	$1.05 \pm 0.07$	$50 \pm 34$	$14 \pm 2$
004	Store Koldewey	93	$0.86 \pm 0.50$	$0.70 \pm 0.05$	$48 \pm 27$	$16 \pm 2$
005	Store Koldewey	617	$30.7 \pm 1.5$	$1.28 \pm 0.08$	$1009 \pm 49$	$18 \pm 2$
005*	Store Koldewey	617	$32.1 \pm 3.1$	-	$1055 \pm 102$	-
007	Store Koldewey	686	$2.75 \pm 0.64$	$4.05 \pm 0.20$	$85 \pm 20$	$51 \pm 6$
008	Store Koldewey	568	$5.27 \pm 0.68$	$6.74 \pm 0.24$	$182 \pm 23$	$97 \pm 10$
010	Store Koldewey	704	$9.55 \pm 0.76$	$13.50 \pm 0.41$	$289 \pm 23$	$178 \pm 16$
011	Store Koldewey	652	$5.07 \pm 0.91$	$2.58 \pm 0.13$	$162 \pm 29$	$33 \pm 4$

<sup>a</sup> Determined by A. Graf and published in: HÅKANSSON, L., GRAF, A., STRASKY, S., IVY-OCHS, S., KUBIK, P.W., HJORT, C. & SCHLÜCHTER, C. 2007. Cosmogenic  $^{10}\text{Be}$ -ages from the Store Koldewey island, NE Greenland. *Geografiska Annaler A*, **89**, 195–202.

<sup>b</sup>  $^{21}\text{Ne}$  ages have to be handled with care (nucleogenic neon). \* Repeat analysis.

**Table II.7.** Neon isotope data of all Greenland samples.

Sample	Heating T ( $^{\circ}\text{C}$ ); time (min)	$^{20}\text{Ne}$ ( $10^9$ atoms $\text{g}^{-1}$ )	$^{21}\text{Ne}/^{20}\text{Ne}$ ( $10^{-3}$ )	$^{22}\text{Ne}/^{20}\text{Ne}$	$^{21}\text{Ne}_{\text{exc}}$ ( $10^6$ atoms $\text{g}^{-1}$ )
001	600; 45	$3.15 \pm 0.15$	$3.44 \pm 0.09$	$0.1044 \pm 0.0022$	$1.5 \pm 1.0$
	800; 20	$1.17 \pm 0.05$	$3.02 \pm 0.16$	$0.0986 \pm 0.0026$	$0.08 \pm 0.38$
	1750; 20	$1.25 \pm 0.04$	$3.87 \pm 0.19$	$0.1021 \pm 0.0016$	$1.14 \pm 0.41$
004	600; 45	$1.63 \pm 0.05$	$3.49 \pm 0.18$	$0.1005 \pm 0.0021$	$0.86 \pm 0.50$
	800; 20	$1.23 \pm 0.05$	$3.79 \pm 0.24$	$0.1032 \pm 0.0030$	$1.02 \pm 0.52$
	1750; 20	$1.52 \pm 0.03$	$3.86 \pm 0.26$	$0.1038 \pm 0.0018$	$1.37 \pm 0.51$
005	600; 45	$4.99 \pm 0.06$	$7.26 \pm 0.13$	$0.1083 \pm 0.0014$	$21.4 \pm 1.1$
	800; 20	$2.64 \pm 0.06$	$6.46 \pm 0.28$	$0.1099 \pm 0.0035$	$9.3 \pm 1.0$
	1750; 20	$2.77 \pm 0.05$	$4.63 \pm 0.22$	$0.1040 \pm 0.0021$	$4.62 \pm 0.81$
005*	600; 45	$19.40 \pm 0.09$	$3.79 \pm 0.08$	$0.1013 \pm 0.0008$	$16.2 \pm 1.9$
	800; 20	$20.91 \pm 0.18$	$3.72 \pm 0.09$	$0.1032 \pm 0.0013$	$15.9 \pm 2.5$
	1750; 20	$9.93 \pm 0.13$	$3.64 \pm 0.15$	$0.1024 \pm 0.0011$	$6.7 \pm 1.9$
007	600; 45	$1.61 \pm 0.05$	$4.67 \pm 0.27$	$0.1026 \pm 0.0014$	$2.75 \pm 0.64$
	800; 20	$1.13 \pm 0.05$	$3.19 \pm 0.22$	$0.0993 \pm 0.0026$	$0.25 \pm 0.45$
	1750; 20	$1.69 \pm 0.06$	$3.32 \pm 0.23$	$0.1026 \pm 0.0025$	$0.61 \pm 0.62$
008	600; 45	$2.03 \pm 0.06$	$5.55 \pm 0.17$	$0.1040 \pm 0.0019$	$5.27 \pm 0.68$
	800; 20	$1.24 \pm 0.03$	$3.59 \pm 0.35$	$0.0988 \pm 0.0027$	$0.78 \pm 0.55$
	1750; 20	$1.71 \pm 0.04$	$3.23 \pm 0.22$	$0.1014 \pm 0.0020$	$0.46 \pm 0.50$
010	600; 45	$2.05 \pm 0.04$	$7.62 \pm 0.25$	$0.1046 \pm 0.0016$	$9.55 \pm 0.76$
	800; 20	$1.83 \pm 0.03$	$3.72 \pm 0.24$	$0.1007 \pm 0.0019$	$1.40 \pm 0.53$
	1750; 20	$1.67 \pm 0.07$	$3.47 \pm 0.19$	$0.1022 \pm 0.0034$	$0.86 \pm 0.61$
011	600; 45	$8.07 \pm 0.09$	$3.59 \pm 0.07$	$0.1029 \pm 0.0008$	$5.07 \pm 0.91$
	800; 20	$2.95 \pm 0.03$	$3.04 \pm 0.07$	$0.1021 \pm 0.0017$	$0.25 \pm 0.33$
	1750; 20	$3.32 \pm 0.03$	$5.77 \pm 0.26$	$0.1032 \pm 0.0008$	$9.3 \pm 1.0$

\* repeat analysis but after physical separation of the quartz instead of chemically HF processing.

*Asia, South America and Europe***Table II.8.** Site details and exposure ages of samples from Asia, South America and Europe.

Sample	Location	Altitude (m a.s.l.)	$^{21}\text{Ne}_{\text{exc}}$ ( $10^6$ atoms $\text{g}^{-1}$ )	$^{10}\text{Be}^{\text{a}}$ ( $10^6$ atoms $\text{g}^{-1}$ )	Apparent $^{21}\text{Ne}$ age (ka)
<i>Tibet</i>					
Ny 2	Nyalam	3902	$11.91 \pm 0.85$	-	$58 \pm 4$
Ny 6 bot	Nyalam	3941	$6.43 \pm 0.65$	-	$30 \pm 3$
Ny 7	Nyalam	3976	$17.0 \pm 1.5$	-	$81 \pm 7$
Ny 10	Nyalam	4301	$6.2 \pm 1.0$	-	$24 \pm 4$
Ny 17	Nyalam	3947	$36.9 \pm 3.4$	-	$172 \pm 16$
<i>Argentina</i>					
A 5		315	$10.24 \pm 0.61$	-	$361 \pm 21$
A 6		315	$8.1 \pm 1.7$	-	$283 \pm 61$
<i>Switzerland</i>					
A-Unten	Arolla, Valais	2220	$0.5 \pm 1.0$	$-0.0002 \pm 0.0013$	-
A-Oben	Arolla, Valais	2220	$0.7 \pm 1.2$	$0.0013 \pm 0.0010$	-
A-3	Arolla, Valais	2220	$0.7 \pm 1.1$	$0.0001 \pm 0.0008$	-
EG-04-02	Eggishorn, Valais	2887	$4.13 \pm 0.73$	-	$23 \pm 4$
<i>Germany</i>					
HS 1	Hoher Stall	44	$7.95 \pm 0.93$	-	-
HS 3	Hoher Stall	44	$5.15 \pm 0.59$	-	-

<sup>a</sup> Determined by L.M. Abbühl and published in: ABBÜHL, L.M., AKÇAR, N., STRASKY, S., GRAF, A., IVY-OCHS, S. & SCHLÜCHTER, C. 2008. A zero-exposure time test on an erratic boulder: evaluating the problem of pre-exposure in Surface Exposure Dating. *Quaternary Science Journal (Eiszeitalter und Gegenwart)*, submitted.

**Table II.9.** Neon isotope data of additional samples from Tibet, Argentina, Switzerland and Germany.

Sample	Heating temperature (°C); time (min)	$^{20}\text{Ne}$ ( $10^9$ atoms $\text{g}^{-1}$ )	$^{21}\text{Ne}/^{20}\text{Ne}$ ( $10^{-3}$ )	$^{22}\text{Ne}/^{20}\text{Ne}$	$^{21}\text{Ne}_{\text{exc}}$ ( $10^6$ atoms $\text{g}^{-1}$ )
<i>Tibet</i>					
Ny 2	600; 45	$1.86 \pm 0.04$	$9.37 \pm 0.31$	$0.1084 \pm 0.0024$	$11.91 \pm 0.85$
	800; 20	$1.32 \pm 0.02$	$3.18 \pm 0.20$	$0.1033 \pm 0.0021$	$0.30 \pm 0.33$
	1750; 20	$1.19 \pm 0.01$	$3.62 \pm 0.22$	$0.1010 \pm 0.0026$	$0.79 \pm 0.31$
Ny 6 bot	600; 45	$2.79 \pm 0.05$	$5.26 \pm 0.15$	$0.1039 \pm 0.0025$	$6.43 \pm 0.65$
	800; 20	$1.80 \pm 0.03$	$3.02 \pm 0.16$	$0.0983 \pm 0.0020$	$0.12 \pm 0.40$
	1750; 20	$2.92 \pm 0.07$	$3.10 \pm 0.18$	$0.1003 \pm 0.0014$	$0.40 \pm 0.77$
Ny 7	600; 45	$14.46 \pm 0.12$	$4.14 \pm 0.07$	$0.1030 \pm 0.0008$	$17.0 \pm 1.5$
	800; 20	$11.01 \pm 0.13$	$3.36 \pm 0.08$	$0.1019 \pm 0.0014$	$4.4 \pm 1.4$
	1750; 20	$4.17 \pm 0.04$	$3.67 \pm 0.15$	$0.1034 \pm 0.0018$	$2.96 \pm 0.76$
Ny 10	600; 45	$4.68 \pm 0.04$	$4.28 \pm 0.19$	$0.1030 \pm 0.0012$	$6.2 \pm 1.0$
	800; 20	$2.63 \pm 0.06$	$2.94 \pm 0.18$	$0.1012 \pm 0.0017$	$0.0 \pm 0.0$
	1750; 20	$2.32 \pm 0.04$	$4.03 \pm 0.29$	$0.0998 \pm 0.0031$	$2.48 \pm 0.83$
Ny 17	600; 45	$27.03 \pm 0.27$	$4.32 \pm 0.08$	$0.1029 \pm 0.0007$	$36.9 \pm 3.4$
	800; 20	$2.79 \pm 0.03$	$3.26 \pm 0.19$	$0.1021 \pm 0.0020$	$0.85 \pm 0.61$
	1750; 20	$1.42 \pm 0.02$	$2.92 \pm 0.31$	$0.1020 \pm 0.0028$	$0.0 \pm 0.0$
<i>Argentina</i>					
A 5	600; 45	$4.23 \pm 0.02$	$5.38 \pm 0.11$	$0.1033 \pm 0.0015$	$10.24 \pm 0.61$
	800; 20	$1.14 \pm 0.02$	$3.21 \pm 0.20$	$0.1007 \pm 0.0019$	$0.28 \pm 0.28$
	1750; 20	$2.09 \pm 0.05$	$3.14 \pm 0.13$	$0.1059 \pm 0.0029$	$0.38 \pm 0.45$
A 6	600; 45	$18.18 \pm 0.11$	$3.40 \pm 0.08$	$0.1023 \pm 0.0011$	$8.1 \pm 1.7$
	800; 20	$2.63 \pm 0.03$	$3.03 \pm 0.16$	$0.1046 \pm 0.0016$	$0.18 \pm 0.53$
	1750; 20	$2.94 \pm 0.03$	$3.41 \pm 0.15$	$0.1016 \pm 0.0027$	$1.34 \pm 0.54$
<i>Switzerland</i>					
A-Unten	600; 45	$7.65 \pm 0.07$	$3.03 \pm 0.10$	$0.1016 \pm 0.0015$	$0.52 \pm 1.03$
	800; 20	$1.70 \pm 0.02$	$2.96 \pm 0.12$	$0.0995 \pm 0.0023$	$0.0 \pm 0.0$
	1750; 20	$1.95 \pm 0.05$	$3.06 \pm 0.20$	$0.1081 \pm 0.0028$	$0.20 \pm 0.55$
A-Oben	600; 45	$10.40 \pm 0.12$	$3.03 \pm 0.08$	$0.1020 \pm 0.0010$	$0.7 \pm 1.2$
	800; 20	$1.43 \pm 0.03$	$3.16 \pm 0.28$	$0.1022 \pm 0.0013$	$0.29 \pm 0.51$
	1750; 20	$1.05 \pm 0.02$	$14.16 \pm 0.52$	$0.1050 \pm 0.0033$	$11.81 \pm 0.70$
A-3	600; 45	$8.43 \pm 0.09$	$3.05 \pm 0.10$	$0.1015 \pm 0.0010$	$0.7 \pm 1.1$
	1750; 20	$1.42 \pm 0.03$	$2.95 \pm 0.25$	$0.1039 \pm 0.0023$	$0.0 \pm 0.0$
EG-04-02	600; 45	$3.40 \pm 0.03$	$4.17 \pm 0.18$	$0.1038 \pm 0.0009$	$4.13 \pm 0.73$
	800; 20	$2.34 \pm 0.07$	$3.51 \pm 0.20$	$0.1018 \pm 0.0022$	$1.29 \pm 0.72$
	1750; 20	$5.01 \pm 0.10$	$3.12 \pm 0.16$	$0.1041 \pm 0.0015$	$0.8 \pm 1.2$
<i>Germany</i>					
HS 1	600; 45	$13.29 \pm 0.11$	$3.56 \pm 0.03$	$0.1026 \pm 0.0002$	$7.95 \pm 0.93$
	800; 20	$4.29 \pm 0.08$	$3.31 \pm 0.05$	$0.1032 \pm 0.0006$	$1.49 \pm 0.57$
	1750; 20	$2.05 \pm 0.06$	$3.41 \pm 0.05$	$0.1038 \pm 0.0007$	$0.92 \pm 0.40$
HS 3	600; 45	$8.85 \pm 0.07$	$3.54 \pm 0.03$	$0.1021 \pm 0.0003$	$5.15 \pm 0.59$
	800; 20	$3.19 \pm 0.05$	$3.10 \pm 0.05$	$0.1030 \pm 0.0003$	$0.46 \pm 0.36$
	1750; 20	$1.53 \pm 0.04$	$3.69 \pm 0.07$	$0.1024 \pm 0.0006$	$1.12 \pm 0.30$

*Calibration standard CREU 1***Table II.10.** Neon isotope data of five aliquots of the CREU 1 quartz standard.

Sample	Heating temperature (°C); time (min)	$^{20}\text{Ne}$ ( $10^9$ atoms $\text{g}^{-1}$ )	$^{21}\text{Ne}/^{20}\text{Ne}$ ( $10^{-3}$ )	$^{22}\text{Ne}/^{20}\text{Ne}$	$^{21}\text{Ne}_{\text{exc}}$ ( $10^7$ atoms $\text{g}^{-1}$ )
<i>grain size: 0.25-0.5 mm</i>					
CREU 1	600; 45	$13.37 \pm 0.10$	$24.23 \pm 0.15$	$0.1266 \pm 0.0008$	$28.45 \pm 0.66$
	800; 20	$9.85 \pm 0.06$	$6.96 \pm 0.11$	$0.1056 \pm 0.0007$	$3.94 \pm 0.15$
	1750; 20	$8.70 \pm 0.05$	$6.22 \pm 0.10$	$0.1066 \pm 0.0010$	$2.83 \pm 0.13$
CREU 1	600; 45	$11.45 \pm 0.07$	$27.78 \pm 0.26$	$0.1292 \pm 0.0007$	$28.41 \pm 0.68$
	800; 20	$8.42 \pm 0.07$	$7.52 \pm 0.13$	$0.1069 \pm 0.0013$	$3.84 \pm 0.16$
	1750; 20	$6.62 \pm 0.04$	$6.70 \pm 0.14$	$0.1059 \pm 0.0010$	$2.48 \pm 0.12$
CREU 1	800; 20	$22.13 \pm 0.12$	$17.15 \pm 0.13$	$0.1171 \pm 0.0003$	$31.41 \pm 0.74$
	1750; 20	$11.16 \pm 0.10$	$5.99 \pm 0.12$	$0.1048 \pm 0.0012$	$3.39 \pm 0.18$
<i>grain size: 0.125-0.25 mm</i>					
CREU 1	600; 45	$8.59 \pm 0.11$	$40.61 \pm 0.34$	$0.1471 \pm 0.0015$	$32.34 \pm 0.86$
	800; 20	$6.78 \pm 0.10$	$6.21 \pm 0.18$	$0.1076 \pm 0.0013$	$2.21 \pm 0.17$
	1750; 20	$8.39 \pm 0.16$	$5.20 \pm 0.11$	$0.1083 \pm 0.0012$	$1.88 \pm 0.18$
CREU 1	600; 45	$9.91 \pm 0.14$	$35.20 \pm 0.31$	$0.1426 \pm 0.0011$	$31.93 \pm 0.88$
	800; 20	$6.24 \pm 0.08$	$6.00 \pm 0.08$	$0.1068 \pm 0.0012$	$1.90 \pm 0.10$
	1750; 20	$8.11 \pm 0.07$	$5.13 \pm 0.15$	$0.1057 \pm 0.0015$	$1.77 \pm 0.15$

### III DANK

Von der Hauptstadt in die Weltstadt, von Bern nach Zürich – ein kleiner Schritt für manche, ein grosser Schritt für einen Berner. Ich habe ihn gewagt, war mir der Grösse meines Abenteuers aber nicht ganz bewusst, als ich nach dem Diplom in jugendlichem Übermut beschloss, in die grosse, weite Welt zu ziehen. Mittlerweile ist mir klar geworden, dass ich die vergangenen vier Jahre in Zürich nur dank der Unterstützung etlicher Personen mehr oder weniger unbeschadet überstanden habe. Ihnen gebührt ein grosses „Merci“.

Bei *Rainer Wieler*, meinem Doktorvater, war die Türe stets offen. Er nahm sich Zeit, meine wissenschaftlichen Fragestellungen und Sorgen anzuhören, und stand mit gutem Rat zur Seite. Seine Kompetenz auf dem Gebiet der Edelgase sowie sein physikalischer und extra-terrestrischer Blickwinkel auf meine irdischen Probleme erhellten so manchen Datensatz. Für die Betreuung meiner Arbeit und das mir entgegengebrachte Vertrauen danke ich ihm ganz herzlich – insbesondere weil ich weiss, dass *Rainer* in der Unterstützung von „Bärner Giele“ sonst eher zurückhaltend ist. Es sei denn, sie spielen gegen den FCB.

*Christian Schlüchter* brachte immer wieder etwas „heimeligi“ Atmosphäre nach Zürich. Obschon sein Terminkalender jenem eines Zürcher Geschäftsmannes in nichts nachsteht und *Christian* wohl mehr in der Welt umherreist als sonst jemand, ist er die Gemütlichkeit in Person. Seine Visiten in Zürich, aber auch die lehrreichen Exkursionen waren bereichernd und brachten eine willkommene Abwechslung. Die Begeisterung für die Quartärgeologie – wie er sie lebt und lehrt – ist ansteckend, und ich bin ihm dankbar dafür. Unvergessen bleibt die Expedition nach Tibet: *Christian* ist und bleibt in Feldgeologie und kulinarischer Experimentierfreudigkeit unerreicht.

*Carlo Baroni* conosce i dintorni di Baia Terra Nova come le tasche dei propri pantaloni. È stato un privilegio poter vivere con lui il periodo nei ghiacci dell'Antartide. Durante il lavoro in Antartide ho potuto non solo approfittare delle sue approfondite conoscenze di geologia glaciale e geomorfologia ma mi è pure stato possibile apprezzare le sue qualità durante i lavori sul campo: Carlo è campione del mondo nel disintegrare massi erratici. Senza di lui la ricerca di campioni da analizzare avrebbe sicuramente avuto un esito meno positivo e voglio ancora ringraziarlo per il suo prezioso operato. Oltre a questo, mi ha introdotto al mito dei cosiddetti „Indigeni“ e ho imparato che il guano dei pinguini non solo puzza, ma può essere

per alcuni aspetti pure interessante. Il lavoro in Antartide è una di quelle cose che a livello geologico mi ha colpito di più e di cui sono rimasto decisamente incantato. L'ambiente di lavoro non ha fatto che migliorare in modo positivo quest'esperienza. *Maria Cristina Salvatore* ha sostenuto i lavori sul campo e si è sempre rivelata una gradevole compagnia durante i picknick (dove cioccolata o torrone erano sempre tenuti pronti per l'evenienza). I miei ringraziamenti vanno inoltre a tutti gli altri partecipanti della XX spedizione italiana in Antartide, che hanno reso indimenticabile il soggiorno presso la Stazione Mario Zucchelli, ed in particolar modo al gruppo che ha mi ha accompagnato sull' „Astrolabe“ durante il terribile viaggio di ritorno attraverso l'oceano.

*Samuel Niedermann* – oder treffender „Neonmann“ – durfte ich als hilfsbereiten Neon-Experten kennenlernen. Sein fundiertes Wissen gab er offenkundig weiter, und er scheute keinen Aufwand, in heiklen Neon-Fragestellungen weiterzuhelfen. Zudem bedanke ich mich bei ihm – wie auch bei *Sean Willett* – für das Übernehmen des Korreferats.

*Peter Oberholzer* schulte mich mit viel Geduld im Umgang mit Tom Dooley und war in mancherlei Hinsicht ein Vorbild. Sein Berner Bike machte ihn von Anfang an sympathisch, und dass er die besten Emails schreibt, ist unumstritten. Bisch e guete Cheib, Pesche. Auch von *Florian Kober* konnte ich einiges über die Analytik von kosmogenen Nukliden lernen und über die Kunst, sich die Laborzeit zu versüssen – etwa mit „Killer-Birnen“. Eine erfolgreiche Laborarbeit war letztlich aber nur möglich dank der stetigen Instandhaltung und Verbesserung der Gerätschaften durch ein wunderbares Team: *Heinrich Baur*, der geistige Vater von Tom Dooley und guter Ratgeber in allen Situationen; *Donat Niederer*, der Notfallelektroniker mit Erste-Hilfe-Koffer; *Urs Menet*, die rechte Hand für mechanische Belange; *Andreas Süsli*, der Mann für alle Öfen; und *Bruno Rütsche*, der Garant für funktionstüchtige Computer.

Bekanntlich gehen einem schwierige Arbeiten leichter von der Hand, wenn das Arbeitsklima im Büro stimmt. *Philipp Heck* sorgte lange Zeit für fernöstliche Schönheiten, die von den Wänden strahlten. Er lancierte die Teebar und sah als einziger auch in der Uni-Mensa immer einen Reiz. Mit *Ansgar Grimberg* verbrachte ich am meisten Zeit im Büro; er ging mit mir auch durch „Dicke-Luft-Zeiten“ und hielt mir die Jahre über stets den Rücken frei. Mit der neuen Bürobelegschaft durch *Yvonne Scheidegger* und dem Sirupier *Matthias Meier* begann eine neue Zeit, die Carac-Ära. Ich wünsche den beiden weiterhin viel Spass im Büro – und dass ihnen der Appetit auf Caracs nie vergehen möge. Ausserhalb des Büros waren es *Ingo*

*Leya, Pieter Vermeesch* und *Veronika Heber*, die den alltäglichen Mensamahlzeiten die Würze verliehen, und *Frowin Pirovino* und *Jörg Rickli*, die stets für gute Laune sorgten. Im Labor waren dafür die Wasserleute zuständig. Allen voran *Rolf Kipfer*, alias *RoKi*. Seine farbenfrohe Haarpracht, sein ruhiges Berner Gemüt und die selbstgebackenen Kuchen erheiterten so manchen Labortag. Aber auch alle anderen, namentlich *Matthias Brennwald*, *Stephan Klump*, *Christian Holzner*, *Helena Amaral* und *Yama Tomonaga*, wurden gerne gesehen und verkürzten die Zeit unter Tage. *Irene Ivanov-Bucher* danke ich für die Unterstützung bei der Mineralienseparation und *Valentina Müller-Weckerle*, *Britt Meyer*, *Barbara Grose* und *Brigitte Schneiter*, den Sekretärinnen in Zürich und Bern, für die Erledigung aller administrativen Angelegenheiten.

Eine wichtige Stütze war für mich der gute Draht zum Institut für Geologie in Bern. Ich war jederzeit willkommen und durfte auf Hilfeleistungen zählen. Die gemeinsamen Projekte im Rahmen paralleler Doktorarbeiten von *Angela Graf* und *Luigia Di Nicola* waren eine grosse Bereicherung für meine Arbeit. Es war stets ein Miteinander mit gegenseitigem Respekt – auch bei unterschiedlichen Daten – und nie ein rivalisierender Konkurrenzkampf. Für die gute Zusammenarbeit mit Angela und Luigia sage ich ganz herzlich „merci“. Für vieles andere danke ich den „Bernern“ *Frank Preusser*, *Naki Akçar*, *Conradin Zahno*, *Andreas Dehnert*, *Sally Lowick*, *Inga Schindelwig* und *Luca Abbühl*. Nicht zu vergessen *Evi Schlüchter* wegen ihrer sagenhaft guten „Happy Ice Age“-Essen und *Ueli Jörin*, der Wahl-Berner, der mich mit dem wöchentlichen Training auch gegen das Ende der Arbeit hin fit gehalten hat.

Nicht selbstverständlich ist die Unterstützung aus meinem privaten Umfeld, die ich immer wieder erfahren durfte und hoffentlich noch lange erfahren darf, die mir Rückhalt bot und mich motivierte. *Meiner ganzen Familie* danke ich für all das, was sie für mich getan hat, für das ständige Interesse an meiner Arbeit und das Teilen von Freud und Leid auf meinem Lebensweg. Dass *Irene* mich während den letzten Jahren auf meinem Weg begleitete, freut mich besonders; sie sorgte für die nötige Abwechslung – und dass ich nie zu lange in Zürich blieb. Aber auch bei meinen Freunden möchte ich mich ganz herzlich bedanken – sie waren immer für mich da. *Merci viu mau Chris, Maya, Stöffu, Flüru, Matti, Benj, Annatina, Urs, Pia, Mamü, Corinne, Löru, Tatjana, Àdàm, Oli* u *GTC Bern Mitglieder*.

Viele liebe Leute unterstützten mich – und standen mir bei auf dem Weg zur Erkenntnis: Der Schritt von der Hauptstadt in die Weltstadt ist doch nicht so gross.





## IV CURRICULUM VITAE

### Stefan Strasky

---

Geburtsdatum	10. Februar 1976
Geburtsort	Bern, Schweiz
Heimatort	Schwändi (GL), Schweiz

---

2003–2007	Doktorat am Institut für Isotopengeologie und Mineralische Rohstoffe der ETH Zürich
1998–2003	Studium der Erdwissenschaften an der Universität Bern
1996–1998	Wirtschaftsgymnasium an der Ecole Supérieure de Commerce in Neuchâtel
1993–1996	Wirtschaftsmittelschule der Stadt Bern
1992–1993	Berufs- Fach- und Fortbildungsschule Bern
1987–1992	Sekundarschule in Ostermundigen/Bern
1983–1987	Primarschule in Ostermundigen

